Power-to-Methane Process Synthesis via Mixed Integer Nonlinear Programming

Dissertation
zur Erlangung des akademischen Grades

doctor rerum naturalium
(Dr. rer. nat.)

von Jennifer Uebbing, M.Sc.
geb. am 09.06.1992 in Soest

genehmigt durch die Fakultät für Mathematik
der Otto-von-Guericke-Universität Magdeburg

Gutachter: Prof. Dr. Sebastian Sager
Prof. Dr. Kai Sundmacher
Prof. Dr. Lorenz T. Biegler

eingereicht am: 11.02.2021
Verteidigung am: 07.05.2021

SUPERVISORS:
Prof. Dr. Sebastian Sager
Prof. Dr. Kai Sundmacher
Dr. Techn. Liisa Rihko-Struckmann

LOCATION:
Magdeburg

TIME FRAME:
February 15, 2017 – February 11, 2021

ZUSAMMENFASSUNG

Um das Ziel der europäischen Union zu erreichen, bis 2050 klimaneutral zu sein, werden erneuerbare Energiequellen stetig weiter ausgebaut. Die Schwankungen in der Energieerzeugung, die mit diesen Energiequellen einhergehen, müssen durch kurz- und langfristige Energiespeicher ausbalanciert werden. Eine Option für langfristige Energiespeicher mit großer Kapazität bieten chemische Energieträger, z.B. Wasserstoff, Methan oder Methanol. Insbesondere Methan, welches durch die Methanisierung (Sabatier Reaktion) von Kohlendioxid und Wasserstoff, welcher durch Elektrolyse von Wasser hergestellt werden kann, zeigt großes Potential als Energieträger. Zum einen ist das Erdgasnetz eine bereits vorhandene Infrastruktur, die zum Speichern und Transport des Gases genutzt werden kann. Des weiteren kann Methan zum Heizen oder als Kraftstoff in Erdgasfahrzeugen genutzt werden und erlaubt so die Kopplung verschiedener Sektoren. Die zusätzlichen chemischen Umwandlungsschritte der Power-to-Methan Prozesskette reduzieren jedoch die Gesamt

ienz des Energiespeichers. Zudem kann Methan aus Erdgas oder Biogas deutlich günstiger hergestellt werden, was Power-to-Methan unwirtschaftlich macht.

Der erste Teil dieser Arbeit widmet sich der Verbesserung von Power-to-Methan Prozessen durch Identifizierung und Optimierung der attraktivsten Prozesse bezüglich Prozesseffizienz und Investitionskosten. Unter Berücksichtigung der Einspeisespezifikationen für das deutsche Erdgasnetz und mit Biogas als Quelle für Kohlendioxid wird die Effizienz verschiedener Prozessalternativen auf Anlagenebene analysiert. Die Ergebnisse der ersten Analyse zeigen, dass Biogas, eine Gasmischung aus Methan und Kohlendioxid, nicht vor der Methanisierung in seine Bestandteile getrennt werden muss. Die Gasmischung kann direkt in den Reaktor geleitet werden, ohne Abtrennung des Methans, was zu einer höheren Prozesseffizienz führt. Dieser Prozess, unter Nutzung von Elektrolyse, Methanisierung, Aufreinigung des Produktgases durch Gastrennung und Wiederverstromung des Methans, hat eine Prozesseffizienz von 23%. Das Ergebnis ist vergleichbar mit einer Studie für Methanol als Energieträger und zeigt eine deutlich höhere energetische Effizienz der Nutzung von Methan.

Der nächste Schritt dieser Arbeit ist die globale Optimierung der Prozessalternativen mittels gemischt-ganzzahliger nichtlinearer Optimierung. Die Arbeit präsentiert eine Superstruktur für den Power-to-Methan Prozess, inklusive indirekter Wärmeintegration. Die Superstruktur beinhaltet 13

alternative, technologisch relevante Prozesselemente in sieben Schichten. Die Ergebnisse dieser Arbeit zeigen die besten Prozesse bezüglich Prozesseffizienz, Investitionskosten und Jahreskosten unter verschiedenen Prozessbedingungen durch die Optimierung des Superstrukturmodels. Die indirekte Wärmeintegration ist ein wichtiger Faktor für die Zielfunktionen in allen Szenarien. Sie bestimmt den Trade-off zwischen Effizienz und Investitionskosten. Ebenso spielen die Spezifikationen des Gasnetzes eine wichtige Rolle für die optimale Prozesskette. Wenn ein Anteil von bis zu 10 vol.-% Wasserstoff ins Gasnetz eingespeist werden darf, werden weniger Prozesselemente zur Gastrennung benötigt, was Investitionskosten senkt und die Prozesseffizienz erhöht. Die beste Prozesseffizienz (65%) von Strom zu Methan wird durch Hochtemperaturelektrolyse, Wärmeintegration und Einspeisung von bis zu 10 vol.-% Wasserstoff ins Gasnetz erreicht.

Der zweite Teil dieser Arbeit fokussiert sich auf die Optimierung von Gastrennung mittels Druckwechseladsorption. Die Druckwechseladsorption ist ein Prozess, der numerisch schwierig zu optimieren ist. Im Kontext von Power-to-Methan Prozessen wird dieser Prozess eingesetzt, um Methan und Kohlendioxid zu trennen. Ein reduziertes Modell wird genutzt, welches für eine Vielzahl von weiteren zyklischen Adsorptionsprozessen Anwendung finden kann, um die Druckwechseladsorption mittels eines Trust-Region Verfahrens zu optimieren. Das Ergebnis zeigt eine Reduzierung der Berechnungszeit des Trust-Region Schrittes gegenüber einer vergleichbaren Studie um drei Größenordnungen von 4800 s auf 4 bis 5 s.

Zuletzt wird ein Algorithmus zur Optimierung von Superstrukturen unter der Nutzung von detaillierten Modellen für Prozesselemente vorgestellt. Der Algorithmus nutzt reduzierte Modelle zur Unterstützung der Optimierung. Diese Arbeit zeigt die nötigen Vorraussetzungen für die Anwendung der Methode zur globalen Optimierung von Superstrukturen in der Verfahrenstechnik.

ABSTRACT

To fulfill the goals of the EU concerning climate neutrality, the share of electrical energy from renewable energy sources has been increasing steadily. The fluctuations in energy supply, which accompany these energy sources, demand for more short and long term energy storage technologies. One option to implement large capacities of long term storage is chemical storage in form of energy carriers, e.g., hydrogen, methane, or methanol. In particular methane, which is produced via methanation (Sabatier reaction) from carbon dioxide and hydrogen available from water electrolysis, shows great potential as an energy carrier. The available infrastructure of the gas grid allows for easy storage and transportation. Furthermore, energy in form of methane can be integrated into other energy sectors (heating and mobility). However, the many conversion steps of the power-to-methane route reduce the process efficiency. Furthermore, cheaper sources of methane, i.e. natural gas and biogas, make the process economically unattractive.

The first part of this thesis aims for the improvement of power-to-methane processes by identification of the most efficient as well as most economically attractive process configurations. Under consideration of the gas specifications of the German gas distribution system, we analyze the exergetic and energetic efficiency of different power-to-methane processes on plant level. Carbon dioxide from biogas plants is considered as carbon source.

The results of the first analysis demonstrate that the mixture of methane and carbon dioxide from anaerobic digestion (AD) can be directly fed-in to the methanation and no prior removal of biogenic methane is necessary. The configuration using the AD mixture is the most efficient process in terms of exergetic efficiency in this study. The process including the electrolysis, methanation, separation via pressure and temperature swing adsorption and gas conversion to electricity has an overall process efficiency of 23%, covering the complete cycle from electricity over chemical storage back to electricity. The obtained efficiency for methanation is clearly higher than that reported in the literature using methanol as chemical intermediate storage.

As a second step we identify the optimal power-to-methane process configuration via global mixed integer optimization. We present a superstructure optimization approach to power-to-methane process design that includes heat integration. The superstructure includes 13 alternative process technologies in seven layers for Power-to-Methane processes at their current stage of development. For different scenarios, the most efficient process in terms of product chemical exergy and the most cost-effective process in terms

of capital and total annual costs are identified. We consider indirect heat integration via utilities, which for all scenarios is determined to be a main contributor to both exergy efficiency and process cost. The product methane must meet the requirements for feed into the gas grid. The requirements for the gas grid have a direct influence on the most efficient process route. The number of necessary process units is reduced, if 10 % hydrogen can be fed to the gas distribution system instead of the 2 % currently specified by law. Furthermore, extent of the heat exchanger network determines the trade-off between efficiency and costs, rather than choice of unit operations. High energetic process efficiencies (65%) can be achieved by combination of SOEC, heat integration, and higher thresholds of H_2 in the gas grid.

In the second part of this thesis, we take a closer look at the pressure swing adsorption unit. Pressure swing adsorption is a numerically challenging gas separation unit, which in the context of power-to-methane can be applied for the pre-treatment of the AD product mixture, as well as for the downstream processing of the methanation product. A reduced model based on equilibrium theory is proposed, which can be applied to optimize a large variety of cyclic adsorption processes, via a trust-region filter (TRF) method. The results show that the reduced model significantly reduces the computational time of the methods trust-region step compared to literature works by three orders of magnitude from over 4800 s to around 4 to 5 s.

Finally, we propose an approach for optimization of high-fidelity superstructures based on branch-and-bound. The algorithm combines different levels of detail for modeling unit operations, which we consider in parts one and two of this thesis. We show the theoretical basis for convergence to global optimality.

PREFACE

The core results of the work described in this thesis are published in scientific journals, including text, data, and graphics. Chapters 4, 5, and 6, and parts of Chapter 2 cite text published by Jennifer Uebbing in the publications listed below. The use of material published in these articles for this dissertation is allowed by the Elsevier journal publishing agreement (P-copyright-v22/2017) as 'personal use'. This section gives an overview over the authors publications and the corresponding overlap with this thesis.

[1] J. Uebbing, L. Rihko-Struckmann, and K. Sundmacher, "Exergetic assessment of CO_2 methanation processes for the chemical storage of renewable energies", Applied Energy, vol. 233-234, 2019.

Chapter 4 and parts of the introduction statement Chapter 2 of this thesis use text, data and figures of this publication. Jennifer Uebbing's contribution to this publication include: software, methodology, visualization, writing of the original draft.

[2] J. Uebbing, L. Rihko-Struckmann, S. Sager, and K. Sundmacher, "CO_2 methanation process synthesis by superstructure optimization", Journal of CO_2 Utilization, vol. 40, 2020.

Chapter 5 and parts of the introduction statement Chapter 2 of this thesis use text, data and figures of this publication. Jennifer Uebbing's contribution to this publication include: software, methodology, visualization, writing of the original draft, conceptualization.

J. Uebbing, L. Biegler, L. Rihko-Struckmann, S. Sager, and K. Sundmacher, "Optimization of pressure swing adsorption via a trust-region filter algorithm and equilibrium theory", submitted to Computers & Chemical Engineering, 2020

Chapter 6 and Section 4.2.2 of this thesis use text, data and figures of this publication. Jennifer Uebbing's contribution to this publication include: software, visualization, writing of the original draft, conceptualization.

CONTENTS

1 INTRODUCTION

1.1 MOTIVATION

The supply of electrical energy originating from renewable energy sources (RES) directly depends on changing environmental conditions such as wind flow and solar irradiation. This results in strong temporal fluctuations and a discrepancy between energy supply and demand, which destabilizes the grid, and impedes the transition towards a more sustainable energy sector [3]. To reach the goals of the EU, namely 32% electrical energy from RES until 2030 and climate neutrality until 2050 [4], an increased implementation of flexible short and long term energy storage is necessary. Furthermore, a key element for reaching the EU's long term goal of climate neutrality, is the integration of RES into heating and mobility sectors. The future energy infrastructure must include cost and energy efficient interfaces between the sectors.

The energy storage technologies available today offer different advantages in terms of power capacity, storage duration, start up time, and potential for utilization of stored energy across sectors. Currently, mechanical storage offers by far the largest potential in terms of power capacity. This is attributed to pumped hydro storage technologies, which have huge capacities for long term storage [4, 5, 6, 7]. However, the implementation of pumped hydro storage depends on suitable geographical conditions and causes significant ecological damage, which limits the expansion in the future [5] and creates demand for alternative long term storage technologies. Furthermore, mechanical storage options have a limited potential for integration of RES into the heating or mobility sectors. Integration of RES into the heating sector is possible via a combination with other energy systems [8, 9], e.g., via utilization of waste heat [10, 11, 12], or via the generation of solar thermal energy [13, 14, 15]. Heat can be stored in form of thermal energy storage, which denotes short term conservation of heat in solids or salts [16], as well as long term storage in phase change materials [3, 17]. More challenging is the integration of RES into the mobility sector. One option is electrochemical storage in form of batteries, which can be placed in electric vehicles. As of today, the technology has significant drawbacks of high cost, high self-discharge rate, and a limited number of charge and discharge cycles [3, 5]. However, the application in the mobility sector via electric vehicles, and

the short response time makes the technology an active field for further development [18, 19].

Because of the current limitations of long term storage technologies and interfaces between the sectors, chemical energy storages have important roles in the future energy transitions scenarios [4, 20, 21]. Chemical energy carriers, i.e., combustible gases or liquids produced via surplus energy from RES, are easier to store and transport than the electrical energy. The process of producing combustible chemicals from RES is referred to as Power-to-X, where X denotes the produced chemical energy carrier. These chemicals can be used as fuels for heating or mobility, as well as for balancing of the electricity supply. As of today, vehicles with natural gas engines are the most ecologically friendly [22] with regards to the German energy mix. Furthermore, they are widely available and require little adjustments from the end user, which increases public acceptance. As a result, vehicles with natural gas engines are considered a bridge technology for the transition towards a sustainable mobility sector [23].

Hydrogen (H_2) [24] is the potential energy carrier with the fewest intermediate conversion steps. In the context of Power-to-X, hydrogen is produced via water electrolysis, free of any carbon emissions. However, the low volumetric energy density at low pressures and the high fugacity of the gas complicate storage and transport [25].

Alternative energy carriers, e.g. methane (CH_4) [26], or methanol (CH_3OH) can be produced from hydrogen. This additional conversion step requires an appropriate carbon source, e.g., carbon dioxide from flue gas, air separation, or product gas of anaerobic digestion, where it is typically considered waste. Furthermore, the conversion step reduces the overall energetic efficiency of the process. However, both methane and methanol are much easier to store and transport than hydrogen: Methane has a higher volumetric energy density than hydrogen at equal pressure, and methanol is in liquid state at ambient conditions [27]. For synthetic methane in particular, which is alike the natural gas from fossil fuels, the gas grid is a well established way for transport and storage [28]. Furthermore, using the established gas grid facilitates sector coupling, i.e., the use of the energy carrier for heating or mobility [29]. All of these advantages make methane a very appealing energy carrier for the transition of the energy systems. Around 30 demonstration units, and over 128 research projects have been reported to exist in Europe so far [29, 30, 31, 32, 33]. Some of which, e.g., the 6 MW e-gas unit in Werlte, Germany [34], produce methane at a product quality suitable for feed to the gas grid. Nonetheless, the cheap alternative of methane from fossil fuels, which are still available in abundance, makes the power-to-methane process economically challenging [31, 35, 36].

1.2 RESEARCH PROBLEM STATEMENT

The goals of this thesis are summarized as follows:

- R1 Exergy efficiency analysis comparing methane and methanol as energy carriers.
- R2 The analysis and scenario-based optimization of power-to-methane processes with respect to thermo-economic aspects such as exergy efficiency, capital costs and total annual costs.
- R3 Conceptual design and optimization of an extensive superstructure, including state-of-the-art technologies and internal heat exchange aiming to identify the most promising process configurations.
- R4 Development of a computationally efficient reduced model for optimization of pressure swing adsorption processes for gas separation.
- R5 Development of a novel superstructure branch-and-bound method to combine detailed unit level models and superstructure optimization.

1.3 THESIS OUTLINE

In Chapter 2 we introduce the power-to-methane process in the context of process systems engineering. We address the methanation reaction, carbon source and electrolyzer technologies needed to produce the reagent hydrogen from RES and water. Furthermore, we present the concept of exergy, which we use to analyze the process efficiency. Chapter 2 gives an overview of the current state of the art in power-to-methane processes.

Chapter 3 discusses briefly the mathematical background of the optimization strategies applied in this thesis. In the context of this dissertation we formulate multiple optimization problems, which have the form of nonlinear programs (NLPs) or mixed integer nonlinear programs (MINLPs). With the exception of the trust-region filter method from Chapter 6 we apply established software libraries to solve the optimization problems. The software libraries include barrier methods for optimization of NLPs to local optimality and branch-and-bound methods for deterministic global optimization of NLPs and MINLPs. Furthermore, we reduce constraints initially expressed as partial differential equations to systems of ordinary differential equations, and solve the obtained ordinary differential equations via integrators in a nonlinear optimization framework. To improve numerical stability, we use the method of direct multiple shooting.

Following these introductions into the background of the thesis, we start addressing the research goals. To get an initial impression of the potential

of different methanation process configurations, we analyze four alternative options in Chapter 4. The configurations include catalytic methanation and gas separation technologies, in particular pressure swing adsorption (PSA). The results allow for a direct comparison with methanol as an energy carrier, addressing the research goal R1.

In Chapter 5 we address the research goals R2 and R3. We expand the process configurations of Chapter 4 to an extensive superstructure. The proposed superstructure includes a large variety of process relevant technologies, as well as a heat exchanger network and utilities for indirect heat integration. We optimize the superstructure with respect to exergy efficiency, capital costs and total annual costs. The results show the effect that different electrolyzer technologies, gas distribution system specifications, and methanation technology have in a power-to-methane framework.

One of the most challenging unit operations to optimize in the power-to-methane process is the PSA unit. In Chapter 6 we optimize the detailed unit level model from Chapter 4 with the aid of a trust-region filter method and a reduced model based on equilibrium theory, according to goal R4. The method is based on previous works on PSA optimization, extended here by the reduced model and applied to a more complex PSA configuration.

In Chapter 7 we combine the results of the previous chapters to introduce a new algorithm for multi-level problem analysis and optimization, which connects different modeling levels, as stated in goal R5. We give the theoretical foundation for application of the proposed algorithm to optimize high-fidelity superstructure optimization problems as they appear in systems engineering with respect to efficiency or economy.

Finally we summarize our findings in Chapter 8.

1.4 BRIEF NOTATION NOTES

Throughout this work we refer to mole fractions with the letter y instead of the often used letter x to avoid any confusion with the general optimization variables, which we refer to as x. We use the notation

$$[x_i]_{i\in\{1,\dots,n\}} := (x_1, \dots, x_n)^\top$$

to shorten some definitions. Furthermore, we use bold letters, e.g., $\mathbf{x}$, when we refer to a single solution candidate instead of the optimization variables x. An extensive list of the notation is attached at the end of this thesis.

2

POWER-TO-METHANE AND EXERGY EFFICIENCY

2.1 POWER-TO-METHANE

Key units of the Power-to-Methane (PtM) conversion process are the methanation reactor, the water electrolyzer, and gas separation units. The process is designed to produce methane, which fulfills the specifications for feed into the gas distribution system (synthetic natural gas). In the following we introduce the key issues to describe the PtM process, as well as process boundaries we apply for the analysis in later chapters.

2.1.1 *Catalytic and Biological Methanation*

The conversion of hydrogen and carbon dioxide to methane via the Sabatier reaction

$$CO_2 + 4H_2 \rightleftharpoons CH_4 + 2H_2O, \qquad \Delta H^0 = -165 \text{ kJ/mol} \tag{1}$$

is carried out in a catalytic or biological methanation reactor.

Many pilot plants, including the aforementioned pilot plant in Werlte, Germany [34], carry out the strongly exothermic reaction in a fixed bed reactor. Nickel-alumina (Ni/Al_2O_3) catalysts are most commonly applied in practice, which are much cheaper than alternative catalysts with very high selectivity, e.g. platinum, or activity, e.g. ruthenium or iron [33].

Nickel-alumina (Ni/Al_2O_3) operate at temperatures between 425 and 975 K [32]. The optimal reactor temperature is a trade-off between favorable chemical equilibrium and a fast reaction rate, as well as avoiding damage to the catalyst by sintering or coking at high temperatures. Figure 1 shows the molar fractions of the components at chemical equilibrium over temperature at different pressures. The products are favored at lower temperatures and higher pressures. On the other hand, the reaction rate, which constraints the achievable conversion of reagents towards the chemical equilibrium, increases with temperature, see Figure 2. In practice, the methanation reaction is carried out below 700 K [32, 37, 38].

However, because of the process costs arising from the compression typically methanation reactors are operated below 8 bar [32, 37, 38].

In this thesis biological methanation is considered as an alternative to catalytic methanation. Biological methanation denotes here the conversion

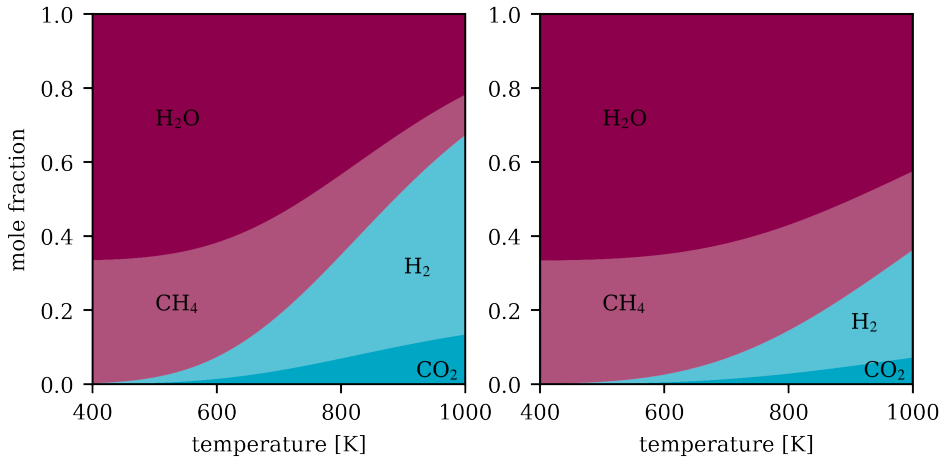

Figure 1: The molar fractions at reaction equilibrium.
The figures show the molar fractions of CO_4, H_2, CH_4, *and* H_2O *at the reaction equilibrium of reaction* (1) *at stoichiometric balance. The water-gas shift reaction, which produces minor concentrations of carbon monoxide, was neglected as a side reaction. The plots show the equilibrium at 1 bar (left) and 15 bar (right) over temperature.*

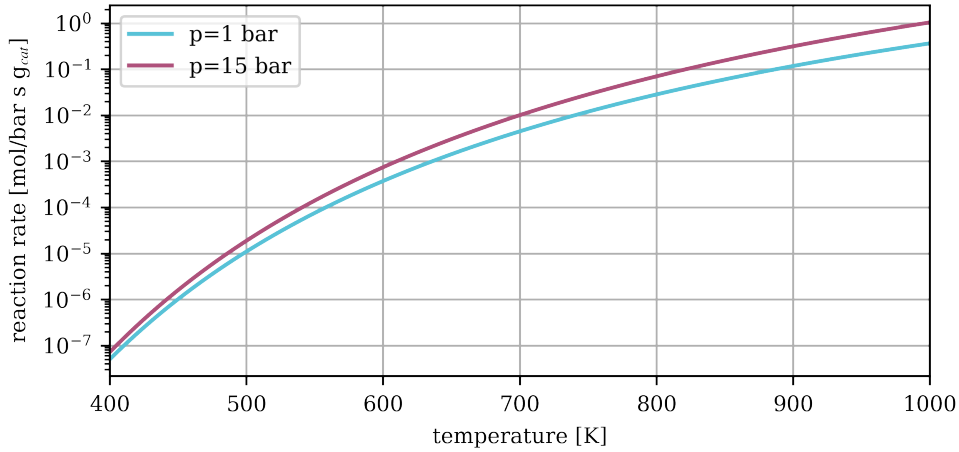

Figure 2: The reaction rate over temperature at reactor inlet.
The figure shows the reaction rate of (1) *according to kinetic equations proposed by Koschany et al. [39] at stoichiometric* CO_2:H_2 *ratio of 1:4 assuming* x_{CH_4}, $x_{H_2O} = 0$.

of hydrogen and carbon dioxide via methanogenic bacteria without the digestion of biomass. The process is typically carried out at moderate conditions of 308 to 370 K and ambient pressure [40, 41]. Variations in type of methanogens, reactor construction, feed, and gas transfer rates in the studies, result in a large range of diversity in the reported conversion rates

in the biological methanation process [31, 42, 43], from low dry product gas concentrations of 58 vol.-% [44] to high concentrations of 96 vol.-% [45, 46].

2.1.2 *Carbon Source*

CO_2, if not otherwise stored, e.g., in form of chemicals or via carbon capture and storage, is often considered as its reuse would reduce carbon emissions to the atmosphere [47]. High concentrations of CO_2 are available in flue gas from industrial processes (cement industry or power plants) [48, 49], in the product gas of anaerobic digestion (AD) from biogas plants or in low concentrations in air (air separation). The extraction of the latter is associated with large costs and therefore not considered for the economically challenging process of power-to-methane. AD product gas, however, is very attractive as a feed gas, because biogas plants produce gas suitable for feed to the gas distribution system, i.e., technologies for gas separation from impurities and odorization are already on site. The AD product gas is a mixture of carbon dioxide, methane, and minor amounts of nitrogen, water, oxygen, ammonia and hydrogen sulfide, of which only oxygen and hydrogen sulfide must be separated prior to feed to the methanation reactor [50] to avoid damage to the process equipment, in particular the catalyst. The gas purification methods on site of a biogas plant remove the smaller impurities to avoid also damage to the gas distribution system. We therefore assume in this thesis that the product gas of anaerobic digestion contains no smaller impurities, e.g. it is a mixture of carbon dioxide and methane. The dry concentrations of the product gas from anaerobic digestion strongly depend on the digested biomass, however 30-50 vol.-% of carbon dioxide can be expected [51]. We assume here that 40 vol.-% of the AD product gas is carbon dioxide corresponding to a molar fraction of $x_{CO_2} = 0.4$.

2.1.3 *Gas Separation*

Gas separation can be applied in different positions of the power-to-methane process, e.g., for the separation of the AD product gas prior to feed to the methanation reactor, or after the methanation reactor to remove reagents, which were not converted. Absorption, adsorption, and membrane separation have been successfully applied on industrial scale [52] for the separation of CH_4/CO_2 mixtures on site of a biogas plant. Absorption can be implemented via chemicals (amine scrubbing) or water (water scrubbing). Typical adsorbents are zeolites or carbon molecular sieves. Furthermore, if the reagent hydrogen should be recovered from the product, adsorbents like activated carbon can be applied [53].

In addition, the gas must be dried from the side product water. We consider condensation in a flash column or temperature swing adsorption to dry the gas.

2.1.4 *Hydrogen Production via Water Electrolysis*

Water electrolysis is a process which uses electrical energy to split water molecules into hydrogen and oxygen according to

$$H_2O \rightarrow H_2 + \frac{1}{2}O_2.$$

The most mature electrolyzer technology are alkaline electrolyzers (AE), which are largely commercially available. AE operate at temperatures of 333 to 353 K and below 30 bar and have reported lifetimes of 30 years [54].

One alternative to AE are polymer electrolyte membrane (PEM) electrolyzers. They operate at the same operating conditions (333-353 K, <30 bar) as AE [54] and are reported to have slightly lower process efficiencies [55]. Because of these similarities we do not include PEM electrolyzers in the presented study. Their benefit in practice is the more flexible operation, which is relevant for dynamic optimization of the PtM process [56], which is out of the scope of this thesis.

Another alternative is high-temperature electrolysis, also called steam electrolysis, via solid oxide electrolyser cells (SOEC). The SOEC operates at much higher temperatures of around 1000 K, which makes the technology suitable for heat integration [57]. The SOEC reports higher efficiency than AE, however it still has a lower technology readiness level than AE or PEM electrolysis. As a result the SOEC electrolyzer is still expensive today, however, Thema et al. [58] predict that the costs for SOEC will reduce drastically in the next years.

2.1.5 *Process Boundaries and Overview*

The specifications of the German gas distribution system according to [59] are

$$\left.\begin{aligned} y_{H_2} &\leqslant 0.02, \\ y_{CO_2} &\leqslant 0.05, \\ 0.95 &\leqslant y_{CH_4}, \\ C_{H_2O} &\leqslant 200\ \mathrm{mg/m^3}, \end{aligned}\right\} \tag{2}$$

where y_i denotes the mole fraction and C_i the concentration of component $i \in \{CO_2, H_2, CH_4, H_2O\}$. All processes designed in this thesis produce synthetic natural gas, which fulfills these specifications, unless otherwise noted.

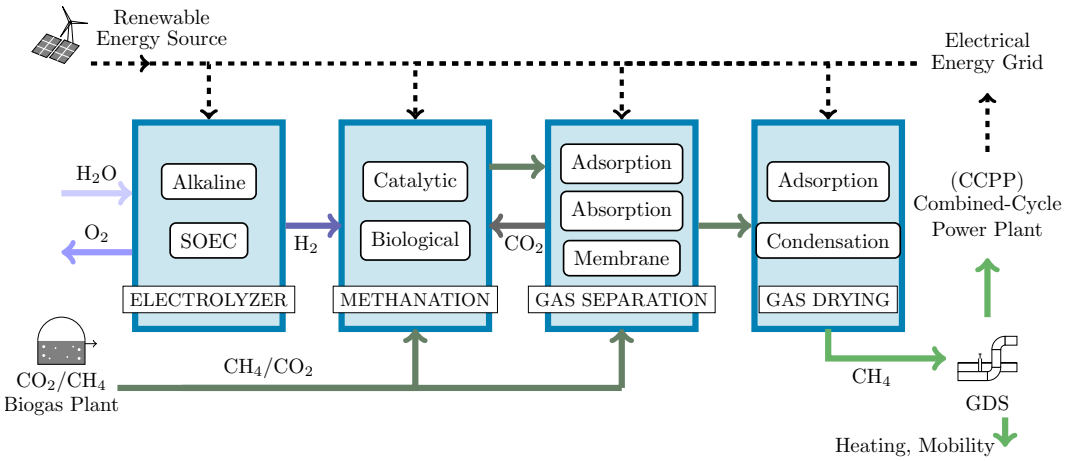

Figure 3: Schematic overview of the process boundaries

The AD product gas (dark green) enters the process free of minor impurities at ambient conditions. It is either directly mixed with hydrogen and supplied to the methanation step, or pre-separated to supply only carbon dioxide for methanation. The boxes indicate the different technologies for the different tasks, also listed in Table 1. The process requires work in form of electrical energy for compression and water electrolysis, here denoted by the dashed lines. Here, GDS denotes the gas distribution system.

Table 1: List of the available technologies.

Task	Unit operation
Water electrolysis	Alkaline electrolyzer (AE)
	High temperature electrolyzer (SOEC)
Methanation	Thermo-catalytic methanation reactor
	Biological methanation reactor
CO_2 separation	Pressure swing adsorption (PSA)
	Water scrubbing (WSC)
	Amine scrubbing (ASC)
	Membrane separation (MEM)
H_2 separation	Pressure swing adsorption (PSA)
Gas drying	Condensation
	Temperature swing adsorption (TSA)

Figure 3 shows a schematic view of the process boundaries. The figure highlights which alternative technologies and connections are considered

to identify the optimal process configuration for production of synthetic natural gas.

2.2 EXERGY EFFICIENCY

The exergy analysis is a unique methodology to estimate not only the classical energy efficiency for a chemical process but to assess the value of all energy contributions in a system [60], first applied as early as 1868 [61]. As opposed to the classical energy approach, exergy analysis considers fully the limitations of the second law of thermodynamics, making qualitative and quantitative assessment of all mass and energy streams in the system possible [62]. This enables the precise identification of irreversibilities in the process paving the way for the thermodynamically feasible energetic improvement.

Exergy analysis allows us to combine the different forms of energy, i.e., electrical energy, heat, and the energy stored in forms of chemical energy carriers, into one unified term. In the exergetic analysis we evaluate all types of streams having energetic value in the system. The exergy value expresses the amount of energy which is thermodynamically convertible to work. In case of electrical energy, the exergetic value is equal to the energetic value. Heat and chemical exergy, however, are determined in relation to a given environment [60], [63].

The exergetic value of a heat stream is directly linked to the temperature level of the heat. The exergy of a unit's heat stream q working in a temperature range from T_{in} to T_{out} above ambient temperature T_{amb} is calculated as

$$e_{heat} = \int_{T_{in}}^{T_{out}} \left(1 - \frac{T_{amb}}{T}\right) q(T) dT. \tag{3}$$

We assume that the heat flow q is constant over the temperature range $[T_{in}, T_{out}]$ and write $q = Q/(T_{out} - T_{in})$ where Q is the overall heat transferred over the corresponding temperature range. For units operating at isothermal conditions at elevated temperature T the heat exergy is then given by

$$e_{heat} = \left(1 - \frac{T_{amb}}{T}\right) Q. \tag{4}$$

This equation corresponds to the efficiency of a Carnot engine [64].

The material streams in a system make the third exergy contribution consisting of kinetic, potential, chemical and physical contributions. The

Table 2: Chemical energy of selected energy carriers [65].
The Table shows chemical exergy $e_{chemical}$ and lower heating value (LHV) of methane, methanol and hydrogen.

Energy carrier	$e_{chemical}$ [kJ/mol]	LHV [kJ/mol]
Methane	831.9	802.3
Hydrogen	236.1	240.0
Methanol	722.3	638.6

chemical exergy of storage media is of foremost interest and is considered in the present analysis, as the possible kinetic and potential exergy of a material stream makes a negligible contribution and cannot be utilized in the same extent. Here, we consider however fully the loss of the physical exergy of the methane product steam due to depressurization prior to the feed into the gas distribution system. Assuming perfect gas, the physical exergy is given by

$$e_{physical} = c_p \left((T - T_{amb}) - T_{amb} \ln \left(\frac{T}{T_{amb}} \right) \right) + R T_{amb} \ln \left(\frac{p}{p_{amb}} \right). \tag{5}$$

Here c_p denotes the specific heat capacity of the material stream and $R = 8.314$ kJ/K/mol the gas constant. We assume here that the gas in the pipes cools down to ambient temperature $T = T_{amb}$, so that the physical exergy is solely dependent on pressure. The remaining expression for the physical exergy of gas at pressure p corresponds to the work demand of compressing the gas from p_{amb} to p at isothermal conditions.

Table 2 summarizes the chemical exergy of different energy carriers, as calculated via the combustion reaction with oxygen [65]. The chemical exergy of a mixture is simply given by

$$e_{chemical} = \sum_i e^i_{chemical} y_i,$$

where y_i denotes the mole fraction of component i in the mixture.

3 MATHEMATICAL OPTIMIZATION

In this chapter we provide a brief overview over the mathematical methods used in this thesis to formulate and solve mathematical optimization problems. We assume that the reader is familiar with Newton or quasi-Newton methods, convexity, and the concept of global and local optimality. For a more detailed overview of nonlinear optimization we refer to Nocedal and Wright [66], which was used as a reference for Section 3.1.

3.1 NONLINEAR PROGRAMMING

Constrained nonlinear programming refers to finding the minimum of an objective function $f : \mathbb{R}^n \longrightarrow \mathbb{R}$ subject to inequality constraints $g : \mathbb{R}^n \longrightarrow \mathbb{R}^{m_g}$ and/or equality constraints $h : \mathbb{R}^n \longrightarrow \mathbb{R}^{m_h}$, where at least one of the functions f, g, and h is nonlinear. A general nonlinear program (NLP) can be written in the form

$$\begin{aligned} \min_{x \in \mathbb{R}^n} \quad & f(x) \\ \text{s.t.} \quad & g(x) \leqslant 0 \\ & h(x) = 0. \end{aligned} \tag{nlp}$$

We assume here that f, g, and h are sufficiently smooth on the feasible set $\Omega = \{x \in \mathbb{R}^n \mid g(x) \leqslant 0,\ h(x) = 0\}$ and that the feasible set Ω is closed and bounded. A bounded feasible set is necessary to guarantee the convergence of most conventional solving strategies and is easy to implement in practice, e.g., by including box constraints on the variables

$$lb \leqslant x \leqslant ub, \qquad lb, ub \in \mathbb{R}^n, \tag{6}$$

in the inequalities g. In the following sections, we briefly introduce the conditions for local optimality, before outlining the method used in this thesis for finding local solutions of NLPs.

3.1.1 *Optimality Conditions*

The first step to identifying a solution candidate $x \in \Omega$ as a local optimum of (nlp), is the check of a constraint qualification (CQ), also referred to as regularity condition. A large variety of CQs exist, some of which imply

others. The choice of which CQ to check is often a compromise between the simplicity of performing the check, and the strength of the CQ, where weaker conditions are preferred due to being less restrictive. One commonly applied example for a CQ is the following linear independence constraint qualification (LICQ).

Definition 3.1.1. *Linear independence constraint qualification (LICQ): Let $x \in \Omega$ be a feasible point of (nlp) and $\mathcal{I}$ be the index set of active inequality constraints, i.e., $g_i(x) = 0 \iff i \in \mathcal{I}$. The LICQ hold in x, if the gradients $\nabla h(x)$ and $\nabla g_{\mathcal{I}}(x)$ are linearly independent.*

The LICQ is a strong assumption implying a variety of weaker CQs, such as the Mangasarian-Fromovitz constraint qualification (MFCQ).

Definition 3.1.2. *Mangasarian-Fromovitz constraint qualification (MFCQ): Let $x \in \Omega$ be a feasible point of (nlp) and $\mathcal{I}$ be the index set of active inequality constraints, i.e., $g_i(x) = 0 \iff i \in \mathcal{I}$. The MFCQ hold in x, if the gradients $\nabla h(x)$ are linear independent and*

$$\begin{aligned} \nabla g_{\mathcal{I}}(x)^\top u &> 0, \\ \nabla h(x)^\top u &= 0 \end{aligned}$$

holds for a $u \in \mathbb{R}^n$.

The constraint qualifications are indicators for the regularity of (nlp) in x and a necessary assumption for the optimality conditions. Let us define the Lagrangian function $\mathcal{L} : \mathbb{R}^n \times \mathbb{R}^{m_g} \times \mathbb{R}^{m_h} \longrightarrow \mathbb{R}$ with Lagrange multipliers $\mu \in \mathbb{R}^{m_g}$ and $\lambda \in \mathbb{R}^{m_h}$ corresponding to (nlp) as

$$\mathcal{L}(x, \mu, \lambda) := f(x) + \sum_{i=1}^{m_g} \mu_i g_i(x) + \sum_{j=1}^{m_h} \lambda_j h_j(x).$$

Then we can introduce the necessary first order condition, also referred to as Karush-Kuhn-Tucker condition, as follows:

Theorem 3.1.1. *Karush-Kuhn-Tucker (KKT) condition: Let a constraint qualification hold in a local optimum $x \in \Omega$ of (nlp). Then the Karush-Kuhn-Tucker condition*

$$\begin{aligned} 0 &= \nabla_x \mathcal{L}(x, \mu, \lambda) = \nabla f(x) + \sum_{i=1}^{m_g} \mu_i \nabla g_i(x) + \sum_{j=1}^{m_h} \lambda_j \nabla h_j(x), \\ 0 &\leqslant \mu_i \quad \forall i \in \{1, \dots, m_g\}, \\ 0 &= \mu_i g_i(x) \quad \forall i \in \{1, \dots, m_g\} \end{aligned}$$

holds in x for some $\mu \in \mathbb{R}^m_g$ and $\lambda \in \mathbb{R}^m_h$. We call μ and λ the Lagrange multipliers.

If the LICQ hold in $x \in \Omega$, then the corresponding Lagrange multipliers μ and λ are uniquely determined by the KKT condition. We call a point $x \in \Omega$, which fulfills the KKT condition, a KKT-point. The KKT condition is not only fulfilled by local minima of (nlp), but also by other stationary points of the Lagrangian, i.e., local maxima or saddle points. Nonetheless, numerical solvers generally focus on finding a KKT-point of (nlp). By creating a series of iterates with descending objective value, the limit point of the iteration is expected to be a minimum in practice. A KKT-point, which fulfills the following second order sufficient condition, is indeed a local minimum.

Theorem 3.1.2. *Second order necessary condition: Let $x \in \Omega$ be a KKT-point of (nlp), for which the LICQ hold, with Lagrange multipliers μ and λ. The second order necessary condition is fulfilled in x, if*

$$u^\top \nabla^2_{xx} \mathcal{L}(x, \mu, \lambda) u \geqslant 0 \qquad \forall u \in \mathcal{C},$$

where

$$\mathcal{C} := \left\{ u \in \mathbb{R}^n \;\middle|\; \left(\nabla g_{\mathcal{I}}(x)^\top, \nabla h(x)^\top\right)^\top u = 0, \; \mathcal{I} \subseteq \{1, \dots, m_g\} \text{ with } g_{\mathcal{I}}(x) = 0 \right\}.$$

3.1.2 *Finding a Local Optimum of an NLP*

The two most common and efficient in practice approaches for solving (nlp) to local optimality are active-set SQP methods and interior-point methods.

Active-set SQP methods focus on determining the active set, i.e., the inequality constraints g that are active in the optimal solution. They iterate over the solutions of quadratic substitute models, utilizing derivative information of f, g, and h. An active-set SQP is implemented for example in the NAG library [67].

Interior-point methods, in particular barrier methods, are a wide-spread alternative to active-set methods for solving NLPs. The solver IPOPT [68], which is the solver we apply in this thesis (Ipopt 3.12.12), uses a barrier approach. For this reason, we take a closer look at this particular method:

We call

$$\begin{aligned} \min_{x \in \mathbb{R}^n, s \in \mathbb{R}^{m_g}} \quad & f(x) - \tau \sum_{i=1}^{m_g} \ln s_i \\ \text{s.t.} \quad & g(x) - s = 0 \\ & h(x) = 0 \end{aligned} \tag{7}$$

the barrier problem to (nlp). The barrier problem (7) differs from (nlp) by adding a slack s to the inequality constraints g and the barrier term

$-\tau \sum_{i=1}^{m_g} \ln s_i$ with parameter $\tau > 0$ to the objective, which assures that the slack s remains positive. The barrier method finds a local solution of (nlp) by iterating over a series of barrier parameters $\tau_k \longrightarrow 0$ and finding an approximate solution to the corresponding barrier problem (7), starting from the approximate solution of the previous barrier problem. The solution of (7) converges to a solution of (nlp) for $\tau_k \longrightarrow 0$. In practice, the solution to the barrier problem is approximated by applying a few iterations of a Newton or quasi-Newton method towards solving the KKT conditions of the problem (7), which are given by

$$\begin{aligned} \nabla f(x) + \sum_{i=1}^{m_g} \mu_i \nabla g_i(x) + \sum_{j=1}^{m_h} \lambda_j \nabla h_j(x) &= 0, \\ \mu_i s_i - \tau &= 0, \qquad \forall i \in \{1, \dots, m_g\}, \\ g(x) - s &= 0, \\ h(x) &= 0. \end{aligned}$$

To guarantee global convergence of the algorithm, IPOPT uses a line-search filter method when solving the KKT conditions of the problem (7). Let $x_{k,l}$ be the current solution candidate, where the index l denotes the iteration of the Newton or quasi-Newton method solving (7) with barrier parameter τ_k. We call the set

$$\mathcal{F}_{k,l} := \{(f(x_{k,i}), \theta(x_{k,i})) \mid i \in \{1, \dots, l\}\}$$

the filter set, where $\theta(x) = \| \left(h(x)^\top, (g(x) - s)^\top\right)^\top \|$ is called the feasibility measure. As by definition, the filter set contains the objective values and feasibility measures of all previous iterates of the Newton or quasi-Newton method for the same barrier parameter τ_k. A proposed step in direction $d_{k,l}$

$$\hat{x}_{k,l} = x_{k,l} + \alpha d_{k,l}$$

is accepted by the filter, if a sufficient progress was made with respect to feasibility

$$\theta(\hat{x}_{k,l}) \leqslant (1 - \gamma_\theta)\theta(x_{k,i}) \tag{8}$$

or optimality

$$f(\hat{x}_{k,l}) \leqslant f(x_{k,i}) - \gamma_f \theta(x_{k,i}) \tag{9}$$

with fixed parameters $\gamma_\theta, \gamma_f \in (0, 1)$ for all $i \in \{1, \dots, l\}$. If a new step is rejected the step width α is reduced, until a point is acceptable to the filter.

If the feasibility measure $\theta(x_{k,l})$ is below a predefined threshold, the Armijo condition

$$f(\hat{x}_k) \leqslant f(x_k) + \gamma_A \alpha \nabla\theta(x_k)^\top d_k \tag{10}$$

replaces the filter condition to determine an acceptable step width. Here $\gamma_A \in (0, 1/2)$ is another fixed parameter. The software IPOPT utilizes additional strategies to make sure that solutions to the barrier problem exist, to make corrections if proposed steps are rejected, and to restore feasibility. Under standard conditions, the algorithm reaches superlinear convergence. We refer to [68] for a more detailed overview of the software. If the optimization problem (nlp) is linear or smooth and convex, IPOPT will give a global optimal solution. For non-convex optimization problems, however, other methods must be used if a global solution if desired. One method for global optimization of non-convex problems is the spatial branch-and-bound method, which we introduce in Section 3.3. Beforehand we discuss a different class of optimization problem for which the branch-and-bound method can be applied.

3.2 MIXED INTEGER PROGRAMMING

An optimization problem, where a subset of the variables is from a discrete domain, i.e., $x_I \in \mathbb{Z}^{n_I}$, is called a mixed integer program. Here $I = \{1, \dots, n_I\}$ denotes the index set of the discrete variables. Mixed integer programs have many applications in practice, such as scheduling problems, network design, or industrial production [69, 70, 71]. In many applications, including this thesis, the integer variables are binary, i.e., $x_I \in \{0, 1\}^{n_I}$. Other integer variables $v \in \mathbb{Z}$ can be reformulated into binary form, e.g., via terms of the form

$$v = \sum_{i \in I} 2^{i-1} x_i,$$

where x_i are binary variables. A general mixed integer optimization problem of the form

$$\begin{aligned} \min_x \quad & f(x) \\ \text{s.t.} \quad & g(x) \leqslant 0 \\ & h(x) = 0 \\ & x_I \in \{0, 1\}^{n_I}, \end{aligned}$$

similar to (nlp) with nonlinear objective function f, can be reformulated to have a linear objective by introducing a new variable x_f, which becomes the

new objective, and an additional constraint $g_f(x) = f(x) - x_f \leqslant 0$. Furthermore, the equality constraints h can be replaced by inequality constraints of the form $g_{h+} := h \leqslant 0$, $g_{h-} := -h \leqslant 0$. Thus, we write a general mixed integer program with binary discrete variables as

$$\begin{aligned} \min_x \quad & c^\top x \\ \text{s.t.} \quad & x \in \Omega = \{x \in \mathbb{R}^n \mid g(x) \leqslant 0,\ x_I \in \{0,1\}^{n_I}\}. \end{aligned} \tag{minlp}$$

If g is linear, we call (minlp) a mixed integer linear program (MILP). Otherwise, (minlp) describes a mixed integer nonlinear program (MINLP). MINLPs combine the difficulties of nonlinear optimization problems (NLP) and mixed integer linear problems (MILP), which also belong to the class of NP-hard problems. Consequently, solving MINLPs is very challenging. While we can reformulate (minlp) to an NLP via constraints of the form $x_I(1 - x_I) = 0$, the strategies we introduced for solving NLPs in Section 3.1 can not be expected to give good solutions. The disconnected domain of the problem makes it impossible for interior point methods, which we introduced in Section 3.1.2, to search in the complete problem domain. Furthermore, mixed integer programs can not be solved by omitting the constraint $x_I \in \{0,1\}^{n_I}$ of (minlp), solving the problem via a solution strategy for NLPs, and then rounding to the closest integer solution, shown in Example 3.2.1.

Example 3.2.1. *Example for a simple MILP*

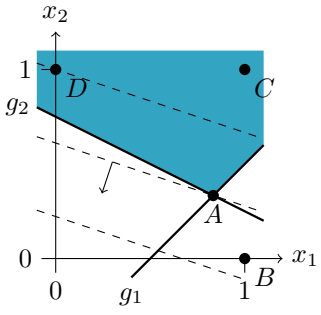

$$\begin{aligned} \min_x \quad & x_3 \\ \text{s.t.} \quad & g_1(x) = x_1 - x_2 - 0.5 \leqslant 0 \\ & g_2(x) = -x_1/2 - x_2 + 0.75 \leqslant 0 \\ & g_3(x) = x_1/3 + x_2 - x_3 \leqslant 0 \\ & x_1, x_2 \in \{0,1\} \\ & 0 \leqslant x_3 \leqslant 10 \end{aligned} \tag{11}$$

Figure 4: Example for a simple MILP

Let us consider the MILP (11). Figure 4 shows the problem in the space of the discrete variables x_1 and x_2. The dashed lines indicate the level sets of the objective, which decreases in the direction of the indicated gradient. The light blue area are points, which are feasible if the integer constraints $x_1, x_2 \in \{0,1\}$ are omitted. We refer to the linear program, gained from (11) by omitting the integer constraints, as relaxed problem. The solution of the relaxed problem is the point $A = (5/6, 1/3)$. The figure shows that the next integer solution $B = (1,0)$, which is obtained from

A via rounding, is not feasible with respect to the inequality constraints g_1 and g_2. Furthermore, the closest feasible solution $C = (1, 1)$ is not optimal. The optimal solution of the MILP is $D = (0, 1)$ as the dashed level sets indicate.

A large variety of strategies have been developed especially for solving (minlp). If the feasible region of (minlp) is a convex set, strategies like outer approximation [72, 73], extended cutting plane [74], or generalized benders decomposition [75] can find the optimal solution. Extended cutting plane can also be applied to special classes of non-convex MINLPs [76]. For general mixed integer problems, however, branch-and-bound methods are most commonly applied.

3.3 BRANCH-AND-BOUND

Branch-and-bound is a more general name for a large group of algorithms, which try to find the global optimum of a non-convex optimization problem via a divide-and-conquer approach. The key steps of the branch-and-bound algorithm are branching, bounding, and pruning. We discuss all steps and the pseudocode, before giving brief examples of the method in Sections 3.3.1 and 3.3.2.

Branching: The branch-and-bound method recursively divides the domain of an optimization problem to get sub-problems on smaller domains. This process is called branching. To illustrate this process, let $P(\Omega)$ be an optimization problem of the form (minlp) over the bounded and closed domain Ω with global optimal solution $x_\Omega \in \Omega$. Branching on $P(\Omega)$ creates new sub-problems $P(\Omega_i)$ with respect to the same objective function on domains $\Omega_i \subset \Omega$ with

$$\cup_i \Omega_i = \Omega$$

and global optimal solutions $x_{\Omega_i} \in \Omega_i$. Then for the minimum of $P(\Omega)$

$$x_\Omega = \min_i \{x_{\Omega_i}\}$$

holds. Typically, but not necessarily, the interiors of the new domains Ω_i are disjoint. The branching process is repeated recursively on the sub-problems, to create problems on smaller and smaller domains. We refer to the relation of the constructed optimization problems as branching tree with the optimization problems as nodes, see Figure 5.

Bounding: During the run of a branch-and-bound method, bounds on the optimal value are calculated. An upper bound UB on the optimal solution

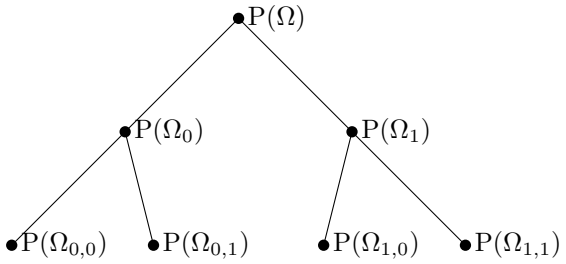

Figure 5: Example for a branching tree

value $c^\top x_\Omega$ is given by the objective value $c^\top x$ of any feasible point $x \in \Omega$. The algorithm uses the objective value of the best feasible point found at the current iteration as a global upper bound on the optimal solution. Lower bounds on the optimal solution value are derived at all nodes in the branching tree individually. They underestimate the lowest value, which the objective can reach on the domain of the corresponding node. To find a lower bound to an optimization problem of the form (minlp), we consider the relaxed problem given by

$$\begin{aligned} \min_x \quad & c^\top x \\ \text{s.t.} \quad & x \in \widetilde{\Omega} = \{x \in \mathbb{R}^n \mid \widetilde{g}(x) \leqslant 0,\ x_I \in \mathcal{X}_I\}, \end{aligned} \tag{minlpr}$$

where $\widetilde{g}(x) \leqslant g(x)$ on the problem domain and $\{0,1\}^{n_I} \subset \mathcal{X}_I \subset \mathbb{R}^{n_I}$. Because for the feasible sets of the problems $\Omega \subset \widetilde{\Omega}$ holds, the global optimum of (minlpr) is a lower bound on the global optimum of (minlp). By constructing a convex relaxed problem, (minlpr) can be solved to global optimality with active-set SQP or interior point methods, or, in the case of a linear relaxation, with the dual simplex algorithm. The global lower bound LB on the complete branching tree is then given by the smallest lower bound of all leaf nodes of the branching tree. By definition, $LB \leqslant c^\top x$ holds for all $x \in \Omega_{(\text{minlp})}$. The branch-and-bound algorithm terminates successfully, if the gap between the bounds is below a predefined threshold $UB - LB < \epsilon_{tol}$. Let x denote the solution candidate with objective value $c^\top x = UB$. At this point $c^\top x - c^\top x \leqslant UB - LB < \epsilon_{tol}$ holds for all $x \in \Omega_{(\text{minlp})}$ and x is an ϵ-optimal solution of (minlp).

Pruning: By dividing the domain of (minlp) recursively, the branching tree grows exponentially. To reduce the number of problems which need to be solved, and thus to improve computational efficiency, the branching tree is pruned. A node is discarded for further branching, i.e., it is pruned from the branching tree, if the created sub-problem is infeasible or the lower bound of a node is larger than the global upper bound UB. To prune nodes as early as possible, many solvers include heuristics to find good upper bounds.

The implementation of branching and bounding differs in practice, depending on the problem class to be solved and the choice of solution strategy. An example for a branch-and-bound pseudo-code is given by Algorithm 1, where $\widetilde{P}$ denotes a relaxed problem to P on the domain $\widetilde{\Omega}$.

Algorithm 1 Branch-and-Bound Method

procedure BRANCH-AND-BOUND METHOD
  Initialize $LB = -\infty$, $UB = \infty$, node queue $\mathcal{P} = \{P(\Omega)\}$, $LB_{P(\Omega)} = -\infty$
  while $|\mathcal{P}| > 0$ and $UB - LB > \epsilon$ **do**
    $LB \longleftarrow \min\{ LB_P : P \in \mathcal{P} \}$
    Choose $P \in \mathcal{P}$, $\mathcal{P} \longleftarrow \mathcal{P} \setminus P$
    Solve $\widetilde{P}$, save lower bound $LB_P \longleftarrow c^\top \mathbf{x}_{\widetilde{\Omega}}$ (if infeasible $LB_P \longleftarrow \infty$)
    if $LB_P \leqslant UB$ **then**
      Branch on P: create new subproblems P_i, $i = 1, \ldots, k$
      $\mathcal{P} \longleftarrow \mathcal{P} \cup P_i$
      $LB_{P_i} \longleftarrow LB_P$
      if A feasible solution $x \in \Omega$ is found **then**
        if $c^\top x < UB$ **then**
          $UB \longleftarrow c^\top x$
          $\mathbf{x}_\Omega \longleftarrow x$
  if $UB \leqslant \infty$ **then**
    return $\mathbf{x}_\Omega$
  else
    Infeasible

3.3.1 *Branch-and-Bound for Optimization of MILPs and Convex MINLPs*

Let us consider a convex MINLP of the from (minlp) as the root, and at the start of the algorithm also a leaf, of the branching tree. During the branching step the branch-and-bound algorithm selects a node in the tree and a discrete variable x_i, $i \in J$ to branch on. Here, $J \subset I$ denotes the index set of discrete variables, which have not been branched on in the selected node of the branching tree. Two new sub-problems are created at the node by fixing $x_i = 0$ in one sub-problem and $x_i = 1$ in the other. The sub-problems are added to the branching tree as child nodes of the previously selected node. Tight convex relaxations to a node, needed to derive lower bounds, are given by replacing the constraint $x_J \in \{0,1\}^{|J|}$ by $x_J \in [0,1]^{|J|}$. If the constraints g are convex, branching on the discrete variables is sufficient to find the global optimal solution of (minlp). The continuous variables can be handled by

local optimization strategies, as introduced in Section 3.1.2, as soon as the integer variables are fixed.

Example 3.3.1. *Solving a simple MILP via branch-and-bound*
Let us consider the MILP

$$\begin{aligned} \min_{x} \quad & x_3 \\ \text{s.t.} \quad & g_1(x) = x_1 - x_2 - 0.5 \leqslant 0 \\ & g_2(x) = -x_1/2 - x_2 + 0.75 \leqslant 0 \\ & g_3(x) = x_1/3 + x_2 - x_3 \leqslant 0 \\ & x_1, x_2 \in \{0, 1\} \\ & 0 \leqslant x_3 \leqslant 10 \end{aligned} \tag{P(Ω)}$$

from Example 3.2.1 again. The relaxed problem, where the integer constraints $x_1, x_2 \in \{0, 1\}$ *are replaced by the convex hull* $x_1, x_2 \in [0, 1]$*, has the optimal solution* $x = [5/6, 1/3, 11/18]$*, which was indicated by the point* A *in Example 3.2.1. The objective value of the relaxed problem* $x_3 = 11/18$ *gives a lower bound* LB *on the optimal solution of* (P(Ω)). *Let us furthermore assume that we have an upper bound* $UB = 4/3$ *given by the feasible point* $x = [1, 1, 4/3]$*. Branching on* (P(Ω)) *by splitting the domain* $\{0, 1\}$ *of variable* x_2 *into* $x_2 = 0$ *and* $x_2 = 1$ *results in two new sub-problems.*

$$\begin{aligned} \min_{x} \quad & x_3 \\ \text{s.t.} \quad & g_1(x) = x_1 - 0.5 \leqslant 0 \\ & g_2(x) = -x_1/2 + 0.75 \leqslant 0 \\ & g_3(x) = x_1/3 - x_3 \leqslant 0 \\ & x_1 \in \{0, 1\} \\ & x_2 = 0 \\ & 0 \leqslant x_3 \leqslant 10 \end{aligned} \tag{P(Ω_0)}$$

$$\begin{aligned} \min_{x} \quad & x_3 \\ \text{s.t.} \quad & g_1(x) = x_1 - 1.5 \leqslant 0 \\ & g_2(x) = -x_1/2 - 0.25 \leqslant 0 \\ & g_3(x) = x_1/3 + 1 - x_3 \leqslant 0 \\ & x_1 \in \{0, 1\} \\ & x_2 = 1 \\ & 0 \leqslant x_3 \leqslant 10 \end{aligned} \tag{P(Ω_1)}$$

Problem ($P(\Omega_0)$) *is infeasible, because constraint* g_2 *can not be fulfilled for* $x_1 \in \{0,1\}$. *The node* ($P(\Omega_0)$) *is pruned from the branching tree, i.e., not considered for further branching. Relaxing the integer constraint* $x_1 \in \{0,1\}$ *of problem* ($P(\Omega_1)$) *results in a relaxed problem with optimal solution* $x = [0,1,1]$, *which gives the lower bound* $LB_1 = LB = 1$. *Because* $x = [0,1,1]$ *is also a feasible point of* ($P(\Omega)$), *the upper bound is updated* ($UB = 1$). *The branch-and-bound method terminates successfully with the optimal solution* $x_\Omega = [0,1,1]$.

3.3.2 *Spatial Branch-and-Bound for Global Optimization of NLPs and MINLPs*

The branch-and-bound algorithm can be used for global optimization of non-convex NLPs and MINLPs by branching on the continuous variables. Let us consider problem (nlp) again, with box constraints $lb_i < ub_i$ on each variable x_i, $i \in \{1,\dots,n\}$. To create new sub-problems from any leaf node in the branching tree, one variable x_i, $i \in \{1,\dots,n\}$, is selected and its domain $[lb_i, ub_i]$ is split into two sets $[lb_i, ub_i^{new}]$, $[lb_i^{new}, ub_i]$ with $ub_i^{new} = lb_i^{new}$. A branch-and-bound algorithm, which includes branching on continuous variables, is referred to as spatial branch-and-bound. To solve non-convex MINLPs, branching on discrete and continuous variables is necessary. Convex envelopes are for example linear or quadratic functions, underestimating the problem constraints on the problem domain.

Example 3.3.2. *Spatial branch-and-bound with quadratic underestimators*
Let us consider a non-convex, univariate function $f(x)$ *on a domain* $x \in \Omega = [lb, ub]$, *see Figure 6. The root problem* ($P(\Omega)$) *is the minimization of this function* f *on the complete domain. Let an upper bound* UB *on the optimal value be given, e.g. via the local minimization of the objective function by use of a solver as introduced in Section 3.1.2. The domain is split into two subsets* $\Omega_0 = [lb_0, ub_0]$ *and* $\Omega_1 = [lb_1, ub_1]$, *which are the domains of the new sub-problems. Convex relaxations* $f_i(x) \leqslant f(x)$, $x \in \Omega_i$ *for the new problems* ($P(\Omega_0)$) *and* ($P(\Omega_1)$) *are derived, here marked with blue lines. The optimal solutions of* ($P(\Omega_0)$) *and* ($P(\Omega_1)$) *give new lower bounds* LB_0 *and* LB_1 *on the optimal value of the objective in this domain. In this case* $UB < LB_1$ *holds. This implies that on the domain* $\Omega_1 = [lb_1, ub_1]$ *no solution candidate exists, with a function value below the current best solution candidate. The node* ($P(\Omega_1)$) *is pruned from the branching tree and the search continues on* ($P(\Omega_0)$). *Note, that while this example shows quadratic envelopes, other convex relaxations, e.g. linear envelopes, can also be applied.*

Finding tight convex envelopes to NLPs or MINLPs is a challenging task in practice. Many approaches exploit certain problem structures to get tight relaxations. One method for finding convex envelopes, called α branch-and-

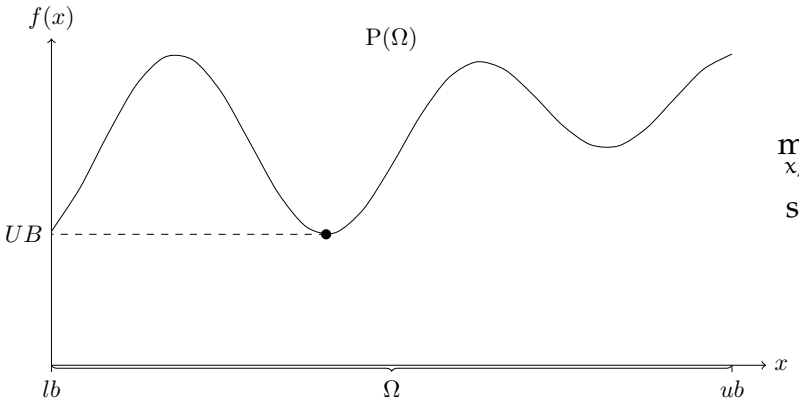

$$\begin{aligned} \min_{x, x_f} \quad & x_f \\ \text{s.t.} \quad & f(x) - x_f \leqslant 0 \\ & lb \leqslant x \leqslant ub \\ & (P(\Omega)) \end{aligned}$$

a) Root node problem $P(\Omega)$

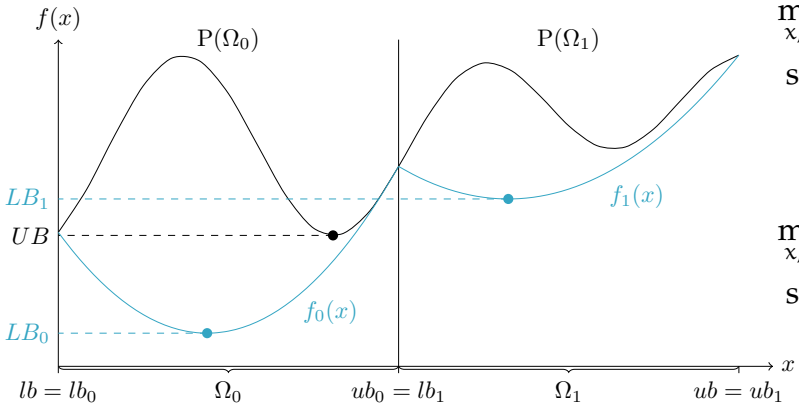

$$\begin{aligned} \min_{x, x_f} \quad & x_f \\ \text{s.t.} \quad & f(x) - x_f \leqslant 0 \\ & lb_0 \leqslant x \leqslant ub_0 \\ & (P(\Omega_0)) \end{aligned}$$

$$\begin{aligned} \min_{x, x_f} \quad & x_f \\ \text{s.t.} \quad & f(x) - x_f \leqslant 0 \\ & lb_1 \leqslant x \leqslant ub_1 \\ & (P(\Omega_1)) \end{aligned}$$

b) Sub-problems $P(\Omega_0)$ and $P(\Omega_1)$

Figure 6: Example for branching and bounding via spatial branch-and-bound

bound, is implemented in the solver ANTIGONE [77, 78]. Idea of the α branch-and-bound is, to find parameters $\alpha \in \mathbb{R}^n$ such that

$$G(x) := g(x) - \sum_{i=1}^{n} \alpha_i (ub_i - x_i)(x_i - lb_i)$$

is convex. To do so, the algorithm uses second order derivative information of the constraint g. Other solvers like Couenne [79] and SCIP [80] use linear underestimators to get lower bounds.

3.3.3 *Branch-and-Bound Solver SCIP*

To solve the MINLPs, we use the software package Solving Constraint Integer Programs (SCIP) [80, 81, 82] (SCIPOpt Suite 6.0.1) together with the Python interface PySCIPOpt [83] (PySCIPOpt 1.2.0). SCIP is a state-of-the-art branch-and-bound solver, with extensive presolving. In the numerical

analysis carried out by Kronqvist [84], the solver SCIP showed performance comparative to the commercial solver Baron [85] for convex problems. As an open-source software, SCIP has the advantage over commercial solvers of being easily extendable by the user. We refer to Vigerske et al. [82] as a reference for the following underestimators used in SCIP.

SCIP uses a spatial branch-and-bound, where linear constraints, also called cuts, are added to the relaxed problem formulation, when constraints are violated. The SCIP algorithm reformulates the problem via expression trees to analyze, which functions are known to be convex or concave. This information makes it possible, to apply tighter bounds on the constraints. SCIP has information about the convexity of simple functions. The convexity information is propagated along the expression tree, if beneficial by introducing new variables, via relations such as

$$g_1, g_2 \text{ convex functions } \implies \begin{cases} \alpha \cdot g_1 \text{ convex for } \alpha \geqslant 0, \\ \alpha \cdot g_1 \text{ concave for } \alpha \leqslant 0, \\ g_1 + g_2 \text{ convex }, \\ \max\{g_1, g_2\} \text{ convex }, \\ \exp(g_1) \text{ convex }. \end{cases}$$

The underestimators are then derived from the following functions:

Corollary 3.3.1. *For a convex function* $g : \mathbb{R}^n \longrightarrow \mathbb{R}^{m_g}$ *a linear underestimator* G *is given by*

$$G(x) = g(\hat{x}) + \nabla g(\hat{x})^\top (x - \hat{x})$$

for any point $\hat{x} \in \mathbb{R}^n$.

Corollary 3.3.2. *For a concave function* $g : \mathbb{R}^n \longrightarrow \mathbb{R}^{m_g}$ *on* $[lb, ub] \subset \mathbb{R}^n$, *a linear underestimator* G *is given by the solution of the following linear optimization problem*

$$\begin{aligned} G(x) = \min_{\alpha \in \mathbb{R}^{2^n}} \quad & \sum_{i=0}^{2^n} \alpha_i \cdot g\left(v^i\right) \\ s.t. \quad & \sum_{i=0}^{2^n} \alpha_i \cdot v^i = x \\ & \sum_{i=0}^{2^n} \alpha_i = 1 \\ & \alpha \geqslant 0 \end{aligned}$$

where $v^i \in \mathbb{R}^n$ *for* $i \in \left\{1, \ldots, \mathbb{R}^{2^n}\right\}$ *denote the vertices of* $[lb, ub]$.

Corollary 3.3.3. *For an indefinite function on* $[lb, ub] \subset \mathbb{R}^n$*, i.e., neither convex nor concave, the underestimator* G *is given by*

$$G(x) = g(\hat{x}) + \sum_{i:x_i \geqslant \hat{x}_i} \underline{d}_i(x_i - \hat{x}_i) + \sum_{i:x_i \leqslant \hat{x}_i} \overline{d}_i(x_i - \hat{x}_i),$$

where $\hat{x} \in \mathbb{R}^n$*, and* $\underline{d}$ *and* $\overline{d}$ *are chosen such that* $\nabla g(x) \in [\underline{d}, \overline{d}]\ \forall x \in [lb, ub]$.

For proofs we refer to [82] and [86]. Automatic differentiation and interval arithmetic is used to calculate $\underline{d}$ and $\overline{d}$ in SCIP.

3.4 PDE CONSTRAINED OPTIMIZATION

Many mathematical problems in process engineering include mass balances and energy balances in form of partial differential equations (PDEs). Formulating these balances as first order PDEs in one spacial dimension $z \in [0, Z]$ and time $t \in [0, t_f]$ results in conservation laws of the form

$$\frac{\partial \psi(z,t)}{\partial t} + \frac{\partial a(\psi(z,t),z,t)}{\partial z} + b(\psi(z,t),z,t) = 0 \tag{12}$$

where $\psi : \mathbb{R}^2 \longrightarrow \mathbb{R}^{n_\psi}$. To handle PDEs in the framework of numerical optimization, we first reduce the PDEs to systems of ordinary differential equations (ODEs) via the following two approaches: In the special case that the PDE is quasi-linear, we apply the method of characteristics. Otherwise, we semi-discretize the PDE via the Finite Volume method (FVM). The ODEs can then be handled in an NLP framework by using numerical integrators, such as IDAS [87]. We apply direct multiple shooting, to increase the numerical stability of solving the ODEs [88].

3.4.1 *Method of Characteristics*

The method of characteristics is used to reduce a linear or quasi-linear PDE into a system of ODEs, which describe the solution along characteristic curves.

Definition 3.4.1. *Characteristic curves*
Let us consider a quasi-linear PDE with boundary conditions

$$\begin{aligned} &\tfrac{\partial \psi(z,t)}{\partial t} + a(\psi(z,t),z,t)\tfrac{\partial \psi(z,t)}{\partial z} + b(\psi(z,t),z,t) = 0, \\ &\psi(0,t) = \psi_0(t), \quad \psi(z,0) = \psi_{iv}(z). \end{aligned} \tag{13}$$

The characteristic curves of PDE (13) *are given by*

$$\begin{aligned} \tfrac{\partial z}{\partial t} &= a(\psi(z,t),z,t), \\ \tfrac{\partial \psi}{\partial t} &= b(\psi(z,t),z,t). \end{aligned} \tag{14}$$

Using the boundary conditions of (13), the ODEs of the characteristic curves can be solved as initial value problems to get the solution of (13). For more details and some illustrative examples we refer to [89].

3.4.2 *Finite Volume method (FVM)*

The FVM is a conservative method for creating a set of ODEs, which approximates the solution of a PDE (12) on a discrete spatial grid.

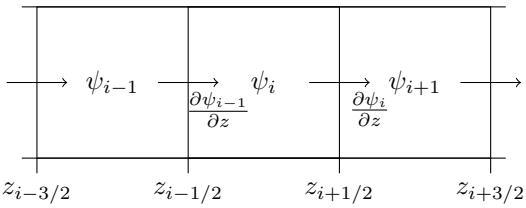

Figure 7: Example for a finite volume grid with upwind-scheme

To apply the FVM we separate the spatial domain $[0, Z]$ into smaller intervals, which we call grid cells. Let $z_{i+1/2}$ with $i \in \{0, \dots, m_{GC}\}$ be a series of strictly ordered points in $[0, Z]$, with $z_{1/2} = 0$ and $z_{m_{GC}+1/2} = Z$. These points denote the end points of the grid cells $[z_{i-1/2}, z_{i+1/2}]$, $i \in \{1, \dots, m_{GC}\}$. Let furthermore

$$\begin{aligned} z_i &:= \frac{z_{i-1/2} + z_{i+1/2}}{2}, && i \in \{1, \dots, m_{GC}\}, \\ \Delta z_i &:= z_{i+1/2} - z_{i-1/2}, && i \in \{1, \dots, m_{GC}\}, \end{aligned}$$

be the centers and the length of the grid cells and

$$\psi_i(t) = \frac{1}{\Delta z_i} \int_{z_{i-1/2}}^{z_{i+1/2}} \psi(z, t)\, dz, \qquad i \in \{1, \dots, m_{GC}\}$$

be the average value of $\psi(z, t)$ on the grid cell $[z_{i-1/2}, z_{i+1/2}]$. Here, we assume that all grid elements are of equal length. We integrate the PDE (12) over the grid cells and get

$$\int_{z_{i-1/2}}^{z_{i+1/2}} \frac{\partial \psi(z,t)}{\partial t}\, dz + \int_{z_{i-1/2}}^{z_{i+1/2}} \frac{\partial a(\psi(z,t), z, t)}{\partial z}\, dz + \int_{z_{i-1/2}}^{z_{i+1/2}} b(\psi(z,t), z, t)\, dz = 0. \tag{15}$$

According to Leibniz integral rule

$$\int_{z_{i-1/2}}^{z_{i+1/2}} \frac{\partial \psi(z,t)}{\partial t}\,dz = \frac{d}{dt}\int_{z_{i-1/2}}^{z_{i+1/2}} \psi(z,t)\,dz = \Delta z_i \frac{d\psi_i(t)}{dt}$$

holds. Furthermore, we can write the convection term as

$$\int_{z_{i-1/2}}^{z_{i+1/2}} \frac{\partial a(\psi(z,t),z,t)}{\partial z}\,dz = a(\psi(z_{i+1/2},t),z_{i+1/2},t) - a(\psi(z_{i-1/2},t),z_{i-1/2},t).$$

We approximate the terms on the borders of the grid cells via the upwind scheme, i.e., for a flow through the grid from $z = 0$ towards $z = Z$ we use

$$a(\psi(z_{i-1/2},t),z_{i-1/2},t) \approx a(\psi_{i-1}(t),z_{i-1},t).$$

The last term $\int_{z_{i-1/2}}^{z_{i+1/2}} b(\psi(z,t),z,t)\,dz$ in Eq. (15) is approximated via a quadrature rule. Here, we apply the mean value theorem to get

$$\int_{z_{i-1/2}}^{z_{i+1/2}} b(\psi(z,t),z,t)\,dz \approx \Delta z_i\, b(\psi_i(t),z_i,t).$$

Combining these results, we approximate Eq. (15) by a system of ODEs

$$\Delta z_i \frac{d\psi_i(t)}{dt} + a(\psi_i(t),z_i,t) - a(\psi_{i-1}(t),z_{i-1},t) + b(\psi_i(t),z_i,t) = 0, \quad i \in \{0,\dots,m_{GC}\},$$

which describe the average value $\psi_i(t)$ of $\psi(z,t)$ on the grid cells $z \in [z_{i-1/2}, z_{i+1/2}]$. Together with the boundary conditions of the PDE, we get an initial value problem (IVP), which can be solved via integrators.

3.4.3 *Direct Multiple Shooting*

Let us consider an IVP

$$\begin{aligned} &\tfrac{d\psi(t)}{dt} = f(\psi(t),t), \quad t \in [0,t_f], \\ &\psi(0) = \psi_0. \end{aligned} \tag{16}$$

The idea of multiple shooting is to solve the IVP (16) on grid cells by introducing intermediate function values as new initial points.

We introduce points $0 = t_0 < t_1 < \cdots < t_l = t_f$ to divide the domain $[0, t_f]$ into a grid and introduce variables $\psi_i = \psi(t_i)$, which represent the function values at the grid points. We define a series of new initial value problems using the grid points

$$\begin{aligned} &\frac{d\psi(t;t_i,\psi_i)}{dt} = f(\psi(t;t_i,\psi_i),t), \quad t \in [t_i, t_{i+1}], i \in \{1,\dots,l\}, \\ &\psi(t_i;t_i,\psi_i) = \psi_i, \qquad\qquad\qquad\qquad\qquad\quad i \in \{1,\dots,l\}, \end{aligned} \tag{17}$$

which represent the solution of (16) on the grid cells. The function values ψ_i are considered variables in an NLP framework and determined iteratively via the constraints

$$\psi_{i+1} = \psi(t_{i+1};\psi_i,t_i), \qquad\qquad i \in \{1,\dots,l-1\},$$

which enforce continuity on $[0, t_f]$. The method of direct multiple shooting is more numerically stable than single shooting, i.e., solving IVP (16) on the complete interval $[0, t_f]$. Alternative approaches for solving time dependent differential equations can be found in [90].

4

EXERGY EFFICIENCY OF CO_2 METHANATION PROCESSES

In this chapter, we investigate the exergetic and energetic efficiency for the conversion process by a detailed exergy analysis for four feasible power-to-gas configurations assuming CO_2 to originate from anaerobic digestion (AD), and make a direct comparison with methanol as an energy carrier. We limit ourselves to technologies which are commercially available, e.g., alkaline electrolyzer for the production of hydrogen from RES as introduced in Chapter 2. We use FVM and multiple shooting, see Chapter 3, to solve the PDAEs which describe some of the process elements.

Methanol is likely the most promising alternative to methane as a C1 energy storage molecule. It is in liquid state under ambient conditions, which greatly facilitates the handling and storage. Castellani et al. [91] have carried out an energy analysis by estimating the ratio of the required process energy input in relation to the stored energy in form of methane or methanol as storage molecules. The energy contributions for the compression of the feed streams as well as the product methane are included in their analysis. They report slightly favorable energy consumption ratio (energy spent/energy stored excluding energy for water electrolysis) for methane, 0.41-0.43 (pressurized at 20 and 200 bar, correspondingly) than that for methanol, 0.45 (at ambient conditions, 1 bar). We would like to emphasize that the present contribution gives a more detailed energy analysis of methane as an energy carrier. Furthermore, the results presented here are fully comparable with the results of a previous study where methanol was assumed as storage molecule for electric power [92]. In both studies, strictly equivalent system boundaries were applied which increases the scientific value of the present analysis. Furthermore, we could identify here a new promising process configuration with fewer units leading finally to a higher energy efficiency than the state-of-the-art reactor cascade configuration.

The exergetic contribution of the excess heat in the methanation is easily identifiable in the results (see Table 7), for the comparison it is however excluded in the presentation of the exergetic efficiency value (Table 9).

We fix a pressure level of 200 kPa for the produced methane. This pressure is suitable for intermediate storage [59] and the methane can be further treated, e.g. by odorization, for feed into the gas distribution system. All process configurations are simulated with the same electrical energy input of 1 MW for the electrolysis of water, where a flow of 9.502 mol/hr of H_2 is

generated with an operational voltage of 1.96 V of the electrolyzer leading to a molar energy consumption of 378.9 kJ/mol_{H_2} [92], as introduced in Section 2.1.4.

The final step of the energy conversion chain in the simulations is the conversion of methane back to electricity, where an efficiency rate η_{LHV} of a combined-cycle power plant (CCPP) with respect to the lower heating value (LHV) of the combustion gas of $\eta_{LHV} = 57\%$ is assumed. Recently, the most sophisticated CCPP units achieve even higher efficiencies ($\eta_{LHV} > 60\%$) [93], but for better comparability of the results we adopt the value used in [92].

4.1 PROCESS CONFIGURATIONS

In this section we introduce the four system level process configurations A, B, C1 and C2. The rate expression and the corresponding parameter values of the catalytic methanation reactor applied in all simulations are taken from Koschany et al. [39]. The rate expression is thermodynamically consistent as expressed in more detail in Section 4.2.1. Each configuration in this contribution includes several gas separation units. The detailed description of the applied dynamic models and the corresponding parameters of the pressure (PSA) and temperature swing adsorption (TSA) units are given in Sections 4.2.2 and 4.2.3. The initial feeding ratio of H_2 and CO_2/CH_4 from anaerobic digestion varies. The process configurations A, B and C1 include separation of the CO_2/CH_4 mixture prior to mixing with H_2 and feeding into the reactor, while a direct feed-in of the anaerobic product gas is considered with the process configuration C2. The initial H_2/CO_2 molar ratio before feed-in to the methanation reactor is in the range of 3.8 to 4.0.

The molar flows of the process streams are shown in Table 3, along with the electric energy demand for the initial separation of CO_2 and CH_4. In the following sections the different process configurations are described in more detail.

4.1.1 *Process A: Reactor Cascade*

Configuration A contains the initial separation of CO_2 and CH_4 of the AD product gas by PSA units. Separation of CO_2 and CH_4 is typically done on site at the biogas plant, following anaerobic digestion, if the product methane is fed into the gas distribution system. Different separation processes are commercially available, such as absorption (e.g. amine scrubbers), adsorption (e.g pressure or vacuum swing adsorption) or membrane separation processes, as described by Kahn et al. [52] and Awe et al. [94]. In particular absorption processes are widely implemented on sites of biogas

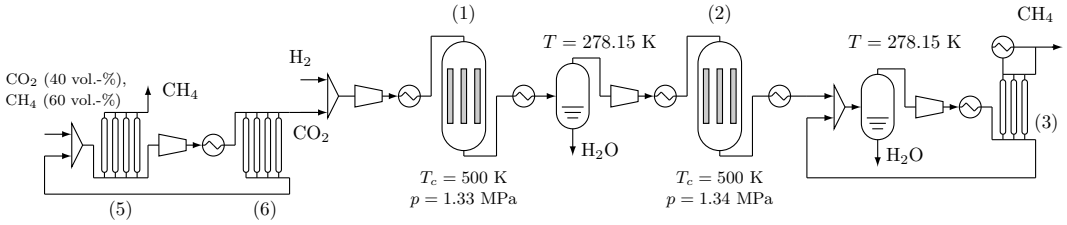

a) Process A.

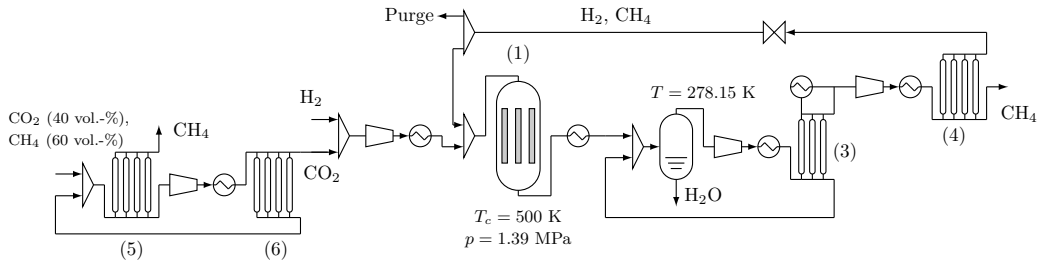

b) Process B.

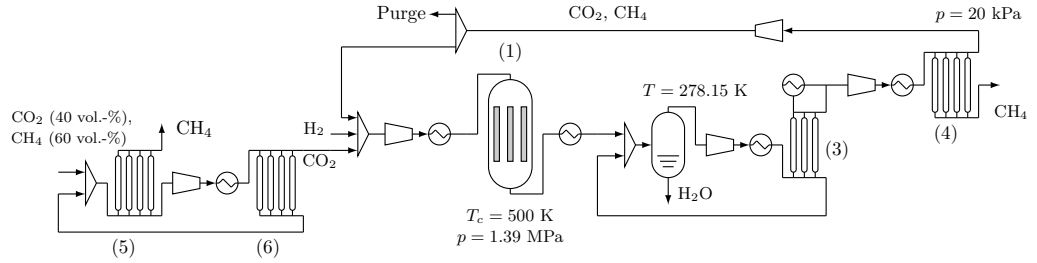

c) Process C1.

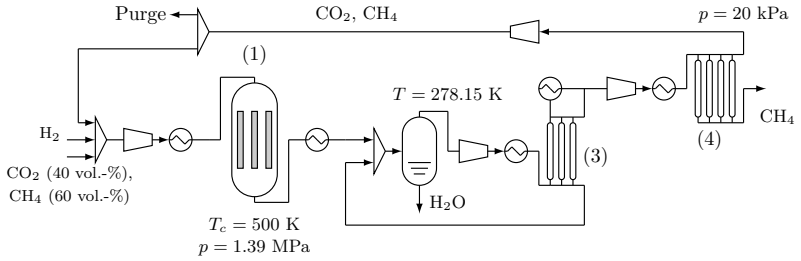

d) Process C2.

Figure 8: Schemes of the process configurations.

Methanation reactors (1,2), TSA unit (3) for gas drying, PSA unit (4) for separation of CH_4 *from* H_2 *(Process B) or* CO_2 *(Processes C1, C2) and PSA units (5,6) for initial separation of* CO_2 *and* CH_4 *from anaerobic digestion.*

plants when a high product purity is required [95]. Because of this, we choose adsorption as the separation process.

The separated CO_2 is mixed with H_2 and supplied into a cascade of methanation reactors with the initial N_{H_2}/N_{CO_2} molar ratio of 4.0 corresponding exactly to the stoichiometric ratio. Intermediate water removal is performed after the first reactor by condensation (T=278.15 K, p=1.365 MPa). Final drying with a combination of condensation (T=278.15 K, p=1.365 MPa) and TSA (T=393.15 K at desorption) units lowers the water concentration C_{H_2O} below the specified threshold of 200 mg/m^3. El Sibai et al. [96] has demonstrated recently that in a reactor cascade with an equilibrium limited second reactor the product gas fulfills the gas distribution system specifications in terms of H_2 and CO_2 concentration after drying. Configuration A is closely similar to the pilot unit operating since 2013 in Germany [97, p. 821] and is therefore seen as a reference in this exergy analysis. The inter-stage removal of water between the reactors by condensation leads to an increased conversion of the reagents in the second reactor. Figure 8a shows a simplified scheme for configuration A. The compression of H_2 and CO_2 to the process pressure (1.39 MPa) is realized by multistage compression with intermediate cooling.

4.1.2 *Process B: H_2 Separation*

Configurations B, C1 and C2 contain only one methanation reactor. The configuration B is simulated applying an initial H_2 molar flow rate N_{H_2} of 2.37, which leads to a H_2 molar fraction of 0.05 in the methane after drying, which is then separated in a following PSA unit. The drying process is performed with the condensation and TSA units, similar to process A. The maximal methane concentration in the product is limited by the substoichiometric amount of CO_2 in the feed. The system configuration is simulated so that the product methane contains max. 0.05 vol.-% CO_2 after the separation of H_2 leading to a gas mixture of H_2 and CH_4 to be recycled to the reactor unit as depicted in Figure 8b. The purge ratio of 1:4 (mol/mol) of the recycled stream is defined to avoid any accumulation of contamination in a closed loop. The purge stream's uses are of low value, e.g. combustion, lowering the overall yield. The recycle ratio R (molar flow ratio of the fresh feed to the reactor input) of 0.95 is established in the system. The detailed description of the separation of H_2 and CH_4 is given in Section 4.2.2.

4.1.3 *Process C1: CO_2 Separation*

The process scheme of configuration C is similar to that of configuration B. Here, a substoichiometric N_{H_2}/N_{CO_2} molar ratio of 3.8 is applied and H_2 is nearly exhausted in the methanation unit ($x_{H_2} < 7.6 \times 10^{-3}$ after water removal). The excess CO_2 is removed from the product gas via a PSA unit, filled with the adsorbent zeolite 5A (Z5A), as described in Section 4.2.2. A mixture of CH_4 and CO_2 is recycled with a purge ratio of 1:4 and R=0.99. The process scheme is illustrated in Figure 8c.

4.1.4 *Process C2: Direct Methanation of the AD Product Gas*

Configuration C2 omits the initial separation of CO_2 and CH_4 prior to the methanation reactor. The product gas from anaerobic digestion is directly mixed with H_2 and fed into the reactor, see Figure 8d. In the methanation reaction operating at T=526 K the thermodynamic reaction equilibrium is strongly on the product side and therefore high conversion of CO_2 with H_2 can be achieved even in the presence of CH_4, as also confirmed by Strangeland et al. [98]. The N_{H_2}/N_{CO_2} molar ratio of 3.8 is equal to that of process C1. After the water removal, excess CO_2 is removed from the product gas similar to process C1. Configuration C2 is simulated with a recycle mixture of CH_4 and CO_2 with a purge ratio of 1:4 and a recycle ratio R=0.98.

Table 3: Amount of CO_2 from anaerobic digestion and electricity required for the separation of CO_2 from CH_4. N_{CH_4}/N_{CO_2}=1.5.

	CO_2	A	B	C1	C2
Molar flow	[kmol/hr]	2.38	2.37	2.50	2.50
Exergy flow	[kW]	19.85	19.80	20.88	0

4.2 MODEL FORMULATION

An object oriented approach is used for the implementation of the process configurations. For each required unit type, e.g. methanation reactor, an individual model is implemented. These unit models are then used as 'building blocks' to put together the different process configurations. We introduce here the unit model 'building blocks', which are used in the simulation of all of the configurations. The combination of the individual unit models to a process configuration model is described in Section 4.2.4. The

superstructure optimization problem from Chapter 5 includes the process configurations of the current chapter.

4.2.1 *Catalytic Methanation Reactor*

We consider the methanation of carbon dioxide, the Sabatier reaction (1), in a fixed bed bundle reactor with a cooling mantle. The side reaction of CO_2 to CO via the reverse water gas shift reaction is neglected.

The expression r describing the reaction rate (18) and the respective parameters for methanation are taken from Koschany et al. [39].

$$
\begin{aligned}
r &= \frac{k_r p_{H_2}^{0.5} p_{CO_2}^{0.5} \left(1 - \frac{p_{CH_4} p_{H_2O}^2}{p_{CO_2} p_{H_2}^4} K_{eq}\right)}{\left(1 + K_{OH} \frac{p_{H_2O}}{p_{H_2}^{0.5}} + K_{H_2} p_{H_2}^{0.5} + K_{mix} p_{CO_2}^{0.5}\right)^2} \\
k_r &= k_0 \exp\left(\frac{-E_A}{R} (1/T_{ref} - 1/T)\right) \\
K_i &= K_{0,i} \exp\left(\frac{-\Delta H_i^r}{R} (1/T_{ref} - 1/T)\right)
\end{aligned}
\tag{18}
$$

The reactor is simulated by a 1D model, adapted from El Sibai et al. [96]. We include the heat transfer resistance of the cooling medium by calculating the thermal conductivity coefficient from radial dispersion and effective wall heat transfer coefficient of the tube in- and outside, as proposed by Schlereth and Hinrichsen [99].

Table 4 shows the reactor inlet temperatures of gas mixture T and cooling medium T_c, pressures and catalyst amount.

Table 4: Operating parameters for the methanation reactors.

Process		A		B	C1	C2
		R1	R2			
T	[K]	450	450	444	526	442
T_c	[K]	500	500	515	500	500
p	[MPa]	1.34	1.34	1.39	1.39	1.39
catalyst	[kg]	56	56	56	56	56

4.2.2 *Pressure Swing Adsorption*

A pressure swing adsorption (PSA) unit was modeled for the purification of methane from either CO_2 or H_2 (unit (3) in Figure 8) to meet the respective

specification of 5 vol.-%. PSA is a process commonly applied for biogas upgrading, as summarized in the reviews by Fendt et al. [100] or Zhou et al. [101]. It is a cyclic process, with alternating adsorption under high pressure (in the present study p_{AS}=2.39 MPa for H_2/CH_4 separation, p_{AS}=1.37 MPa for CO_2/CH_4 separation) and desorption (purging) under low pressure (p_{DE}=0.10 MPa for H_2/CH_4 separation, p_{DE}=0.02 MPa for CO_2/CH_4 separation).

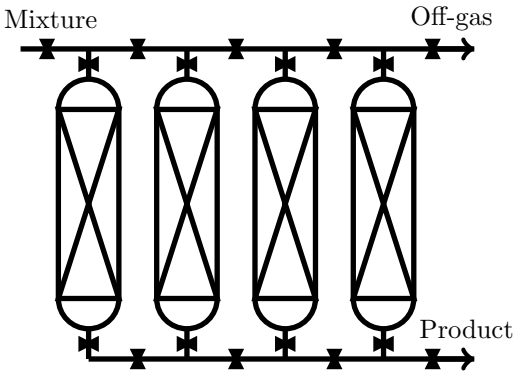

Figure 9: Pressure swing adsorption unit scheme.

A configuration of four adsorption columns, as shown in Figure 9, perform the adsorption/desorption cycles shifted in time, such that always one column of the unit executes the adsorption step. This operation results in a steady output (CH_4 in case of H_2/CH_4 separation, CO_2 with CH_4 residues in case of CO_2/CH_4 separation). The second outgoing stream (purging gas) is assumed to be collected in a vessel before leaving the unit, balancing out the intermittent flow, so that a steady state can be calculated for the process on the system level.

The use of PSA units to separate H_2 and CH_4 is a well studied process. Several studies for the process exist, such as Jee et al. [102], who included the co-adsorption of nitrogen, carbon dioxide and carbon monooxide, Yang et al. [103], who focused on separation of mixtures with high fractions of hydrogen, or Park et al. [53], who studied a complete ad- and desorption cycle with four component mixtures. Here, we simulate a PSA unit to separate H_2 from the product methane of process B, using activated carbon (AC) as the adsorbent. The adsorbent zeolite 5A (Z5A), owning higher selectivity regarding CH_4 and CO_2 than AC, is simulated for processes C1 and C2.

The advantage of the PSA process is the high purity of the product methane which however can only be achieved through the cost of limited recovery. In our simulations we apply a 1-dimensional model for the separation of H_2, CH_4 and CO_2 mixtures on AC and Z5A, adapted from the model

published by Park et al. [53]. Radial gradients, axial dispersion, temperature gradients and pressure gradients are assumed to be negligible. Furthermore, ideal gas behavior and thermal equilibrium between gas and adsorbent is assumed. The dynamic system behavior is then fully described by a system of 11 differential equations and 15 algebraic equations in a combined system of partial differential algebraic equations (PDAEs) as given in the following sections.

Mass balances

The mass balances of each component i in the gas phase are given by

$$\frac{\partial y_i}{\partial t} + v\frac{\partial y_i}{\partial z} + \frac{1-\epsilon}{\epsilon}\rho_s\frac{RT}{p}\left(\frac{\partial q_i}{\partial t} - y_i\sum_j \frac{\partial q_j}{\partial t}\right) = 0, \tag{19}$$
$$i \in \{CO_2, H_2, CH_4, H_2O\},$$

where v denotes the interstitial velocity, T the temperature of the gas phase, ϵ the void fraction of the adsorption bed, p the pressure and q_i the amount adsorbed of component i.

The overall mass balance of the gas phase

$$\frac{\partial C}{\partial t} + \frac{\partial(vC)}{\partial z} + \sum_i \frac{1-\epsilon}{\epsilon}\rho_s\frac{\partial q_i}{\partial t} = 0$$

is used in combination with the ideal gas law $C = p/RT$ to gain

$$\frac{\partial p}{\partial t} + p\frac{\partial v}{\partial z} - \frac{p}{T}\left(\frac{\partial T}{\partial t} + v\frac{\partial T}{\partial z}\right) - RT\sum_i \frac{1-\epsilon}{\epsilon}\rho_s\frac{\partial q_i}{\partial t} = 0. \tag{20}$$

Eq. (20) was used to determine the interstitial velocity v.

Energy balances

The temperatures of the gas phase T and of the column wall T_w are given by the equations

$$(\epsilon c_g C + (1-\epsilon)c_s\rho_s)\frac{\partial T}{\partial t} + \epsilon c_g v C\frac{\partial T}{\partial z} - \sum_i(-\Delta H_i)(1-\epsilon)\rho_s\frac{\partial q_i}{\partial t} + \frac{2h_w}{R_i}(T - T_w) = 0, \tag{21}$$

$$c_w\rho_w a_w\frac{\partial T_w}{\partial t} - 2\pi(h_w R_i(T - T_w) - U_w R_o(T_w - T_{amb})) = 0. \tag{22}$$

The parameters ρ_s and ρ_w are the densities of the adsorbent and column wall, ΔH_i the heat of adsorption of component i and c_g, c_s, and c_w are the heat capacities of the gas phase, adsorbent and column wall, respectively. The ambient temperature T_{amb} is set to be 298.15 K.

Mass transfer

The mass transfer on the adsorbent is modeled by the linear driving force (LDF) model

$$\frac{\partial q_i}{\partial t} = k_i(q_i^* - q_i), \qquad i \in \{CO_2, H_2, CH_4, H_2O\}, \tag{23}$$

where q_i^* is the multicomponent adsorption equilibrium of component i.

Adsorption equilibrium

We describe the adsorption equilibrium q_i^* of components $i \in \{CO_2, H_2, CH_4\}$ by the Langmuir isotherm (24).

$$\begin{aligned} \hat{q}_i^* &= q_{max,i}\frac{b_i p y_i}{1 + b_i p y_i} \\ b_i &= b_{i0}\exp(b_{i1}/T) \\ q_{max,i} &= a_{i1} + a_{i2}/T \end{aligned} \tag{24}$$

In all process configurations, the water content is initially lowered by cooling and condensation (T=278.15 K) and a TSA column (T=393.15 K at desorption) before the gas is fed into the PSA column. The adsorption of water traces on the adsorbent can modeled by the Qi-Hay-Rood (QHR) isotherm:

$$\begin{aligned} \hat{q}_{H_2O}^* &= \frac{\rho V_0}{1 + \exp(\omega_{H_2O}(\frac{P_{1/2}}{P_0} - \frac{P}{P_0}))} \\ \rho &= \sum_{j=0}^{4} c_j (T - 273.15)^j \\ \omega_{H2O} &= A exp(-E_a/RT) \\ \frac{p_{1/2}}{p_0} &= 0.121 + 1.3 \cdot 10^{-3} K^{-1} \cdot T \end{aligned} \tag{25}$$

The amount of water adsorbed on the AC at equilibrium is a sigmoid function with respect to partial pressure, as shown by Lopes et al. [104] and Rudisill et al. [105]. The QHR isotherm, introduced in [106], reproduces this behavior. We assume ideal adsorption behavior of the gases to combine these models with the Ideal Adsorbed Solution Theory (IAST). A multicomponent

adsorption model can be obtained from the pure component isotherms (24) and (25) by solving the system of equations

$$\left.\begin{aligned} p y_i &= p_i^0(\Pi_i)\hat{y}_i \\ \Pi^* &= \frac{\Pi_i}{RT} = \int_0^{p_i^0} \frac{\hat{q}_i^0(p)}{p} dp \\ \frac{1}{n_t} &= \sum_i \frac{\hat{y}_i}{\hat{q}_i^0(p_i^0)} \\ \sum_i \hat{y}_i &= 1 \\ q_i^* &= \hat{y}_i n_t \end{aligned}\right\} \; i \in \{CO_2, H_2, CH_4, H_2O\} \tag{26}$$

for the equilibria q_i^*. In this formulation $\hat{q}_i^0$ denotes the pure component adsorption equilibrium, calculated from (24) and (25), n_t is the total amount adsorbed, and $\hat{y}_i$ denotes the mole fraction of component i, which is adsorbed on the adsorbent.

Parameters for Eqs. (19)-(24) to simulate the behavior of CH_4, CO_2 and H_2 on adsorbents AC and Z5A are taken directly from Park et al. [53]. The multicomponent adsorption equilibrium by Park et al. showed excellent agreement between the model output and experimental validation.

The QHR model for water adsorption was applied only in the PSA simulation of activated carbon, as water and CO_2 show non-ideal co-adsorption behavior on Z5A [107]. Furthermore, to desorb water from zeolites high temperatures are preferable due to the strong adsorption of water on zeolites [104]. Therefore, the water concentration of the gas supplied to the Z5A PSA unit had to be lowered far below the specified threshold (2) of 200 mg/m^3 by the corresponding TSA unit.

Pressure

The change in pressure over time is given by the equation

$$\frac{\partial p}{\partial t} = \alpha(p_{end} - p). \tag{27}$$

The parameters α and p_{end} are dependent on the step within the adsorption cycle, namely adsorption step (AS), desorption step (DE), pressure equalization step (PEQ), pressurization step (PR) or depressurization step (DP). During pressurization the factor α has a value of 0.5, during depressurization a value of 0.3 and during pressure equalization a value of 0.2. We use a configuration with 4 adsorption columns and 9 steps, including an adsorption and desorption phase. This setting is introduced in further detail by Ruthven [108]. Both re- and depressurization of the column include two pressure equalization steps. During these steps, the gas from a depressurizing column is used to repressurize a corresponding column. A scheme of the configuration is depicted in Figure 14a.

Bed length and adsorption time of the PSA units are shown in Table 6. The 4 column setting is simulated with one adsorption column. The data for the gas streams leaving the column are saved and utilized as input at a different time step for the same column. An example for the mole fractions of H_2 and CH_4 inside the adsorption column is shown in Figure 11. We simulate that the total flow rate is split up to a number of n_{PSA} equivalent PSAs. Thus the interstitial velocity throughout the bed is reduced which results in a strong adsorption into the adsorbent at the beginning of the column, giving higher purity and recovery of the desired product.

During the different steps of the adsorption cycle different boundary conditions apply. The boundary conditions show the connections of the four internal recycle streams. The gas concentrations during the desorption step $y_{i,purge}$ are calculated from the average product gas of DP I. The interstitial velocity v_{purge} is calculated such that the complete product of the step DP I is fed back to the column during the DE step. In the same way, the feed concentrations and velocities of the pressurizing PEQ I and PEQ II steps are connected to the respective depressurizing steps. Here, the parameter α is free to avoid over-determination of the system variables. For the other PSA cycle steps the value of α is fixed; to $\alpha = 0.01$ during the DP I step, to $\alpha = 0.5$ for the DP II step and $\alpha = 0.1$ otherwise. This results in the rate of pressure change adapting to the gas flow into the column. The composition of the gas fed to the column during the pressurization step PR is equal to the product gas of the adsorption step AS, i.e. a part of the product gas is used to re-pressurize the column. For the pressure parameters $p_{AS} > p_{PEQI} > p_{DPI} > p_{PEQII} > p_{DE}$ holds. The intermediate pressures are determined as linear functions of the ad- and desorption pressure. The time of the respective PSA step is determined as $t_s \cdot t_f$, where t_f denotes the total cycle time. Table 5 shows the boundary conditions of the PDAE system at the time of the PSA step. The pressure changes according to $p_{end}(t)$ which is constant during each step of the PSA cycle. The value assigned to p_{end} in each PSA step is shown in Table 5. Figure 10 shows an example of the pressure in the adsorption column over time.

Pressure swing adsorption for gas pretreatment

The CO_2/CH_4 mixture from AD can either be fed directly to the reactor, as in process C2, or it is separated into two streams: CH_4, which leaves the process as a product gas, and CO_2 which is fed to the methanation reactor. The separation implemented for configurations A, B and C1 consists of two PSA units, as shown in Figure 12. This set-up has been introduced by Augelletti et al. [109], who have shown that a high purity of CH_4 and CO_2 can be achieved. The separated methane fulfills the specifications to be fed

Table 5: PSA boundary conditions and pressure change

The boundary conditions determine the velocity, concentration, and temperature of gas flowing into the column. If $u = 0$ holds at the end of a column, Neumann boundary conditions of the form $\frac{\partial y}{\partial t} = 0$ hold for the mole fractions y_i and gas temperature T. The pressure in the column changes towards the value of p_{end} according to Eq. (27). Each PSA step is active for a duration of $t_s \cdot t_f$, where t_f denotes the time of a complete operation cycle.

PSA step	p change	p_{end}	boundary conditions	t_s
1 AS	constant	p_{AS}	$v(z = L) = v_{feed}$,	
			$y_i(z = L) = y_{i,feed}$,	1/4
			$T(z = L) = T_{feed}$	
2 DEQ I	decreasing	p_{PEQI}	$v(z = L) = 0$	1/20
3 DP I	decreasing	p_{DPI}	$v(z = L) = 0$	3/20
4 DEQ II	decreasing	p_{PEQII}	$v(z = L) = 0$	1/20
5 DP II	decreasing	p_{DE}	$v(z = 0) = 0$	1/20
6 DE	constant	p_{DE}	$v(z = 0) = v_{purge}$,	
			$y_i(z = 0) = y_{i,purge}$,	3/20
			$T(z = 0) = T_{purge}$	
7 PEQ II	increasing	p_{PEQII}	$v(z = L) = 0$,	
			$v(z = 0) = v_{PEQII}$,	1/20
			$y_i(z = 0) = y_{i,PEQII}$,	
			$T(z = 0) = T_{PEQII}$	
8 PEQ I	increasing	p_{PEQI}	$v(z = L) = 0$,	
			$v(z = 0) = v_{PEQI}$,	1/20
			$y_i(z = 0) = y_{i,PEQI}$,	
			$T(z = 0) = T_{PEQI}$	
9 PR	increasing	p_{AS}	$v(z = L) = v_{BF}$,	
			$y_i(z = L) = y_{i,PR}$,	1/5
			$T(z = L) = T_{PR}$	

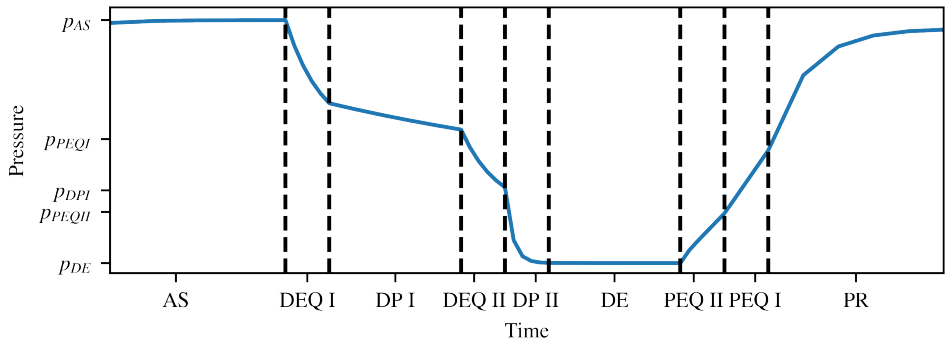

Figure 10: Pressure change in an adsorption column
The figure shows the pressure in column 1 over time during the operation in 9 steps. The pressure is constant during adsorption (AS) and desorption (DE) step and changes in the intermediate steps.

Table 6: Values of the operating parameters of the PSA adsorption columns.

Process		B	C1	C2
Adsorption bed length	[cm]	20	30	20
Adsorption time	[s]	70	300	90
n_{PSA}	[–]	2	12	8
Adsorption pressure p_{AS}	[kPa]	2,391.27	1,365	1,365
Desorption pressure p_{DE}	[kPa]	101.325	20	20

into the German gas distribution system according to (2).

Augelletti et al. [109] have determined the energy consumption of the two PSA separation units to be 1250 kJ per kg of CH_4 from a 2:3 mixture of CO_2 and CH_4. A product quality of $> 99\%$ was reached for CO_2. We use these results to calculate the energy consumption of the initial separation of the product gas from AD, assuming a final CO_2 concentration of 100%.

4.2.3 *Temperature Swing Adsorption*

The methanation product gas needs to be dried to fulfill the specifications of the gas distribution system. The combination of the TSA unit with a condensation unit is shown in Figure 13. The wet gas is cooled and water is removed by a flash column at a temperature of 278.15 K. The pretreated gas is dried in the TSA unit below the specified threshold (2) of 200 mg/m^3 using a desorption temperature of 393.15 K. As the unit has a poor recovery rate (e.g. process C1 had only 1.18 mol.-% water in the column purge stream),

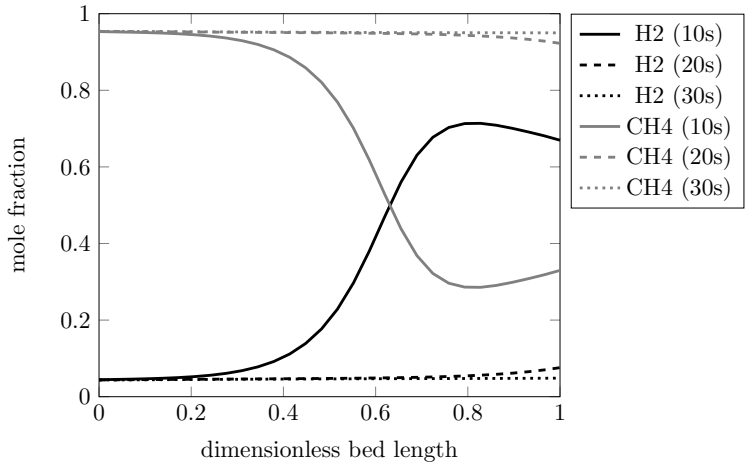

Figure 11: Gas phase mole fractions in the adsorption column.

The gas phase mole fractions of CH_4 *and* H_2 *are shown during the adsorption step on activated carbon. The separation of* CH_4 *and* H_2 *is simulated in process configuration B. The adsorption phase is performed until a high concentration of* CH_4 *leaves the column. The AC adsorbs large amounts of* CH_4*, which is desorbed in high concentrations during the desorption phase.*

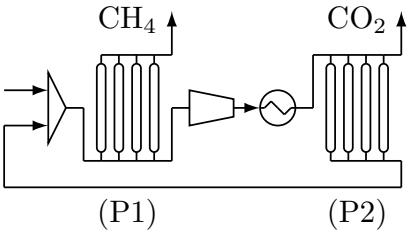

Figure 12: Two PSA configuration for CO_2 and CH_4 separation.

The PSA unit (P1) produces CH_4 *with a high purity (>* 97%*) at adsorption pressure (*p=1,365 *kPa). The purge stream of (P1) contains a mixture of* CO_2 *and* CH_4 *at desorption pressure (*p=20 *kPa), which is repressurized to adsorption pressure and fed into the PSA unit (P2). This unit produces* CO_2 *with a very high purity (>* 99%*) at desorption pressure and a* CO_2/CH_4 *mixture at adsorption pressure, which is recycled to the PSA unit (P1).*

the purge gas is recycled to the flash column. A compressor compensates for the pressure loss in the flash unit, keeping the pressure at p=1.39 MPa.

The TSA is modeled with the mass balances (19), (20), energy balances (21), (22) and mass transfer (23) as introduced for the PSA. The TSA column is assumed to be adiabatic, that means $U_w = 0$. The Langmuir isotherms from Ohlin et al. [110] are used to simulate the adsorption equilibrium

on zeolite Na-ZSM-5. Although Ohlin et al. [111] have stated that the multicomponent model simulation deviates from their measurements, we resort to these values due to a lack of other model parameters.

The TSA column is operated with a four step configuration, including an adsorption step with a duration of $5 \cdot 10^3$ seconds and a desorption step with a duration of $2 \cdot 10^3$ seconds, as depicted in Figure 14b. As especially desorption of water from the bed is comparatively slow, a complete regeneration of the bed is not achieved in the desorption step. However, in the simulation a complete regeneration was not needed for the unit to operate in a cyclic steady state and is also not applied in practice, as reported by Ruthven [108]. We simulate multiple columns ($n_{PSA} = 10$) operating shifted in time and thus reducing the interstitial velocity and giving a steady output. The concentrations and temperatures of two outgoing gas streams, leaving the column during the adsorption or desorption cycle respectively, are averaged out.

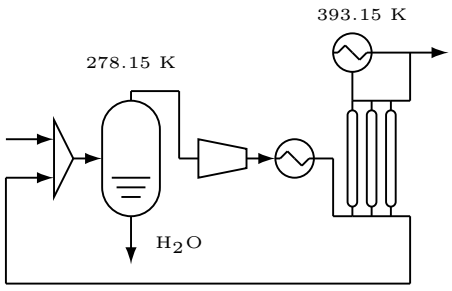

Figure 13: Gas drying with condensation and TSA units.

4.2.4 *Implementation*

We discretize the PDEs (19), (20) and (21) with the Finite Volume method, see Section 3.4.2, using an equidistant spatial grid consisting of 20 grid volumes. The resulting system of ODEs and AEs is solved with MATLAB and CasADi [112]. CasADi is a symbolic framework which allows for quick ODE integration via an interface to IDAS. The PSA and TSA columns are simulated to operate in a cyclic steady state via successive substitution, also called Picard-Iteration. For each iteration step an adsorption/desorption cycle of the PSA column is simulated via integration of the PDE system, starting with the initial value x_i^{PSA}. The final values of the states after this iteration step are stored in a vector x_{i+1}^{PSA} and used as the initial values of the next iteration step. The implemented Picard-Iteration terminates, when

1	AS ↓			DEQ I ↓	DP I ↓	DEQ II ↓	DP II ↑	DE ↑	PEQ II ↑	PEQ I ↑	PR ↑	
2	PEQ I ↑	PR ↑		AS ↓			DEQ I ↓	DP I ↓	DEQ II ↓	DP II ↑	DE ↑	PEQ II ↑
3	DP II ↑	DE ↑	PEQ II ↑	PEQ I ↑	PR ↑		AS ↓			DEQ I ↓	DP I ↓	DEQ II ↓
4	DEQ I ↓	DP I ↓	DEQ II ↓	DP II ↑	DE ↑	PEQ II ↑	PEQ I ↑	PR ↑		AS ↓		

a) PSA column configuration.

1	AS ↑	DE ↓

b) TSA column configuration.

Figure 14: PSA column configuration of 9 different steps during an adsorption/desorption cycle over time.

A total of four adsorption columns periodically perform different steps of the adsorption cycle. The 9 steps include adsorption (AS), pressure equalization with decreasing pressure (DEQ), pressure equalization with increasing pressure (PEQ), depressurization (DP), desorption (DE) and pressurization (PR). Arrows indicate the direction of flow through the column. The pressure is constant during AS and DE. The product gas methane is produced at high pressure during the adsorption step at partially returned to the column during PR. The off-gas is produced at low pressure during DP II and DE. Gas is exchanged during the pressure equalization steps, from DEQ I to PEQ I and from DEQ II to PEQ II. Furthermore, gas from the depressurization DP I is used to purge the column at DE and a fraction of the AD product gas repressurizes the column at PR. We determine the final product gas concentration at cyclic steady state (CSS).

$\|x_i^{PSA} - x_{i+1}^{PSA}\|_2 < 10^{-5}$, returning the material and energy streams computed to leave the adsorption column at the last iteration step. The system of ODEs describing the reactor are likewise integrated by Matlab and CasADi.

The system level process configuration is simulated with ASPEN Plus V8.8. ASPEN is a commercially available process simulation environment, which offers large thermodynamic databases and predefined unit models. Furthermore, ASPEN allows the combination of individual unit models to one process configuration model. The software CAPE-OPEN [113] acts as the interface between MATLAB and ASPEN. ASPEN provides MATLAB with the necessary variables, such as composition, temperature and pressure of the connected input stream of the reactor, PSA or TSA unit and fetches the results once MATLAB has finished the computations. For a more detailed discussion about CAPE OPEN we refer to Peshev and Livingston [114], where this interface was used for the implementation of a unit model for organic solvent nanofiltration.

4.2.5 *Exergy Calculation*

We calculate the exergy of a heat stream Q according to Eqs. (3) and (4). The values for Q of the units, with exception of the PSA, TSA and reactor, are taken from the ASPEN simulation results. The heat transfer Q^{PSA} of a PSA unit is calculated from the energy balance (22). The heat demand of the TSA column is calculated via the equation

$$Q^{TSA} = N c_p (T_{DE} - T_{AS}), \tag{28}$$

where T_{AS} denotes the average temperature over time of the gas leaving the end of the column during an adsorption step, N denotes the purge gas molar flow rate and c_p the corresponding heat capacity. The excess heat of the reactors is calculated as the difference of the enthalpies of the in- and outgoing streams.

For the overall process exergy, we consider internal heat integration. Excess heat from the reactor can be used for the desorption of the TSA unit and the reactor pre-heating. Due to the high exothermicity of the methanation however, only a small fraction of the heat can be used internally. We assume a temperature difference of 10 K between heating and cooling material streams to determine the internal utilization range of the produced heat. The excess heat of the process, outside of the internal utilization range, is a contribution of exergy.

The exergetic overall process efficiency is defined as the ratio of the electrical energy attainable from the product with a combined-cycle power plant and the initial electrical energy input.

4.3 RESULTS AND DISCUSSION

4.3.1 *Comparison of the Process Configurations*

Table 7 lists in detail the energy and exergy contributions of methanation including the multistage compression to the process pressure with intermediate cooling, the methanation reactors and the separation after the reactors. Due to the large volumetric flow rate in the process feed and the recycle stream, configuration C2 requires the largest amount of electrical power for compression. The methanation reaction is very strongly exothermic (ΔH_{CH_4}=−165 kJ/mol) making the methanation reactor a significant heat source. The multistage compression and the separation by condensation are additional heat sources. The excess heat can be used only in the desorption of the TSA column, in the heating of the feed to reactor inlet temperature ($T \approx 440$ K) and for the minor heat demand of the PSA unit. As the PSA requires negligible heat at ambient temperatures, shown in Table 8, it could

also be ignored in the energy analysis. Considering the overall process, the excess heat of the process could also be used in the AD unit.

Table 7: The heat duty, exergy and compressor work, divided into gas compression, reactor and separation.

Heat duty, Q [kW]	A	B	C1	C2
Compression to methanation pressure	8.7	17.0	18.1	25.1
Reactor(s)	106.8	107.2	109.6	105.3
Separation	89.1	84.6	80.7	94.8
Compressor work, W [kW]				
Compression to methanation pressure	32.8	33.1	34.3	46.0
Separation[a]	0.2	3.0	0.7	1.7
Exergy, E [kW]				
Compression to methanation pressure	2.1	3.4	3.7	5.1
Reactor(s)	43.19	45.1	44.3	42.5
Separation	19.1	18.5	16.9	19.1

[a] The displayed values do not include the initial separation of the CO_2/CH_4 mixture from AD for processes A, B and C1.

The temperatures and molar flow rates of the gas streams leaving the PSA unit (4) in Figure 8 are given in Table 8. Configuration A has no gas recycle and the recycle gas composition in configurations B, C1 and C2 vary strongly. In configuration B the recycle gas contains mostly CH_4 and H_2, which causes exergy losses due to the purge. For configuration C1 the exergy loss due to the purge is minor because the recycle gas contains mainly CO_2. In configuration C2 the amount of recycled gas is higher compared to the other configurations and it contains both CH_4 and CO_2 in molar ratio of 0.30/0.54, see Table 8. The heat demands of the PSA units are provided at ambient temperature.

The material and energy flows and the corresponding exergy values of the four process configurations are summarized in Table 9. The electrical energy being used for the production of hydrogen is denoted as $w_{el,in}$ and directly corresponds to its exergy value. The exergetic values for CH_4 as given in Table 9 are calculated from the chemical exergy according to Table 2.

The required power input of process B is increased due to compression of the product gas to the outlet pressure of 200 kPa, from atmospheric pressure, which is the desorption pressure of the last PSA unit. Due to this, the aforementioned higher exergy loss for the purge stream, as well as the high adsorption pressure (p=2.39 MPa), process B has the highest

Table 8: Material and energy streams leaving the PSA columns averaged out over the adsorption/desorption cycle.

B	Product	Recycle	Unit
Temperature T	328	308	[K]
CH_4	2.22	0.70	[kmol/hr]
CO_2	0.01	$7 \cdot 10^{-4}$	[kmol/hr]
H_2	0.01	0.14	[kmol/hr]
exergy E	2.55		[W]
C1	Product	Recycle	Unit
Temperature T	297	291	[K]
CH_4	2.35	0.08	[kmol/hr]
CO_2	0.08	0.25	[kmol/hr]
H_2	0.03	$4 \cdot 10^{-4}$	[kmol/hr]
exergy E	1.01		[W]
C2	Product	Recycle	Unit
Temperature T	297	289	[K]
CH_4	6.11	0.30	[kmol/hr]
CO_2	0.08	0.54	[kmol/hr]
H_2	0.06	$6 \cdot 10^{-4}$	[kmol/hr]
exergy E	0.41		[W]

electrical energy demand of the four process configurations. The electrical energy input is lowest for configuration C2 due to the completely avoided initial separation of CO_2 and CH_4 for the AD product gas. Configurations A, C1 and C2 release the product methane at pressure > 1.3 MPa, which is the adsorption pressure of the corresponding PSA unit. Without energy recuperation exergy is lost by the pressure release after the PSA units. By depressurization to 200 kPa a physical energy of 3.2 kW, 3.3 kW and 8.3 kW is lost for processes A, C1 and C2 respectively, calculated via Eq. (5), see Chapter 2, assuming perfect gas behavior.

The quantities of produced methane in the methanation of the four process configurations are similar. The largest quantity of 2.36 kmol/hr is produced in configuration A, as it has no gas recycle and therefore no reagents and products are lost through the purge stream, which is the case for configurations B, C1 and C2. The respective molar flow rates of the produced methane are given in Table 9.

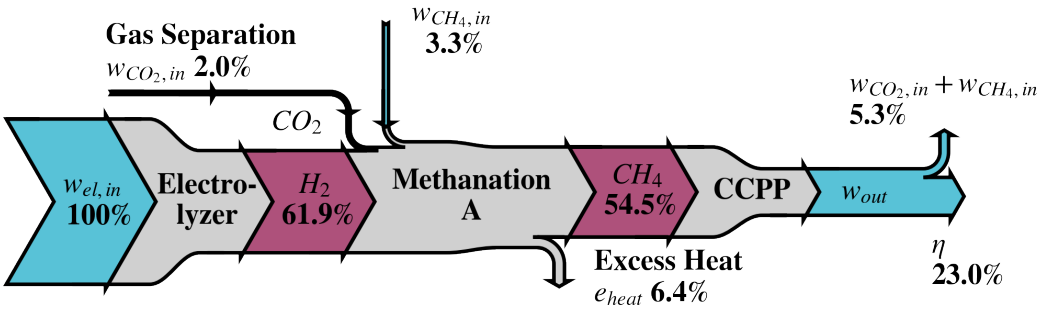

a) Process A

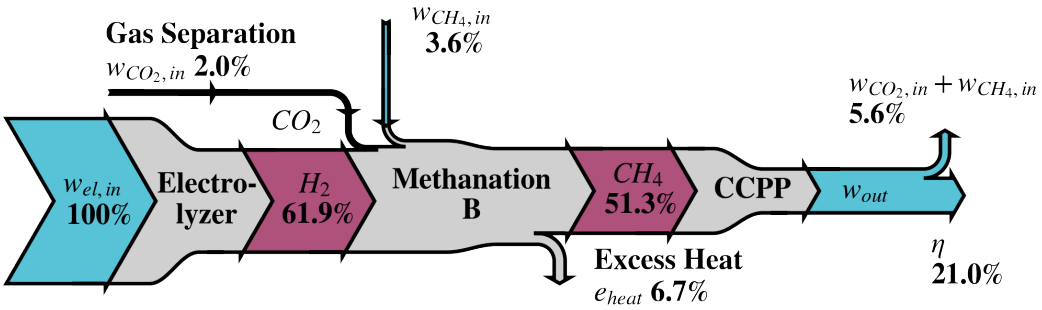

b) Process B

Figure 15: Exergy diagrams including the considered processes A and B. *The figures show the exergy conversion from 1 MW of electrical energy over the storage medium methane back to electrical energy via a combined-cycle power plant (CCPP). The red marks exergy calculated as the chemical exergy of a substance.*

Figures 15 and 16 depict the exergetic flow diagram of the complete processes graphically. The energy efficiency η is calculated as $\eta = (w_{out} - w_{CH_4,in} - w_{init})/w_{el,in}$, where $w_{CH_4,in}$ is the exergetic workload required for conversion processes A, B, C1 or C2 respectively, w_{init} denotes the power input for the initial separation of CO_2 and CH_4 from AD. The w_{out} denotes the electrical energy obtained in a CCPP from the produced methane. As configuration A produces the largest amount of CH_4, it gives the most electrical energy w_{out} after combustion in the CCPP (28.2%), see Table 9. After the electric energy output is reduced by the power input for the methanation process, configuration C2 shows the highest efficiency at η=23.4%. All methanation configurations have an excess heat contribution (denoted as e_{heat} in Figures 15 and 16) however the differences between the configurations are minor in this sense. The exergetic efficiency of the chemical conversion includes the excess heat. Assuming, that the heat flow could be utilized to its exergetic value, we calculate the exergetic efficiency as

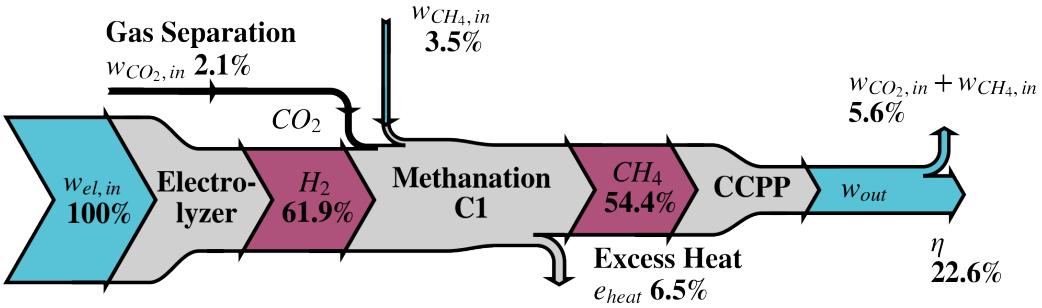

a) Process C1

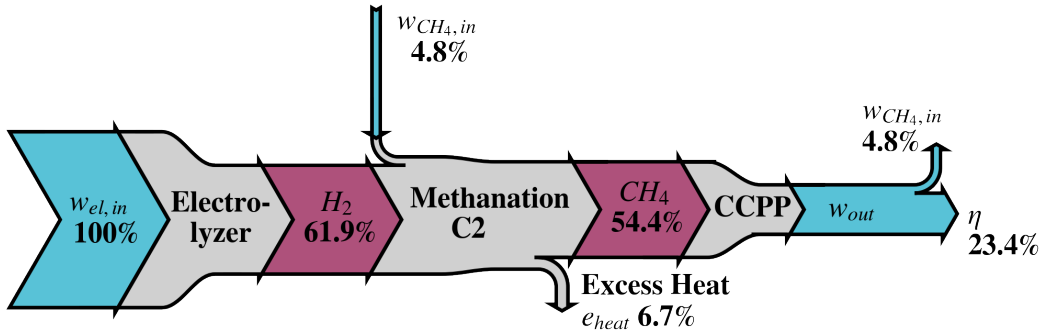

b) Process C2

Figure 16: Exergy diagrams including the considered processes C1 and C2. *The figures show the exergy conversion from* 1 *MW of electrical energy over the storage medium methane back to electrical energy via combined-cycle power plant (CCPP). The red marks exergy calculated as the chemical exergy of a substance.*

$\eta_E = (w_{out} + e_{heat} - w_{CH_4,in} - w_{init})/w_{el,in}$, gaining a value of $\eta_E = 30.1\%$ for configuration C2. The methanol synthesis, having a comparatively low excess heat contribution, see Table 10, has an exergetic efficiency of 18.2%.

Table 9: Overview over the process's mass and exergy flows.

		A	B	C1	C2
Additional methane yield[a]	[kmol/hr]	2.36	2.22	2.35	2.36
Chemical exergy of the methane	[kW]	545.1	513.0	543.8	544.3
Compressor work	[kW]	32.8	36.1	35.0	47.7
Electric energy input $w_{CH_4,in}$	[kW]	52.7	55.9	55.9	47.7
Electric energy output CCPP w_{out}	[kW]	282.4	265.8	281.7	282.1
Electrical energy output	[kW]	229.7	209.9	225.8	234.4

[a] Methane leaving the process reduced by the methane in the process feed.

4.3.2 *Comparison with Methanol Synthesis*

A comparison between material and energetic streams for the two alternative chemical storage media CH_4 and CH_3OH is listed in Table 10. In the study in [92] the energy efficiency for the comparable energy conversion chain using methanol as the chemical storage medium was 17.6%, not considering the possible energy expenditure for CO_2 purification (to 100%). For comparison, we estimated that the energy consumption would be 18.1 kW for 2.167 kmol/h when CO_2 from the AD product gas (40 vol.-% CO_2) is completely separated from CH_4. Reducing the net electrical output of the methanol synthesis by this 18.1 kW gives an exergetic efficiency of 15.8% with respect to the 1000 kW of electrical energy input. Our present study clearly shows higher efficiency (η=23.4) for the utilization of methane as a chemical storage medium than that reported for the methanol. Configuration C2, which obtained the highest exergetic efficiency in the present study, does not include the initial purification of CO_2 to 100% from the AD product gas because this configuration used the AD product gas directly as feed for the methanation reactor with the assumed CO_2/CH_4 molar ratio of 2:3.

The mass flow of methanol was reported to be 3.03 kmol/h [92] and in the present study the CO_2 methanation produced 2.36 kmol/h methane assuming the same initial reference hydrogen input (9.502 kmol/h). This means that a wind turbine with a power output of 1 MW can produce 37.8 kg CH_4 per hour, provided that the biogas plant supplies the required amount of CO_2.

By comparing the heating values of the product streams (CH_3OH 541 kW, CH_4 495 kW) we can state an 8.5% better energetic value for methanol energy storage. However, by also considering the electric energy input for both processes, one notes that the methanation process clearly requires lower electric energy input. The main reason for the significant difference in exergetic efficiency between the two alternatives we identified, is the higher reactor pressure (p=5.0 MPa) for methanol synthesis compared to the pressure of 1.34 to 1.39 MPa assumed to be the reactor pressure for the four configurations in methanation. The reactor pressure directly influences the electrical energy consumption for gas compression and in the simulations we did not consider possible recuperation of energy during the pressure release.

Noticeable is the comparatively high amount of excess heat e_{heat} of around 7%, which is produced by the power-to-methane processes. The methanol synthesis includes a distillation unit, the reboiler of which requires a significant heat input and acts as a heat sink for the process allowing for reasonable heat integration. Furthermore, the methanation reaction is more exothermic (ΔH_{CH_4}=−165 kJ/mol) compared to the synthesis of methanol

(ΔH_{CH_3OH}=−49.6 kJ/mol) and heat is required only for the preheating and the TSA gas drying.

Table 10 explicates the efficiencies of methanol and methane as energy carrier mediums. The values shown for the methanol synthesis from [92] are extended with the additional compressor work of 18.1 kW for the AD product gas separation. Without the initial separation, the methanol synthesis requires a compressor work of 129.7 kW. If the electrical energy required for the methanation process $w_{CH_4,in}$ can also be acquired from renewable energy sources, the efficiency of the process can be calculated with respect to the overall energy input, i.e. $\eta = \frac{w_{out}}{w_{el,in}+w_{CH_4,in}+w_{init}}$. This increases the efficiency for process C2 to 26.9 %. Likewise, the efficiency of methanol as the energy carrier is increased to 26.6 %.

Table 10: Comparison between chemical energy storage mediums.

	CH_3OH*			CH_4		
		Exergy	Energy		Exergy	Energy
	kmol/hr	kW	kW	kmol/hr	kW	kW
Electric energy input electrolyzer		1000			1000	
Hydrogen	9.502	619.4	361.7[a]	9.502	619.4	361.7[a]
Energy carrier product	3.03	597.8	541.2[a]	2.36	544.3	494.7[a]
Compressor work		147.8			47.7	
Excess heat		24.2	63.8		66.7	225.2
Electric energy from CCPP		305.8			282.1	
Net energy output		158.0			234.4	
Net energy efficiency		**15.8**			**23.4**	
Net exergy efficiency		**18.2**			**30.1**	

[a] lower heating value of the energy carrier, * results from [92].

4.4 CHAPTER SUMMARY

We showed feasible alternatives for state-of-the-art methanation processes, requiring less equipment while at the same time gaining a higher process efficiency. The results demonstrate that especially the pressure swing adsorption which can be applied for various gas separation tasks in the methanation process is a feasible and efficient alternative to multi-reactor configurations. The most efficient process configuration, utilizing a PSA unit for CO_2/CH_4 separation, attained an efficiency of 23.4 %. The efficiency of the process was improved by avoiding the separation of the product gas from anaerobic

digestion prior to the methanation reactor. Configuration C2 however has the drawback that it is not suitable for intermittent operation of a plant, due to the fact that the CO_2/CH_4 mixture from anaerobic digestion can not be fed into the gas distribution system without methanation. This could lead to large production costs, as described by Collet et al. [115]. Configurations A, B and C1 however include the separation of the anaerobic digestion product gas, thus decoupling the feed of CH_4 from anaerobic digestion to the gas distribution system and the methanation of the remaining CO_2.

By comparing the results of the present analysis with the results of using methanol as a chemical storage medium we can conclude that methane is a highly promising alternative.

The availability of CO_2 was neglected in this study. In the present work it was assumed that the amount of CO_2/CH_4 mixture from anaerobic digestion was sufficient, which may not be the case for large scale applications.

In the present study we focused on re-conversion of the methane back to electrical energy, considering the gas as a temporal chemical storage medium. However methane can also be utilized in the mobility sector, as fuel for gas-powered vehicles. The exergy efficiency of this application may vary and call for further comparison with methanol in this sector.

The presented assessment and comparison cannot be fully exhaustive, since minor modifications in the configurations might possibly lead to higher efficiencies than the ones analyzed in this study. For example an additional PSA unit could be included to reduce the estimated losses through the purge stream. Implementing two PSA units as introduced for the pretreatment of the CO_2 from AD in Section 4.2.2 (see Figure 12) could increase recovery of the product. Additional energy input arises, however, from the repressurization of a stream between the two units from desorption pressure p_{DE} to adsorption pressure p_{AS}. For process B this would require increasing the pressure from 100 kPa to 2,390 kPa and for processes C1 and C2 from 20 kPa to 1,390 kPa respectively.

Furthermore other units could be considered, e.g. biological methanation in a bioreactor or amine scrubbing for CO_2 separation, to analyze the full range of power-to-methane processes. Chapter 5 widens the scope of the analysis to include the electrolyzer and a wider range of separation and methanation technologies.

As the focus of this Chapter is on the energy and exergy efficiencies of the processes, it does not include a detailed cost analysis. However, a few quantitative remarks can be made on the complexity of the plants and respective running and acquisition costs. As mentioned above, avoiding initial CO_2/CH_4 separation increases the costs for intermittent operation of configuration C2. For continuous operation, however, the running costs for the electrical energy input of configuration C2 as shown in Table 9, are the

lowest of the four configurations. We furthermore expect the acquisition cost of process C2 to be lower than that of processes B and C1. While the larger flow rate of reagents and products of process C2 requires larger separation units after the methanation reactor, the numbers of pressure swing adsorption units, heat exchangers and compressors are reduced, as can be seen from Figure 8. The process costs are evaluated in more detail in the superstructure analysis of the next chapter.

5

PROCESS SYNTHESIS OF CO_2 METHANATION VIA SUPERSTRUCTURE OPTIMIZATION

In this chapter we extend the process configurations of Chapter 4 to an extensive superstructure by including alternative relevant technologies for the methanation process. We identify promising combinations of these technologies via superstructure optimization at the steady state operating conditions. We focus on optimization of thermo-economic aspects of the process alternatives via exergy efficiency, capital costs and total annual costs. As opposed to Chapter 4, we represent the process units via shortcut models, which are more compatible with the computationally expensive superstructure optimization.

Superstructure optimization is a powerful tool for determining the optimal process configuration from a large variety of technologies and their respective combinations. As heat integration plays an important role in improving the process efficiency, we further include indirect, simultaneous heat integration via pinch analysis in the superstructure model.

Superstructures have been widely applied in systems engineering and process design. They are applied for designing heat exchanger networks [70, 116, 117], distillation columns [118], optimization of process flowsheets [119], and process synthesis [120]. Further applications can be found in the excellent reviews of Chen and Grossmann [121] and Trespalacios and Grossmann [122]. As most of the above examples, we formulate the superstructure as a MINLP.

The key novelty of the current work is a detailed designed superstructure for the power-to-methane process, which includes the most relevant unit operations for catalytic CO_2 methanation and additionally simultaneous heat integration. The numerical results represent the global optimal value of the optimization problem as determined by the global optimization solver SCIP, see Section 3.3.3. The optimization of the resulting MINLP model allows for an exhaustive technical analysis of a large variety of possible process configurations.

We describe the superstructure model, including the individual process unit models, in Section 5.1. The objectives of the superstructure optimization are maximizing the process efficiency and minimizing the investment costs, as addressed in detail in Section 5.1.2. We introduce different case studies in Section 5.2 and show the respective optimization results.

5.1 MODELING

To derive the process superstructure model, we introduce two levels of modeling: On the unit level we describe the behavior of a single process unit mathematically, e.g., the temperature dependence of a chemical reactor. We introduce the models used for the power-to-methane process in Section 5.1.1. On the next modeling level, the individual unit models are embedded into the superstructure model, which is introduced in Section 5.1.2.

5.1.1 *Unit Models*

Unit level models represent the behavior of single-process units in terms of material and energy balances. The scheme of a unit model U is shown in Figure 17. We formally define a unit model U with in- and outgoing material streams (MS) as

$$
\begin{aligned}
& x_U \in \mathbb{R}^{n_U} && \text{variables} \\
& x_U^{in} \in \mathbb{R}^{m \cdot d_U^{in}} && \text{unit input MS} \\
& g_U(x_U, x_U^{in}) \leqslant 0 && \text{unit inequality constraints} \\
& h_U(x_U, x_U^{in}) = 0 && \text{unit equality constraints} \\
& lb_U \leqslant x_U \leqslant ub_U && \text{box constraints} \\
& X_U^{out} : \mathbb{R}^{n_U} \times \mathbb{R}^{m \cdot d_U^{in}} \to \mathbb{R}^{m \cdot d_U^{out}} && \text{map to unit output MS} \\
& W_U : \mathbb{R}^{n_U} \to \mathbb{R}_+ && \text{work demand} \\
& Q_U : \mathbb{R}^{n_U} \to \mathbb{R}^{n_q} && \text{heat demand/surplus} \\
& CAPEX_U : \mathbb{R}^{n_U} \to \mathbb{R}_+ && \text{investment cost} \\
& d_U^{in}, d_U^{out} \in \mathbb{N} && \text{\# in- and outgoing MS} \\
& m \in \mathbb{N} && \text{dim. of a single MS}
\end{aligned}
\tag{29}
$$

A uniform formulation of all unit models enables the connection of individual models to a superstructure. Material streams are sets of variables that represent physical properties of the material flows entering or leaving a unit. In the superstructure model, these variables are shared between connected unit models. The dimension of material streams m is equal for all considered unit models, to allow for the connection of arbitrary models. The number of in- and outgoing material streams is specific to a unit. For example, separation units have typically $d_U^{out} = 2$ outgoing material streams, whereas for a reactor, $d_U^{out} = 1$ holds. The information passed to a subsequent unit are molar flows N, temperature T, and pressure p.

In the following, the molar gas flow rates are indicated by the variable N, and the subscript indicates the component, respectively, e.g. N_{H_2} indicates the molar gas flow rate of hydrogen. For example, an input stream to unit U

takes the form $x_U^{in} = \left(N_{CO_2}^{in,U}, N_{H_2}^{in,U}, N_{CH_4}^{in,U}, N_{H_2O}^{in,U}, T^{in,U}, p^{in,U}\right)^\top$, thus, for the dimension of the material stream $m = 6$ holds.

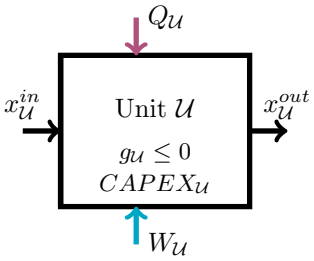

Figure 17: Scheme of a process unit model

A unit model consists of in- and outgoing material streams, here denoted x_U^{in} *and* x_U^{out}*. Furthermore, energy is supplied to or produced by the unit in form of work* W_U *(only supplied to) and heat* Q_U*. The individual unit behavior is modeled by constraints* g_U

In the following sections, the individual unit models are introduced. Here, we drop the subscript U to increase simplicity and readability. Thus x for example refers to the variables of a process unit model. We include it again in the superstructure description in Section 5.1.2.

Electrolysis

For the electrolyzer we consider two different technologies, as introduced in Section 2.1.4, namely AE and SOEC. We implemented AE as a simplified black box model assuming the electrical energy demand to be linearly dependent on the produced H_2 amount according to

$$W(x) = w_{AE} \cdot N_{H_2}^{out}$$

with $w_{AE} = 378.9\ \mathrm{kJ/mol_{H_2}}$ [92]. The variables of the process unit model are here the produced hydrogen, i.e., $x = \left(N_{H_2}^{out}\right)$. The output material stream is given by

$$X^{out}(x, x^{in}) = \left(N_{CO_2}^{in}, N_{H_2}^{in} + N_{H_2}^{out}, N_{CH_4}^{in}, N_{H_2O}^{in}, T^{in}, p^{in}\right),$$

which means that the produced hydrogen is mixed to the input material stream. The model furthermore includes a work demand for gas compression of the hydrogen to pressure p^{in}, as introduced in Section 5.1.1. We calculate the electrical energy demand W for SOEC from the value of 3.37 $\mathrm{kWh/m^3}$ given by Gruber et al. [123] corresponding to 269.9 $\mathrm{kJ/mol_{H_2}}$. In addition, high temperature electrolysis at $T = 1023$ K has a heat demand of

66 kJ/mol_{H_2} and a heat production caused by the stack overpotential of 87 kJ/mol_{H_2}, resulting in an external excess heat of 21 kJ/mol_{H_2}. Furthermore, the heat demand for the preheating and vaporization of water is considered. We scale the process to 1 MW electrical energy for water electrolysis, with 2.64 mol_{H_2}/s (AE) or 3.71 mol_{H_2}/s (SOEC) entering the methanation process. We use the corresponding stoichiometric amount of 0.66 mol_{CO_2}/s (AE) or 0.93 mol_{CO_2}/s (SOEC) in the feed gas from anaerobic digestion as a reference for a priori size estimations of the biological methanation reactor, black box separation models.

Catalytic Methanation Reactor

To model the reaction in a catalytic methanation reactor, we allow conversion up to thermodynamic equilibrium under isothermal conditions. The output molar flow rates N_i are constrained by thermodynamic equilibrium according to

$$p_{CO_2} p_{H_2}^4 \geqslant p_{H_2O}^2 p_{CH_4} K_{eq}(T^{in}) \qquad \text{with } p_i = p^{in} \frac{N_i}{\sum_{j \in C} N_j}, \tag{30}$$

where N_i denotes the molar flow rate in mol/s and p_i is the partial pressure of component $i \in C = \{CO_2, H_2, H_2O, CH_4\}$. The reaction equilibrium is calculated according to Koschany et al. [39]

$$K_{eq}(T) = 137 \cdot T^{-3.998} \exp\left(\frac{158.7}{RT}\right).$$

We logarithmize Equation (30) and introduce new variables $\hat{p}_i$, $\hat{K}_{eq}$ to get

$$\begin{aligned}
&\hat{p}_{CO_2} + 4\hat{p}_{H_2} \geqslant 2\hat{p}_{H_2O} + \hat{p}_{CH_4} + \hat{K}_{eq} && \\
&\exp(\hat{p}_i) \leqslant p_i && \text{for } i \in \{CO_2, H_2\} \\
&\exp(\hat{p}_i) \geqslant p_i && \text{for } i \in \{CH_4, H_2O\} \\
&\hat{K}_{eq} = \ln(137) - 3.998 \ln(T^{in}) + \frac{158.7}{RT^{in}} &&
\end{aligned}$$

which we implement instead of Equation (30). In addition the reaction stoichiometry

$$N_i^{out} - (\zeta \nu_i + N_i^{in}) = 0 \qquad \text{for } i \in C$$

must hold, where ζ denotes the extent of reaction and ν_i the stoichiometric coefficient of component i. Thus, we have variables given by

$$x = \left([\hat{p}_i, p_i, N_i^{out}]_{i \in C}, \hat{K}_{eq}, \zeta\right)^\top.$$

The reaction is highly exothermic. Consequently, the isothermally operating methanation unit generates excess heat. The heat of reaction ΔH_{rxn} is linearly approximated over the relevant temperature interval.

$$
\begin{aligned}
&X^{out}(x, x^{in}) = (N^{out}_{CO_2}, N^{out}_{H_2}, N^{out}_{CH_4}, N^{out}_{H_2O}, T^{in}, p^{in})^\top \\
&W(x) = 0 \\
&Q(x) = -\zeta \Delta H_{rxn}
\end{aligned}
$$

During the superstructure optimization the pressure of the methanation reactor was fixed to 0.6 MPa, and the temperature was allowed to vary in the range of 580 to 650 K. These conditions are typically applied to heterogeneously catalyzed methanation reactors [39, 97, 37].

Investment cost is estimated based on equipment sizing via the Guthrie relation [124]. Biegler et al. [124] also refer to these costs as bare module costs. The Guthrie equation is used to estimate the unit capital cost via size and cost of a known reference unit. We estimate the reactor costs without heat exchange by equations given for pressure vessels. A unit of height L_0 and diameter D_0 is used as reference to estimate the unit cost from reference cost C_0 via

$$
\mathrm{CAPEX}(L, D) = \mathrm{MF}\ \mathrm{CE}\ C_0 \left(\frac{L}{L_0}\right)^{\alpha} \left(\frac{D}{D_0}\right)^{\beta}. \tag{31}
$$

The parameter CE corresponds to the CE index, which updates prices to account for inflation. As for the catalytic methanation reaction equilibrium (30), we logarithmize the CAPEX functions of all unit models and express them as inequalities to get

$$
\begin{aligned}
&\ln(\mathrm{CAPEX}(L, D)) \geqslant \ln(\mathrm{MF}\ \mathrm{CE}\ C_0) + \alpha(\hat{L} - \ln(L_0)) + \beta(\hat{D} - \ln(D_0)), \\
&\exp(\hat{D}) \leqslant D, \\
&\exp(\hat{L}) \leqslant L.
\end{aligned}
$$

We use the reference value given by Biegler et al. [124] for the cost estimation. To adapt these values to recent 2017 prices, the parameter CE has a value of $\mathrm{CE} = \frac{\mathrm{CEPCI}_{2017}}{\mathrm{CEPCI}_{ref}} = \frac{558.3}{115}$. Furthermore, the price is updated with the material and pressure factor $\mathrm{MF} = 1.15$ [124]. Finally, we include the cost of the catalyst $C_{cat} = 840$ \$.

$$
\mathrm{CAPEX}(x) = \mathrm{MF}\ \mathrm{CE}\ C_0 \left(\frac{L}{L_0}\right)^{\alpha} \left(\frac{D}{D_0}\right)^{\beta} + C_{cat} \tag{32}
$$

Parameters for (32) were taken from Biegler et al. [124] as $C_0 = 690$ \$, $L_0 = 1.22$ m, $D_0 = 0.91$ m, $a = 0.78$, $b = 0.98$. We assume the reactor to be a

bundle reactor with 100 pipes with L = 1.26 m and D = 0.02 m, containing a total of 56 kg of catalyst. The price is estimated from commercial price quotations [125, 126] to be 15 $ per kg. Note that the investment cost (32) does not cover the equipment for reactor cooling. Cost estimates for heat transfer equipment are introduced in Section 5.1.2.

Biological Methanation Reactor

A wide range of operational process data can be found in the literature, particularly regarding the product gas concentrations. As mentioned in Chapter 2 the reported values range from 58 mol.% [44] to 96 mol.% [45, 46]. The overall process design is strongly dependent on the product methane concentration of the biological unit. Therefore, we consider two optional bioreactor models: A bioreactor reaching 96% CH_4 (BIO1) and one reaching 65% CH_4 (BIO2) in the dry product gas. The product gas leaving the biological methanation reactor is moist. Thus, we calculate the water in the gas stream according to the vapor-liquid equilibrium calculation, shown in Section 5.1.1. Both reactor models operate at ambient pressure and 363.15 K and lose 5% of the reactants to biomass growth. For the CAPEX, we choose an estimate from the literature of EUR 658K [41], corresponding to $723.8K. The reference is the smallest fermenter studied by Graf et al. [41] producing 1 MW_{CH_4}, which is slightly larger than the 0.8 MW_{CH_4} needed for converting the aforementioned 2.64 mol_{H_2}/s (AE) to CH_4.

Flash Separation

Flash separation is applied to reduce the amount of water in the gas mixture. The process requires cooling, owing to the condensation of the liquid product. The separation result is calculated from the vapor-liquid equilibrium at fixed temperature. We describe the separation by the equilibrium conditions, here directly expressed in terms of the molar flow rates:

$$\frac{N_i^l}{\sum_j N_j^l} = K_i \frac{N_i^{in} - N_i^l}{\sum_j N_j^{in} - N_j^l}, \qquad i \in \{CO_2, H_2O, CH_4\},$$

$$K_i - \frac{p_{vp,i}}{p_{in}} = 0, \qquad i \in \{CO_2, H_2O, CH_4\}$$

where N_i^l denotes the molar flow rate of component i in the liquid phase. Phase equilibrium constants K_i are calculated from the pure component vapor pressure $p_{vp,i}$, with the exception of hydrogen, which is assumed to

stay in the gas phase owing to its high volatility. The vapor pressure of a component i is calculated from

$$T_{r,i} = 1 - \frac{T}{T_{c,i}}$$
$$p_{vp,i} = p_{c,i} \exp\left(\frac{T_{c,i}}{T}\left(\alpha_{1,i}T_{r,i} + \alpha_{2,i}T_{r,i}^{1.5} + \alpha_{3,i}T_{r,i}^{3} + \alpha_{4,i}T_{r,i}^{6}\right)\right),$$

where $T_{c,i}$ and $p_{c,i}$ are the critical temperature and pressure of component i. The parameters $\alpha_{k,i}$, $k \in \{1,2,3,4\}$ are taken from [127]. We consider a point of operation at

$$T^{in} = 298.15 \text{ K},$$
$$p^{in} = 6 \text{ bar}.$$

The variables of the process unit are $x = \left([N_i^l, K_i]_{i\in C}\right)^\top$. The unit material stream output is

$$X^{out}(x, x^{in}) = \left(X^{out,1}(x, x^{in}), X^{out,2}(x, x^{in})\right)^\top,$$
$$X^{out,1}(x, x^{in}) = (N_{CO_2}^l, 0, N_{CH_4}^l, N_{H_2O}^l, T^{in}, p^{in}),$$
$$X^{out,2}(x, x^{in}) =$$
$$(N_{CO_2}^{in} - N_{CO_2}^l, N_{H_2}^{in}, N_{CH_4}^{in} - N_{CH_4}^l, N_{H_2O}^{in} - N_{H_2O}^l, T^{in}, p^{in}),$$

where the liquid phase is considered as waste stream, i.e., it is not considered for recycling. The flash unit requires heat removal to condensate water, but no supply of electrical energy.

$$W(x) = 0$$
$$Q(x) = -\sum_i N_i^l \Delta H_{c,i}$$

The cost is calculated similarly to the reactor model via

$$\text{CAPEX}(x) = \text{CE } C_0 \left(\frac{L}{L_0}\right)^\alpha \left(\frac{D}{D_0}\right)^\beta$$

with parameters $C_0 = 2,950$ \$, $L_0 = 1.22$ m, $D_0 = 0.91$ m, $\alpha = 0.81$, $\beta = 1.05$ from [124]. Unit parameters L and D were calculated from the liquid flow rate $F^l = \sum_i N_i^l$ via

$\rho = 55345 \text{ mol/m}^3$	Liquid density (mostly water)
$\tau = 300$ s	residence time
$V = 2F^l\tau/\rho$	vessel volume
$D = (V/\pi)^{(1/3)}$	vessel diameter
$L = 4D$	vessel length

in accordance with [124].

Black Box Separation Models

We describe the adsorption, absorption, and membrane separation (MEM) processes by simplified black box models. Adsorption, absorption, and membrane separation are technologies commonly applied in practice [52, 128]. The variables are the molar flow rates of the chemical components.

$$x = \left(N_{1,CO_2}, N_{1,H_2}, N_{1,CH_4}, N_{1,H_2O}, N_{2,CO_2}, N_{2,H_2}, N_{2,CH_4}, N_{2,H_2O}\right)^\top$$

We determine the two product streams

$$\begin{aligned} X^{out}(x, x^{in}) &= \left(X^{out,1}(x, x^{in}), X^{out,2}(x, x^{in})\right)^\top, \\ X^{out,i}(x, x^{in}) &= \left(N_{i,CO_2}, N_{i,H_2}, N_{i,CH_4}, N_{i,H_2O}, T_i, p_i\right), \qquad i = 1, 2 \end{aligned}$$

of a separation unit from a single input stream

$$x^{in} = \left(N^{in}_{CO_2}, N^{in}_{H_2}, N^{in}_{CO}, N^{in}_{CH_4}, T^{in}, p^{in}\right)^\top$$

by predefined parameters T_1, T_2, p_1, p_2 and $\iota \in [0,1]^4$ as

$$\left.\begin{aligned} N_{1,j} &= \iota_j N_{in,j}, \\ N_{2,j} &= (1-\iota_j) N_{in,j}, \end{aligned}\right\} \; j \in \{CO_2, H_2, CH_4, H_2O\},$$

as well as further energy balances distinct for the specific separation process. The investment costs are calculated from

$$CAPEX(x) = C_0 \sum_i N_i.$$

Tables 11 and 12 list the values of the parameter C_0, which were adapted from the review [52] corresponding to the commercial separation units of the size to treat 500 Nm^3/h, which is closest to the aforementioned a priori gas flow estimate.

We consider the Pressure Swing Adsorption (PSA) process to separate CO_2 and CH_4. A large variety of established adsorbent materials are suitable for this particular separation task, e.g., zeolites, silica gel, and activated carbon (AC) [129]. Adsorption processes can separate a component to a very high purity. As is well known from literature [109], CH_4 can be extracted with a purity of more than 99% from CO_2 with zeolites. A drawback of this method, however, is that large quantities of methane remain in the off-gas. In accordance with studies on the adsorbent zeolite 5A [109] we chose parameters denoted PSA (Z) in Table 11. We constrain the inlet pressure to the adsorption pressure $p^{in} \geqslant p_1$, making additional compression at this unit unnecessary. Decompression of the column is performed via a

Table 11: Parameters of adsorption black box models

	PSA (Z)	PSA (AC)	PSA (Z II)	PSA (AC II)
ι	[0.01,1,0.85,0]	[0.05,0.99,0.1,0]	[0.15,1,0.99,0]	[0.7,0.99,0.85,0]
p_1 [bar]	6	23	6	23
p_2 [bar]	0.2	1.0325	0.2	1.0325
C_0 [$\frac{10^3\$}{mol/s}$]	475.4	475.4	950.7	950.7

$T_1 = T_2 = 298.15$ K

subsequent state changer model, see Section 5.1.1. Furthermore, we assume that no technical work can be recuperated from the depressurization state to the desorption pressure p_2 and that the temperature oscillations during adsorption and desorption result in negligible heat flows, thus

$$W(x) = 0,$$
$$Q(x) = 0.$$

In a similar manner, we consider the separation of hydrogen via the adsorbent AC [53]. Table 11 gives the parameters in the column labeled PSA (AC). This technology can be applied after methanation to recycle super-stoichiometric amounts of H_2.

To avoid damage to the adsorbent, the gas stream entering the PSA unit must be dry; therefore, we add the constraint

$$N^{in}_{H_2O} = 0$$

to the model.

To separate both CO_2 and CH_4 with a very high purity, two PSA units are used in parallel [109]. The setup is depicted and described in Figure 18. The unit in position (P1) in Figure 18 has the operating parameters given by PSA (Z) or PSA (AC) in Table 11. The unit in position (P2) has the parameters given in Table 11 by PSA (Z II) or PSA (AC II), respectively. We calculate the additional work for the repressurization via the state changer model (see Section 5.1.1). We consider the two-PSA setup as a single-unit alternative to the one-PSA model in the superstructure.

We apply Temperature Swing Adsorption (TSA) to dry the gas mixture with parameters shown in Table 12. Furthermore, heat is required for the desorption of the adsorbent.

$$Q(x) = \sum_i N_{2,i} c_{p_i} (T_2 - T_1)$$

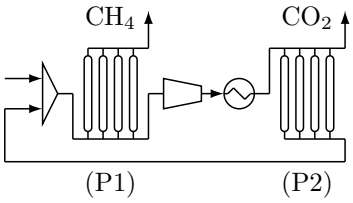

Figure 18: Two connected PSA units for CO_2/CH_4 separation

A typical PSA unit for separation of binary mixtures produces only one product gas stream at a very high purity. In this application, the unit (P1) produces high-purity CH_4 and a mixture of CH_4 and CO_2. We achieve high product gas concentrations for both product streams by redirecting the second gas stream to another PSA unit (P2). This unit extracts CO_2 at a high concentrations and redirects the second stream, again a mixture, back to the first unit. To implement the cyclic depressurization and repressurization of the PSA unit, we add an additional compressor between the units.

Table 12: Parameters of adsorption, absorption and membrane separation black box models

	TSA	ASC	WSC	MEM
ι	[0.95,1,0.99,0]	[0.95,1,0.99,0]	[0.95,1,0.99,0]	[0.95,1,0.99,0]
T_1 [K]	298.15	333.15	298.15	298.15
p_1 [bar]	6	1.0325	6	6
T_2 [K]	418.15	413.15	-	298.15
p_2 [bar]	6	1.5	-	0.2
C_0 $[\frac{10^3\$}{mol/s}]$	475.4	907.5	172.9	570.4

An alternative process to separate CO_2 from CH_4 is absorption. Both water and amine scrubbing are widely applied in the industry [128, 130]. In alignment, we include the separation via chemical scrubbing with amines (ASC) and that with water scrubbing (WSC) in the analysis with parameters shown in Table 12. Note, that WSC is modeled to have a single output material stream containing mostly methane, because the off-gas is a mixture of carbon dioxide, oxygen, and nitrogen not suitable for further utilization in the process. For ASC, work and heat demands are calculated via

$$W(x) = w_{ASC}\left(\sum_i N_{1,i} + \sum_i N_{2,i}\right),$$

$$Q(x) = q_{ASC}\left(\sum_i N_{1,i} + \sum_i N_{2,i}\right),$$

where $w_{ASC} = 13.8$ and $q_{ASC} = 54.1$. The parameters for MEM were taken from [128, 130]. As for PSA, drying of the gas stream is performed prior to application of this unit.

State changer

To model the temperature and pressure changes of a material stream between unit operations, we include state changers. We model the isothermal compression ($T^{out} = T^{in}$) to calculate the reversible work demand by via

$$\begin{aligned} x &= \left(T^{out}, p^{out}, \hat{p}, W^{rev}, Q^{SC}\right)^\top \\ W^{rev} &\geqslant \sum_i N_i R T^{in}\left(\hat{p} - \ln\left(p^{in}\right)\right), \\ \exp(\hat{p}) &\leqslant p^{out}. \end{aligned}$$

Assuming a working efficiency of 80%, we get $W(x) = W^{rev}/0.8$ and an additional heat stream

$$Q^{(1)}(x) = -W(x).$$

Furthermore, a temperature change is calculated according to

$$\begin{aligned} Q^{SC} &= \sum_i N_i c_{p_i}(T^{in})(T^{out} - T^{in}), \\ Q^{(2)}(x) &= Q^{SC}. \end{aligned}$$

The capital cost of a compressor is calculated via

$$CAPEX(x) = MF\ CE\ C_0\left(\frac{W(x)}{S_0}\right)^\alpha$$

with $C_0 = 23000$ \$, $S_0 = 74.6$ kW, $\alpha = 0.77$, MF= 3.61.

5.1.2 *Superstructure Model*

To describe the setup of a superstructure, we use a directed, acyclic graph $\mathcal{G} = (\mathcal{V}, \mathcal{E})$, where nodes $\mathcal{V}$ denote the unit models and edges $\mathcal{E}$ represent the intermediate material streams. For each process unit $U \in \mathcal{V}$ we assign a binary indicator variable $x_{T,U} \in \{0, 1\}$. Indicator variables indicate whether the respective node U is active ($x_{T,U} = 1$) or inactive ($x_{T,U} = 0$), given a

solution to the superstructure problem. We use the subscript U for a unit model $U \in \mathcal{V}$ again to describe unit models as introduced in (29). The constraints of active nodes must hold, whereas for inactive nodes, they are deactivated. Constraints corresponding to a unit operation model U can be deactivated via different formulations. A classic example is the big M formulation, where a parameter $M \in \mathbb{R}$ is chosen large enough such that a constraint $g_U(x_U, x_U^{in}) \leqslant 0$ is not enforced if $x_{T,U} = 0$,

$$g_U(x_U, x_U^{in}) \leqslant M(1 - x_{T,U}).$$

The big M formulation has the advantages of being linear if g_U is linear, and that CQs are not violated. However, weak relaxations and ill-conditioning make this formulation unsuitable for practical applications if the upper bound on the constraints is unknown or very large [131]. Therefore, we apply this formulation only to the box constraints and to calculate the material stream x_U^{in} entering unit U from the output streams $X_{pre(U)}^{out} := \{X_V^{out} \mid V \in pre(U)\}$ of connected units, where a suitable upper bound is known a priori. The box constraints are used to fix variables of inactive models. A variable is forced to zero via Eq. (33) or to the lower bound via Eq. (34) if zero is not part of its domain.

$$x_{T,U} \cdot lb_U \leqslant x_U \leqslant x_{T,U} \cdot ub_U \qquad \text{if } 0 \in [lb_U, ub_U],\ U \in \mathcal{V} \tag{33}$$

$$lb_U \leqslant x_U \leqslant lb_U + x_{T,U} \cdot (ub_U - lb_U) \qquad \text{if } 0 \notin [lb_U, ub_U],\ U \in \mathcal{V} \tag{34}$$

An alternative to the big M formulations is the complementary formulation or vanishing constraint. A general vanishing constraint takes the form

$$x_{T,U} \cdot g_U(x_U, x_U^{in}) \leqslant 0, \qquad U \in \mathcal{V}, \tag{35}$$

which violates LICQ and MFCQ in points for which $g_U(x_U, x_U^{in}) = 0$ and $x_{T,U} = 0$ holds [131, 132]. This can cause feasible points to be falsely identified as optimal by NLP solvers applied in subpoblems. Therefore, regularization or smoothing is necessary, for example via the relaxation

$$x_{T,U} \cdot g_U(x_U, x_U^{in}) \leqslant \epsilon.$$

This relaxation fulfills the CQs, but results in an ill-conditioned optimization problem and inexact solutions. The smooth perspective function [132]

$$\hat{g}\left((1-\epsilon)x_{T,U} + \epsilon, x_U, x_U^{in}\right) + \epsilon(x_{T,U} - 1) \cdot g_U(0,0) \leqslant 0$$

with

$$\hat{g}\left(\hat{x}_{T,U}, x_U, x_U^{in}\right) := \hat{x}_{T,U} \cdot g_U\left(x_U/\hat{x}_{T,U}, x_U^{in}/\hat{x}_{T,U}\right)$$

avoids this problem and does not violate CQs. However, the runtime of solving the corresponding optimization problem is increased [132].

So instead of applying the perspective function, we use the general vanishing constraint (35). Having feasible points, which violate CQs, is a problem for NLP optimization. Degenerate, feasible points are falsely classified as locally optimal by general NLP solvers. However, in the global optimization framework of branch-and-bound solvers with linear underestimators, this is not the case. The optimality conditions come from the convergence of the upper and lower bounds. Feasible points, which give the upper bound do not need to be locally optimal for the algorithm to work, thus the upper bound is still correct. Furthermore, the optimization problem, which gives the lower bound is a linear problem. Linear problems fulfill the Abadie CQ, which is a sufficient CQ for the application of KKT conditions [133]. Thus, the lower bound is also correct and we do not expect degenerate points to impact the final result of the optimization, only the runtime. For a discussion of a reformulation of the superstructure problem, which fulfills the LICQ, we refer to the Appendix B. Such an alternative formulation might be necessary if other optimization algorithms with nonlinear underestimators are applied.

We use the directed graph $\mathcal{G} = (\mathcal{V}, \mathcal{E})$ to formulate the topology of the superstructure. We define

$$\begin{aligned} &\mathrm{pre} : \mathcal{V} \to \mathcal{P}(\mathcal{V}), && \mathrm{pre}(U) := \{V \in \mathcal{V} \mid (V, U) \in \mathcal{E}\} \\ &\mathrm{post} : \mathcal{V} \to \mathcal{P}(\mathcal{V}), && \mathrm{post}(U) := \{V \in \mathcal{V} \mid (U, V) \in \mathcal{E}\} \end{aligned}$$

where $\mathcal{P}(\mathcal{V})$ denotes the power set of $\mathcal{V}$. With these mappings, we can derive special ordered set (SOS) constraints restricting solutions to a single path through the connection graph.

$$x_{T,U} \leqslant \sum_{V \in \mathrm{pre}(U)} x_{T,V} \leqslant 1 \qquad \forall U \in \mathcal{V} \tag{36}$$

$$x_{T,V} \leqslant \sum_{U \in \mathrm{post}(V)} x_{T,U} \leqslant 1 \qquad \forall V \in \mathcal{V} \tag{37}$$

Recycle and material streams

The superstructure includes recycling from separation units back to the reactor. For a recycle stream from model $V \in \mathcal{V}$, variable $r_V \in [0, 0.95]$ describes the fraction of the product stream recycled back to the process. The rest is purged, i.e., considered a waste stream. PSA, ASC and MEM are considered for recycling. For processes with a recycle loop, we add the costs

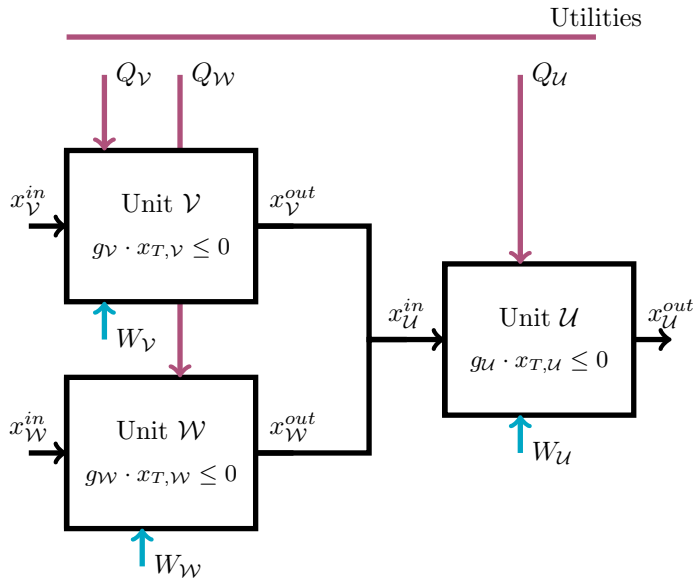

Figure 19: Scheme of connected unit level models to a structure with connections $\mathrm{pre}(U) = \{V, W\}$

We route material streams of parent nodes V and W to a child node U. The corresponding indicator variables $x_{T,U}, x_{T,V}, x_{T,W}$ determine whether a unit is part of a solution candidate. We obtain the work demand of the process by summing up the work demand of the individual nodes. We collect the heat flows and consider them for indirect heat integration.

of an additional mixer to the CAPEX. The material stream entering a unit model $U \in \mathcal{V}$ is fixed by

$$x_U^{in} - \sum_{V \in \mathrm{pre}(U)} x_{T,V} x_V^{out} - \sum_{V \in \mathrm{rec}(U)} r_V x_V^{out,rec}, \qquad \text{for } U \in \mathcal{V}. \tag{38}$$

where $\mathrm{rec}(U) \subset \mathcal{V}$ are the units which can recycle reagents back to unit U and $r_V \leqslant x_{T,V}$.

Heat Integration

Heat integration between the unit models and utilities covers the heat and cooling demands of the process units. In addition, heat sinks and sources throughout the process are identified to detect the internal utilization potential of the heat flows. To implement this, heat flows must entail information regarding the temperature, as heat can only be supplied from sources of higher temperature.

Heat integration is performed indirectly, according to the method proposed by Schack et al. [134] and Liesche et al. [135]. For this purpose,

we assume that we have utilities at temperatures $\hat{T}_i, i \in \{1, \dots, n_E\}$, where $n_E \in \mathbb{N}$ denotes the number of utilities. A minimal temperature difference of $\Delta T = 10$ K must hold for the heat integration between a utility and a unit for realistic heat transfer rates. As opposed to the model introduced by Schack et al. [134], we consider the unit temperatures to be variables; therefore, we do not classify the heat flows into the three cases (full, partial, or no heat integration) a priori. Instead, we differentiate between two types of heat flows: Heat flow with a temperature change between two temperatures T_{in}, T_{out} (type I) and heat flow at a constant temperature (type II), e.g., excess heat from the isothermal reactor model. For heat flows of type I, we calculate the heat flow $\dot{Q}^I_{j,i}$ between utility $i \in \{1, \dots, n_E\}$ and unit $u \in \mathcal{V}$ with $\dot{Q}^I_u = c_{pu}(T^I_{u,out} - T^I_{u,in})$ via the constraints

$$\underline{c}_{u,i} c_{pu} \leqslant \dot{Q}^I_{u,i} \leqslant \overline{c}_{u,i} c_{pu}, \qquad \text{for } i \in \{1, \dots, n_E\},\ u \in \mathcal{V}, \tag{39}$$

with

$$\begin{aligned}
\overline{c}_{u,i} &= \max\left\{\min\left\{T^I_{u,out}, \hat{T}_i - \Delta T\right\} - T^I_{u,in}, 0\right\}, \\
\underline{c}_{u,i} &= \min\left\{\max\left\{T^I_{u,out}, \hat{T}_i + \Delta T\right\} - T^I_{u,in}, 0\right\}.
\end{aligned}$$

If the direction of the heat flow is known a priori (e.g., heating of the TSA desorption gas), some of the minimum and maximum functions can be omitted. This reduces the constraints to

$$\left.\begin{aligned}
\overline{c}_{u,i} &= 0, \\
\underline{c}_{u,i} &= \max\left\{T^I_{u,out}, \hat{T}_i + \Delta T\right\} - T^I_{u,in},
\end{aligned}\right\} \text{for } i \in \{1, \dots, n_E\},\ u \in \mathcal{V} \tag{40}$$

for hot and

$$\left.\begin{aligned}
\overline{c}_{u,i} &= \min\left\{T^I_{u,out}, \hat{T}_i - \Delta T\right\} - T^I_{u,in}, \\
\underline{c}_{u,i} &= 0,
\end{aligned}\right\} \text{for } i \in \{1, \dots, n_E\},\ u \in \mathcal{V} \tag{41}$$

for cold material streams. Note that the remaining min/max functions can also be omitted for the outer utilities, i.e., for the hottest and for the coldest utility. Other min/max functions are implemented as

$$\min\{a, b\} = (a + b - |a - b|)/2, \qquad \max\{a, b\} = (a + b + |a - b|)/2$$

with the use of SCIPs abs() function. The abs() function is implemented via the use of new continuous and/or binary variables and secant cuts. For heat flows of type II, the general constraints

$$\min\left\{Q_u^{II}, 0\right\} \leqslant Q_{u,i}^{II} \leqslant \max\left\{Q_u^{II}, 0\right\}$$
$$\min\left\{\sum_{i\in I} Q_{u,i}^{II}, 0\right\}\left(\min_{i\in I}\left\{\hat{T}_i + \Delta T - T_u^{II}, 0\right\}\right) \geqslant 0$$
$$\max\left\{\sum_{i\in I} Q_{u,i}^{II}, 0\right\}\left(\max_{i\in I}\left\{\hat{T}_i - \Delta T - T_u^{II}, 0\right\}\right) \geqslant 0$$

for $i \in \{1, \ldots, n_E\}$ can be simplified significantly, if the flow direction, and therefore the sign of the heat flow $Q_{u,i}$, is known a priori. This is the case for all heat flows of type II in the current application. The simplified constraints are given by

$$Q_{u,i}^{II}\left(\hat{T}_i + \Delta T - T_u^{II}\right) \geqslant 0, \qquad \text{for } i \in \{1, \ldots, n_E\},\ u \in \mathcal{V} \tag{42}$$

for hot and

$$Q_{u,i}^{II}\left(\hat{T}_i - \Delta T - T_u^{II}\right) \geqslant 0, \qquad \text{for } i \in \{1, \ldots, n_E\},\ u \in \mathcal{V} \tag{43}$$

for cold heat flows. Furthermore,

$$\sum_{i\in\{1,\ldots,n_E\}} Q_{u,i}^{I} = Q_u^{I}, \qquad u \in \mathcal{V}, \tag{44}$$
$$\sum_{i\in\{1,\ldots,n_E\}} Q_{u,i}^{II} = Q_u^{II}, \qquad u \in \mathcal{V} \tag{45}$$

holds for all heat flows. Figure 20 shows an example of indirect heat integration.

The external heat demand/surplus of a utility i is denoted by

$$Q_{ext,i} = \sum_{u\in\mathcal{V}} Q_{u,i}^{I} + \sum_{u\in\mathcal{V}} Q_{u,i}^{II}, . \qquad \text{for } i \in \{1, \ldots, n_E\}. \tag{46}$$

To cover the external heat demand of utilities, we add directly fired heaters. Cooling is performed via water cooling towers. We calculate the capital costs of heat exchangers and directly fired heaters via the Guthrie equation. For heat exchangers, the parameters $C_0 = 5,000$ \$, $S_0 = 37.2$ m^2, $\alpha = 0.65$, MF $= 3.3$ and for directly fired heaters $C_0 = 20,000$ \$, $S_0 = 1465$ m^2, $\alpha = 0.77$, MF $= 2.73$ were taken from Biegler et al. [124]. The cooling of utilities is performed via a cooling tower. The capital cost of a cooling tower was

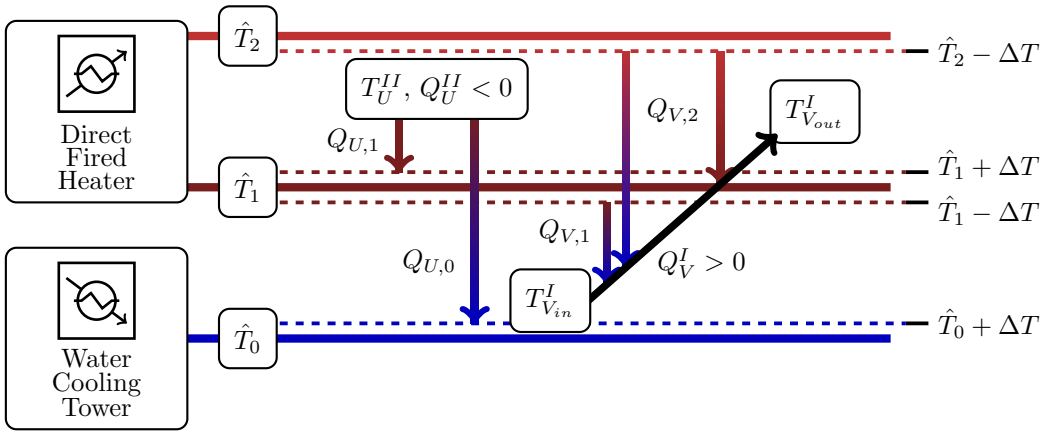

Figure 20: Scheme for the indirect heat integration

The Figure shows an example for the heat flows between units and utilities. The example has three utilities at temperatures $\hat{T}_0 < \hat{T}_1 < \hat{T}_2$*, one unit* U *producing excess heat at isothermal conditions at temperature* T_U^{II} *(*$\hat{T}_1 + \Delta T < T_U^{II} < \hat{T}_2 - \Delta T$*), and one unit* V *heating up a material stream from temperature* $T^I_{V,in}$ *(*$\hat{T}_0 + \Delta T < T^I_{V,in} < \hat{T}_1 - \Delta T$*) to temperature* $T^I_{V,out}$ *(*$\hat{T}_1 + \Delta T < T^I_{V,out} < \hat{T}_2 - \Delta T$*). Eq. (42) assures that* $Q_{U,2} = 0$*, since excess heat can only be supplied to utilities of lower temperature. The solver can freely distribute the excess heat* Q_U^{II} *to the utilities* 0 *and* 1*. A fraction of the heat flow* Q_V^I *can be fed to utility* 1*. As the temperature rises above* $\hat{T}_1 - \Delta T$*, however only utility* 2 *can provide heat to unit* V*. The fraction of the heat, which can be supplied by either utility* 1 *or utility* 2 *is given by Eq. (40).*

calculated by EWK [136], specifically to meet the cooling demand of the coldest utility ($T = 288.15$ K). The cost including frost protection but without transport is 38,477 €. Assuming a rate of exchange of 1.1, this corresponds to 42,305 $.

Note that the hottest and coldest utility temperatures are fixed by the process temperature boundaries, i.e., $\hat{T}_1 = T_{min} - \Delta T$, $\hat{T}_{n_E} = T_{max} + \Delta T$. This is necessary to make heat transfer realistic and the integration feasible. Temperatures of additional utilities $\hat{T}_i \in [T_{min}, T_{max}]$, $i \in \{2, \dots, n_E\}$ if $n_E > 2$ are optimized by the solver. Increasing the number of heat exchangers is expected to increase the heat network cost and, therefore, the capital cost of the plant. In the case of two utilities, no indirect heat integration can be performed. All heat is flowing from the hot utility to the process and from the process to the cold utility. Therefore, we chose $n_E = 3$.

Objective

We optimize the superstructure with regards to two objectives: to maximize the exergetic efficiency, which is a goal of many climate change mitigation

actions both nationally and internationally, and to minimize investment costs, which is relevant for plant operators. Furthermore, the two objectives are combined via linear combination to get Pareto optimal solutions to this multi-objective optimization problem.

We describe efficiency via chemical exergy of the produced methane and the investment cost via total process CAPEX. The efficiency η is calculated in reference to the 1 MW used for water electrolysis as

$$\begin{aligned}\eta &= \frac{F_{CH_4} - F_W - F_Q}{F_{ref}} \\ &= \frac{\sum\limits_{j\in\{1,\dots,n_P\}} F^j_{CH_4} - F^{feed}_{CH_4} - \sum\limits_{u\in\mathcal{V}} W_U - \sum\limits_{i\in\{1,\dots,n_E\}} (1-\frac{T_0}{\hat{T}_i})\max\{0, Q_{ext,i}\}}{1000\ \text{kW}}\end{aligned} \tag{47}$$

where $F^j_{CH_4}$ denotes the chemical exergy of material stream j leaving or entering the process. The heat demand of the utilities is weighted by the term $(1-\frac{T_0}{\hat{T}_i})$, which is the efficiency of a Carnot engine. The fraction $\frac{T_0}{\hat{T}_i}$ relates the temperature of the utility i to the ambient temperature $T_0 = 298.15$ K. Electrical energy directly relates to its exergetic value.

A material stream leaving the superstructure is evaluated via the chemical exergy of methane $e_{CH_4} = 831.2$ kJ/mol and hydrogen $e_{H_2} = 236.1$ kJ/mol if the requirements for feed into the gas distribution system, see Eqs. (G1) to (50), are met. If the requirements are not met, the respective product stream has no contribution to the objective.

The process CAPEX acts as a penalty term. The most efficient solutions tend to include extensive heat exchanger networks to integrate even very small heat flows back into the process. This leads to very costly processes. By adding the penalty term to the objective, these solutions to the superstructure are avoided. The objective is given by

$$f_1(x) = w_C \text{CAPEX} - w_\eta \eta \tag{48}$$

where the weights w_C and w_η determine the position of the solution along the Pareto front.

The process CAPEX is the sum of the unit model CAPEX contributions:

$$\text{CAPEX} = \sum_{u\in\mathcal{V}} \text{CAPEX}_U(x_U)$$

Alternatively to multi-objective optimization, we consider the total annual costs (TAC) as an objective for optimization. The TAC are calculated from the CAPEX and the operating costs (OPEX) as

$$\text{TAC} = \text{OPEX} + \left(\frac{\sigma}{1-(\sigma+1)^{-t_{payback}}}\right)\text{CAPEX} \tag{49}$$

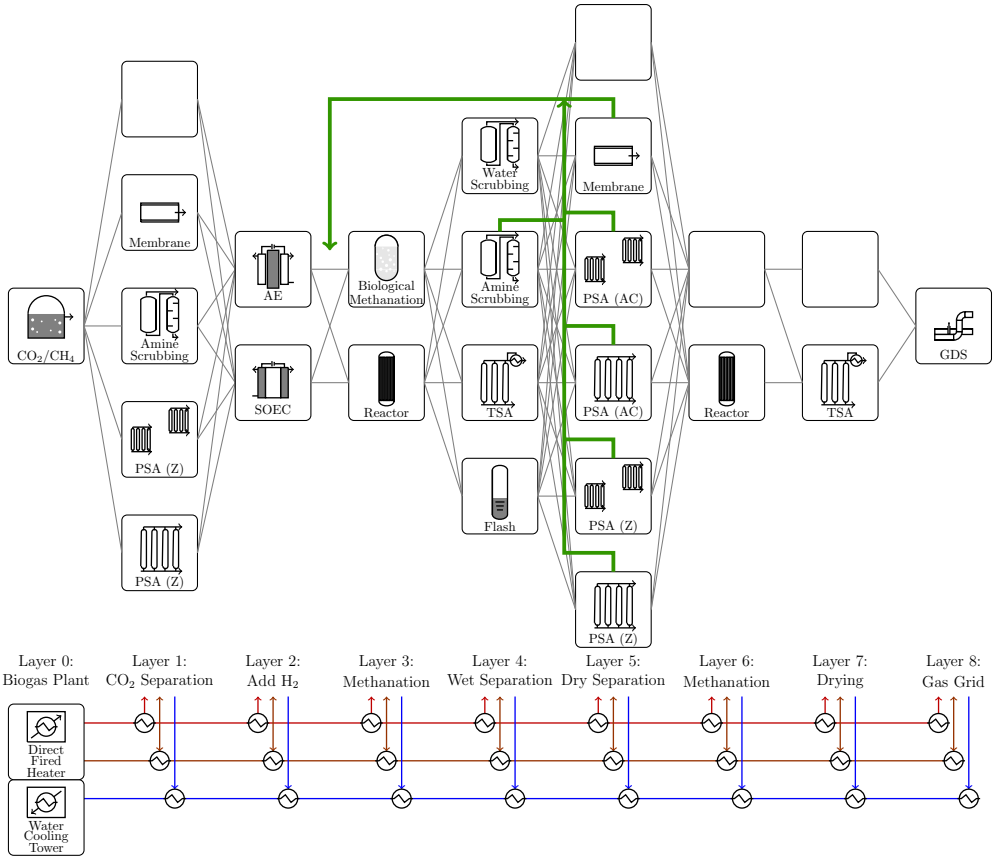

Figure 21: Graph of the superstructure

The superstructure graph has 7 layers between the biogas plant and gas distribution system. Recycling is considered from layers 4 and 5 to the reactor at layer 3. Layers 1, 5, 6, and 7 may be skipped by the solution, which is indicated in the figure by the empty boxes. We have different technologies for the purification of CO_2 in layer 1. Layer 2 includes the choice of electrolyzer, and layer 3 provides the choice of the first methanation step. After methanation, the gas mixture includes water as a side product. Therefore, we consider separation technologies which are not damaged by water in layer 4. These separation technologies in layer 4 can separate either reactants or water from the gas mixture. In layer 5, reagents can be separated from a dry gas mixture and recycled back to the reactor. Finally, a second reactor can be added in layer 6, which makes a final drying effort in layer 7 necessary. Each unit has the option to take or supply heat to the utilities. Finally, the gas is fed to the gas distribution system (GDS).

with an interest rate $\sigma = 0.06$ and a payback time $t_{payback} = 20$ a. For the calculation of the OPEX, we assume prices of 22 ct/kWh for electrical energy, 1.89 \$/kg water, 2.64 \$/kg waste water removal, and 2.53 ct/kWh steam.

Composite Model

A superstructure, including a methanation reactor, AE, SOEC, PSA (zeolite), PSA (AC), double PSA, TSA, flash condensation, ASC, WSC, MEM, compression, heating/cooling, a mixer, recycling and indirect heat integration was built. The overall superstructure optimization problem is given by

$$
\begin{aligned}
\min_{x=(x_T,x_\mathcal{V},x_{MS},x_e)^\top} \quad & f(x) \\
\text{s.t. } & (33)-(46) \\
& x_U \in \mathbb{R}^{n_U} && \forall U \in \mathcal{V} \\
& x_\mathcal{V} = [x_U]_{U\in\mathcal{V}} \\
& x_T \in \{0,1\}^n \\
& x_{MS} = [x_U^{in},\ x_U^{out}]_{U\in\mathcal{V}},
\end{aligned}
$$

where $x_e = \big([\overline{c}_{U,i}, \underline{c}_{U,i}, Q^I_{U,i}, Q^{II}_{U,i}]_{U\in\mathcal{V},i\in\{1,\dots,n_E\}}, [T^I_{U,in}, T^I_{U,out}, T^{II}_U]_{U\in\mathcal{V}}, \dots$ $[\hat{T}_i, Q_{ext,i}]_{i\in\{1,\dots,n_E\}}\big)^\top$ includes all variables of the heat integration, and $f(x)$ relates to either the linear combination of efficiency and CAPEX (48) or the TAC (49). The structure is shown in Figure 21, with a total of 600 alternative process routes.

5.2 RESULTS

5.2.1 *Catalytic Methanation*

We solve the superstructure model introduced in the previous section under various conditions.

- **Electrolyzer technology (AE or SOEC)**
  AE are well-established technologies, commercially available at various scales. Because of this, they have lower cost than other water electrolysis technologies. However, AE have comparably low efficiency. SOEC operate at high temperatures, significantly increasing cell efficiency. The technology is in its early stage and, therefore, still quite expensive. Instead of allowing the solver to choose between these two technologies, we manually choose one of the technologies. This allows

us to directly observe the influence of the choice of electrolyzer on the optimization result.

- **Weight of linear combinations of the objectives**
  To compare the different alternative solutions, we select different points along the Pareto front via linear scaling of the objectives. We consider the weights $w_\eta = 1$, $w_C = 10^{-8}$ to focus on the process efficiency (O1). This typically leads to very extensive heat integration networks that utilize heat flows within the process. This is expected to lead to high capital costs. Therefore, we consider $w_\eta = 1$, $w_C = 10^{-5}$ as an alternative (O2). These weights scale efficiency and capital costs to roughly the same order of magnitude. Thus, we can obtain an efficient process with reasonable capital costs. We do not optimize with regard to only capital costs, as this typically leads to solutions close to an efficiency of 0%. Alternatively, we optimize the system with respect to the TAC (O3).

- **Constraints for feed into the gas distribution system**
  We consider two different thresholds for the amount of hydrogen allowed in the gas distribution system. Currently restrictive constraints of 2 mol-% H_2 need to be fulfilled in some areas. However, to facilitate the implementation of power-to-gas technologies in the future, these constraints are under discussion. Local distributors already allow for the feed-in of gas with up to 10 mol-% H_2. We consider the less restrictive bound of 10 mol-% H_2 as an alternative to the 2 mol-% H_2 constraint. The constraints for the two cases are given by (G1) and (G2), where x_i and C_i denote the molar fraction and concentration of component i.

$$\left.\begin{aligned} y_{H_2} &\leqslant 0.02 \\ 0.95 &\leqslant y_{CH_4} \end{aligned}\right\} \tag{G1}$$

$$\left.\begin{aligned} y_{H_2} &\leqslant 0.1 \\ 0.90 &\leqslant y_{CH_4} \end{aligned}\right\} \tag{G2}$$

In both cases

$$\left.\begin{aligned} y_{CO_2} &\leqslant 0.05 \\ C_{H_2O} &\leqslant 200\ \mathrm{mg/m^3} \\ p &= 16\ \mathrm{bar} \\ T &= 298.15\ \mathrm{K} \end{aligned}\right\} \tag{50}$$

must hold in addition. We perform global optimization for the 12 different introduced cases. In all cases we could identify a single optimal process configuration. For most of the results an optimality gap of below 0.1% with respect to process efficiency and a relative optimality gap of 1% with respect to CAPEX or TAC was reached, which is very tight given the low accuracy of shortcut models and the estimation of the process costs via CAPEX, which only has an accuracy of 25-40% [124]. For the optimization with respect to the TAC (O3) with water electrolysis via SOEC the optimization exceeded the hardware's memory limitation. In the worst case, SOEC (G1) (O3) had a relative optimality gap of 5%, upon reaching the memory limitation, which implies that a process cost of \$6.048M instead of \$6.366M could be possible. SOEC (G2) (O3) had a relative optimality gap of 3.5%. However, we stress again that even in these cases one single process configuration could be clearly identified as optimal and that a gap of 5% is small given the accuracy of the CAPEX is 25-40% with regard to the real process costs. Reaching the hardware limitations is attributed to the model of the heat exchanger network, which is described by highly nonlinear functions and, in case of the high temperature electrolysis, is very extensive.

After fixing the choice of electrolyzer, we have a total of 3175 variables of which 33 are binary. The values of the objective functions after optimization are shown in Table 13. Figure 22 shows a comparison of the CAPEX values of the different cases. More detailed capital investment costs of the solutions can be found in the Appendix, Tables 20-31. We note here, that for the optimization with respect to objective (O3) of the process using AE for water electrolysis gave a point which is Pareto dominant over the optimization with respect to (O2). This behavior can be caused by the feasibility thresholds. The different numerical accuracy of the optimization problems can be caused by different presolving steps or branching within SCIP.

Two different process routes were chosen by the solver. A cascade of two reactors with intermediate water separation was used, if only 2 mol-% of hydrogen can be supplied to the gas distribution system, according to the constraints (G1). The configuration is shown in Figure 24. If a higher concentration of hydrogen can be supplied to the grid (G2), a second reactor for methanation is not needed. In this case, focusing on the efficiency results in the process configuration shown in Figure 25. The cases for which this configuration was optimal are marked blue in Table 13. This configuration results in increased process efficiency. This effect occurs because less hydrogen is converted to methane. This reduces the exergetic losses in the chemical conversion steps.

If the weights of the objective favor the efficiency objective (O1), the optimal intermediate utility temperature is 570 K. This temperature is directly below the optimal reactor temperature with a difference equal to $\Delta T = 10$ K.

Table 13: Objective values

Values of the efficiency and CAPEX for the 12 considered cases after global optimization. The results with respect to objectives (O1) and (O2) give different values on the Pareto front of efficiency and CAPEX. Meanwhile, objective (O3) corresponds to the TAC. The solutions marked in blue correspond to the optimal configuration shown in Figure 25. The other solutions correspond to the optimal configuration shown in Figure 24.

Electrolyzer		AE		SOEC	
H_2 constraint		Eq. (G1)	Eq. (G2)	Eq. (G1)	Eq. (G2)
η [%]	(O1)	50.0	50.8	65.1	65.8
CAPEX [10^{-6}· $]		3.274	2.811	5.645	5.276
η [%]	(O2)	45.3	45.3	58.6	65.0
CAPEX [10^{-6}· $]		2.538	2.538	5.204	4.990
η [%]	(O3)	45.7	45.8	64.5	61.4
CAPEX [10^{-6}· $]		2.475	2.479	6.366	5.474

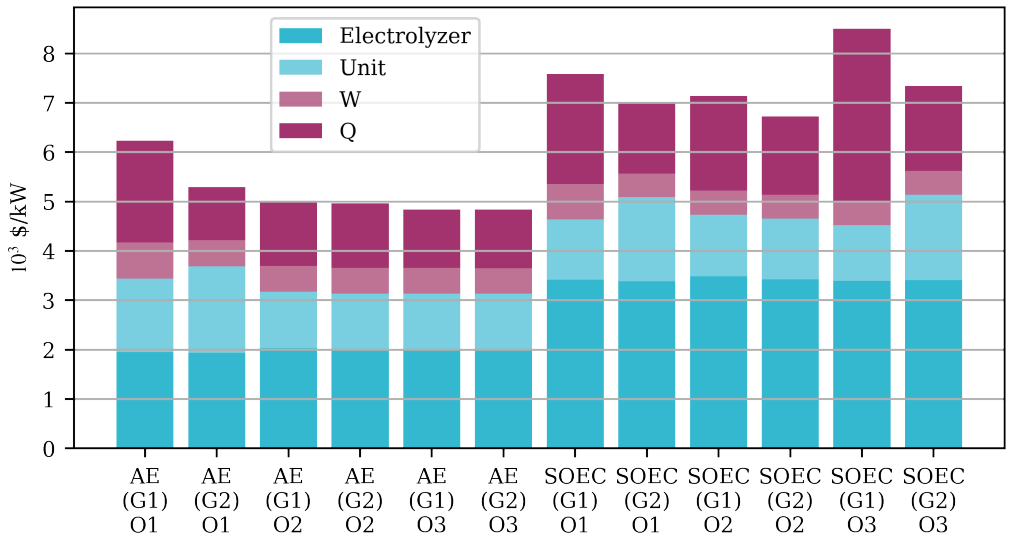

Figure 22: CAPEX values of the optimization results

The figure shows the contributions of the unit, compressor (W), and heat exchanger (Q) costs to the CAPEX. The CAPEX is scaled to the plant's product capacity of total CH_4 in terms of LHV in kW. Note that SOEC is a technology on demonstration level and has potential for cost improvement.

Table 14: Contribution of product, heat, and work to the exergetic efficiency η
The exergy values of F_{CH_4}, F_W, *and* F_Q *at the optimal solution determine the efficiency* η *via Eq. (47). In addition the lower heating value of the product stream (*LHV*) is shown. Note, that this value includes the contribution of hydrogen in the product gas.*

Case			η %	LHV [kW]	F_{CH_4} [kW]	F_W [kW]	F_Q [kW]
AE	(G1)	(O1)	50.0	525.0	544.1	40.8	2.8
AE	(G2)	(O1)	50.8	530.8	550.3	41.4	1.5
AE	(G1)	(O2)	45.3	505.6	522.3	33.2	36.1
AE	(G2)	(O2)	45.3	510.7	528.3	39.2	36.1
AE	(G1)	(O3)	45.7	511.2	529.1	39.3	32.8
AE	(G2)	(O3)	45.8	511.7	529.0	39.3	31.7
SOEC	(G1)	(O1)	65.1	744.2	771.3	54.6	65.2
SOEC	(G2)	(O1)	65.8	750.9	778.2	55.2	65.2
SOEC	(G1)	(O2)	58.6	728.6	755.1	75.3	93.4
SOEC	(G2)	(O2)	65.0	742.0	769.0	54.8	64.6
SOEC	(G1)	(O3)	64.5	748.3	775.5	54.8	75.8
SOEC	(G2)	(O3)	61.4	745.1	772.2	55.1	103.0

This allows the maximal supply of excess heat of the reactor to this utility. The excess heat is then used to heat other process elements. If the CAPEX is weighted higher (O2), internal heat integration is omitted. Instead all heat is supplied and withdrawn externally. This reduces the costs of the heat integration network significantly, as the detailed costs in the Appendix show. For example in the case of AE and grid constraints (G1), the costs for the heat exchanger network are reduced from 2063 $\$/kW_{CH_4}$ to 1263 $\$/kW_{CH_4}$ by avoiding internal heat integration, where kW_{CH_4} denotes the energy of the product gas calculated by the lower heating value. Results of optimization of the superstructure with respect to TAC (O3) give very similar results. The results show adaptation of the extent of the heat exchanger network to the objective.

By using SOEC for water electrolysis, a higher process efficiency can be reached. This comes with a great increase in capital costs, roughly double than for using AE for water electrolysis, because of the still high costs of SOEC, as noted in Chapter 2. The excess heat of the reactor(s) (roughly 150 kW) covers the main bulk of the heat required for pre-heating of the SOEC at 373 K (roughly 150 kW for vaporization of water at 373 K). This

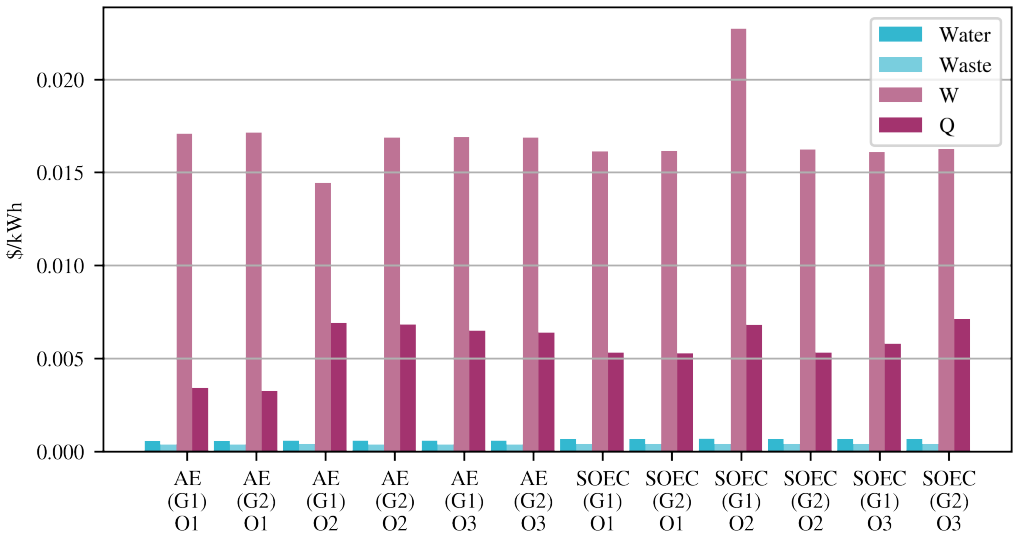

Figure 23: OPEX, Operating costs of the optimization results

The figure shows the contribution of feed water, waste water, work (W) and heat (Q) to the OPEX. The 220 $/hr for 1 MW of electrical energy for water electrolysis, equivalent to around 1.25 (SOEC) to 2 (AE) $/kWh, are not included in this figure. The costs for feed water and waste water are small in comparison to the costs from work and heat.

result shows that the positive effect of the heat integration on the efficiency does not improve with higher temperatures of the reactor.

Furthermore, the results show that if heat integration is avoided to reduce capital costs, supplying heat to the system greatly reduces the system efficiency.

For the solutions of (O1) and (O2), we estimate the OPEX after optimization. The results are shown Figure 23. The cost of electrical energy, denoted as *W*, does not include electricity for water electrolysis, which adds up to an additional cost contribution of 220 $/hr, corresponding to 1.25 to 2 $/kWh. The costs associated with the heat flows include the costs for hot steam and the electrical costs for the operation of the cooling tower, which needs around 7.5 kW of electrical energy.

The shortcut models used are afflicted with inaccuracies, which propagate to the optimal solution. Other solutions to the superstructure problem have objective values close to the global optimum, such that a clear optimal process must be determined with more accurate models. We consider a few other configurations to compare with the global optimal solution.

For the case of AE and grid specification (G1), another interesting configuration includes the separation of the CH_4/CO_2 gas mixture prior to the

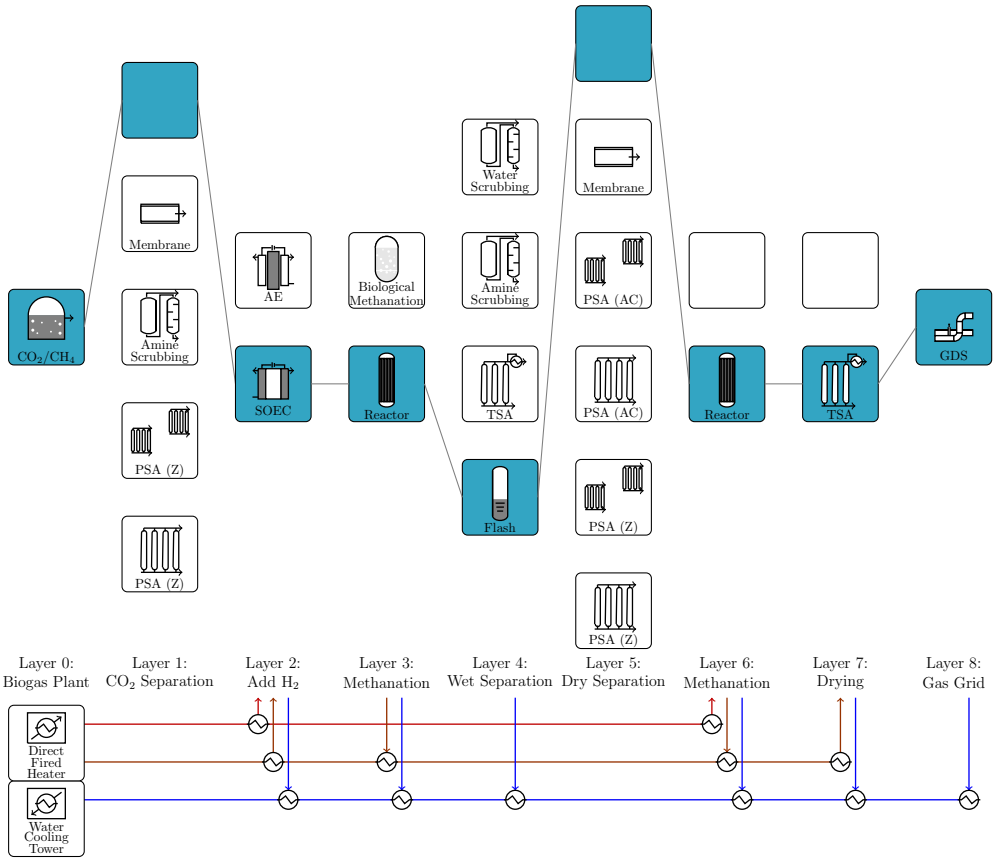

Figure 24: Solution path: Two reactor configuration.

The configuration is optimal in terms of efficiency and CAPEX for the choice of SOEC electrolyzer. If we replace SOEC by AE in layer 2, the same path through the rest of the superstructure is chosen, with changes to the heat exchanger network.

methanation reactor. Utilization of membrane separation for this task gives an efficiency of 49.4 % for (O1), compared with the 50.0% of the optimal solution. Furthermore, the unit costs increase from \$1.804M to \$1.817M, which is negligible with the given accuracy of the models.

Alternatively, we calculate the objective value of replacing the second methanation reactor by the separation and recycling of reactants. This process configuration has promising efficiency at higher process pressures of 13 bar [1]. For the current study, at lower process pressure of 6 bar, the configuration has an efficiency of 47.9%. We attribute the decrease in efficiency to the shortcut model for gas separation. For the gas separation, we used a more detailed PSA model in Chapter 4, which resulted in better separation properties.

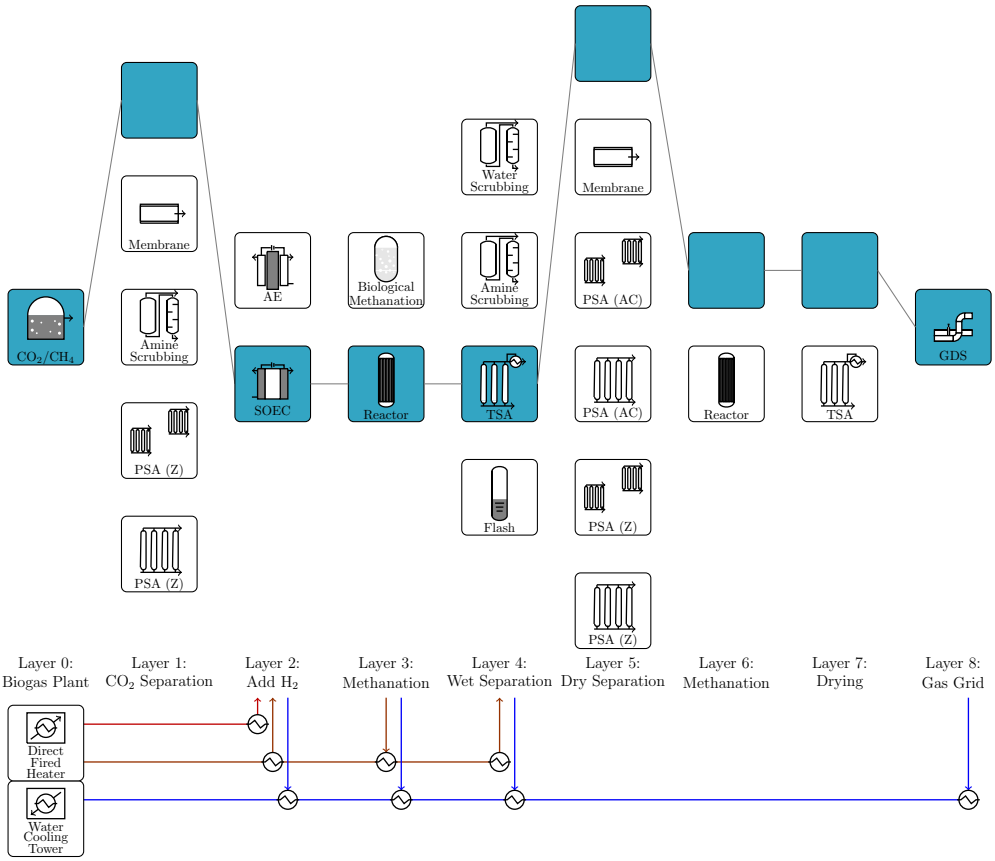

Figure 25: Solution path: Single reactor configuration.

The configuration is optimal in terms of efficiency for the choice of SOEC electrolyzer if a large quantity of hydrogen can be supplied to the gas distribution system. If we replace SOEC by AE in layer 2, the same path through the rest of the superstructure is chosen, with changes to the heat exchanger network.

5.2.2 *Biological Methanation*

None of the previous process design solutions included the biological methanation in layer 3. To compare the biological methanation process with the previous results, we enforce the biological methanation to be chosen by the solver by fixing the corresponding indicator variable to be 1. The results of the optimization, including AE and SOEC, are shown in Table 15. In the previous section, the methanation reactor was found to act as a significant heat source. The bioreactor, however, operates at lower temperatures, strongly limiting the heat integration within the process. This contributes to the decrease in the overall process efficiency shown in Table 15, as compared with that of the previous section.

Table 15: Results of the optimization with biological methanation
The table shows the results of the optimization with biological methanation with respect to (O1). We consider the two bioreactors BIO1 and BIO2 with 96 % and 65 % of CH_4 in the dry product gas, respectively. Optimization with respect to (O2) or (O3) shows almost identical results to the result of (O1). This is due to the limitation of the heat integration for this case.

Electrolyzer		AE		SOEC	
Bioreactor		BIO1	BIO2	BIO1	BIO2
η [%]	(O1)	47.0	46.5	56.1	55.3
CAPEX [10^{-6}· $]		3.554	3.839	5.709	6.134

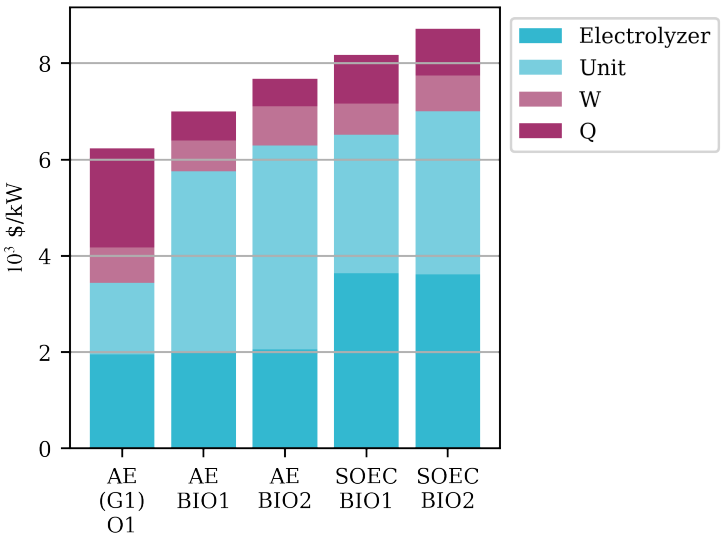

Figure 26: CAPEX values of the optimization results for biological methanation
The figure shows the contributions of the unit, compressor (W), and heat exchanger (Q) costs to the CAPEX. The CAPEX is scaled to the plants product capacity of total CH_4 in terms of LHV in kW. For reference, the value AE (G1) O1 for catalytic methanation is shown, which is also included in Figure 22.

For the bioreactor BIO1 with a high concentration of methane in the output gas of 96 %, the product gas does not need further purification apart from drying. Figure 28 shows the corresponding process configuration. The bioreactor BIO2 produces gas with a concentration of 65 % CH_4, which is not suitable for direct feeding to the gas distribution system. The result for this case shown in Figure 29 includes additional purification via membrane

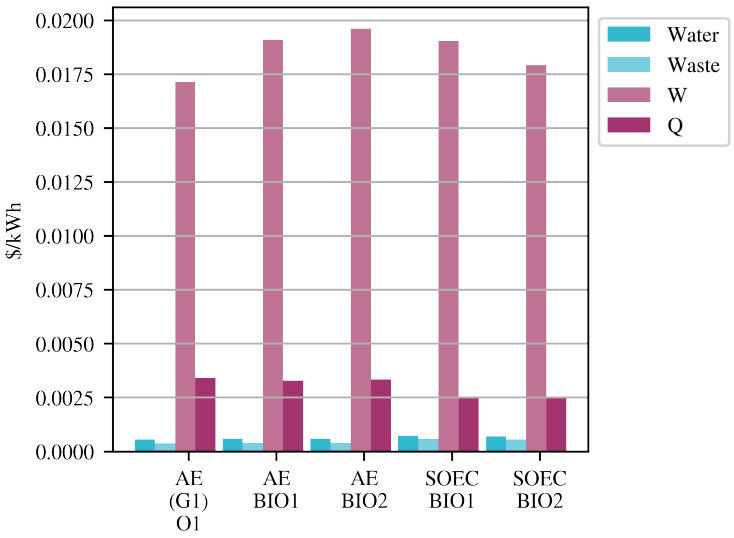

Figure 27: OPEX, Operating costs of the optimization results
The figure shows the contribution of water, waste water, work (W) and heat (Q) to the OPEX for the biological methanation. We do not include 220 $/hr for 1MW of electrical energy for water electrolysis, which would be equivalent to around 1.5 (SOEC) to 2 (AE) $/kWh. For reference, we show the value AE (G1) O1 for catalytic methanation, which is also included in Figure 22.

separation. However, the second-best solution utilizing PSA instead of membrane separation was very close to this result (within 0.4 % of the objective value with respect to efficiency). A more detailed analysis for this case is needed.

The processes using biological methanation show increased capital costs compared to the processes using catalytic methanation. The increase in cost is contributed to the increased cost of the biological methanation unit itself. However, capital costs of the heat integration network for the AE process are reduced significantly, as shown in Figure 26 and Figure 27 in terms of CAPEX and OPEX respectively. Combining the high efficiency of the SOEC with a high conversion rate in the bioreactor results in a large amount of product gas (SOEC BIO1). Nonetheless, the SOEC processes have a higher CAPEX per product in terms of LHV than the AE processes, as Figure 26 shows. If the conversion rate is low (SOEC BIO2), a large quantity of gas is recycled from the membrane separation unit. This results in large mass flow rates within the process and high costs for compression and heat exchanger equipment.

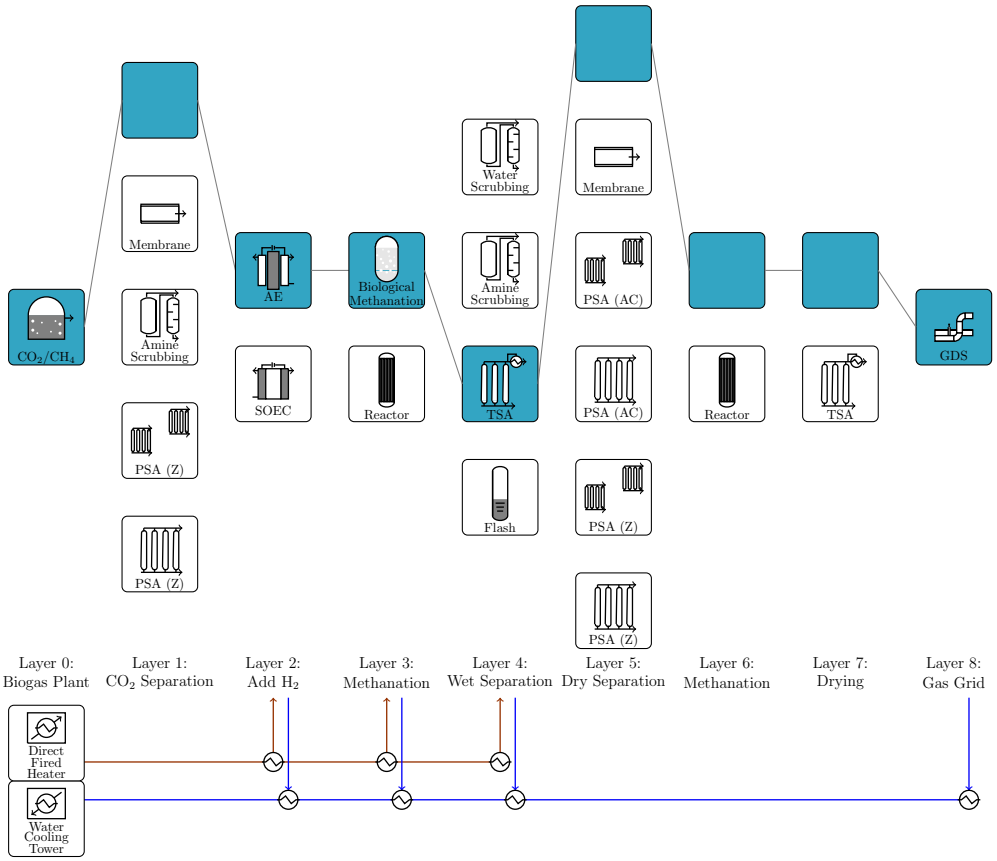

Figure 28: Solution path: Biomethanation with high CH_4 product concentration.

The configuration is optimal in terms of efficiency for the choice of AE if a high concentration of methane can be produced by the bioreactor.

5.2.3 *Methane as Chemical Energy Carrier*

To estimate the efficiency of methane as an energy carrier, we compute the power-to-power efficiency, as in Chapter 4, for the optimal process configurations of the current results. For comparability we again assume an efficiency of 57% for the CCPP corresponding to the lower heating value of the product gas. The exergetic values of the chemical exergy of the product, the required heat and work, and the lower heating value are shown in Table 14. We assume that all electrical energy required for the process comes from RES. The process has a heat demand at high temperatures, at which district heating is typically not available. Instead, the heat demand of the process is covered by using a part of the product methane in the direct fired heater. The amount of methane which is required is calculated from the energetic value of the heat demand and the lower heating value of the methane. We assume a thermal efficiency of the direct fired heater of 92%. We note here

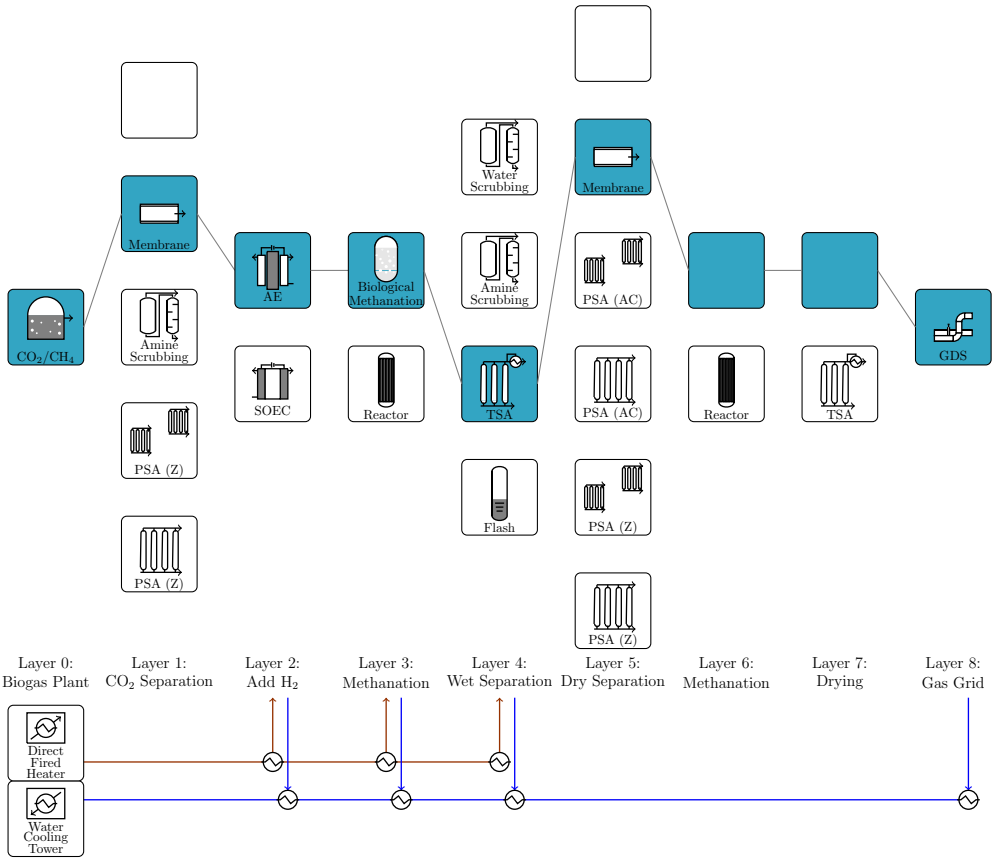

Figure 29: Solution path: Biomethanation with low CH_4 product concentration.

The configuration is optimal in terms of efficiency for the choice of AE if a low concentration of methane can be produced by the bioreactor. Membrane separation is chosen twice in the process, prior to and after methanation.

that the heat demand of the processes with SOEC as shown in Table 14 could be reduced further by using direct heat integration instead of indirect heat integration. The 21 kJ/mol of heat, which are produced by the electrical energy dissipation within the SOEC producing 3.71 mol/s of hydrogen could pre-heat the water steam prior to the electrolysis, significantly reducing the energetic heat demand by 77.9 kW, i.e., the exergetic heat demand F_Q of high temperature heat by about 55 kW. We thus calculate the power-to-power efficiency of the processes as

$$\eta_P = \frac{0.57(LHV_{CH_4} - Q_{ext}/0.92)}{F_W + 1000}$$

where Q_{ext} denotes the external energetic heat demand of the processes covered by methane combustion, corresponding to the exergetic heat demand F_Q, which in case of the SOEC processes is reduced assuming direct heat

Table 16: Efficiency η_P of using methane as an energy carrier from power to power.

Case			η_P %	Case			η_P %
AE	(G1)	(O1)	28.4	SOEC	(G1)	(O1)	39.4
AE	(G2)	(O1)	28.9	SOEC	(G2)	(O1)	39.7
AE	(G1)	(O2)	23.3	SOEC	(G1)	(O2)	35.5
AE	(G2)	(O2)	23.5	SOEC	(G2)	(O2)	39.3
AE	(G1)	(O3)	24.0	SOEC	(G1)	(O3)	38.7
AE	(G2)	(O3)	24.1	SOEC	(G2)	(O3)	36.3

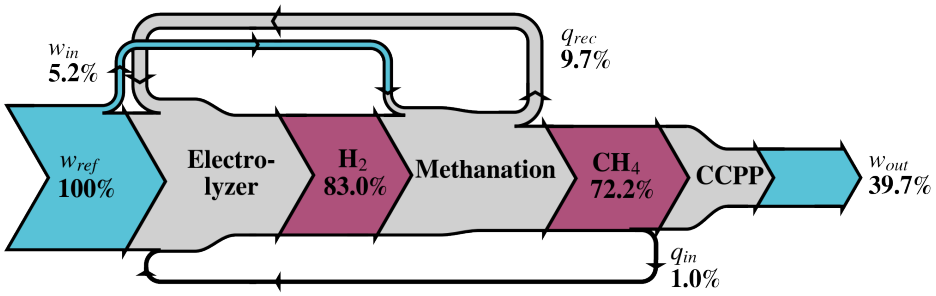

Figure 30: Exergy diagram of the optimal solution of the case SOEC (G2) (O1)
This diagram shows the exergy efficiency of the optimal power-to-power route with respect to efficiency. All energy and material flows are depicted in their exergetic value. Here, w_{in} denotes the work demand of compressors in the methanation process. The process excess heat q_{rec} and some of the product methane q_{in} are used for pre-heating of water for the SOEC. Finally, the work produced from the product methane is labeled w_{out}.

integration for the gas pre-heating and LHV_{CH_4} denotes the lower heating value of the product as shown in Table 14.

The results are shown in Table 16. Via optimization we could identify better alternatives than the process C2 from Chapter 4. An exergy flow diagram for power-to-power conversion is shown in Figure 30 for the optimal steady-state process of the case SOEC (G2) (O1) assuming the additional heat integration for pre-heating of water for the SOEC. The figure shows that using SOEC for the production of hydrogen improves the efficiency of the process. A significant amount of energy is lost at reconversion of methane to electrical energy via the CCPP.

The efficiency of storing electrical energy in form of methane is low compared to other energy storage technologies, such as compressed air energy storage systems (42-55%) and pumped hydro energy storage (70-80%) [3]. However, as mentioned in Chapter 1, the extension of pumped hydro energy storage is limited due to geographical prerequisites.

Instead of converting methane back to electrical energy, it can be used as transportation fuel in vehicles with gas combustion engines. If we use an estimated consumption of synthetic methane of 4 kg/100 km and a best case scenario of a methane production of 0.874 mol/MJ of electrical energy used for the methanation process, this results in 2.85 MJ/km. For comparison, electric cars report efficiencies of approximately 540 to 900 kJ/km.

5.3 CHAPTER SUMMARY

We applied a superstructure optimization approach to power-to-methane processes, related to 12 different scenarios. The processes were optimized in terms of exergy efficiency, which unifies the contributions of electrical, heat, and chemical flows to one energetic value. Alternatively, the processes were optimized with respect to the economic objectives CAPEX and TAC.

- The most efficient process with an efficiency of 65.8% utilizes SOEC for water electrolysis and includes heat integration within the process. The catalytic methanation was found to be a suitable heat source for preheating the steam for water electrolysis. The excess heat of the reactor covers the main bulk (vaporization of water) of the pre-heating process. However, an extensive heat exchanger network and the SOEC electrolyzer technology lead to high capital costs.
- The indirect heat integration, as included in the superstructure, showed a significant influence both on the process costs and efficiency, which was especially pronounced in the case of high-temperature electrolyzer, SOEC, where the catalytic methanation reactor can act as heat source for steam generation and/or pre-heating of the SOEC feed stream. Including internal heat integration increased the efficiency of processes with AE by 5%, while the efficiency of processes with SOEC increased by 7%.
- We showed, that the specification of the gas distribution system has an influence on the optimal process configuration. Increasing the threshold for feed of hydrogen to the gas distribution system reduces the number of necessary unit operations.

Furthermore, we assessed the potential of substituting the conventional chemical methanation unit with a biological one.

- The downstream configuration of the biological methanation was found to be dependent on the expected methane concentration of the unit, and as shown in the analysis a membrane separation unit was preferred for a methane concentration of 65 mol-% in the product gas. However, using other separation units such as pressure swing adsorption results in similar efficiency and cost, so that we can not determine a clear best solution given the limited accuracy of the black box models.
- Process configurations with biological methanation have a limited potential for internal heat integration because of the low temperature level at which heat from the methanation is released. This results in decreased efficiency, especially for processes equipped with a SOEC.

6

OPTIMIZATION OF PRESSURE SWING ADSORPTION VIA A TRUST-REGION FILTER ALGORITHM AND EQUILIBRIUM THEORY

In this chapter we take a closer look at the gas separation via pressure swing adsorption, which is a process commonly applied to many gas separation tasks, such as oxygen separation from air, flue gas separation, and biogas upgrading [137, 138, 129, 139]. For our application of biogas upgrading, PSA processes have an important advantage compared to other separation technologies. Namely, that other impurities, such as H_2S, N_2, and O_2 can be extracted from the product mixture of anaerobic digestion [140]. The process is frequently applied in industry, usually for purification of a gas mixture to up to 99 mol.-% purity [128], which we also applied in the previous chapters. To feed into the gas distribution system, however, only a purity of 95 mol.-% is required. This gives room to improve the process operation in regard to our application.

Another incentive to consider high-fidelity optimization of the PSA process in a PtM framework is the reduction of required storage units for the carbon source for dynamic plant operation. To use power-to-methane processes as a way to balance out supply of electricity from RES and demand, dynamic process operation must match the availability of RES. Storing large quantities of a CH_4/CO_2 mixture, rather than pure CO_2 increases the overall process cost. While technologies such as gas bags or gas cylinders [141, 142, 143] are readily available, storing a 3:2 mixture of CH_4/CO_2 significantly increases the volume of the gas to be stored. Furthermore, methane is flammable, which denotes a safety hazard for large quantities of stored mixtures. In practice, these are incentives to consider gas separation technologies for dynamic operation, despite the advantage of directly supplying the gas mixture to the methanation process, which we showed for steady state processes in the previous chapter. A holistic dynamic process optimization is out of the scope of this thesis. However, we take a first step in the direction of a high-fidelity process model by taking a closer look at the very challenging optimization of a high-fidelity PSA model.

Because of the technology's broad application in industry many studies exist on the simulation and optimization of PSA processes to maximize operation efficiencies and adsorbent materials [144, 145, 146, 147]. Despite the corresponding improvement in mathematical modeling of the process, optimization of the PSA process is still a challenging task. Typical mathe-

matical models for PSA processes describe the sharp adsorption fronts, cyclic behavior, and internal recycle streams by systems of stiff PDEs. Spatial discretization of these models results in systems of differential algebraic equations (DAEs), which are time consuming or numerically difficult to solve. The problem formulations are often ill-conditioned and internal recycle streams and the cyclic behavior result in dense constraint Jacobians of the nonlinear programs (NLPs).

Different successful approaches to PSA optimization have been demonstrated over the years. One key factor of the optimization of PSA processes is the determination of the cyclic steady state (CSS), i.e., when the initial and final states of the system coincide. Many publications utilize successive substitution (i.e. Picard iteration) [145]. This method iterates by integrating over the model equations, starting with the final state of the previous iteration as the new initial value. This process is repeated until the difference between initial and final states is smaller than a predefined threshold. This method has the advantage of being numerically stable, but it features slow convergence properties. Another approach to finding a solution to a PSA model with respect to the CSS condition, is the addition of algebraic constraint [137, 148, 149, 150]. The convergence of this method is much faster, and it converges globally [147]. Simultaneous solving of the fully discretized PDEs and the CSS condition has been successfully applied to set-ups with two columns. To give a few examples: Smith et al. [151] proposed a MINLP approach with a fully discretized PDE to optimize the operation cycle and the number of beds. The SQP method was successfully applied to optimize fully discretized PSA models by Biegler et al. [147] and Tao et al. [152]. Vetukuri et al. [153] proposed a quasi-Newton method, which approximates the dense constraint Jacobian of the NLP, and could show a significant reduction in computational costs. Dowling et al. [154] formulated the PSA as an optimal control problem to determine optimal cycle times. This approach was further improved by Wang et al. [146], who used flux limiter schemes for reducing computational costs. Agarwal et al. [155] developed a reduced model via proper orthogonal decomposition, which was used by a trust-region filter (TRF) method for PSA optimization [156]. The TRF method uses a reduced model to assist the optimization of the PDE constrained problem by reducing the evaluations of the PDE model. Agarwal pointed out that the computational effort of the TRF method can still be improved by choosing a different reduced model in the trust-region step.

Another challenge arises with the complexity of the PSA cycle. In the literature many optimization examples for 2-column PSA cycles can be found, as well as simulation studies for more complex cycles. To the author's knowledge, only Jiang et al. [148] optimized an adsorption cycle with more

than two adsorption columns. We therefore perform the optimization of a more complex 4-column PSA cycle with a 9-step operating cycle, including 4 internal recycle streams, as opposed to the two column set-ups common in the literature.

We apply here the TRF method as used by Agarwal et al. [156]. We propose a different reduced model based on equilibrium theory [157] for the application of the TRF method to minimize the computational time of the trust-region step. Despite the increased complexity of the PSA cycle, the equilibrium model has fewer variables than the proper orthogonal decomposition (POD) approach by Agarwal.

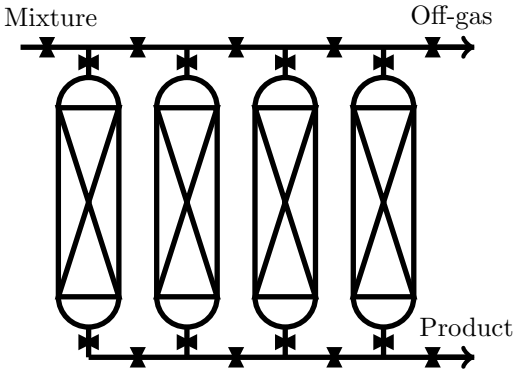

a) Pressure swing adsorption unit scheme.

1	AS ↓			DEQ I ↓	DP I ↓	DEQ II ↓	DP II ↑	DE ↑	PEQ II ↑	PEQ I ↑	PR ↑	
2	PEQ I ↑	PR ↑		AS ↓			DEQ I ↓	DP I ↓	DEQ II ↓	DP II ↑	DE ↑	PEQ II ↑
3	DP II ↑	DE ↑	PEQ II ↑	PEQ I ↑	PR ↑		AS ↓			DEQ I ↓	DP I ↓	DEQ II ↓
4	DEQ I ↓	DP I ↓	DEQ II ↓	DP II ↑	DE ↑	PEQ II ↑	PEQ I ↑	PR ↑		AS ↓		

b) Periodic cycle steps of the four columns over time.

Figure 31: PSA column configuration.

To recall the PSA set-up from Chapter 4, we repeat here the scheme of the adsorption cycle steps. These 9 steps include adsorption (AS), pressure equalization with decreasing pressure (DEQ), pressure equalization with increasing pressure (PEQ), depressurization (DP), desorption (DE) and pressurization (PR), with arrows indicating the direction of flow through the column.

The PSA cycle is repeated from Chapter 4 in Figure 31, including adsorption (AS), pressure equalization with decreasing pressure (DEQ), pressure equalization with increasing pressure (PEQ), depressurization (DP), desorption (DE) and pressurization (PR). The cycle includes four recycle material streams: two pressure equalization streams, one purge stream, and one stream to repressurize the column prior to the adsorption step. The pressure is constant during AS and DE. The product gas methane is produced at high pressure during the adsorption step at partially returned to the column

during PR. The off-gas is produced at low pressure during DP II and DE. Gas is exchanged during the pressure equalization steps, from DEQ I to PEQ I and from DEQ II to PEQ II. Furthermore, gas from the depressurization DP I is used to purge the column at DE and a fraction of the AD product gas repressurizes the column at PR. We determine the final product gas concentration at cyclic steady state (CSS). As an example, we model the separation of methane and carbon dioxide, as commonly applied for biogas upgrading. Goal is the purification of the light component methane from the mixture via adsorbents such as carbon molecular sieves with a focus on product purity, recovery and process efficiency. As a second example, we consider the separation of a ternary mixture, including hydrogen. This application may arise with the production of synthetic natural gas from hydrogen and carbon dioxide [2], see for example process routes B, C1, C2 from Chapter 4. As hydrogen is almost inert on the adsorbent, hydrogen remains in the product methane. Only carbon dioxide is separated from the mixture as an impurity.

We note that these applications are examples to model the separation process in the framework of PtM processes. The method and the proposed reduced model can be applied to any other adsorption separation task by applying different model parameters and boundary conditions.

6.1 MODELING

In this section we introduce the high-fidelity and reduced PSA models: In Section 6.1.1 we describe the PSA model, which we aim to optimize in this work. The high-fidelity PSA model is described by a set of PDAEs with changing boundary conditions, according to the cycle configuration in Figure 14a. Optimization of this PDAE model is computationally and numerically quite challenging. Much simpler representations for PSA models have been derived in the past. One example is the equilibrium model by Knaebel et al. [157], which we introduce in Section 6.1.2. The equilibrium theory allows for reformulation of the PDAEs to algebraic equations, which are much easier to evaluate and optimize.

6.1.1 *PSA Modeling via PDAEs*

The PSA is described by a system of partial differential and algebraic equations assuming ideal gas behavior, no axial pressure gradient, no accumulation in the shockwaves, non-isothermal adsorption behavior, adsorption according to the linear driving force model (LDF) and Langmuir-type equilibrium isotherms. The mass balances do not include diffusion terms to

avoid smearing of the steep adsorption fronts. We introduced this model in Section (4.2.2) with a different approach for calculating the adsorption equilibrium. Instead of applying the Ideal Adsorbed Solution Theory (IAST) (26), which is numerically difficult in practice, the adsorption equilibrium q_i^* for component $i \in \{CO_2, CH_4\}$ is given as a multi-component extension of the multi-site Langmuir isotherm.

$$q_i^* = q_{max,i} K_i p y_i \left(1 - \sum_{j \in \{CO_2, CH_4\}} \frac{q_j^*}{q_{max,j}}\right)^{\alpha_i} \tag{51}$$

$$K_i = K_{i0} \exp(-\Delta H_i / RT) \tag{52}$$

$$\frac{\partial q_i}{\partial t} = k_i (q_i^* - q_i) \tag{53}$$

Parameters for the adsorption of methane and carbon dioxide of the adsorbent CMS-KP 407, are taken from Canevesi et al. [139]. Hydrogen is assumed to behave as a non-adsorbing gas component.

The PDAE system is semi-discretized with respect to the space coordinate via a finite volume method to get a system of differential algebraic equations (DAEs) on a spatial grid with 50 elements. We consider the cyclic operation with 4 columns and 9 steps [1], shown in Figure 31, including pressure equalization steps between the columns.

Semi-discretization of the PDAE model results in a DAE system of differentiation index 1 with differential states

$$x^{PSA} = \left(y_{CO_2}^\top, y_{CH_4}^\top, q_{CO2}^\top, q_{CH_4}^\top, T^\top, T_W^\top, p\right)^\top$$

determined by the discretized PDEs (19), (23), (21), (22), and (27). The algebraic states

$$y^{PSA} = \left(y_{H_2}^\top, {q_{CO2}^*}^\top, {q_{CH_4}^*}^\top, v^\top, \alpha_{PEQI}, \alpha_{PEQII}\right)^\top$$

are given by the sum of mole fractions, (51), (20), and the additional boundary conditions in Table 5. Note here that x^{PSA} does not correspond to the variables x of the TRF method introduced in Section 6.2.

The system is difficult to solve directly via full discretization to an NLP. The sharp adsorption fronts result in stiff differential equations and internal recycle streams during the pressure equalization steps complicate the solving process further. Therefore, we calculate the CSS via the stable method of successive substitution. The successive substitution terminates when the CSS error is below a predefined threshold

$$\|x_0^{PSA} - x^{PSA}(t_f)\| \leqslant CSS_{tol}$$

where x_0^{PSA} denotes the states of the PSA model at $t = 0$. Implementation of a direct method to reach the CSS, as mentioned at the beginning of this chapter, can further improve the proposed method.

6.1.2 *PSA Modeling via Equilibrium Theory*

The PSA model introduced by Knaebel et al. [157] is able to represent the dynamic behavior within the PSA columns without the need for partial differential equations. Additional assumptions on the PSA, namely isothermal behavior, amount of gas adsorbed is always at adsorption equilibrium, linear adsorption isotherms and a binary gas mixture, facilitate the PDAE model. The result is a model, for which it is possible to find analytical solutions. We give a brief overview over the model equations and refer to Knaebel et al. [157] for the detailed derivation.

The different steps of the PSA operation cycle shown in Figure 14a can be classified into two types: PSA steps with changing pressure (DEQ I, DP I, DEQ II, DP II, PEQ II, PEQ I, PR) and PSA steps with constant pressure (AS, DE). The linear adsorption isotherm for adsorbed amount of q_i of component i is given by

$$q_i = k_i C_i = k_i \frac{p_i}{RT}, \qquad i \in \{CO_2, CH_4\}.$$

Furthermore, let $z \in [0, 1]$ be the dimensionless position in the adsorption bed, and $\beta_{CO_2} = 1/(1 + (1-\epsilon)k_{CO_2}/\epsilon)$, $\beta = \frac{\beta_{CO_2}}{\beta_{CH_4}} \leqslant 1$. We also consider the component mass balance in terms of the partial pressure of CO_2 and the total mass balance

$$\epsilon\left(\frac{\partial p_{CO_2}}{\partial t} + \frac{\partial v p_{CO_2}}{\partial z}\right) + RT(1-\epsilon)\frac{\partial q_{CO_2}}{\partial t} = 0$$
$$\epsilon\left(\frac{\partial p}{\partial t} + \frac{\partial v p}{\partial z}\right) + RT(1-\epsilon)\frac{\partial q}{\partial t} = 0.$$

Using the assumption of linear adsorption, we reformulate these mass balances to get

$$\frac{\partial y_{CO_2}}{\partial t} + \frac{\beta_{CO_2} v}{1 + (\beta - 1)y_{CO_2}}\frac{\partial y_{CO_2}}{\partial z} = \frac{(\beta-1)(1-y_{CO_2})y_{CO_2}}{1 + (\beta+1)y_{CO_2}}\frac{1}{p}\frac{dp}{dt} \tag{54}$$
$$\frac{1}{\beta_B}\frac{\partial p}{\partial t} + (\beta - 1)\frac{\partial v p y_{CO_2}}{\partial z} + \frac{\partial v p}{\partial z} = 0. \tag{55}$$

Applying the method of characteristics to Eq. (54) gives

$$\frac{dz}{dt} = \frac{\beta_{CO_2} v}{1 + (\beta - 1) y_{CO_2}} \tag{56}$$

$$\frac{dy_{CO_2}}{dp} = \frac{(\beta - 1)(1 - y_{CO_2}) y_{CO_2}}{(1 + (\beta - 1) y_{CO_2}) p}. \tag{57}$$

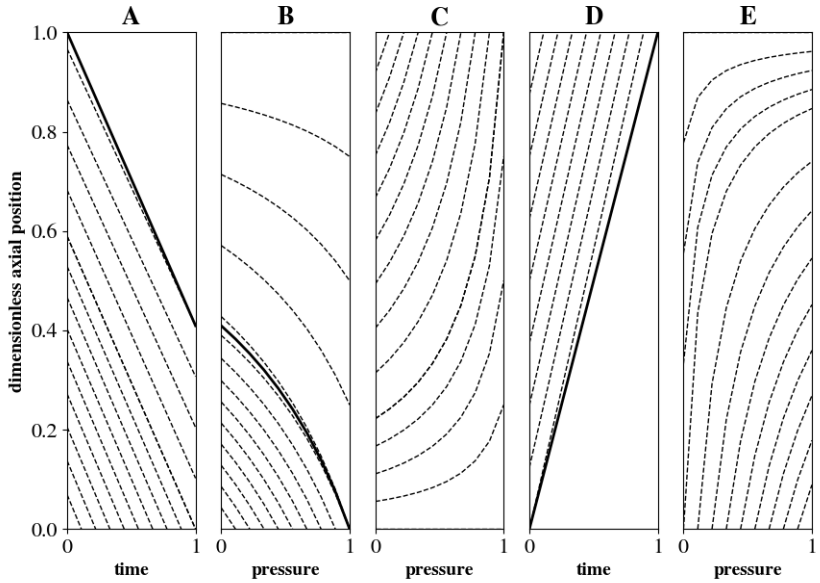

Figure 32: Characteristics and shockwaves for different boundary conditions of the column.

The plots show the dimensionless position of characteristics in the column as dashed lines. The position of waves and shockwaves is depicted as solid lines. In Figure A the characteristics represent the AS step (and the shockwave), with feed gas entering the column from the top and product gas leaving the bottom at constant pressure. Figures B and C show different depressurization steps (and a shockwave). In both Figures the characteristics change with pressure and gas leaves one end of the column. In Figure B the top of the column is closed, gas leaves at the bottom, representing the steps DEQ I, DP I, and DEQ II. Figure C shows the reversed case of step DP II, during which gas is leaving the column at the top. The DE step is represented by Figure D (along with a wave), where purge gas enters the column from the bottom and off-gas leaves the column at the top at constant pressure. Repressurization of the column is done via gas entering the column from the bottom, as is shown in Figure E. This corresponds to the steps PEQ I, PEQ II, and PR.

The model includes the position of shockwaves and waves within the adsorption column. Shockwaves appear, if a gas mixture moves towards a gas mixture of higher concentration of light component. If a gas mixture

moves towards a gas mixture of lower concentration of light component, a wave occurs. A shockwave occurs during the steps AS, DEQ I, DP I, and DEQ II, a wave appears during the steps DE, PEQ II, PEQ I, and PR. In these cases, the reference points, to determine the state of the column, are chosen from the same side of the shockwave or wave. Under the assumption that there is no accumulation at the shockwave,

$$v_s = \left.\frac{dz}{dt}\right|_s = \beta_{CO_2} \frac{v_T y_T - u_L y_L}{y_T - y_L} \tag{58}$$

holds for the interstitial velocity of the shockwave v_s. The subscript L denotes a value directly in front (lead) of the shockwave and T denotes a value directly after (trail).

If the pressure in the adsorption bed changes, $u = 0$ holds at one of the ends of the adsorption bed. We assume w.l.o.g. that $u = 0$ at $z = 0$. Then integration of (55) gives

$$v = \frac{-z}{\beta_{CH_4}(1 + (\beta - 1)y_{CO_2})p} \frac{dp}{dt} \tag{59}$$

and from (57) and (59) we get

$$\frac{y_{CO_2}}{y_{CO_2,0}} = \left(\frac{1 - y_{CO_2}}{1 - y_{CO_2,0}}\right)^{\beta} \left(\frac{p}{p_0}\right)^{\beta-1}$$

$$\frac{z}{z_0} = \left(\frac{y_{CO_2}}{y_{CO_2,0}}\right)^{\frac{\beta}{(1-\beta)}} \left(\frac{1 - y_{CO_2,0}}{1 - y_{CO_2}}\right)^{\frac{1}{(1-\beta)}} \left(\frac{1 + (\beta - 1)y_{CO_2}}{1 + (\beta - 1)y_{CO_2,0}}\right),$$

where the subscript 0 denotes a reference value on the same characteristic. From (58) follows

$$v_s = \frac{-\beta z}{(1 + (\beta - 1)y_T)(1 + (\beta - 1)y_L)p} \frac{dp}{dt}.$$

By considering v and v_s as functions over pressure, we get a system of algebraic equations to describe the PSA steps with changing pressure.

If the pressure is constant, i.e., $\frac{\partial p}{\partial t} = 0$, integration of Eq. (55) results in

$$\frac{v}{v_0} = \frac{1 + (\beta - 1)y_0}{1 + (\beta - 1)y}.$$

From (57) follows that the concentration along the characteristic is constant

$$y_{CO_2} = y_{CO_2,0}$$

and according to (58)

$$v_s = \beta_{CO_2} \frac{u_L y_L - u_T y_T}{y_L - y_T}$$

holds for the shockwave.

To determine the initial conditions of the adsorber bed in the next PSA step, we consider linear approximations of the previous state, still preserving the position of shockwaves. If a shockwave is in the column during a change in PSA steps, the states above and below the shockwave are approximated separately. The CSS condition is added to the model as an algebraic constraint. Figure 32 shows an example of the behavior of the characteristics for the different boundary conditions of the PSA cycle.

6.2 TRUST-REGION FILTER METHOD

In this section we introduce the TRF method for optimization of nonlinear optimization problems as developed by Eason [158]. We first present the main idea, before highlighting the additional parts of the algorithm. Finally, we summarize the assumptions needed for convergence of the TRF method. For a detailed proof of the convergence of the TRF method we refer to [158, 159].

6.2.1 *Main Idea of the TRF Method*

The TRF method finds the optimal solution of a nonlinear problem of the form

$$\begin{aligned} \min_{x=(x_v,x_w,x_y)^\top \in \mathbb{R}^n} \quad & f(x) \\ \text{s.t.} \quad & g(x) \leqslant 0 \\ & h(x) = 0 \\ & d(x_w) = x_y \end{aligned} \tag{NLP}$$

We denote constraints g and h as glass box constraints, as they are easy to evaluate and differentiate. The constraints d, on the other hand, are very time-consuming and numerically difficult to evaluate. The TRF method reduces the number of calls to $d(x_w) : \mathbb{R}^{n_w} \longrightarrow \mathbb{R}^{n_y}$ during the optimization, by replacing d with a local surrogate model. A local surrogate model $r_k(x_w) : \mathbb{R}^{n_w} \longrightarrow \mathbb{R}^{n_y}$, i.e., a reduced model (RM) at the current iterate,

replaces $d(x_w)$, which we call the truth model (TM), in each iteration of the algorithm. Instead of the (NLP) a series of subproblems

$$\begin{aligned} \min_{x=(x_v,x_w,x_y)^\top \in \mathbb{R}^n} \quad & f(x) \\ \text{s.t.} \quad & g(x) \leqslant 0 \\ & h(x) = 0 \\ & r_k(x_w) = x_y \\ & \|x - x_k\| \leqslant \Delta_k \end{aligned} \tag{TRSP$_k$}$$

is solved within a respective trust-region Δ_k.

Definition 6.2.1. κ*-fully linear: The reduced model* $r_k(x_w)$ *is* κ*-fully linear on* $B(x_{w,k}, \Delta_k)$ *if for constants* $\kappa_f, \kappa_g > 0$

$$\begin{aligned} \|r_k(x_w) - d(x_w)\| &\leqslant \kappa_f \Delta_k^2 \\ \|\nabla r_k(x_w) - \nabla d(x_w)\| &\leqslant \kappa_g \Delta_k \end{aligned} \tag{60}$$

holds $\forall x_w \in B(x_{w,k}, \Delta_k)$.

For the convergence of the TRF method, $r_k(x_w)$ must be κ-fully linear in the trust-region at each iteration. This condition assures that for $\Delta_k \longrightarrow 0$ the difference between the two models and their sensitivities within the trust-region converge to zero. If the model sensitivities $\nabla d(w_k)$ are known, we get a κ-fully linear reduced model $r_k(x_w)$ from any sufficiently smooth model $\hat{r}_k(x_w) : \mathbb{R}^{n_w} \longrightarrow \mathbb{R}^{n_y}$ by applying the first order correction, defined by

$$\begin{aligned} r_k(x_w) = FOC(\hat{r}_k(x_w)) := \hat{r}_k(x_w) + d(x_{w,k}) - \hat{r}_k(x_{w,k}) + \\ (\nabla d(x_{w,k}) - \nabla \hat{r}_k(x_{w,k}))^\top (x_w - x_{w,k}). \end{aligned} \tag{FOC}$$

6.2.2 *Additional Strategies and Pseudocode of the TRF Algorithm*

The TRF method includes additional strategies to handle infeasible subproblems and to determine conditions for termination. The algorithm's pseudocode is shown in Algorithm 2.

To make sure that a feasible point to (TRSP$_k$) close to the trust-region center exists, where the approximation of the κ-fully linear RM is more reliable, the TRF method solves a series of compatible problems (TRSP$_k$).

Algorithm 2 Trust-Region Filter Algorithm

procedure TRUST-REGION FILTER ALGORITHM
  Initialize x_0, Δ_0, $\omega \in (0,1)$, $\gamma_c \in (0,1)$, $\theta_0 \leftarrow \|x_{y,0} - d(x_{w,0})\|$
  for iteration $= 0, 1, 2, \ldots$ **do**
    Generate κ-fully linear surrogate model $r_k(x_w)$ wrt. x_k, Δ_k
    if trust-region step from (TRSP_k) wrt. $r_k(x_w)$, Δ_k is compatible **then**
      Compute criticality measure χ_k
      if $\chi_k < \zeta\Delta_k$ **then**
        $\Delta_k \leftarrow \omega\Delta_k$
      Optimize trust-region step from (TRSP_k) wrt. $r_k(x_w)$, Δ_k and obtain $\mathbf{x}_k$.
      if $\hat{x}_k$ acceptable to the filter **then**
        $x_{k+1} \leftarrow \mathbf{x}_k$
        $\theta_{k+1} \leftarrow \|\mathbf{x}_{y,k+1} - d(\mathbf{x}_{w,k+1})\|$, $f_{k+1} \leftarrow f(\mathbf{x}_k)$
        Update Δ_k according to the switching condition
        if switching condition (SW) does not hold **then**
          Add (f_k, θ_k) to the filter
      else
        $\Delta_{k+1} \leftarrow \gamma_c\Delta_k$, $x_{k+1} \leftarrow x_k$
        $\theta_{k+1} \leftarrow \theta_k$, $f_{k+1} \leftarrow f_k$
      if $\chi_{k+1} < \chi_{tol}$ and $\theta_{k+1} < \theta_{tol}$ **then**
        Terminate successfully
    else
      Restoration: Find x_{k+1}, which is feasible for (NLP)

Definition 6.2.2. *Compatibility: The trust-region step from* ($TRSP_k$) *is compatible, if for* $\kappa_\Delta \in (0,1)$, $\kappa_\mu > 0$ *there exists an* $x = (x_v, x_w, x_y)^\top \in \mathbb{R}^n$ *with*

$$\begin{aligned} g(x) &\leqslant 0 \\ h(x) &= 0 \\ r_k(x_w) &= x_y \\ \|x - x_k\| &\leqslant \kappa_\Delta \Delta_k \min\{1, \kappa_\mu \Delta_k^\mu\}. \end{aligned}$$

If ($TRSP_k$) is not compatible, the algorithm enters a restoration phase to create a new iterate x_{k+1} and a new RM $r_{k+1}(x_w)$, which results in a compatible subproblem ($TRSP_{k+1}$). For the restoration phase to be successful it is sufficient to find a feasible point to (NLP). If x_{k+1} is a feasible point to (NLP) and $r_{k+1}(x_w)$ was created via the correction (FOC), the new subproblem ($TRSP_{k+1}$) is guaranteed to be compatible, as the trust-region center x_{k+1} is a feasible point. For example, a feasible point to (NLP) can be found by repeatedly solving the optimization problem

$$\begin{aligned} \min_{x=(x_v,x_w,x_y)} \quad & \|d(x_{w,i}) - x_y\| \\ \text{s.t.} \quad & g(x) \leqslant 0 \\ & h(x) = 0 \end{aligned}$$

via iteration over the tear stream $x_{w,i}$ and choosing $x_{w,i+1} = \mathbf{x}_w$ from the optimal solution.

To get an indicator of how close the current iterate is to an optimal point, we consider the criticality measure. We now define $x_{c,k}$ to be a feasible point for ($TRSP_k$) close to the trust-region center according to $\|x_c - x_k\| \leqslant \kappa_\Delta \Delta_k \min\{1, \kappa_\mu \Delta_k^\mu\}$. According to Definition 6.2.2, this point $x_{c,k}$ exists for any compatible subproblem ($TRSP_k$) and may indeed be x_k itself.

Definition 6.2.3. *Criticality measure: Let* ($TRSP_k$) *be compatible and* $\phi(x)$ *be the optimal solution of the linear program*

$$\begin{aligned} \phi(x) = \min_{\Delta x=(\Delta x_v,\Delta x_w,\Delta x_y)\in\mathbb{R}^n} \quad & \nabla f(x)^\top \Delta x \\ \textit{s.t.} \quad & g(x) + \nabla g(x)^\top \Delta x \leqslant 0 \\ & \nabla h(x)^\top \Delta x = 0 \\ & \nabla r_k(w)^\top \Delta x_w - \Delta x_y \\ & \|\Delta x\|_\infty \leqslant 1 \end{aligned}$$

where $\Delta x_v \in \mathbb{R}^{n_v}$, $\Delta x_w \in \mathbb{R}^{n_w}$, $\Delta x_y \in \mathbb{R}^{n_y}$. *Then the criticality measure* χ_k *is given by*

$$\chi_k = |\phi(x_{c,k})|$$

The criticality measure χ_k goes to zero, if the iterate x_k approaches a KKT-point of ($TRSP_k$) without the trust-region constraint. Because the RM is κ-fully linear, the error of the RM approaches zero for $\Delta_k \longrightarrow 0$, and a KKT-point of ($TRSP_k$) without the trust-region constraint approaches a KKT-point of (NLP). Hence, if the criticality measure is small with respect to the trust-region radius, the trust-region radius is reduced and the TRF method continues until Δ_k approaches zero. On the other hand, shrinking Δ_k to 0 is not needed if the RM is generated via the first order correction (FOC), $\nabla r_k(x_{w,k}) = \nabla d(x_{w,k})$ holds, and $\chi_k = 0$ indicates a KKT-point of (NLP). In this case. optimality holds, even if Δ_k is large.

The TRF method furthermore includes a filter check. A filter is defined as the set

$$\mathcal{F}_k = \{(f(x_i), \theta(x_i)) \text{ for } i \in I_{\mathcal{F}} \subset \{1, \dots, k\}\}$$

where $\theta(x_i) = \|x_{y,i} - d(x_{w,i})\|_\infty$ is the infeasibility measure. A new iterate x_{k+1} is accepted by the filter $\mathcal{F}_k$, if $\theta(x_{k+1}) \leqslant (1-\gamma_\theta)\theta_i$ or $f(x_{k+1}) \leqslant f_i - \gamma_f \theta_i$ holds $\forall (f_i, \theta_i) \in \mathcal{F}_k$ i.e., if sufficient progress was made to improve feasibility or objective of the previous iterates. If a new step is rejected by the filter, the iteration continues with $x_{k+1} = x_k$ and a reduced trust-region radius. If a step is accepted, the switching condition

$$f_k - f(x_{k+1}) \geqslant \kappa_\theta \theta(x_k)^{\gamma_s} \tag{SW}$$

is checked. If (SW) holds, the iterate is an f-type step. In this case, the new iterate is accepted and the trust-region radius Δ_k is increased. If (SW) does not hold, the iterate is a θ-type step. The previous iterate (f_k, θ_k) is added to the filter, and the trust-region radius is changed according to

$$\upsilon_k := 1 - \frac{\theta(x_{k+1})}{\theta_k}$$

$$\Delta_{k+1} = \begin{cases} \gamma_c \Delta_k & \text{if} \quad \upsilon_k < \eta_1 \\ \Delta_k & \text{if} \quad \eta_1 \leqslant \upsilon_k < \eta_2 \\ \gamma_e \Delta_k & \text{if} \quad \eta_2 \leqslant \upsilon_k \end{cases}$$

An exception is made if $\upsilon_k < 0$ holds. In this case a new step is rejected, despite making small progress in f_k.

6.2.3 *Convergence*

Eason [158] showed that the TRF method converges to a first order KKT point of (NLP), given the following assumptions hold:

A1 The functions f, g, h, and d defining (NLP) are twice continuously differentiable.

A2 The problem domain is closed and bounded.

A3 MFCQ holds for (NLP) at all limit points of the TRF iteration.

A4 The reduced model is κ-fully linear, twice-continuous differentiable and the second derivatives are uniformly bounded.

A5 The solution $\hat{x}_k$ of ($TRSP_k$) reduces the objective function value according to the fraction of Cauchy decrease

$$f(x_{c,k}) - f(\hat{x}_k) \geqslant \kappa_t \chi_k \min\{\chi_k/\beta_k, \Delta_k\}$$

for a $\kappa_t > 0$ and a bounded sequence $\beta_k > 1$. In other words, the solver used for optimizing the trust-region step must make sufficient progress in relation to the criticality measure evaluated in $x_{c,k}$.
In practice this condition is fulfilled, by using an NLP optimization strategy to solve ($TRSP_k$), which is initialized in the feasible point $x_{c,k}$.

A6 The condition $\|x_{c,k} - x_k\| \leqslant \kappa_u \theta_k$ holds for small $\theta_k < \delta$ and a $\kappa_u > 0$. If $r_k(x_{w,k}) = d(x_{w,k})$ holds, as is the case if the first order correction (FOC) is used to generate the RM, this condition is fulfilled.

Eason shows that the TRF method will create a subsequence $\{k_i\}$ with compatible trust-region steps ($TRSP_{k_i}$) and

$$\lim_{i\longrightarrow\infty} \chi_{k_i} = 0, \lim_{i\longrightarrow\infty} \theta_{k_i} = 0, \lim_{i\longrightarrow\infty} \Delta_{k_i} = 0, \lim_{i\longrightarrow\infty} x_{k_i} = \mathbf{x}$$

where $\mathbf{x}$ is a KKT-point of (NLP). For the convergence proof we refer to Eason [158].

6.2.4 *Simplifications of the TRF Method*

Trust-region radius

As shown by Yoshio and Biegler [160], the trust-region radius in the subproblem ($TRSP_k$) must not necessarily extend to all model variables x. Instead it can be formulated in terms of the degrees of freedom alone. We partition $x = (\hat{x}, \bar{x})^\top$, where $\bar{x} = (x_{v_{\bar{x}}}, x_{w_{\bar{x}}})^\top$ are the degrees of freedom and $\hat{x} = (x_{v_{\hat{x}}}, x_{w_{\hat{x}}}, x_y)^\top$ are determined by the equality constraints

$\hat{h} = (h(x)^\top, (d(x_w) - x_y)^\top)^\top$. As long as the model sensitivities are non-singular, the trust-region constraint on the degrees of freedom propagates to the remaining variables according to

$$\begin{aligned}\|x - x_k\| &\leqslant \|\bar{x} - \bar{x}_k\| + \|\hat{x} - \hat{x}_k\| \\ &\leqslant \|\bar{x} - \bar{x}_k\| + \|\nabla_{\bar{x}}\hat{h}(\bar{x}_k)^{-\top}\nabla_{\hat{x}}\hat{h}(\hat{x}_k)^\top(\bar{x} - \bar{x}_k)\| \\ &\leqslant (1 + \|\nabla_{\bar{x}}\hat{h}(\bar{x}_k)^{-\top}\nabla_{\hat{x}}\hat{h}(\hat{x}_k)^\top\|)\|(\bar{x} - \bar{x}_k)\|.\end{aligned}$$

For a detailed proof we refer to [160]. We can therefore rewrite the trust-region radius as

$$\|\bar{x} - \bar{x}_k\| \leqslant \Delta_k. \tag{61}$$

In the current work, the degrees of freedom correspond to $\bar{x} = x_w$. We apply both strategies, the full trust-region radius and the trust-region radius regarding the degrees of freedom, and compare the results.

Regularity and feasibility of the trust-region step

To ensure that MFCQ holds, which is required in the limit point of the iteration to ensure convergence according to assumption **A3**, for all $x \in \mathbb{R}^n$, one can introduce artificial variables x_p, x_n, x_q, and ℓ_1 penalties, and rewrite (NLP) as:

$$\begin{aligned}\min_{\substack{x=(x_v,x_w,x_y)^\top\in\mathbb{R}^n,\\ x_p,x_n\in\mathbb{R}^{n_h+n_y},\\ x_q\in\mathbb{R}^{n_h}}} \quad & f(x) + \beta((x_p + x_n)^\top e_h + x_q^\top e_g) \\ \text{s.t.} \quad & g(x) \leqslant x_q \\ & \left(h(x)^\top, (x_y - d(x_w))^\top\right)^\top = E(x_p - x_n) \\ & x_p, x_n, x_q \geqslant 0\end{aligned} \tag{62}$$

where $e_h \in \mathbb{R}^{n_h}$ and $e_g \in \mathbb{R}^{n_h+n_y}$ are vectors with elements of 1 and E is a scaling matrix. Note here that the artificial variables only need to be added to constraints which may violate the MFCQ. The corresponding trust-region subproblem

$$\begin{aligned}\min_{\substack{x=(x_v,x_w,x_y)^\top\in\mathbb{R}^n,\\ x_p,x_n\in\mathbb{R}^{n_h+n_y},\\ x_q\in\mathbb{R}^{n_h}}} \quad & f(x) + \beta((x_p + x_n)^\top e_h + x_q^\top e_g) \\ \text{s.t.} \quad & g(x) \leqslant x_q \\ & \left(h(x)^\top, (x_y - r_k(x_w))^\top\right)^\top = E(x_p - x_n) \\ & \|x_w - x_{w,k}\| \leqslant \Delta_k \\ & x_p, x_n, x_q \geqslant 0\end{aligned} \tag{63}$$

has a feasible solution with $x_{q,j} = \max(0, g_j(x))$, $x_p \perp x_n$, $x_{p,i} + x_{n,i} = |\left(h(x)^\top, (x_y - r_k(x_w))^\top\right)_i^\top|$ and the compatibility check can be skipped. In this case, we compute the infeasibility measure as

$$\theta_k = \| \left(\left(d(x_{w,k}) - x_{y,k}\right)^\top, x_{p,k}^\top, x_{n,k}^\top, x_{q,k}^\top \right)^\top \|$$

and enter the restoration phase if $\Delta_k \leqslant \Delta_{tol}$ and $\theta_k > \theta_{tol}$.

6.2.5 *Application of the TRF Method to PSA Optimization*

We show here, how we optimize the PDAE model from Section 6.1.1 with the TRF method and how the model based on equilibrium theory from Section 6.1.2 is used as a local surrogate model. In Section 6.2.5 we define the function $d(w)$, which is used to apply the TRF method. The TM $d(w)$ represents the correlation between the columns design and cycle operation, given by the variable w, and the product gas flow and concentrations of the PDE model at cyclic steady state (CSS), denoted y. In Section 6.2.5 we show the corresponding reduced model $r(w)$, which calculates the correlation between design and product via a set of algebraic equations derived from equilibrium theory. Finally, we discuss the calculation of derivatives of the TM, which are needed to apply the first order correction.

The Truth Model $d(x_w)$

To optimize the separation performance of the PSA via the TRF method, we need to introduce the variables x_w, x_y, and the TM function $d(x_w)$. The degrees of freedom of the PSA model are the adsorption pressure p_{AS}, desorption pressure p_{DE}, column diameter R_i, column length L, cycle time t_f, and a fraction of product gas fed back to the column during the PR step B_f. With proper scaling of the variables, we define $w = (p_{AS}, p_{DE}, R_i, L, t_f, B_f)^\top$. The model response is given by the gas flow rates of the product stream $d(x_w) = (N_{CO_2}, N_{CH_4}, N_{H_2})^\top$ at CSS, where N_i denotes the mole flow rate of component i in mol/s. The product stream gas flow rates are given by

$$N_i = \epsilon a_s (1 - B_f) \int_{t=0}^{t_f/4} \frac{p(t)}{RT(t, z=0)} y_i(t, z=0) v(t, z=0)\, dt.$$

which is the flow rate of the gas leaving adsorption column during the adsorption step AS. This implies that for each function call $d(x_w)$ the CSS of the DAE system must be evaluated.

Building a Reduced Model

The reduced model $r(x_w)$, which is needed for the TRF method, has the same output stream $r_k(x_w) = (N^k_{CO_2}, N^k_{CH_4}, N^k_{H_2})^\top$ as the TM. The reduced model is calculated based on dimensionless pressure and time. The parameters R_i, L, and t_f are scaling the interstitial velocity of the gas flowing in and out of the column. In addition to the inputs x_w for the truth model, the equilibrium model has additional degrees of freedom, which are the adsorption parameters k_{CO_2}, k_{CH_4} as well as the concentration of the gas entering the column during DE and PR, denoted y_{DE} and y_{PR}. We allow for different values of the adsorption parameters in various step of the PSA process, i.e. $k_{CO_2} = (k^{AD}_{CO_2}, k^{DPI}_{CO_2}, k^{PR}_{CO_2}, \dots)$ and let p_{RM} denote the additional DOFs $p_{RM} = (k_{CO_2}, k_{CH_4}, y_{DE}, y_{PR})^\top$. We use these additional DOFs to derive a local reduced model $r_k(x_w)$ from the equilibrium model at a current iterate $x_{w,k}$ of the TRF algorithm:

Let $r(x_w, p_{RM})$ denote the model response of the equilibrium model, which is the product gas flow rates of the separation at CSS. We minimize the error of the equilibrium model to the TM response $d(x_{w,k})$ at the current iterate according to

$$p^*_k = \arg\min_p \quad \|d(x_{w,k}) - r(x_{w,k}, p)\|_2$$

and define $\hat{r}_k(x_w) = r(x_w, p^*_k)$. To guarantee convergence of the TRF Equations (6o) must hold for the reduced model at the current iterate $x_{w,k}$. We can assure that these conditions hold, by applying the first order correction (FOC).

6.2.6 *Derivatives*

To apply the first order correction (FOC) we need to calculate the sensitivities $\nabla d(x_{w,k})$ of the TM at CSS. One option to calculate the sensitivities is the Finite Difference approach, which is simple to implement, but has several disadvantages in practice. Firstly, the evaluation of the Finite Differences is very time consuming. It requires multiple function evaluations of the TM, each of which include the calculation of the CSS via successive substitution. Furthermore, the successive substitution calculates the CSS only up to a predefined tolerance $\|x^{PSA}_0 - x^{PSA}(t_f)\| \leqslant CSS_{tol}$, where $x^{PSA}(t_f)$ denotes the states of the system of ODEs of the TM at final time t_f, and x^{PSA}_0 denotes the corresponding initial value. This CSS tolerance results in an error in the model response $d(x_w)$, which is amplified in the finite difference calculation and results in a large error in $\nabla d(x_{w,k})$.

An alternative is to consider d as a function of the input x_w and $x^{PSA}(0, x_w)$ at CSS, which is implicitly depending on x_w via the CSS equation

$$h_{CSS}(x_w) = x^{PSA}(0, x_w) - x^{PSA}(t_f, x_w) = 0.$$

Then we calculate $\nabla d(x_{w,k})$ via

$$\begin{aligned}\nabla d(x_{w,k}) &= \frac{d d(x_w, x^{PSA}(0, x_w))}{d x_w}(x_{w,k}) \\ &= \frac{\partial d(x_w, x^{PSA}(0, x_w))}{\partial x_w}(x_{w,k}) + \\ &\quad \frac{\partial d(x_w, x^{PSA}(0, x_w))}{\partial x^{PSA}(0, x_w)}(x_{w,k})^\top \frac{d x^{PSA}(0, x_w)}{d x_w}(x_{w,k})\end{aligned} \tag{64}$$

where the partial derivatives $\frac{\partial d(x_w, x^{PSA}(0, x_w))}{\partial x_w}$ and $\frac{\partial d(x_w, x^{PSA}(0, x_w))}{\partial x^{PSA}(0, x_w)}$ are the backward sensitivities of the PSA model equations. Furthermore, we apply the implicit function theorem to get

$$\frac{d x^{PSA}(0, x_w)}{d x_w}(x_{w,k}) = -\nabla h_{CSS,x}^{-\top}(x_{w,k}) \nabla h_{CSS,x_w}(x_{w,k}) \tag{65}$$

from the CSS equation. We then use automatic differentiation of CasADi [112] to calculate (65) and the backwards sensitivities.

6.3 RESULTS

6.3.1 *Comparison of TM and RM*

To get an impression of the accuracy of the RM, we compare the results at the reference point $x_{w,ref}$ for separation of a binary gas mixture. The values of the reference point are shown in Table 17. For comparison, we consider the separation of a binary mixture of CO_2 and CH_4. Figure 33 shows the mole fraction of CH_4 in the gas phase of one column over bed length (ordinate) and time (abscissa), starting with the adsorption step AS.

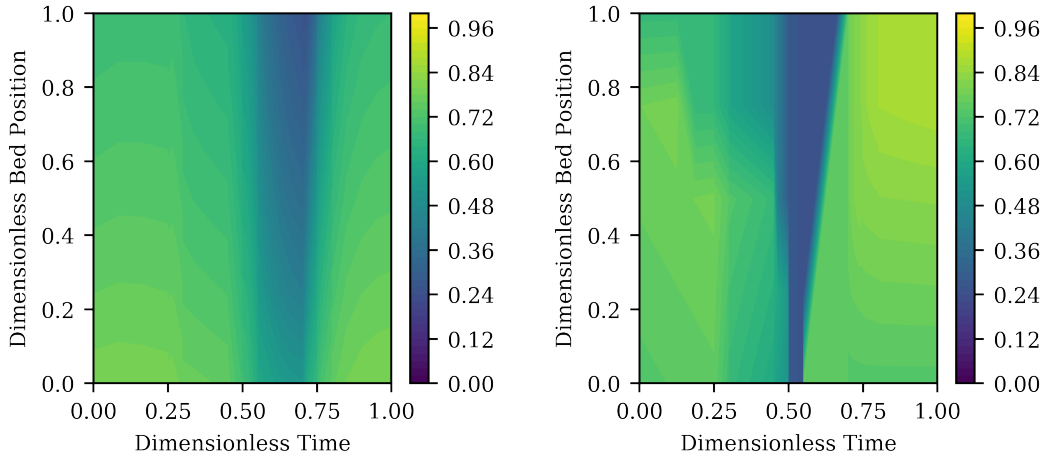

a) PDAE model. **b)** Equilibrium model.

Figure 33: Mole fraction of CH_4 in the gas phase over the position in the column and time

The plots show the result of the CH_4 mole fraction at cyclic steady state with parameter $x_{w,ref}$ and feed $y_{CO_2} = 0.4$, $y_{CH_4} = 0.6$. While the states of the TM indicate a mixing of gases entering the column at different points in time, the RM shows a clear separation at the shockwaves and waves. This effect is particularly pronounced during the DE step, at 0.5 to 0.7 on the dimensionless time scale.

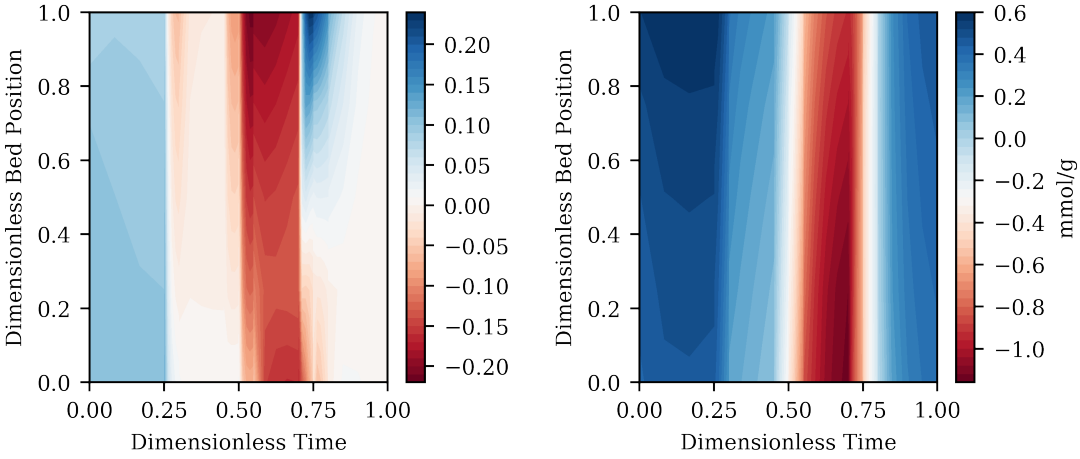

a) CO_2. **b)** CH_4.

Figure 34: The difference $q^* - q$ between amount adsorbed q and amount adsorbed at equilibrium q^* in mmol/g.

The plots show the difference of the amount adsorbed q and the amount adsorbed at adsorption equilibrium q^* with parameter $x_{w,ref}$ and feed $y_{CO_2} = 0.4$, $y_{CH_4} = 0.6$ for the components CH_4 and CO_2 in mol/g.

Table 17: Values of the reference point $x_{w,ref}$ prior to scaling.

p_{AS}	p_{DE}	R_i	L	t_f	B_f
13 bar	1 bar	0.3 m	2 m	200 s	0.7

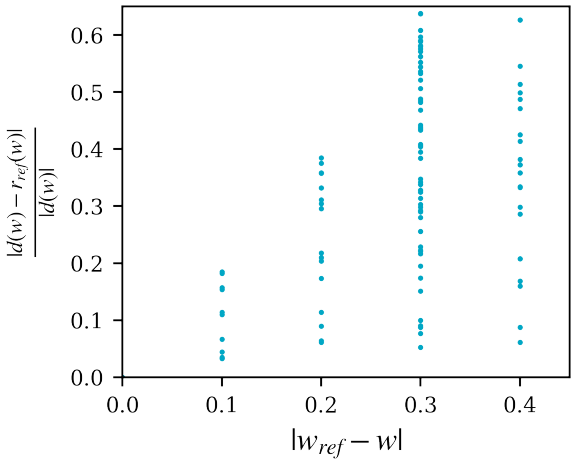

Figure 35: Relative difference between the model response of the TM and the RM corresponding to the reference point $x_{w,ref}$.

The plots show the error $\frac{\Delta y}{|d(x_w)|_\infty} = \frac{|r_{ref}(x_w)-d(x_w)|_\infty}{|d(x_w)|_\infty}$ *of the RM created at reference point* $x_{w,ref}$ *prior to application of the first order correction (FOC). After fitting the parameters of the equilibrium model to the model response of the TM at reference point* $x_{w,ref}$*, the resulting RM was evaluated at different inputs* x_w *on a grid around* $x_{w,ref}$*. The x-axis shows the difference* Δw *of the input* x_w *to the reference point* $x_{w,ref}$*. At* $\Delta w = 0$ *the error of the parameter fitting, which was used for building the RM, is shown. The plot shows the increasing error of the model with greater distance from the reference point* $x_{w,ref}$*.*

Notable is a shift in time of the desorption of CO_2 from the adsorbent, which is indicated by the vertical dark blue area in this figure at times 0.5 to 0.7. Also, while the TM shows a monotonic decrease of CH_4 concentration over space, the RM has increased CH_4 concentrations near the end of the column. Both of these phenomena can be explained by the adsorption kinetics of the models. The ad- and desorption happens instantaneously in the equilibrium RM, while the TM has adsorption kinetics that slow the ad- and desorption. Figure 34 shows the divergence of amount adsorbed and the adsorption equilibrium in the column of the TM. The strong adsorption of CO_2 during the desorption step, at times 0.5 to 0.7 on the dimensionless time scale, is clearly visible, causing the aforementioned shift in time. The difference in the amount adsorbed and the amount adsorbed at equilibrium is higher for

CH_4, which is the light component, because of the faster adsorption kinetic of CO_2.

Important for the speed of convergence of the TRF method is not the accurate representation of the states within the column, but an accurate representation of the TM model response, $d(w)$, close to the reference point at which the RM was created. Figure 35 shows the relative error of the model response with respect to the distance to the reference point $x_{w,ref}$. This figure shows that the error is small close to the reference point, as desired, and increases linearly with greater distance.

6.3.2 *Optimization of PSA Processes via the TRF Method*

We apply the TRF algorithm to optimize the PSA model with respect to recovery and purity of the product gas CH_4. The variables x_w, x_y, and the function $d(x_w)$ are as defined as in Section 6.2.5. We introduce additional variables, $x_v = (v_p, v_r)^\top$, which represent the purity and recovery of the product methane and define the optimization problem

$$
\begin{aligned}
\max_{x=(x_v,x_w,x_y)^\top \in \mathbb{R}^n} \quad & f(x) = v_p + v_r \\
\text{s.t.} \quad & v_r - \frac{N_{CH_4}}{N_{CH_4}^{feed}} = 0 \\
& v_p - \frac{N_{CH_4}}{N_{CH_4} + N_{H_2} + N_{CO_2}} = 0 \\
& d(x_w) = x_y \\
& lb_w \leqslant x_w \leqslant ub_w \\
& 0 \leqslant x_{y,i} \leqslant N_i^{feed} \qquad i \in \{CO_2, H_2, CH_4\} \\
& 0 \leqslant x_v \leqslant 1
\end{aligned}
$$

The objective corresponds to finding a Pareto optimal point with respect to product purity and recovery.

The superscript $feed$ refers to the mole flow rate of the feed gas. We choose a CSS tolerance of

$$CSS_{tol} = 10^{-3}\Delta_k \tag{66}$$

to assure that the error of the model evaluation decrease with the trust-region radius. The results we show here have a trust-region radius of 10^{-4} to 10^{-6} upon termination, which implies a CSS tolerance of 10^{-7} to 10^{-9}. The parameters of the TRF algorithm for the different cases we consider in the following are shown in Table 18.

We also validate the assumptions for convergence of the TRF method introduced in Section 6.2.3. Assumption A2 is fulfilled by having box

constraints for the problem variables. By using the first order correction (FOC) and proper formulation and scaling of the RM, Assumptions A4 and A6 hold. Initializing the optimization of the subproblem in the trust-region step with $x_{c,k}$ and returning a local optimum results in sufficient progress with respect to $x_{c,k}$ to fulfill A5. During the optimization run, we check, whether the linear independence constraint qualification (LICQ) holds for (NLP). The LICQ holds at every iterate of our optimization runs and implies the MFCQ, which is needed for A3. Finally, Assumption A1 may not always hold, because the model response $d(x_w)$ and sensitivities $\nabla d(x_w)$ include the error of the CSS calculation and the integration of the discretized model DAEs. During the optimization this is noticeable by oscillations in the objective value, feasibility measure and criticality measure. We terminate the TRF method here, when $\theta_k, \chi_k \leqslant 10^{-5}$.

In the following, we separate a 4:6 binary mixture of CO_2 and CH_4. Figure 36 shows the development of objective $f_k = f(x_k)$, infeasibility measure $\theta_k = \|x_{y,k} - d(x_{w,k})\|$ and criticality measure χ_k over time, where the trust-region radius is calculated with respect to all variables. Termination occurs after 72 iterations. We validated the calculation of derivatives described in Section 6.2.6 with a straightforward Finite Differences approach. Qualitatively, the calculated derivatives were identical. However, as expected the unavoidable numerical noise in the Finite Differences led to an increase in the number of iterations (roughly 300).

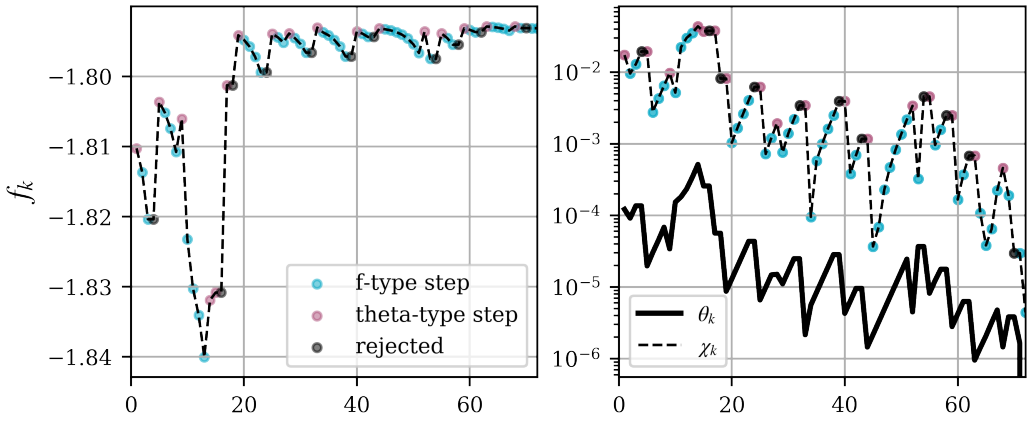

Figure 36: Objective f_k, infeasibility measure θ_k, and criticality measure χ_k over the number of iterations (trust-region radius: Full).

The plots show the development of objective value f_k, infeasibility measure θ_k and criticality measure χ_k at each iteration. Objective is to find a Pareto optimal point with respect to purity and recovery. The trust-region radius is calculated with respect to all variables x.

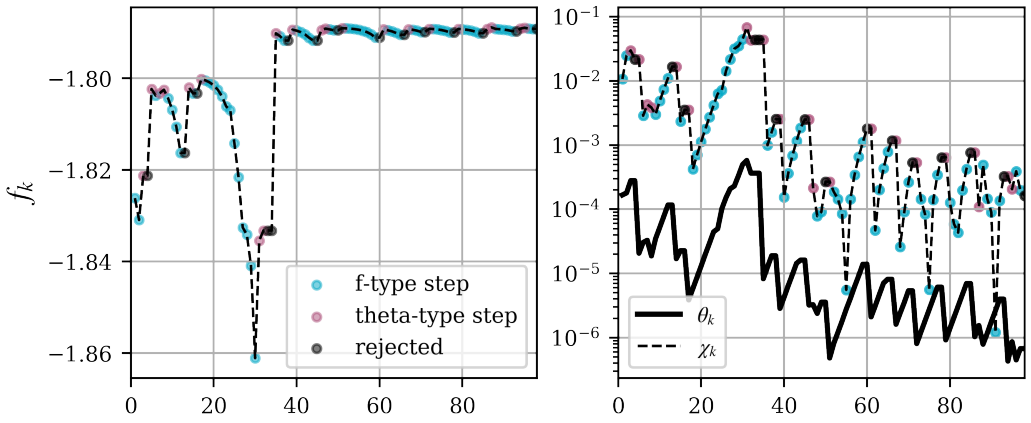

Figure 37: Objective f_k, infeasibility measure θ_k, and criticality measure χ_k over the number of iterations (trust-region radius: DoFs).
As in Figure 36, but now the trust-region radius is calculated with respect to the degrees of freedom.

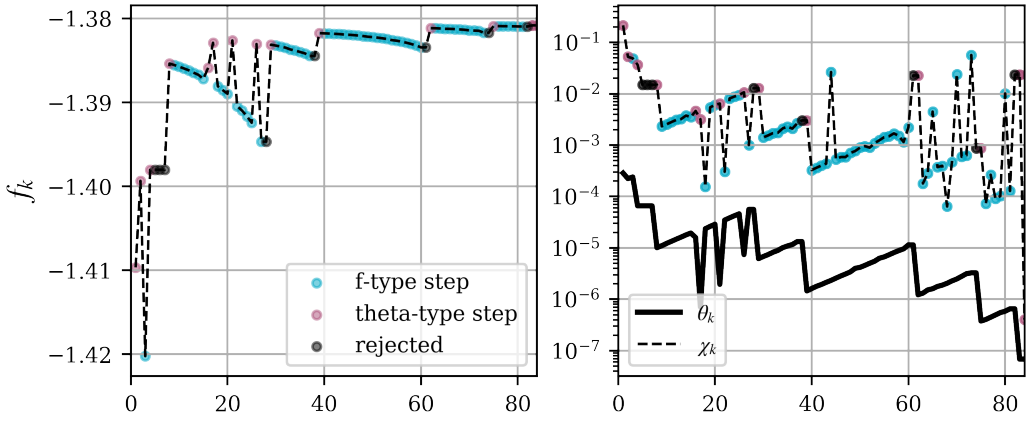

Figure 38: Objective f_k, infeasibility measure θ_k, and criticality measure χ_k over the number of iterations (mixture with hydrogen, trust-region radius: DoFs).
As in Figure 37, but a ternary mixture with hydrogen is the feed gas to the PSA columns.

The number of iterations needed and the total time spent in the calculations of the trust-region step are summarized in Table 19 as case A (TR: full). In the previous work of Agarwal et al. [156] a reduced model based on proper orthogonal decomposition (POD) was used for the optimization of a 2 column PSA cycle, which has 52247 algebraic variables. For a direct comparison we note that the study of Agarwal differs from the present one in multiple aspects, such as the PSA set-up, the number of modeled columns,

the cycle configuration, and the direct determination of the CSS via Newton method. Considering these differences, we can make the following observations; our approach requires more iterations, presumably due to the lower model accuracy of the RM and the more complex PSA set-up. However, the total accumulated time spend in the trust-region step is significantly lower. We attribute the reduction in computational time to the smaller size of the RM. The proposed RM based on equilibrium theory has a total of 67 variables for our 4-column, 9-step configuration and required a total of 5.5 seconds to solve over 72 iterations. If the trust-region radius is only calculated with respect to the degrees of freedom, termination occurs after 55 iterations. The results are shown in Figure 37 and Table 19 as case A (TR: DoFs).

As a second case, we consider the calculation of the trust-region radius with respect to the degrees of freedom according to (61). The optimization results are shown in Figure 37 and in Table 19 as case A (TR: DOFs). Table 19 shows that fewer iterations are needed in this case.

The equilibrium model which we apply as the reduced model has the drawback of only modeling binary mixtures in the gas phase. To analyze if the optimization of a ternary mixture is possible nonetheless, we optimize the separation of a 1:1:1 mixture of CO_2, CH_4 and H_2, which we denote as case B (H_2, TR: DoFs) in Table 19. The hydrogen in the gas phase is here approximated only by the first order correction term. In this case the criticality measure did not reach the threshold of $\chi_{tol} = 10^{-5}$ with the adaptive CSS tolerance (66) even after 200 iterations. We attribute this to the lower accuracy of the reduced model in this case, and chose a fixed CSS tolerance of $CSS_{tol} = 10^{-8}$ instead of using (66). While this increases the overall computational costs, it converges successfully and improves the reliability of the function evaluations and corresponding gradients.

6.3.3 *Optimizing the PSA Work Demand*

In the following we use the introduced algorithm and the reduced model to the application of biogas upgrading. Carbon dioxide must be removed from the product gas of anaerobic digestion, which is a gas mixture of CO_2 and CH_4, prior to feed to the gas distribution system. Typically, product gas from anaerobic digestion contains 50-70 mol.-% of CH_4 [51]. We assume here that the mixture contains 60 mol.-% CH_4 and 40 mol.-% CO_2. The purity of the product gas must meet specifications of the local gas distribution system, i.e., 95 mol.-% of CH_4 after the separation, according to [59].

We formulate a new objective

$$f(x) = W_{rev}/0.8 - 831.9\nu_r,$$

which we aim to minimize, where

$$W_{rev} = RT_{amb} \cdot 10^{-3} \ln\left(\frac{p_{AS}}{p_{DE}}\right)$$

is the reversible isothermal specific work demand in kJ/mol for the gas compression at $T_{amb} = 298.15$ K with ideal gas constant $R = 8.3145$ J/K/mol and 831.9 kJ/mol is the chemical exergy of the product methane. The objective reflects the chemical exergy of the produced methane reduced by the work demand for the purification in kJ/mol. Furthermore, we add the constraint

$$\nu_p \geqslant 0.95$$

to the model to ensure the desired product quality. We use this optimization problem to compare the two approaches to ensure feasibility of the trust-region step, which we introduced in Section 6.2.4: On the one hand, we use the compatibility check to test the feasibility of the trust-region step. If the trust-region step is infeasible, the restoration phase is called. We refer to this approach as case C (Compatibility Check) in the results of Table 19. Alternatively, the trust-region step is always feasible if artificial variables are added as described in Section 6.2.4. We call this approach case C (Artificial Variables). A fixed CSS tolerance of $CSS_{tol} = 10^{-8}$ was applied as for case B. The parameters of the TRF algorithm are shown in Table 18.

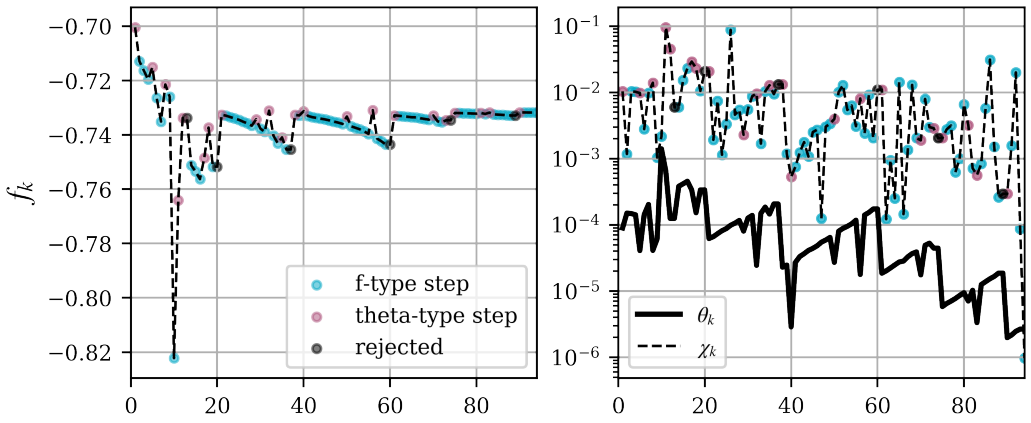

Figure 39: Objective f_k, infeasibility measure θ_k, and criticality measure χ_k over the number of iterations (with Compatibility Check).

As in Figure 36, but the objective is to maximize the units efficiency with respect to a product purity of at least 95 %. The feasibility of the trust-region step is enforced by performing the compatibility check and calling the restoration phase if necessary.

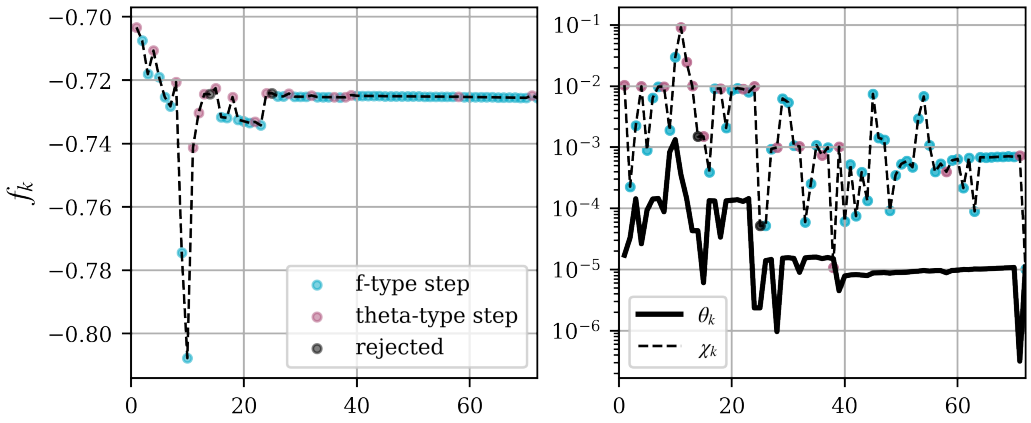

Figure 40: Objective f_k, infeasibility measure θ_k, and criticality measure χ_k over the number of iterations (with Artificial Variables).

The difference to the case shown in Figure 39 is that the trust-region step is always feasible because of artificial variables, which are penalized in the objective. The restoration phase is called if an iteration is not feasible or optimal, but the trust-region size is below the predefined threshold.

Figure 39 shows the optimization of the PSA model with the compatibility check until termination with $\theta_k = \chi_k = 10^{-5}$. The computational time is listed in Table 19. The iteration terminates after 94 iterations. The final optimization leads to a specific work demand of 12.0 kJ/mol for the purification of raw biogas. According to Bauer et al. [128] a work demand of 0.15 to 0.3 kWh/Nm^3 is typical in the industrial application of PSA processes for biogas upgrading. Assuming a mole density of 44.44 mol/Nm^3 for the raw biogas, this corresponds to 12.2 to 24.3 kJ/mol. The result of our optimization is therefore slightly below the minimum level of technology reported in the industry.

Alternatively, Figure 40 shows the optimization of the PSA model with artificial variables. In this case we stop the optimization at iteration 73, when a criticality measure of $\chi_k = 1.02 \cdot 10^{-5}$ is reached. To reach a point with $\chi_k \leqslant 10^{-5}$ a total of 209 iterations are needed here, despite that almost no progress is made after iteration 73 (relative difference of the objectives at iteration 73 and 209 below 0.0001 %). The final objective value is shown in Table 19 as case C (Artificial Variables). The value is slightly larger than the final objective of the comparative case C (Compatibility Check). We attribute this to the fact that we apply a local solver to a non-convex NLP, which can result in termination at a different local optimum.

Table 18: Parameters of the TRF algorithm.

case	γ_e	γ_c	η_1	η_2	ω	κ_Δ
A	1.5	0.5	0.05	0.2	0.8	0.8
B & C (Compatibility Check)	1.1	0.5	0.05	0.5	0.1	0.8
C (Artificial Variables)	1.01	0.5	0.05	0.5	0.1	0.8

Table 19: Number of iterations and computational time.
*The table shows the number of iterations and the total computational time spend in the trust-region step of the different optimization runs. The computation time is obtained using an Intel Quad core i5 3.30 GHz system with 6 GB RAM. Agarwal et al. used an Intel Quad core 2.4 GHz system with 8 GB RAM. Considering the different specifications of the devices, the results show a clear decrease in computational time of the current method over the POD approach. Agarwal et al. considered three different optimization runs: the optimization via a filter method, as we applied here, and the optimization via an exact penalty method with first (FOC) and zero order correction (ZOC). The * marks a case for which the iteration was stopped at* $\chi_k = 1.02 \cdot 10^{-5}$ *instead of* $\chi_k = 1.0 \cdot 10^{-5}$.

case	objective	# vars	# iterations	t_{TM} [s]
A (TR: full)	1.7892	67	72	5.5
A (TR: DoFs)	1.7896	67	55	4.5
B (H_2, TR: DoFs)	1.3808	67	84	5.0
C (Compatibility Check)	-0.7318	67	94	5.3
C (Artificial Variables)*	-0.7257	67	73	5.1
Agarwal et al. [156] (filter)		52247	51	4896.0
Agarwal et al. [156] (ZOC, exact penalty)		52247	13	2142.0
Agarwal et al. [156] (FOC, exact penalty)		52247	92	6768.0

6.4 COMPARISON WITH THE PREVIOUS CHAPTERS

In the previous chapters we answered the questions of the most energy and cost efficient power-to-methane processes at steady state. We successfully identified a cascade of multiple catalytic methanation reactors without prior gas separation as the most ideal process choice. As a result of the simulation in Chapter 4 we could identify a process configuration with gas separation as the most efficient process route. We reevaluate this route, by using the same models for the units and heat integration as used for the superstructure of Chapter 5 and a PSA model, which is updated with the optimization

result of this chapter. We apply the grid specifications (G1) and use the alkaline electrolyzer. Focusing on the efficiency of the process, we chose the objective (O1). The result here is therefore directly comparable with the case AE (G1) (O1) from Chapter 5, which had an efficiency of 50.0%. Using the result of the optimization of this chapter to model the PSA, we reach an efficiency of 48.3%. This is very close to the optimal solution, given the low model accuracy of the unit operations in the superstructure of Chapter 5. An simultaneous optimization of the PSA and the methanation reactor could increase the process efficiency further. If pressure of the unit operation after the PSA unit is high, which is the case here with the methanation reactor, then there is no benefit from reducing the pressure of the PSA to reduce the units work demand. This offers optimization potential for a simultaneous optimization.

6.5 CONCLUSIONS

We propose a reduced model based on equilibrium theory, suitable for optimization of PSA processes within the trust-region filter (TRF) algorithm. Our reduced model results in a significant reduction in computational cost of the trust-region step, even for complex PSA cycles, over a comparative study by Agarwal et al. [156]. We attribute the reduction in computational time to the reduced number of variables of the model. Nevertheless, by sampling the truth model (TM), the TRF method converges to the optimal solution for the truth model. The reduced model was applied successfully to optimize a 9-step 4-column PSA process. The optimization required more iterations than the comparative study, yet the overall computational time spent in the trust-region steps was reduced significantly, from 4 to 6 seconds as opposed to 4896 seconds with a POD approach. The trust-region filter method we applied required fewer iterations until termination if the trust-region is calculated only in the degrees of freedom (55 iterations) as opposed to all variables (72 iterations). The solution of the reduced model based on equilibrium theory differs from the PDAE (TM) solution within the column. We identified that assuming adsorption to be at equilibrium is the main reason for the differences between the two models. We expect processes with fast ad- and desorption kinetics to be represented more accurately by the reduced model which could reduce the number of iterations needed for convergence.

The bottleneck of the proposed method is the calculation of the cyclic steady state (CSS). An implementation of simultaneous methods for CSS calculations, as previously applied in the literature [148, 153, 149, 161, 162], would shorten runtime and improve the accuracy of calls to the PSA model.

7

INTEGRATION OF DETAILED UNIT LEVEL MODELS INTO SUPERSTRUCTURE OPTIMIZATION

Finding the global optimum of a superstructure Chapter 5 with detailed unit level models, as used for example in Chapters 4 and 6, is not possible in reasonable time with widely applied global solvers, as it is too computationally expensive. In practical applications, shortcut models are used to replace the detailed unit models [163], as we have done in Chapter 5. However, shortcut models often lack in accuracy or modeling capability. For instance, dynamic process behavior is difficult to represent by simplified models. One option to circumvent this problem is to select the best process route via shortcut models, as done in Chapter 5, and then optimize the best process configuration via detailed models as a second step. A drawback of this method is that the solution is not guaranteed to deliver the best process configuration with regard to the detailed models.

In the following chapter we propose an alternative approach, using shortcut and detailed models together in a branch-and-bound framework to find the global optimal solution of a superstructure with high-fidelity unit level models. By using shortcut models for fractional solutions, promising process configurations are identified. We give criteria under which the shortcut models are guaranteed to underestimate the optimal solution of

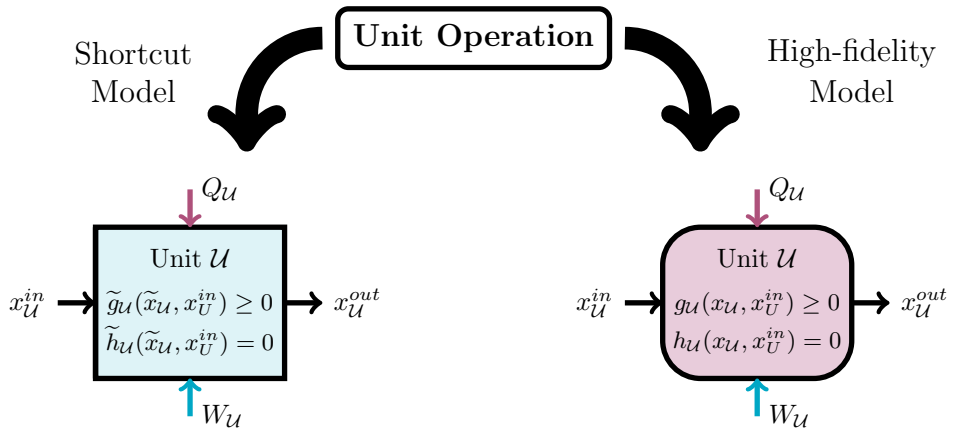

Figure 41: Representation of one unit operation by two models.
Unit models are represented by a shortcut model, which is easy to evaluate, as well as a high-fidelity model. Both models have the same in- and output stream representation.

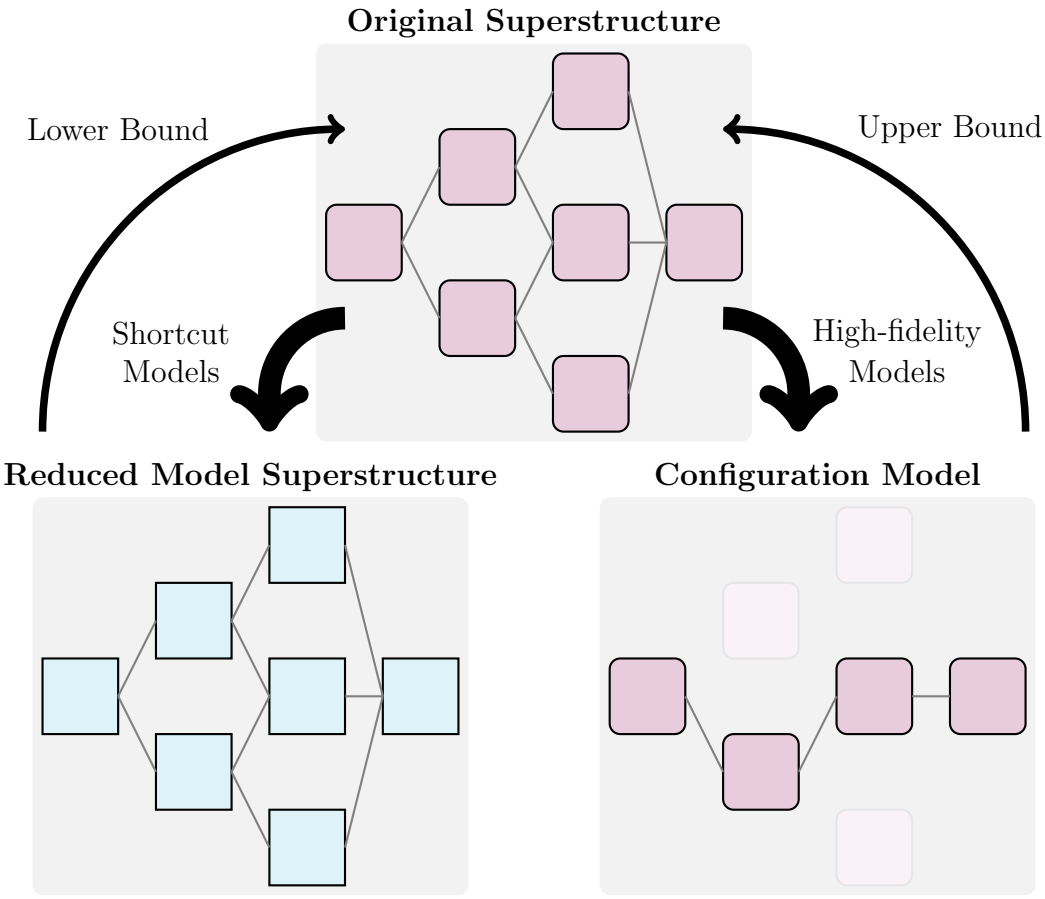

Figure 42: Representation of the high-fidelity superstructure by the shortcut models and configurations of the high-fidelity models.

Instead of solving the high-fidelity superstructure, we solve two types of subproblems. The reduced superstructure model replaces the high-fidelity unit operations with reduced model and gives a lower bound on the optimal solution of the original superstructure for fractional solution candidates. Single configurations, which are extracts of the original superstructure, are evaluated for integer solution candidates. The solution of a configuration model corresponds directly to a feasible solution candidate of the original model, thus is an upper bound of the optimal solution of the original problem.

the original superstructure. The shortcut models give lower bounds, while the detailed models, which are evaluated upon finding an integer solution candidate in the branching tree, give the feasible solution candidates and the upper bound, as indicated in Figure 42. The subproblems must fulfill certain criteria, i.e.:

- the reduced model must be guaranteed to give a lower bound on the original superstructure.

- the optimal solution must be represented by one path in the superstructure.

- inactive unit models must not contribute to the objective value.

We address these points individually in the following sections. To show an example of how to guarantee a lower bound of the reduced model, we focus here on the example of exergy efficiency as the objective function.

7.1 THE OPTIMIZATION PROBLEM

We use an alternative representation of the superstructure we considered in Chapter 5. Here, the unit model constraints g_U extend the unit model constraints $g_U(x_U, x_U^{in})$ from Chapter 5 by including the effect of the indicator variables by constraints such as (33) and (34), thus they also become functions of the indicator variables. We define the variable $x_{MS} := [x_U^{in},\ x_U^{out}]_{U\in\mathcal{V}}$ to include all material streams and the variable $x_e := \left([x_{e,U}]_{U\in\mathcal{V}}^{\top},\ x_E\right)^{\top}$, which includes work demand or heat flows of individual units $x_{e,U}$, corresponding to a particular unit model $U \in \mathcal{V}$, and of the overlaying heat integration model. The variables $x_{e,U}$ include work demand w_U, heat flows q_U^I, q_U^{II} and corresponding temperatures $T_{in,U}^I$, $T_{out,U}^I$, T_U^{II}, and variables necessary for modeling the heat integration. Both material and energy flows corresponding to a unit model $U \in \mathcal{V}$ are fixed to the value given by the unit model via the constraints h_U^{out}. In our application the constraints h_U^{out} are defined as

$$
\begin{aligned}
&x_U^{out} - X_U^{out}(x_U) = 0\\
&w_U - W_U(x_U) = 0\\
&\left(q_U^I, T_{in,U}^I, T_{out,U}^I, q_U^{II}, T_U^{II}\right)^{\top} - Q_U(x_U) = 0.
\end{aligned}
$$

We call $g_{\mathcal{V}} : \{0,1\}^{n_{\mathcal{V}}} \longrightarrow \mathbb{R}^{n_{g_{\mathcal{V}}}}$ the superstructure topology and g the superstructure overhead, which includes constraints modeling the heat integration

and the connections of material streams between unit models. Then we get a superstructure optimization problem of the form

$$
\begin{aligned}
\min_{x=(x_T,x_\mathcal{V},x_{MS},x_e)^\top\in\mathbb{R}^n} \quad & f(x_{MS},\, x_e) \\
\text{s.t.} \quad & g(x_{MS},\, x_e) \leqslant 0 \\
& g_\mathcal{V}(x_T) \leqslant 0 \\
& g_u(x_{T,u},\, x_u,\, x_u^{in}) \leqslant 0, \qquad u \in \mathcal{V} \\
& h_u(x_{T,u},\, x_u,\, x_u^{in}) = 0, \qquad u \in \mathcal{V} \\
& h_u^{out}(x_u,\, x_u^{out},\, x_{e,u}) = 0, \quad u \in \mathcal{V} \\
& x_T \in \{0,1\}^{n_\mathcal{V}} \\
& x_\mathcal{V} = [x_u]_{u\in\mathcal{V}} \\
& x_{MS} = [x_u^{in},\, x_u^{out}]_{u\in\mathcal{V}} \\
& x_e = \left([x_{e,u}]_{u\in\mathcal{V}}^\top,\, x_E\right)^\top,
\end{aligned}
\tag{op}
$$

where x_T are the indicator variables and $x_\mathcal{V}$ the unit model variables. In the following, $\Omega_{(op)}$ denotes the bounded and closed feasible set of (op). Let furthermore

$$\mathcal{X}_{(op)} := \{x_T \in \{0,1\}^{n_\mathcal{V}} \mid \exists y \in \Omega_{(op)} \text{ with } x_T = y_T\}$$

be the set of feasible integer values of $\Omega_{(op)}$ and

$$\mathcal{X}^g_{(op)} := \{x_T \in \{0,1\}^{n_\mathcal{V}} \mid g_\mathcal{V}(x_T) \leqslant 0\}$$

the set of integer values which satisfy the topology constraint. Note that

$$\mathcal{X}_{(op)} \subseteq \mathcal{X}^g_{(op)}$$

holds. We furthermore define

$$\Omega^n := \{0,1\}^{n_\mathcal{V}} \times \mathbb{R}^{n-n_\mathcal{V}} \subset \mathbb{R}^n$$

To introduce the superstructure branch-and-bound (SBnB) algorithm we need two different optimization problems, which are derived from the original problem (op) as follows.

7.2 THE REDUCED MODEL

If the unit operations are represented by detailed models, such as for example the PDAE model for PSA separation from Chapter 6, the superstructure (op) can become too complex to solve via a branch-and-bound approach

in reasonable computational time. Replacing the unit models by reduced models results in the MINLP

$$
\begin{aligned}
\min_{x=(x_T,\widetilde{x}_\mathcal{V},x_{MS},x_e)^\top\in\mathbb{R}^{\tilde{n}}} \quad & f(x_{MS},x_e) \\
\text{s.t.} \quad & g(x_{MS},x_e)\leqslant 0 \\
& g_\mathcal{V}(x_T)\leqslant 0 \\
& \widetilde{g}_u(x_{T,u},\ \widetilde{x}_u,\ x_u^{in})\leqslant 0, && u\in\mathcal{V} \\
& \widetilde{h}_u(x_{T,u},\ \widetilde{x}_u,\ x_u^{in})= 0, && u\in\mathcal{V} \\
& \widetilde{h}_u^{out}(x_{T,u},\ \widetilde{x}_u,\ x_u^{out},\ x_{e,u})= 0, && u\in\mathcal{V} \\
& x_T\in\{0,1\}^{n_\mathcal{V}} \\
& \widetilde{x}_\mathcal{V}=[\widetilde{x}_u]_{u\in\mathcal{V}} \\
& x_{MS}=[x_u^{in},x_u^{out}]_{u\in\mathcal{V}} \\
& x_e=\left([x_{e,u}]_{u\in\mathcal{V}}^\top,x_E\right)^\top.
\end{aligned}
\tag{rp}
$$

which represents the same superstructure, but is significantly easier to solve. We call (rp) the reduced problem to the original problem (op). Note that the topology $g_\mathcal{V}$, the objective function f, the overhead of the superstructure g, and the variables x_T, x_{MS}, x_e of the reduced problem (rp) are the same as for the original problem (op). Only the representation of the unit models, i.e., the variables x_u and the constraints g_u, h_u and h_u^{out} changed. In the following we call $\Omega_{(rp)}$ the feasible set of the problem (rp), which we assume to be closed and bounded. Our algorithm is formulated under the following Assumption 7.2.1. We will show later in Section 7.5, how we fulfill this assumption for the optimization of exergy efficiency.

Assumption 7.2.1. *For all $\boldsymbol{x}_T\in\mathcal{X}_{(op)}$ there exists a $\widetilde{x}=(\widetilde{x}_T,\widetilde{x}_\mathcal{V},\widetilde{x}_{MS},\widetilde{x}_e)^\top\in\Omega_{(rp)}$ with $\boldsymbol{x}_T=\widetilde{x}_T$. Furthermore (rp) gives a lower bound on (op) according to*

$$
\min_{\widetilde{x}}\ (rp)\ \ s.t.\ \ \widetilde{x}_T=\boldsymbol{x}_T \quad\leqslant\quad \min_{x}\ (op)\ \ s.t.\ \ x_T=\boldsymbol{x}_T, \qquad \forall\boldsymbol{x}_T\in\mathcal{X}_{(op)}.
$$

Note. *The reduced problem acts as a lower bound on the original problem in the branch-and-bound framework which we introduce in this chapter. In practice this means that a trade-off between simplicity, which preferably implies convexity, and tightness of (rp) must be made. If the problem (rp) is non-convex, the solution of a convex envelope can also act as a lower bound in the branch-and-bound algorithm. We will come back to this when we describe the algorithm in Section 7.4.*

7.3 THE CONFIGURATION MODEL

In this section we introduce the process configuration model, which considers only active unit models of a solution candidate.

Definition 7.3.1. *Partitioning of a solution candidate: We define a partitioning of a solution candidate* $\boldsymbol{x} = (\boldsymbol{x}_T, \boldsymbol{x}_\mathcal{V}, \boldsymbol{x}_{MS}, \boldsymbol{x}_e)^\top \in \Omega^n$ *according to the value of the indicator variables* $\boldsymbol{x}_T \in \{0,1\}^{n_\mathcal{V}}$ *as*

$$\begin{aligned}
\mathrm{part}_0(\boldsymbol{x}) &= \left([\boldsymbol{x}_u]_{u\in\mathcal{V}_{\setminus \boldsymbol{x}_T}},\ [\boldsymbol{x}_{MS,u}]_{u\in\mathcal{V}_{\setminus \boldsymbol{x}_T}},\ [\boldsymbol{x}_{e,u}]_{u\in\mathcal{V}_{\setminus \boldsymbol{x}_T}}\right)^\top,\\
\mathrm{part}_1(\boldsymbol{x}) &= \left([\boldsymbol{x}_u]_{u\in\mathcal{V}_{\boldsymbol{x}_T}},\ [\boldsymbol{x}_{MS,u}]_{u\in\mathcal{V}_{\boldsymbol{x}_T}},\ [\boldsymbol{x}_{e,u}]_{u\in\mathcal{V}_{\boldsymbol{x}_T}},\ \boldsymbol{x}_E\right)^\top,
\end{aligned}$$

where $\mathcal{V}_{\setminus \boldsymbol{x}_T} = \{u \in \mathcal{V} \mid \boldsymbol{x}_{T,u} = 0\}$ *and* $\mathcal{V}_{\boldsymbol{x}_T} = \{u \in \mathcal{V} \mid \boldsymbol{x}_{T,u} = 1\}$. *We call*

$$\Omega_{(op)}^{0,\boldsymbol{x}_T} = \begin{cases} \{x_0 = \mathrm{part}_0(x) \mid x \in \Omega_{(op)}, x_T = \boldsymbol{x}_T\} \subseteq \mathbb{R}^{n_{0,\boldsymbol{x}_T}} & \text{if } \boldsymbol{x}_T \in \mathcal{X}_{(op)} \\ \emptyset & \text{else} \end{cases}$$

the domain of the inactive part and

$$\Omega_{(op)}^{1,\boldsymbol{x}_T} = \begin{cases} \{x_1 = \mathrm{part}_1(x) \mid x \in \Omega_{(op)}, x_T = \boldsymbol{x}_T\} \subseteq \mathbb{R}^{n_{1,\boldsymbol{x}_T}} & \text{if } \boldsymbol{x}_T \in \mathcal{X}_{(op)} \\ \emptyset & \text{else} \end{cases}$$

the domain of the active part of an integer configuration $\boldsymbol{x}_T \in \{0,1\}^{n_\mathcal{V}}$. *Note that* $n_{0,\boldsymbol{x}_T} + n_{1,\boldsymbol{x}_T} = n$.

Assumption 7.3.1. *We assume in the following that*

$$\begin{aligned} &f(x_{MS}, x_e) = f(y_{MS}, y_e),\\ &g(x_{MS}, x_e) = g(y_{MS}, y_e), \end{aligned} \quad \forall x, y \in \Omega_{(op)} \text{ with } \begin{aligned} &x_T = y_T,\\ &\mathrm{part}_1(x) = \mathrm{part}_1(y). \end{aligned}$$

Assumption 7.3.1 assures that inactive unit models do not contribute to the objective function value.

Definition 7.3.2. *Extension: We call a function* $\phi_{\boldsymbol{x}_T} : \mathbb{R}^{n_{1,\boldsymbol{x}_T}} \longrightarrow \mathbb{R}^n$ *with*

$$\mathrm{part}_1(\phi_{\boldsymbol{x}_T}(x_1)) = x_1, \qquad \forall x_1 \in \mathbb{R}^{n_{1,\boldsymbol{x}_T}}$$

an extension if

$$\phi_{\boldsymbol{x}_T}(\Omega_{(op)}^{1,\boldsymbol{x}_T}) \subseteq \Omega_{(op)}$$

holds.

The extension maps the active part of a solution candidate back to a full solution of (op) by assigning feasible values for the inactive part. With the extension ϕ_{x_T} we define the functions $f_{x_T} : \mathbb{R}^{n_{1,x_T}} \longrightarrow \mathbb{R}$ and $g_{x_T} : \mathbb{R}^{n_{1,x_T}} \longrightarrow \mathbb{R}^{n_g}$ as

$$f_{x_T}(x_1) = f(x_{MS}, x_e), \tag{67}$$
$$g_{x_T}(x_1) = g(x_{MS}, x_e), \tag{68}$$

where $(x_T, x_\mathcal{V}, x_{MS}, x_e)^\top = \phi_{x_T}(x_1)$.

Lemma 7.3.1. *The functions f_{x_T} and g_{x_T} are independent of the choice of ϕ_{x_T}.*

Proof. Let $x, y \in \Omega^n$ be such that

$$x = \phi_{\mathbf{x}_T}(x_1)$$
$$y = \hat{\phi}_{\mathbf{x}_T}(x_1)$$

for $x_1 \in \mathbb{R}^{n_{1,x_T}}$ and extensions ϕ_{x_T} and $\hat{\phi}_{x_T}$. From Definition 7.3.2 follows that

$$part_1(x) = part_1(\phi_{\mathbf{x}_T}(x_1)) = x_1 = part_1(\hat{\phi}_{\mathbf{x}_T}(x_1)) = part_1(y)$$

holds and according to Assumption 7.3.1

$$f(x_{MS},\ x_e) = f(y_{MS},\ y_e),$$
$$g(x_{MS},\ x_e) = g(y_{MS},\ y_e).$$

□

Assumption 7.3.2. *Let Ω be the set of all $x_1 = (\hat{x}_\mathcal{V}, \hat{x}_{MS}, \hat{x}_e)^\top \in \mathbb{R}^{n_{1,x_T}}$ which fulfill*

$$g_{\mathbf{x}_T}(x) \leqslant 0$$
$$g_u(1,\ x_u,\ x_u^{in}) \leqslant 0, \qquad u \in \mathcal{V}_{\mathbf{x}_T}$$
$$h_u(1,\ x_u,\ x_u^{in}) = 0, \qquad u \in \mathcal{V}_{\mathbf{x}_T}$$
$$h_u^{out}(1,\ x_u,\ x_u^{out},\ \hat{x}_{e,u}) = 0, \qquad u \in \mathcal{V}_{\mathbf{x}_T}$$
$$\hat{x}_\mathcal{V} = [x_u]_{u\in\mathcal{V}_{\mathbf{x}_T}}$$
$$\hat{x}_{MS} = [x_u^{in}, x_u^{out}]_{u\in\mathcal{V}_{\mathbf{x}_T}}$$
$$\hat{x}_e = \left([x_{e,u}]_{u\in\mathcal{V}_{\mathbf{x}_T}}, x_E\right)^\top.$$

for $\mathcal{V}_{\mathbf{x}_T} = \{u \mid \mathbf{x}_{T,u} = 1, u \in \mathcal{V}\}$. Then

$$\Omega \subseteq \Omega_{(op)}^{1,\mathbf{x}_T}$$

holds for all $\mathbf{x}_T \in \mathcal{X}_{(op)}^g$.

Note. *Assumption 7.3.2 enforces restrictions on the constraints of the original problem (op), namely on the inactive unit models. The assumption is for example violated if there exists a unit model constraint which causes the problem to become infeasible for $x_{T,u} = 0$. In this case, including in the topology constraints $g_\mathcal{V}(x_T)$ that $x_{T,u} = 1$ must hold makes sure that Assumption 7.3.2 holds. The purpose of this assumption is to make sure that no additional solutions of (op) exist in terms of the active part, if an inactive unit model is removed from the superstructure.*

With these functions we can now define a configuration model:

Definition 7.3.3. *Configuration model: We call an optimization problem of the form*

$$
\begin{aligned}
\min_{x=(\hat{x}_{\mathcal{V}},\hat{x}_{MS},\hat{x}_e)^\top \in \mathbb{R}^{n_1,x_T}} \quad & f_{x_T}(x) \\
s.t. \quad & g_{x_T}(x) \leqslant 0 \\
& g_u(1,\, x_u,\, x_u^{in}) \leqslant 0, && u \in \mathcal{V}_{x_T} \\
& h_u(1,\, x_u,\, x_u^{in}) = 0, && u \in \mathcal{V}_{x_T} \\
& h_u^{out}(1,\, x_u,\, x_u^{out},\, \hat{x}_{e,u}) = 0, && u \in \mathcal{V}_{x_T} \\
& \hat{x}_{\mathcal{V}} = [x_u]_{u\in\mathcal{V}_{x_T}} \\
& \hat{x}_{MS} = [x_u^{in},\, x_u^{out}]_{u\in\mathcal{V}_{x_T}} \\
& \hat{x}_e = \left([x_{e,u}]_{u\in\mathcal{V}_{x_T}},\, x_E\right)^\top.
\end{aligned}
\tag{cp}
$$

the configuration problem (cp(x_T)) of $x_T \in \{0,1\}^{n_\mathcal{V}}$ with $\mathcal{V}_{x_T} = \{u \mid x_{T,u} = 1, u \in \mathcal{V}\}$.

The configuration model (cp(x_T)) models a single configuration in the superstructure given by (op) according to the index set of unit models $\mathcal{V}_{x_T}$, which are active in (op) according to a solution candidate x_T. Note that the problem size of (cp(x_T)) is significantly smaller than the problem size of (op). Furthermore, (cp(x_T)) is an NLP, because all the integer variables have been fixed to x_T. A configuration problem cp(x_T)) is equivalent to adding the constraint $x_T = x_T$ to (op) and removing inactive unit models and corresponding variables from the superstructure as is shown in the following lemmas:

Lemma 7.3.2. *The feasible set of (cp(x_T)) is the domain of the first partitioning of solutions of* (op) *corresponding to $x_T \in \mathcal{X}^g_{(op)}$, i.e.,*

$$\Omega^{1,x_T}_{(op)} = \Omega_{(cp(x_T))}, \qquad \forall x_T \in \mathcal{X}^g_{(op)}.$$

Proof. From Assumption 7.3.2 follows that $\Omega_{(cp(x_T))} \subseteq \Omega^{1,x_T}_{(op)}$. To prove that the converse holds, we show that every $x_1 \in \Omega^{1,x_T}_{(op)}$ corresponds to a feasible point of (cp(x_T)). By construction in Definition 7.3.1, each point $x_1 \in \Omega^{1,x_T}_{(op)}$ for $x_T \in \mathcal{X}_{(op)}$ corresponds to a feasible solution of (op), which fulfills the unit model constraints. This implies that x_1 fulfills the active unit constraints in (cp(x_T)). From (68) follows that x_1 also fulfills the constraint g_{x_T}

$$g_{x_T}(x_1) = g(x_{MS}, x_e) \leqslant 0$$

where $\mathbf{x} = (\mathbf{x}_T,\ \mathbf{x}_\mathcal{V},\ \mathbf{x}_{MS},\ \mathbf{x}_e)^\top = \phi_{\mathbf{x}_T}(\mathbf{x}_1)$ which makes $\mathbf{x}_1$ a feasible solution candidate of (cp($\mathbf{x}_T$)).

If $\mathbf{x}_T \in \{0,1\}^{n_\mathcal{V}} \setminus \mathcal{X}_{(op)}$ then $\Omega_{(op)}^{1,\mathbf{x}_T} = \emptyset$ according to Definition 7.3.1 and from $\Omega_{(op)}^{1,\mathbf{x}_T} \subseteq \Omega_{(cp(\mathbf{x}_T))}$ follows that $\Omega_{(cp(\mathbf{x}_T))} = \emptyset$. □

Note. *Lemma 7.3.2 shows that we can apply any extension ϕ_{x_T} to map any $x_1 \in \Omega_{(cp(x_T))}$ to an $x = \phi_{x_T}(x_1)$, $x \in \Omega_{(op)}$ such that*

$$x_1 = part_1(x).$$

Lemma 7.3.3. *For all $\boldsymbol{x}_T \in \mathcal{X}_{(op)}$ the optimal solution value of (cp($\boldsymbol{x}_T$)) is equal to the optimal solution value of*

$$\begin{aligned} \min_x \quad & (op) \\ s.t. \quad & x_T = \boldsymbol{x}_T. \end{aligned}$$

Proof. We show in the following that to each feasible point of (cp($\mathbf{x}_T$)) corresponds a feasible point $x \in \Omega_{(op)}$ of (op) with $x_T = \mathbf{x}_T$ and the same objective value and vice versa. Then this implies that the optimal solution values of the two problems are identical.

Let $x_1 \in \Omega_{(cp(\mathbf{x}_T))}$ be a feasible point with objective value $f_{\mathbf{x}_T}(x_1)$. According to Eq. (67)

$$f_{\mathbf{x}_T}(x_1) = f(x_{MS}, x_e)$$

holds, where $x = (x_T, x_\mathcal{V}, x_{MS}, x_e)^\top = \phi_{\mathbf{x}_T}(x_1)$ with $x_T = \mathbf{x}_T$ and f is the objective function of (op). According to Lemma 7.3.2 $\Omega_{(cp(\mathbf{x}_T))} = \Omega_{(op)}^{1,\mathbf{x}_T}$ holds, thus $x_1 \in \Omega_{(op)}^{1,\mathbf{x}_T}$. From Definition 7.3.2 follows that $\phi_{\mathbf{x}_T}(x_1) \in \Omega_{(op)}$, which implies that x is a feasible point of (op) s.t. $x_T = \mathbf{x}_T$ with the same objective value as x_1.

Conversely, let $x = (x_T, x_\mathcal{V}, x_{MS}, x_e)^\top$ be a feasible point of (op) s.t. $x_T = \mathbf{x}_T$ with objective value $f(x_{MS}, x_e)$. Then $part_1(x) = x_1 \in \Omega_{(op)}^{1,\mathbf{x}_T}$ is a feasible point of $\Omega_{(cp(\mathbf{x}_T))}$ according to Lemma 7.3.2 for which $f_{\mathbf{x}_T}(x_1) = f(x_{MS}, x_e)$ holds with the same argumentation as used for the other direction. □

Lemma 7.3.4. *Let (op) have a feasible solution. Then*

$$\min_{\boldsymbol{x}_T \in \mathcal{X}_{(op)}} \left(\min_{x \in \mathbb{R}^{n_1, x_T}} (cp(\boldsymbol{x}_T)) \right)$$

is a global optimal solution of (op).

Proof. According to Lemma 7.3.3 (cp($\mathbf{x}_T$)) is equivalent to fixing the integer variables of (op) to $x_T = \mathbf{x}_T$ for $\mathbf{x}_T \in \mathcal{X}_{(op)}$. Thus

$$\min_{\mathbf{x}_T \in \mathcal{X}_{(op)}} \left(\min_{x \in R^{n_1, x_T}} (cp(\mathbf{x}_T)) \right) = \min_{\mathbf{x}_T \in \mathcal{X}_{(op)}} \begin{array}{ll} \min\limits_{x} & (op) \\ \text{s.t.} & x_T = \mathbf{x}_T. \end{array}$$

We can reformulate the right hand side to

$$\min_{\mathbf{x}_T \in \mathcal{X}_{(op)}} \begin{array}{ll} \min\limits_{x} & (op) \\ \text{s.t.} & x_T = \mathbf{x}_T \end{array} = \begin{array}{ll} \min\limits_{x} & (op) \\ \text{s.t.} & x_T \in \mathcal{X}_{(op)} \end{array} = \min_{x} \ (op) \ ,$$

where the second equality holds according to the Definition of $\mathcal{X}_{(op)}$. □

7.4 THE SUPERSTRUCTURE BRANCH-AND-BOUND ALGORITHM

We start by solving (rp), which approximates the solution of (op), via a branch-and-bound method. When an integer solution candidate $\mathbf{x}_T \in \mathcal{X}_{(op)}$ is found during the solving process, a process configuration model (cp($\mathbf{x}_T$)) corresponding to $\mathbf{x}_T$ is solved. The upper bound is updated to be the minimum of all solutions of configuration problems (cp) evaluated at the current iteration.

Furthermore, for each evaluated configuration model, a cut is added, which stops the branch-and-bound algorithm from considering this integer solution for further branching. Let $\mathbf{x}$ denote the solution of a configuration model (cp($\mathbf{x}_T$)). Then we add the cut variable c and the linear constraints

$$\left.\begin{array}{ll} 0 \leqslant c \leqslant 1 & \\ c \leqslant \mathbf{x}_{T,u} + x_{T,u} - 2x_{T,u}\mathbf{x}_{T,u} & \forall u \in \mathcal{V} \\ f(x) \geqslant f(\mathbf{x})(1-c) & \end{array}\right\} \tag{69}$$

to problem (rp) and continue with the branch-and-bound search.

Note. *The lower bound LB_P on a node P, as calculated in line 6 of Algorithm 3, does not need to be the global optimal solution. The solution of an underestimator (e.g. a linear envelope) is sufficient and more computationally efficient, given that the problems in the nodes can be non-convex. Here, we want to only branch on the integer variables, because knowing the values of the variables in the solution of* (rp) *does not aid the solving process of* (cp).

Note. *In practice, where a plant designer is solely interested in the optimal process configuration and its design parameters, the extension ϕ is not needed, and the algorithm may return x_T^* and $x^* \in \Omega^{n_{1,x_T^*}}$ directly instead of $\phi_{x_T^*}(x^*)$.*

Algorithm 3 Superstructure Branch-and-Bound Method

procedure SUPERSTRUCTURE BRANCH-AND-BOUND METHOD
  Initialize $LB = -\infty$, $UB = \infty$, node queue $\mathcal{P} = \{(rp)\}$, $LB_{(rp)} = -\infty$
  while $|\mathcal{P}| > 0$ and $UB > LB$ **do**
    Choose $P \in \mathcal{P}$, $\mathcal{P} \longleftarrow \mathcal{P} \setminus \{ P \}$
    Update lower bound on P, $LB_P \longleftarrow c^\top x^*_{\widetilde{P}}$ (if infeasible $LB_P \longleftarrow \infty$)
    $LB \longleftarrow \min \{ LB_P : P \in \mathcal{P} \}$
    if $LB_P < UB$ **then**
      if An integer solution $\widetilde{x} \in \Omega_{(rp)}$ is found **then**
        Add cut to remove $\widetilde{x}_T$ from $\Omega_{(rp)}$
        Solve $(cp(\widetilde{x}_T))$
        if $(cp(\widetilde{x}_T))$ is feasible and $f_{x^*_T}(x^*_{(cp)}) < UB$ **then**
          $UB \longleftarrow f_{x^*_T}(x^*_{(cp(\widetilde{x}_T))})$
          $x^* \longleftarrow x^*_{(cp(\widetilde{x}_T))}$, $x^*_T \longleftarrow \widetilde{x}_T$
      else
        Integer branching on P: new subproblems P_i, $i = 1, 2$
        $\mathcal{P} \longleftarrow \mathcal{P} \cup \{ P_i : i \in \{1, 2\} \}$
        $LB_{P_i} \longleftarrow LB_P$
  if $UB < \infty$ **then**
    return $\phi_{x^*_T}(x^*)$
  else
    Infeasible

In the following, the set $\Omega_P \subseteq \Omega_{(rp)}$ denotes the feasible set of a subproblem P from the node queue and $\mathcal{X}_P \subseteq \mathcal{X}^g_{(op)} \subseteq \{0,1\}^{n_\mathcal{V}}$ the set of binary variables, for which there exists a feasible solution in Ω_P. Since Algorithm 3 performs only integer branching starting with the root node (rp), we can write any subproblem P as

$$\begin{aligned} \min_x \quad & (rp) \\ \text{s.t.} \quad & x_T \in \mathcal{X}_P \subseteq \{0,1\}^{n_\mathcal{V}}. \end{aligned}$$

Corollary 7.4.1. *If (op) has a feasible solution $\boldsymbol{x} = (\boldsymbol{x}_T, \boldsymbol{x}_\mathcal{V}, \boldsymbol{x}_{MS}, \boldsymbol{x}_e)^\top \in \Omega_{(op)}$, then as long as Algorithm 3 has not found a solution candidate $x^*_T \in \mathcal{X}_{(op)}$, $x^* \in \Omega^{1,x^*_T}_{(op)}$ with $f_{x^*_T}(x^*) \leqslant f_{x_T}(part_1(\boldsymbol{x}))$, there is a node P in the node queue with a feasible point $\widetilde{x} = (\widetilde{x}_T, \widetilde{x}_\mathcal{V}, \widetilde{x}_{MS}, \widetilde{x}_e)^\top \in \Omega_P$ and $\boldsymbol{x}_T = \widetilde{x}_T$.*

Proof. Let $\mathbf{x} = (\mathbf{x}_T, \mathbf{x}_\mathcal{V}, \mathbf{x}_{MS}, \mathbf{x}_e)^\top \in \Omega_{(op)}$ be a solution candidate of (op) with objective value $f(\mathbf{x}_{MS}, \mathbf{x}_e)$, which is equal to $f_{x_T}(part_1(\mathbf{x}))$ according to Eq. (67). At the root node (rp) there is a point $\widetilde{x} = (\widetilde{x}_T, \widetilde{x}_\mathcal{V}, \widetilde{x}_{MS}, \widetilde{x}_e)^\top \in \Omega_P$ with

$x_T = \widetilde{x}_T$ according to Assumption 7.2.1. During each integer branching on a node $P \in \mathcal{P}$ a new subproblem P_i is created with $x_T \in \mathcal{X}_{P_i}$. Because $\widetilde{x} \in \Omega_{P_i}$ holds, the subproblem P_i is feasible and

$$\begin{aligned} LB_P \leqslant \min_x\ & (rp) \\ \text{s.t.}\ & x_T \in \mathcal{X}_P \subseteq \{0,1\}^{n_V} \\ & \mathbf{x}_T \in \mathcal{X}_P \end{aligned} \leqslant \begin{aligned} \min_x\ & (rp) \\ \text{s.t.}\ & x_T \in \mathcal{X}_{P_i} \subseteq \{0,1\}^{n_V} \\ & \mathbf{x}_T \in \mathcal{X}_{P_i} \end{aligned}$$

$$\leqslant \begin{aligned} \min_x\ & (rp) \\ \text{s.t.}\ & x_T = \mathbf{x}_T \end{aligned} \leqslant \begin{aligned} \min_x\ & (op) \\ \text{s.t.}\ & x_T = \mathbf{x}_T \end{aligned} \leqslant f_{\mathbf{x}_T}(part_1(\mathbf{x}))$$

The upper bound UB is the objective value of the best solution candidate found so far, or $UB = \infty$ if no solution has been found yet. This implies that as long as no solution candidate $x_T^* \in \mathcal{X}_{(op)}$ and $x^* \in \Omega_{(op)}^{1,x_T^*}$ with $f_{x_T^*}(x^*) \leqslant f_{x_T}(part_1(x))$ was found, the upper bound fulfills

$$f_{x_T}(part_1(x)) < UB.$$

Thus $LB_P < UB$ holds and P_i is added to the node queue. □

Lemma 7.4.1. *If there exists a feasible solution to* (op) *and the configuration models* (cp) *are solved to ϵ-global optimality, Algorithm 3 finds an ϵ-global optimal solution of* (op)*. Otherwise it terminates with $UB = \infty$.*

Proof. Algorithm 3 performs only integer branching on the indicator variables $x_T \in \{0,1\}^{n_V}$ and fixes one indicator variable at each branching. Therefore, the algorithm considers at most $2^{n_V+1} - 1$ branching nodes before termination.

First, let us consider the case that (op) is not feasible. Then (cp($\mathbf{x}_T$)) is infeasible for all $\mathbf{x}_T \in \{0,1\}^{n_V}$, because a feasible solution of (cp($\mathbf{x}_T$)) would correspond to a feasible solution of (op) according to Lemma 7.3.2. Therefore, the upper bound is never updated from the initial value and the algorithm terminates with $UB = \infty$.

If (op) is feasible, there exists an ϵ-global optimal solution candidate $\mathbf{x} = (\mathbf{x}_T, \mathbf{x}_V, \mathbf{x}_{MS}, \mathbf{x}_e)^\top \in \Omega_{(op)}$. Corollary 7.4.1 still holds, because the reduced model still gives a correct lower bound on the solutions of the original problem. As long as no other ϵ-global optimal solution was found, Corollary 7.4.1 implies that a node P in the node queue exists with $\mathbf{x} \in \Omega_P$. In this case

$$LB \leqslant LB_P \leqslant f_{\widetilde{x}_T}(part_1(\widetilde{x})) \leqslant f_{x_T}(part_1(x)) < UB$$

holds and branching continues until an ϵ-global optimal solution is found. □

Lemma 7.4.2. *If there exists a feasible solution to* (op) *and the configuration models* (cp) *are solved to local optimality, Algorithm 3 examines the detailed configuration model* (cp) *of an* ϵ*-global optimal solution of* (op) *during the solving process.*

Proof. As in the proof of Lemma 7.4.1, if a feasible point exists, $LB < UB$ holds and branching continues until an ϵ-global optimal solution is considered. The algorithm terminates with a solution which is not ϵ-global optimal if solving the configuration models corresponding to ϵ-global optimal solutions returns a local optimum of (cp) which is greater than the upper bound and the configuration is cut from the feasible set. □

Note. *Lemmas 7.4.1 and 7.4.2 show that while solving* (cp) *locally reduces the computational costs of solving the subproblem, more subproblems might need to be solved before termination.*

7.5 CALCULATION OF A LOWER BOUND: PROCESS EXERGY EFFICIENCY

Let us consider an optimization problem of the form (mp) which represents a superstructure model, as proposed in Chapter 5. It is a special case of the more general problem formulation (op).

$$
\begin{aligned}
\min_{x_T, x_\mathcal{V}, x_{MS}, x_e, w} \quad & f(x_{MS}, x_e, w) = \frac{e_{ch}^\top x_{MS} + \sum e + \sum w}{w_{ref}} \\
\text{s.t.} \quad & \text{Eqs. (70)} \\
& \left.\begin{aligned}
& g_U(x_{T,U}, x_U, x_U^{in}) \leqslant 0 \\
& h_U(x_{T,U}, x_U, x_U^{in}) = 0 \\
& h_U^{out}(x_{T,U}, x_U, x_U^{out}, x_{e,U}, w_U) = 0
\end{aligned}\right\} \; U \in \mathcal{V}
\end{aligned}
\tag{mp}
$$

$$
\left.\begin{aligned}
&\text{material stream constraints} && g_{MS}(x_{MS}) \leqslant 0 \\
&\text{heat exergy demand} && g_E(x_e) \leqslant 0 \\
&\text{exergy demand} && e, w \geqslant 0 \\
&\text{superstructure topology} && g_\mathcal{V}(x_T) \leqslant 0 \\
&\text{integer constraints} && x_T \in \{0,1\}^{n_\mathcal{V}} \\
&\text{unit model variables} && x_\mathcal{V} = [x_U]_{U \in \mathcal{V}} \\
&\text{material streams} && x_{MS} = [x_U^{in}, x_U^{out}]_{U \in \mathcal{V}} \\
&\text{work and heat integration} && x_e = \left([x_{e,U}]_{U \in \mathcal{V}}^\top, Q_{ext}, e\right)^\top \\
& && x_{e,U} = \left(q_U^I, T_{U,in}^I, T_{U,out}^I, \right. \\
& && \qquad q_U^{II}, T_U^{II}, w_U, \\
& && \qquad \left.[Q_{U,i}^I, Q_{U,i}^{II}]_{i \in \{1,\dots,n_U\}}^\top\right)^\top
\end{aligned}\right\} \tag{70}
$$

The variables x_{MS} represent the material streams between the unit models, e.g. x_U^{in}, as well as process product streams, which are weighted according to the chemical exergy in the objective. The vector e_{ch}, which weights the material streams in the objective, is equal to zero for waste and internal material streams. We here explicitly differentiate between the variables describing the heat integration x_e and the work demand w, because w does not enter the heat integration constraints. The reference value $w_{ref} = 1$ MW is the electrical energy used for water electrolysis, as in Chapters 4 and 5. Material stream constraints, heat exergy demand, and exergy demand together correspond to what was denoted as superstructure overhead in the previous Section. The function g_E represents the constraints Eqs. (39)-(46) of the indirect heat integration, as considered in Chapter 5. In addition, g_E includes

$$e_i \geqslant \left(1 - \frac{T_{amb}}{\hat{T}_i}\right) Q_{ext,i}, \qquad \text{if } \hat{T}_i \geqslant T_{amb}, \tag{71}$$

$$e_i \geqslant \left(\frac{\hat{T}_i}{T_{amb}} - 1\right) Q_{ext,i}, \qquad \text{if } \hat{T}_i < T_{amb}, \tag{72}$$

where $\hat{T}_i$ denotes the temperature of utility i and e is the exergy, which is required from external sources for heating or cooling of the utility. Instead of calculating the exergy of the heat flow, as done here, the exergy of a fuel used for heating, e.g., methane, could be used to assess the exergetic value of heat supplied to the process. Let $\hat{T}_{max}$ and $\hat{T}_{min}$ denote the utilities at highest or lowest temperature for which

$$\begin{aligned}
&\hat{T}_{max} - \Delta T \geqslant T_{in}^{I} \geqslant \hat{T}_{min} + \Delta T \\
&\hat{T}_{max} - \Delta T \geqslant T_{out}^{I} \geqslant \hat{T}_{min} + \Delta T \\
&\hat{T}_{max} - \Delta T \geqslant T^{II} \geqslant \hat{T}_{min} + \Delta T
\end{aligned}$$

holds.

Assumption 7.5.1. *We have a utility at ambient temperature, with*

$$\begin{aligned}
&|T_{out}^{I} - \hat{T}_{amb}| \geqslant \Delta T \\
&|T^{II} - \hat{T}_{amb}| \geqslant \Delta T.
\end{aligned}$$

Furthermore, if $T_{out}^{I} > \hat{T}_{amb} + \Delta T$ *then* $T_{in}^{I} > \hat{T}_{amb} - \Delta T$ *and, vice versa, if* $T_{out}^{I} < \hat{T}_{amb} - \Delta T$ *then* $T_{in}^{I} < \hat{T}_{amb} + \Delta T$.

Note. *Assuming that all units can supply or take heat from a utility at ambient temperature if the heat flow temperature change is directed towards ambient temperature, is necessary for Lemma 7.5.1, which is following in Section 7.5, as a way of*

discarding excess heat or heat sinks below ambient temperature. This assumption is reasonable, if all heat flows close to ambient conditions are negligible, e.g., the heat flows of the PSA in Chapters 4 and 5. Heat flows of type I, which cross over the ambient temperature towards a temperature with sufficient distance to the ambient temperature, can simply be split into two separate heat flows to fulfill this assumption.

Assumption 7.5.2. *No work can be generated from excess heat above or heat sinks below ambient temperature, thus* $e \geqslant 0$.

The heat flows are denoted according to their type as defined in Chapter 5, i.e., type I denotes a heat flow between temperature T^{I}_{in} and T^{I}_{out}, while type II denotes a heat flow at constant temperature T^{II}. The constraints $g_v(x_T)$ restrict the binary variables x_T according to a given superstructure topology, see Eqs. (36), (37).

Replacing a unit model U by a shortcut model $\widetilde{U}$ must result in a lower bound on the detailed model superstructure (mp), as postulated by Assumption 7.2.1. We fulfill this assumption by making use of the units interface with the rest of the superstructure. Each unit model interacts with the rest of the superstructure via in- and outgoing material streams x^{in}_U, x^{out}_U, work demand w_U and heat flows q^{I}_U, q^{II}_U at temperatures $T^{I}_{U,in}$, $T^{I}_{U,out}$, T^{II}_U.

Let $\Omega_U(x^{in}_U)$ be the set of unit variables $x_U \in \mathbb{R}^{n_U}$ which for a given in-going material stream x^{in}_U fulfill the unit constraints

$$g_U\left(1, x_U, x^{in}_U\right) \leqslant 0,$$
$$h_U\left(1, x_U, x^{in}_U\right) = 0.$$

Lemma 7.5.1. *Lower Bound via Replacement of a Unit Model : Switching a unit model* U *out for a reduced model* $\widetilde{U}$ *gives a lower bound on* (mp) *with respect to exergy efficiency, if*

A *The output space of model* U *is a subset of the output space of model* $\widetilde{U}$ *for each input* x^{in}_U.

$$\left\{x \;\middle|\; x = X^{out}_U(x_U), x_U \in \Omega\left(x^{in}_U\right)\right\} \subseteq \left\{x \;\middle|\; x = \widetilde{X}^{out}_U(x_U),\ x_U \in \widetilde{\Omega}\left(x^{in}_U\right)\right\}$$

Note. *It is a priori not clear, how the output of a single unit model must change to improve the overall objective function. If the process has one desired product, e.g. methane, one could argue under which conditions an increase of the amount of methane or a decrease of the amount of impurities in the material stream improves the overall objective function. Other changes of*

the material stream, however, e.g. decrease of the amount of methane and impurities simultaneously, can not be evaluated at unit level and must be considered at superstructure level. We therefore create a lower bound by relaxing the output space of the model.

B *For the work demand*

$$\widetilde{w}_u\left(\widetilde{x}_u\right) \leqslant w_u\left(x_u\right)$$

holds $\forall\, x_u \in \Omega\left(x_u^{in}\right), \widetilde{x}_u \in \widetilde{\Omega}\left(x_u^{in}\right)$, *with* $X_u^{out}\left(x_u\right) = \widetilde{X}_u^{out}\left(\widetilde{x}_u\right)$.

Note. *A decrease of a unit's work demand with the same in- and output material streams (which include the pressure) always improves the process efficiency.*

C *For the heat flows of type I*

$$\left(q_u^I, T_{u,in}^I, T_{u,out}^I\right)^\top = Q_u^I(x_u)$$
$$\left(\widetilde{q}_u^I, \widetilde{T}_{u,in}^I, \widetilde{T}_{u,out}^I\right)^\top = \widetilde{Q}_u^I\left(\widetilde{x}_u\right)$$

the following applies for all $x_u \in \Omega\left(x_u^{in}\right)$, $\widetilde{x}_u \in \widetilde{\Omega}\left(x_u^{in}\right)$ *with* $X_u^{out}(x_u) = \widetilde{X}_u^{out}\left(\widetilde{x}_u\right)$*:*

a) if $q_u^I > 0, T_{u,out}^I \leqslant T_{amb} - \Delta T$ *then*

$$\widetilde{q}_u^I \geqslant q_u^I,\ \hat{T}_{min} + \Delta T \leqslant \widetilde{T}_{u,in}^I \leqslant T_{u,in}^I, \widetilde{T}_{u,in}^I \leqslant \widetilde{T}_{u,out}^I \leqslant T_{u,out}^I$$

b) if $q_u^I > 0, T_{u,in}^I > T_{amb} - \Delta T$ *then*

$$0 \leqslant \widetilde{q}_u^I \leqslant q_u^I,\ \hat{T}_{min} + \Delta T \leqslant \widetilde{T}_{u,in}^I \leqslant \widetilde{T}_{u,out}^I,$$
$$\widetilde{T}_{u,in}^I \leqslant \widetilde{T}_{u,out}^I \leqslant T_{u,out}^I$$

c) if $q_u^I < 0, T_{u,out}^I \geqslant T_{amb} + \Delta T$ *then*

$$\widetilde{q}_u^I \leqslant q_u^I,\ \hat{T}_{max} - \Delta T \geqslant \widetilde{T}_{u,in}^I \geqslant T_{u,in}^I, \widetilde{T}_{u,in}^I \geqslant \widetilde{T}_{u,out}^I \geqslant T_{u,out}^I$$

d) if $q_u^I < 0, T_{u,in}^I < T_{amb} - \Delta T$ *then*

$$0 \geqslant \widetilde{q}_u^I \geqslant q_u^I,\ \hat{T}_{max} - \Delta T \geqslant \widetilde{T}_{u,in}^I \geqslant T_{u,in}^I,$$
$$\widetilde{T}_{u,in}^I \geqslant \widetilde{T}_{u,out}^I \geqslant T_{u,out}^I$$

e) if $q_U^I = 0$ *then*

$$\widetilde{q}_U^I \geqslant q_U^I,\ \hat{T}_{min} + \Delta T \leqslant \widetilde{T}_{U,in}^I \leqslant T_{U,in}^I, \widetilde{T}_{U,in}^I \leqslant \widetilde{T}_{U,out}^I \leqslant T_{U,in}^I$$
or
$$\widetilde{q}_U^I \leqslant q_U^I,\ \hat{T}_{max} - \Delta T \geqslant \widetilde{T}_{U,in}^I \geqslant T_{U,in}^I, \widetilde{T}_{U,in}^I \geqslant \widetilde{T}_{U,out}^I \geqslant T_{U,out}^I$$

D *For the heat flows of type II*

$$\left(q_U^{II}, T_U^{II}\right)^\top = Q_U^{II}(x),$$
$$\left(\widetilde{q}_U^{II}, \widetilde{T}_U^{II}\right)^\top = \widetilde{Q}_U^{II}(\widetilde{x})$$

the following applies $\forall\, x \in \Omega\left(x_U^{in}\right), \widetilde{x} \in \widetilde{\Omega}\left(x_U^{in}\right)$, *with* $X_U^{out}(x) = \widetilde{X}_U^{out}(\widetilde{x})$*:*

a) if $q_U^{II} > 0, T_U^{II} \leqslant T_{amb} - \Delta T$ *then*

$$\widetilde{q}_U^{II} \geqslant q_U^{II},\ \hat{T}_{min} + \Delta T \leqslant \widetilde{T}_U^{II} \leqslant T_U^{II}$$

b) if $q_U^{II} > 0, T_U^{II} > T_{amb} + \Delta T$ *then*

$$\widetilde{q}_U^{II} \leqslant q_U^{II},\ \hat{T}_{min} + \Delta T \leqslant \widetilde{T}_U^{II} \leqslant T_U^{II}$$

c) if $q_U^{II} < 0, T_U^{II} \geqslant T_{amb} + \Delta T$ *then*

$$\widetilde{q}_U^{II} \leqslant q_U^{II},\ \hat{T}_{max} - \Delta T \geqslant \widetilde{T}_U^{II} \geqslant T_U^{II}$$

d) if $q_U^{II} < 0, T_U^{II} < T_{amb} - \Delta T$ *then*

$$\widetilde{q}_U^{II} \geqslant q_U^{II},\ \hat{T}_{max} - \Delta T \geqslant \widetilde{T}_U^{II} \geqslant T_U^{II}$$

e) if $q_U^{II} = 0$ *then*

$$\widetilde{q}_U^{II} \geqslant q_U^{II},\ \hat{T}_{min} + \Delta T \leqslant \widetilde{T}_U^{II} \leqslant T_U^{II}$$
or
$$\widetilde{q}_U^{II} \leqslant q_U^{II},\ \hat{T}_{max} - \Delta T \geqslant \widetilde{T}_U^{II} \geqslant T_U^{II}$$

Note. *A decrease of a unit's demand for heating above or cooling below ambient temperature reduces the overall external heat exergy demand of the superstructure, as soon as this demand can not be met by other units. This corresponds to cases b) and d). Simultaneously, an increase of the exergy, which a unit model produces in terms of excess heat above ambient temperature can be used internally to reduce the external heat demand, here cases a), c), and e).*

Proof. Let us assume, that $\widetilde{U}$ is a shortcut model, which fulfills **A**, **B**, **C**, and **D**. Let $\mathbf{x} = (\mathbf{x}_T, \mathbf{x}_\mathcal{V}, \mathbf{x}_{MS}, \mathbf{x}_e)^\top$ denote the global minimum of (mp) and let $U \in \mathcal{V}$ denote the unit model, which was switched for shortcut model $\widetilde{U}$. We show, that under these conditions, the reduced problem gives a lower bound on (mp), by constructing a point $\widetilde{x} = (\widetilde{x}_T, \widetilde{x}_\mathcal{V}, \widetilde{x}_{MS}, \widetilde{x}_e)^\top$ which is feasible for the reduced problem, with an objective value $f(\widetilde{x}) \leqslant f(\mathbf{x})$.

For the trivial case that $\mathbf{x}_{T,U} = 0$, we have a feasible solution of the reduced problem with $part_1(\widetilde{x}) = part_1(\mathbf{x})$ and therefore $f(\widetilde{x}_{MS}, \widetilde{x}_e, \widetilde{w}) = f(\mathbf{x}_{MS}, \mathbf{x}_e, \mathbf{w})$. Let us consider the case, that $\mathbf{x}_{T,U} = 1$. From Assumption 7.2.1 follows that we can choose

$$\widetilde{x}_T = \mathbf{x}_T.$$

According to **A**, we can furthermore choose

$$\widetilde{x}_U^{out} = \mathbf{x}_U^{out},$$

which implies that

$$\begin{aligned} &\widetilde{x}_{MS} = \mathbf{x}_{MS}, && \\ &\widetilde{x}_V = \mathbf{x}_V, && V \in \mathcal{V} \setminus U \end{aligned} \tag{73}$$

is feasible within the unit model constraints. From this follows

$$\begin{aligned} &\widetilde{q}_V^I = \mathbf{q}_V^I, && V \in \mathcal{V} \setminus U, \\ &\widetilde{T}_{V,in}^I = \mathbf{T}_{V,in}^I, && V \in \mathcal{V} \setminus U, \\ &\widetilde{T}_{V,out}^I = \mathbf{T}_{V,out}^I, && V \in \mathcal{V} \setminus U, \\ &\widetilde{q}_V^{II} = \mathbf{q}_V^{II}, && V \in \mathcal{V} \setminus U, \\ &\widetilde{T}_V^{II} = \mathbf{T}_V^{II}, && V \in \mathcal{V} \setminus U, \\ &\widetilde{w}_V = \mathbf{w}_V, && V \in \mathcal{V} \setminus U. \end{aligned}$$

With this, we can choose

$$\begin{aligned} &\widetilde{Q}_{V,i}^I = \mathbf{Q}_{V,i}^I && V \in \mathcal{V} \setminus U, \\ &\widetilde{Q}_{V,i}^{II} = \mathbf{Q}_{V,i}^{II} && V \in \mathcal{V} \setminus U, \end{aligned}$$

where $Q_{V,i}^I$ and $Q_{V,i}^{II}$ are the heat flows from unit V to utility i at temperature $\hat{T}_i$. According to **B**, $\widetilde{w}_U \leqslant \mathbf{w}_U$ holds and therefore

$$\sum_{U \in \mathcal{V}} \widetilde{w}_U \leqslant \sum_{U \in \mathcal{V}} \mathbf{w}_U. \tag{74}$$

For heat flows of type I the following holds: If $\mathbf{q}^I_U > 0$, $\mathbf{T}^I_{U,out} \leqslant T_{amb} - \Delta T$ then $\widetilde{q}^I_U \geqslant \mathbf{q}^I_U$, $\hat{T}_{min} + \Delta T \leqslant \widetilde{T}^I_{U,in} \leqslant \mathbf{T}^I_{U,in}$, $\widetilde{T}^I_{U,in} \leqslant \widetilde{T}^I_{U,out} \leqslant \mathbf{T}^I_{U,out}$ holds according to **C** a). From Eq. (44) follows

$$\sum_i \widetilde{Q}^I_{U,i} = \widetilde{q}^I_U \geqslant \mathbf{q}^I_U = \sum_i \mathbf{Q}^I_{U,i},$$

where $Q^I_{U,i}$ is the heat flow from unit U to utility i at temperature $\hat{T}_i$. Since $\widetilde{T}^I_{U,out} \leqslant T^I_{U,out} \leqslant T_{amb} - \Delta T$, the utility at ambient temperature is available for heat integration according to Eq. (40) and we can choose

$$\begin{aligned} &\widetilde{Q}^I_{U,amb} \geqslant \mathbf{Q}^I_{U,amb}, \\ &\widetilde{Q}^I_{U,i} = \mathbf{Q}^I_{U,i}, \qquad\qquad \text{for } i \neq amb, \end{aligned}$$

from which follows

$$\begin{aligned} &\sum_{V\in\mathcal{V}} \widetilde{Q}^I_{V,amb} \geqslant \sum_{V\in\mathcal{V}} \mathbf{Q}^I_{V,amb}, \\ &\sum_{V\in\mathcal{V}} \widetilde{Q}^I_{V,i} = \sum_{V\in\mathcal{V}} \mathbf{Q}^I_{V,i}, \qquad\qquad \text{for } i \neq amb. \end{aligned} \tag{75}$$

The cases **C** c) and e) lead to Eq. (75) in the same way with some reversed inequalities by using Eq. (41) instead of Eq. (40). For the case **C** b) $\mathbf{q}^I_U > 0$, $\mathbf{T}^I_{U,in} > T_{amb} + \Delta T$, $0 \leqslant \widetilde{q}^I_U \leqslant \mathbf{q}^I_U$, $\hat{T}_{min} + \Delta T \leqslant \widetilde{T}^I_{U,in} \leqslant \widetilde{T}^I_{U,out}$, $\widetilde{T}^I_{U,in} \leqslant \widetilde{T}^I_{U,out} \leqslant \mathbf{T}^I_{U,out}$ holds, thus according to Eq. (44)

$$\sum_i \widetilde{Q}^I_{U,i} = \widetilde{q}^I_U \leqslant \mathbf{q}^I_U = \sum_i \mathbf{Q}^I_{U,i}.$$

From Eqs. (39) - (41) follows that utilities at and below ambient temperature are not available for heat integration (note that $\mathbf{T}^I_{U,in} < \mathbf{T}^I_{U,out}$ holds for heat flows of type I with $\mathbf{q}^I_U > 0$), i.e.,

$$\mathbf{Q}^I_{U,i} = 0, \qquad \text{for } i \in \{1,\dots,n_E\} \text{ with } \hat{T}_i \leqslant T_{amb}.$$

Eq. (40) in combination with $\hat{T}_{min} + \Delta T \leqslant \widetilde{T}^I_{U,in} \leqslant T^I_{U,in}$, $\widetilde{T}^I_{U,in} \leqslant \widetilde{T}^I_{U,out} \leqslant \mathbf{T}^I_{U,out}$ also shows that all utilities which are available for heat integration of $\mathbf{q}^I_U$ are also available for $\widetilde{q}^I_U$. We can therefore choose

$$0 \leqslant \widetilde{Q}^I_{U,i} \leqslant \mathbf{Q}^I_{U,i} \qquad \text{for } i \in \{1,\dots,n_E\}$$

and get

$$\sum_{V\in\mathcal{V}} \widetilde{Q}^I_{V,i} = \sum_{V\in\mathcal{V}} \mathbf{Q}^I_{V,i}, \qquad \text{for } i \in \{1,\dots,n_E\} \text{ with } \hat{T}_i \leqslant T_{amb}, \tag{76}$$

$$\sum_{V\in\mathcal{V}} \widetilde{Q}^I_{V,i} \leqslant \sum_{V\in\mathcal{V}} \mathbf{Q}^I_{V,i}, \qquad \text{for } i \in \{1,\dots,n_E\} \text{ with } \hat{T}_i > T_{amb}. \tag{77}$$

In the same way we get

$$\sum_{V\in\mathcal{V}} \widetilde{Q}^{I}_{V,i} \geqslant \sum_{V\in\mathcal{V}} \mathbf{Q}^{I}_{V,i}, \qquad \text{for } i \in \{1,\dots,n_E\} \text{ with } \hat{T}_i < T_{amb}, \tag{78}$$

$$\sum_{V\in\mathcal{V}} \widetilde{Q}^{I}_{V,i} = \sum_{V\in\mathcal{V}} \mathbf{Q}^{I}_{V,i}, \qquad \text{for } i \in \{1,\dots,n_E\} \text{ with } \hat{T}_i \geqslant T_{amb}. \tag{79}$$

for the case **C** d).

Combining the results of the different cases, i.e., Eqs. (75) - (79), results in

$$\sum_{V\in\mathcal{V}} \widetilde{Q}^{I}_{V,i} \geqslant \sum_{V\in\mathcal{V}} \mathbf{Q}^{I}_{V,i}, \qquad \text{for } i \in \{1,\dots,n_E\} \text{ with } \hat{T}_i < T_{amb}, \tag{80}$$

$$\sum_{V\in\mathcal{V}} \widetilde{Q}^{I}_{V,i} \leqslant \sum_{V\in\mathcal{V}} \mathbf{Q}^{I}_{V,i}, \qquad \text{for } i \in \{1,\dots,n_E\} \text{ with } \hat{T}_i > T_{amb}. \tag{81}$$

for the heat flows of type I.

The results for the heat integration of type II follow similarly:

If $\mathbf{q}^{II}_U > 0$ and $\mathbf{T}^{II}_U \leqslant T_{amb}$, then $\widetilde{q}^{II}_U \geqslant \mathbf{q}^{II}_U$, $\widetilde{T}^{II}_U \leqslant \mathbf{T}^{II}_U$ holds according to **D** a). From Eq. (45) follows, that

$$\sum_i \widetilde{Q}^{II}_{U,i} = \widetilde{q}^{II}_U \geqslant \mathbf{q}^{II}_U = \sum_i \mathbf{Q}^{II}_{U,i}$$

for the heat flows $Q^{II}_{U,i}$ from unit U to utility i at temperature $\hat{T}_i$. Since $\widetilde{T}^{II}_U \leqslant \mathbf{T}^{II}_U \leqslant T_{amb} - \Delta T$, the utility at ambient temperature is available for heat integration according to Eq. (43) and we can choose

$$\begin{aligned} &\widetilde{Q}^{II}_{U,amb} \geqslant \mathbf{Q}^{II}_{U,amb} \\ &\widetilde{Q}^{II}_{U,i} = \mathbf{Q}^{II}_{U,i} \qquad\qquad \text{for } i \neq amb \end{aligned}$$

Then

$$\begin{aligned} &\sum_{V\in\mathcal{V}} \widetilde{Q}^{II}_{V,amb} \geqslant \sum_{V\in\mathcal{V}} \mathbf{Q}^{II}_{V,amb} \\ &\sum_{V\in\mathcal{V}} \widetilde{Q}^{II}_{V,i} = \sum_{V\in\mathcal{V}} \mathbf{Q}^{II}_{V,i} \qquad\qquad \text{for } i \neq amb \end{aligned} \tag{82}$$

holds for the external heat flows of the utilities. Eq. (82) follows from cases **D** c) and e) accordingly with some inverted inequalities by using Eq. (42) instead of Eq. (43).

If $\mathbf{q}^{II}_U > 0$ and $\mathbf{T}^{II}_U \geqslant T_{amb} + \Delta T$, then $0 \leqslant \widetilde{q}^{II}_U \leqslant \mathbf{q}^{II}_U$, $\widetilde{T}^{II}_U \leqslant \mathbf{T}^{II}_U$ holds according to **D** b). From Eq. (44) follows

$$\widetilde{q}^{II}_U = \sum_i \widetilde{Q}^{II}_{U,i} \leqslant \sum_i \mathbf{Q}^{II}_{U,i} = \mathbf{q}^{II}_U.$$

According to Eqs. (42) and (43), the utilities below ambient temperature are not available for heat integration of $\mathbf{q}_U^{II}$, i.e.,

$$\mathbf{Q}_{U,i}^{II} = 0 \qquad \text{for } i \in \{1,\dots,n_E\} \text{ with } \hat{T}_i < T_{amb}$$

According to Eq. (43) and $\widetilde{T}_U^{II} \leqslant \mathbf{T}_U^{II}$ we can choose

$$0 \leqslant \widetilde{Q}_{U,i}^{II} \leqslant \mathbf{Q}_{U,i}^{II} \qquad \text{for } i \in \{1,\dots,n_E\} \tag{83}$$

from which follows that

$$\sum_{V\in\mathcal{V}} \widetilde{Q}_{V,i}^{II} = \sum_{V\in\mathcal{V}} \mathbf{Q}_{V,i}^{II}, \qquad \text{for } i \in \{1,\dots,n_E\} \text{ with } \hat{T}_i \leqslant T_{amb}, \tag{84}$$

$$\sum_{V\in\mathcal{V}} \widetilde{Q}_{V,i}^{II} \leqslant \sum_{V\in\mathcal{V}} \mathbf{Q}_{V,i}^{II}, \qquad \text{for } i \in \{1,\dots,n_E\} \text{ with } \hat{T}_i > T_{amb}. \tag{85}$$

As before, we get

$$\sum_{V\in\mathcal{V}} \widetilde{Q}_{V,i}^{II} \geqslant \sum_{V\in\mathcal{V}} \mathbf{Q}_{V,i}^{II}, \qquad \text{for } i \in \{1,\dots,n_E\} \text{ with } \hat{T}_i < T_{amb}, \tag{86}$$

$$\sum_{V\in\mathcal{V}} \widetilde{Q}_{V,i}^{II} = \sum_{V\in\mathcal{V}} \mathbf{Q}_{V,i}^{II}, \qquad \text{for } i \in \{1,\dots,n_E\} \text{ with } \hat{T}_i \geqslant T_{amb}. \tag{87}$$

for the case **D** d) in a similar way. For the heat flows of type II then

$$\sum_{V\in\mathcal{V}} \widetilde{Q}_{V,i}^{II} \geqslant \sum_{V\in\mathcal{V}} \mathbf{Q}_{V,i}^{II}, \qquad \text{for } i \in \{1,\dots,n_E\} \text{ with } \hat{T}_i < T_{amb}, \tag{88}$$

$$\sum_{V\in\mathcal{V}} \widetilde{Q}_{V,i}^{II} \leqslant \sum_{V\in\mathcal{V}} \mathbf{Q}_{V,i}^{II}, \qquad \text{for } i \in \{1,\dots,n_E\} \text{ with } \hat{T}_i > T_{amb} \tag{89}$$

holds according to Eqs. (82) - (87).

For the external heat demand of utility i above ambient temperature $\hat{T}_i > T_{amb}$ according to Eqs. (46), (81), (89) we then get

$$\widetilde{Q}_{ext,i} = \sum_{V\in\mathcal{V}} \widetilde{Q}_{V,i}^{I} + \sum_{V\in\mathcal{V}} \widetilde{Q}_{U,i}^{II} \leqslant \sum_{V\in\mathcal{V}} \mathbf{Q}_{V,i}^{I} + \sum_{V\in\mathcal{V}} \mathbf{Q}_{U,i}^{II} = \mathbf{Q}_{ext,i}$$

and thus

$$\widetilde{e}_i = \min\{(1 - \frac{T_{amb}}{\hat{T}_i})\widetilde{Q}_{ext,i}, 0\} \leqslant \min\{(1 - \frac{T_{amb}}{\hat{T}_i})\mathbf{Q}_{ext,i}, 0\} = \mathbf{e}_i$$

holds with Eq. (71) for the exergy demand for heating above ambient temperature. Similarly, for a utility i below ambient temperature $\hat{T}_i < T_{amb}$ according to Eqs. (46), (80), (88)

$$\widetilde{Q}_{ext,i} = \sum_{V\in\mathcal{V}} \widetilde{Q}_{V,i}^{I} + \sum_{V\in\mathcal{V}} \widetilde{Q}_{U,i}^{II} \geqslant \sum_{V\in\mathcal{V}} \mathbf{Q}_{V,i}^{I} + \sum_{V\in\mathcal{V}} \mathbf{Q}_{U,i}^{II} = \mathbf{Q}_{ext,i}$$

and according to Eq. (72)

$$\widetilde{e}_i = \min\{(\frac{\hat{T}_i}{T_{amb}} - 1)\widetilde{Q}_{ext,i}, 0\} \leqslant \min\{(\frac{\hat{T}_i}{T_{amb}} - 1)\mathbf{Q}_{ext,i}, 0\} = \mathbf{e}_i$$

For the utility at ambient temperature

$$\widetilde{e}_i = 0 = \mathbf{e}_i$$

holds according to Eq. (71) and finally

$$\sum_{i\in\{1,\dots,n_E\}} \widetilde{e}_i \leqslant \sum_{i\in\{1,\dots,n_E\}} \mathbf{e}_i. \tag{90}$$

As a result, for the objective function

$$\begin{aligned} f(\widetilde{x}_{MS}, \widetilde{x}_e, \widetilde{w}) &= \frac{e_{ch}^\top \widetilde{x}_{MS} + \sum \widetilde{e} + \sum \widetilde{w}}{w_{ref}} \\ &\leqslant \frac{e_{ch}^\top \mathbf{x}_{MS} + \sum \mathbf{e} + \sum \mathbf{w}}{w_{ref}} = f(\mathbf{x}_{MS}, \mathbf{x}_e, \mathbf{w}) \end{aligned}$$

holds according to Eqs. (73), (74), (90). □

An example illustrating an estimation for the heat flow is shown in Figure 43.

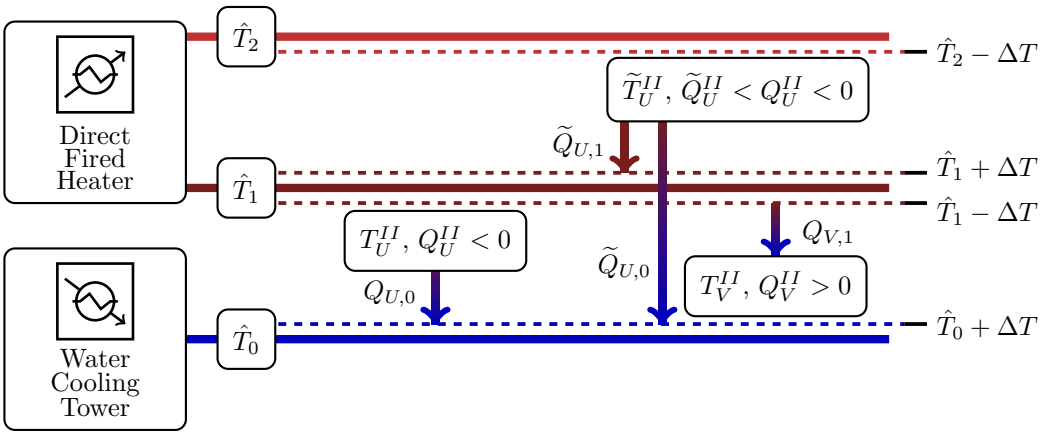

Figure 43: Example for the heat integration of a replacement model. *The figure shows an example for the case c) of type II. Here, the excess heat* Q_U^{II} *is discarded, as it can not be used internally. Increasing the heat flow* $\widetilde{Q}_U^{II} > Q_U^{II}$ *does not increase the objective. Is the excess heat emitted at a higher temperatures, the potential for internal use increases. If another unit, here unit* V*, can use the heat from unit* $\widetilde{U}$*, the objective value decreases.*

Note. *Economic objectives like the CAPEX can be considered similarly. The unit costs can be easily evaluated on unit level (in the same way as the work demand here). The costs of the heat exchanger network are reduced, if less heat is transferred ($|\tilde{q}_u| \leqslant |\boldsymbol{q}_u|$), or temperature differences between units and utilities are larger. This contradicts the requirements of $\boldsymbol{C}$, $\boldsymbol{D}$, which makes a simultaneous optimization of efficiency and capital costs difficult. This is illustrated by the results of Chapter 5, where the choice of the objective strongly effects the extent of the heat exchanger network. Using reduced models, which give lower bounds for minimizing efficiency and cost simultaneously might result in bounds which are not tight.*

7.6 EXAMPLES

In this section we show a few examples of pairs of unit models, of which one works as a reduced model to the other. We discuss the catalytic methanation reactor and the pressure swing adsorption, for which we introduce the short-cut and the original model. Furthermore, we calculate the exergy efficiency for different process configurations, which use either the reduced or the original model. The other models of the configuration, e.g., heat exchangers or flash separation, are the same for both models and are represented by the models introduced in Chapter 5.

Example 7.6.1. *Catalytic Methanation Reactor*

Let us consider the catalytic methanation in a plug flow reactor at steady state and at isobaric conditions. Using the reaction kinetic of Koschany et al. [39] and energy balances for the gas and a cooling medium (subscript cool*) we get*

$$
\begin{aligned}
&\nu \frac{dN_i}{dz} = \zeta_i r f_c \\
&\nu \rho_g c_{p,g} \frac{dT}{dz} = \alpha(T_{cool} - T) - f_c r \Delta H \\
&m_{cool} c_{p,cool} \frac{dT_{cool}}{dz} = \epsilon A \alpha (T - T_{cool}) \\
&r = \frac{k_r p_{H_2}^{0.5} p_{CO_2}^{0.5} \left(1 - \frac{p_{CH_4} p_{H_2O}^2}{p_{CO_2} p_{H_2}^4} K_{eq}(T)\right)}{\left(1 + K_{OH} \frac{p_{H_2O}}{p_{H_2}^{0.5}} + K_{H_2} p_{H_2}^{0.5} + K_{mix} p_{CO_2}^{0.5}\right)^2} \\
&k_r = k_0 \exp\left(\frac{-E_A}{R}\left(1/T_{ref} - 1/T\right)\right) \\
&K_i = K_{0,i} \exp\left(\frac{-\Delta H_i^r}{R}\left(1/T_{ref} - 1/T\right)\right) \\
&x^{out}(x_u, x^{in}) = (N_{CO_2}|_{z=L}, N_{H_2}|_{z=L}, N_{CH_4}|_{z=L}, N_{H_2O}|_{z=L}, T|_{z=L}, p^{in})^\top
\end{aligned}
$$

$$
\begin{aligned}
&W(x_U) = 0\\
&\dot{Q}^I(x_U) = \dot{m}_{cool} c_{p,cool}(T_{cool}|_{z=0} - T_{cool}|_{z=L})\\
&T^I_{in}(x_U) = T_{cool}|_{z=L}\\
&T^I_{out}(x_U) = T_{cool}|_{z=0}
\end{aligned}
$$

where $f_c = \rho_c \frac{1-\epsilon}{\epsilon}$, $\dot{m}_{cool}$ *is the flow rate of the coolant, and* $\Delta H = -165$ *kJ/mol denotes the heat of reaction. We discretize the ODEs on a spatial grid* $z \in [0, L]$ *and add the box constraint* $400\ K \leqslant T, T_c \leqslant 700\ K$ *on each grid point. Furthermore,* $400\ K \leqslant T_c \leqslant 500\ K$ *holds at inlet* $z = 0$.

As a reduced model, we use the equilibrium model from Chapter 5:

$$
\begin{aligned}
&x_U = (N_{CO_2}, N_{H_2}, N_{CH_4}, N_{H_2O}, \xi, T)^\top\\
&g(x_U) = p_{CO_2} p^4_{H_2} - p^2_{H_2O} p_{CH_4} K_{eq}(T) && \text{with } p_i = p^{in} \frac{N_i}{\sum_{j \in C} N_j}\\
&h(x_U) = N_i - (\xi \nu_i + N^{in}_i) && \text{for } i \in C\\
&400 \leqslant T \leqslant 700\\
&x^{out}(x_U, x^{in}) = (N_{CO_2}, N_{H_2}, N_{CH_4}, N_{H_2O}, T, p^{in})^\top\\
&W(x_U) = 0\\
&\dot{Q}^I(x_U) = \xi \Delta H + \dot{m}_g c_{p,g}(T - T_{in})\\
&T^I_{in}(x_U) = 700\ K\\
&T^I_{out}(x_U) = 500\ K
\end{aligned}
$$

The extent of the reaction ξ *is for the reduced model only limited by the reaction equilibrium. The equilibrium depends on the temperature, which can be chosen freely by the solver. The plug flow reactor on the other hand is limited by a thermodynamically consistent kinetic expression, i.e., it can only approach the reaction equilibrium for* $L \longrightarrow \infty$. *Thus the output space of the reduced model is relaxed according to* ***A****. Both models do not have an additional work demand, thus* ***B*** *is fulfilled. The methanation reactor produces excess heat at high temperature, so case* ***D*** *c) applies. We set the temperatures* $T^I_{in}(x_U)$ *and* $T^I_{out}(x_U)$ *to the respective upper bounds of* 700 *K and* 500 *K. The heat flow* $\xi \Delta H$ *is the thermal energy which is created by the methanation reaction. To calculate the amount of heat which is transferred to the coolant, we subtract the enthalpy of the products temperature change from the heat of the reaction. Thus, if the product material streams of the two models is identical, their heat flow* $\dot{Q}^I(x_U)$ *is equal and the requirements of* ***D*** *c) are fulfilled.*

Example 7.6.2. *Pressure Swing Adsorption*

The black box separation model from Section 5.1.1 gives a lower bound on the PDAE from Chapter 6. We treat the separation fraction s of the components CO_2 and CH_4 as variables and add the constraints

$$s_{CH_4} - 0.8 - s_{CO_2} \leqslant 0$$
$$s_{CH_4} - 0.65 - 7s_{CO_2} \leqslant 0.$$

*The output space of the black box model and the PDAE model are shown in Figure 44. It shows that the output space of the black box model is indeed a relaxation of the PDAE model and **A** is fulfilled. The model has no additional work or heat flows, thus the black box model is a reduced model.*

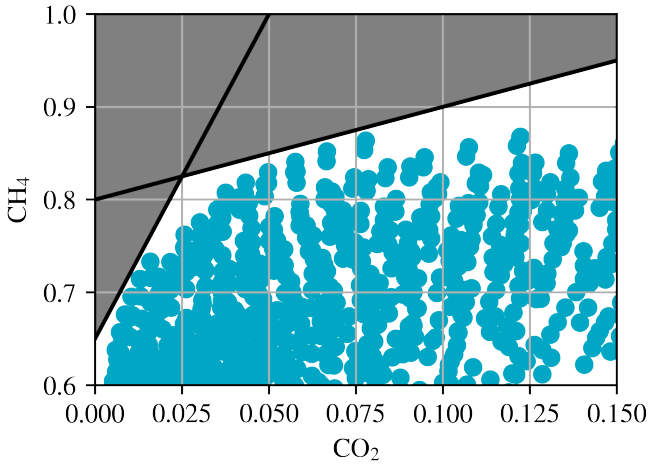

Figure 44: Feasible output space of the shortcut model.
The output space of the shortcut model is the area in white, limited by the black lines. The blue dots indicate the output space of the PDAE model, evaluated with different model parameters. The figure illustrates that the output space of the shortcut model is a relaxation of the output space of the PDAE model.

7.7 CHAPTER SUMMARY AND THOUGHTS FOR FURTHER WORK

We propose a method, which allows for optimization of detailed unit level models within a superstructure. The approach has the advantage of combining different levels of process design, i.e. decisions on plant level are considered simultaneously to unit level design choices. It converges to global optimality, if so desired. A large library of unit models is necessary with the appropriate shortcut unit underestimators. Available chemical engineering toolboxes can be used to get models for different units, e.g. COMSOL [164]. While the computational time can get large, as difficult subproblems must be solved, the method can be terminated at any time, and the LB gives

information about the optimality of the current best solution. Key elements for the runtime of a branch-and-bound type method are the chosen relaxed shortcut models [165]. Effort must be put into making sure the reduced models give tight bounds. Overall, we gave a theoretical background of the method for application to process synthesis. Further studies are required to observe the application in practice. The implementation of the proposed method in SCIP is possible via the interface of constraint handlers.

8

CONCLUSIONS AND FUTURE WORK

The results of this thesis can be divided into three main parts: Firstly, this thesis contributes to research in the field of power-to-methane by identification of the alternative technologies and the optimal process route for methanation at steady state. Secondly, this work progresses the computational methods for the optimization of cyclic adsorption processes such as pressure or temperature swing adsorption processes. Finally, a new branch-and-bound based algorithm to combine the previous results and to allow for more in depth analysis and optimization of processes at plant level is proposed. The overarching results of this work pave the road for further studies of dynamic power-to-methane processes, which are of interest for the storage of electrical energy from volatile renewable energy sources.

8.1 CONTRIBUTIONS TO POWER-TO-METHANE PROCESSES

We identified the best process route for steady state methanation from process relevant technologies in terms of energy efficiency, capital costs and total annual costs. The best process route considering all three objectives includes a cascade of catalytic methanation reactors and gas drying. Especially, the question whether the CH_4/CO_2 mixture should be supplied to the reactor directly or prior separation of CH_4 and CO_2 is beneficial to increase the methane yield in the subsequent methanation unit was addressed: The analysis demonstrated that it is beneficial to supply the mixture to the methanation reactor. This reduces the process costs and increases process efficiency at steady state. We note however that a process, which includes pressure swing adsorption for gas separation prior to the methanation was close to the optimal solution (48.3% process efficiency instead of 50.0% using alkaline electrolyzer in both cases). This process with gas pre-treatment motivates further studies of dynamic process operation to reduce storage of the carbon source.

The proposed superstructure model includes not only the process relevant technologies, but also a detailed heat integration network for indirect heat recovery, which was identified as the key element in the trade-off between process efficiency and cost. The power-to-methane process offers significant heat integration potential because the exothermic methanation reaction occurs at elevated temperature (~580 K). To increase the process efficiency the excess heat can be used internally, in particular in combination with

high temperature electrolysis (SOEC), which requires pre-heating of the steam to a temperature of over 1000 K. The methanation excess heat can be used for the first part of the pre-heating, up to reactor temperature. This increased the process efficiency by up to 7%. Because it is in an early state of development, SOEC is still expensive today. The electrolyzer was by far the largest contribution to the process costs. However, in terms of efficiency, using the SOEC was shown to be significantly better (65.1%) than the established alkaline electrolyzer (AE) (50.0%) on plant level.

A comparison of catalytic and biological methanation showed that at the current state of technologies catalytic methanation is the preferred option, both with respect to efficiency and costs. We attribute this to the presently limited technology readiness of biological methanation, which is still in the research phase. As a result, the technology is expensive and the reported conversion rates of different methanogens in the literature varied significantly. If a high conversion rate from carbon dioxide to methane can be reached in the biological reactor ($\geqslant$ 95 mol.-% CH_4 in the dried product gas), the investment costs of the process are only slightly larger than the investment costs for a process with catalytic methanation. However, for lower conversion rates additional gas separation technologies are necessary prior to feed to the gas distribution system, which significantly increases the process costs. The decrease of the process efficiency is primarily attributed to the limited heat integration potential. This becomes especially obvious in the case of using SOEC for water electrolysis. In this case, the efficiency is reduced from 65% (catalytic methanation) to 56.1% (biological methanation).

As demonstrated in this thesis, the heat integration potential makes catalytic methanation favorable over biological methanation for the power-to-methane process.

We compared methane with methanol as an energy carrier in a power to chemical to power scenario, showing that methane is more efficient (23.4%) than methanol (15.8%) in terms of exergy efficiency when using technologies which are commercially available today.

8.2 CONTRIBUTIONS TO OPTIMIZATION OF CYCLIC ADSORPTION PROCESSES

A trust-region filter (TRF) method for the optimization of pressure swing adsorption (PSA) processes was implemented, which uses local surrogates for the optimization of high-fidelity models. The 4-column, 9-step PSA process was modeled via a system of partial differential algebraic equations, and included internal recycle streams. By using a reduced model based on equilibrium theory, the trust-region step of the method, i.e., finding the optimal solution of the reduced model within the trust region, was speed

up by three orders of magnitude compared to a prior study using the same TRF method for PSA optimization. We could successfully optimize the high-fidelity PSA model under different approaches of the TRF method for this particular example. Despite the restricted ability of the reduced model to approximate the states of the truth model in the adsorption column, the approximation of the product gas composition was sufficient for convergence in 55 to 209 iterations. We compared different variations of the TRF method and found that calculating the trust-region radius in terms of the degrees of freedom instead of all variables reduced the number of iterations needed from 72 to 55 iterations.

8.3 CONTRIBUTIONS TO HIGH-FIDELITY PROCESS SYNTHESIS

Furthermore, in this thesis the theoretical foundation for high-fidelity process synthesis using multiple modeling levels in a branch-and-bound framework was developed. Criteria for application of the method to optimization of process efficiency, or alternatively for capital costs are discussed. The method guarantees convergence to global optimality. However, one can expect the local convergence of the nonlinear parts of the superstructure to be more computationally efficient. In this case the optimal process configuration is certainly considered during the solving process. Storing intermediate integer solution candidates is therefore beneficial to compare possible optimal solution candidates. The models as proposed in this work are well suited for the application of this method to different process optimization tasks.

8.4 FUTURE WORK

Jeanmonod et al. [166] recently reported that the use of SOEC for co-electrolysis shows promising results for power-to-methane processes. This technology is still far from industrial application, yet process efficiency and costs could be compared with the current results once the technology reaches a higher technology readiness level.

The next step in optimizing power-to-methane processes is the dynamic operation. Studies focusing on the dynamic operation of the methanation reactor [38, 167] exist in the literature. Dynamic operation of water electrolysis can be implemented via polymer electrolyte membrane (PEM). Combination of the dynamic gas separation model with dynamic methanation and PEM electrolyzer could give first insights to the optimization potential of dynamic energy storage. This thesis as a whole proposes a first step towards dynamic optimization of the complete methanation process. The TRF framework can efficiently handle problematic unit level models, as we have shown

for the pressure swing adsorption unit. It can therefore be applied to the methanation route as a whole to find the optimal solution.

The optimization of cyclic adsorption processes still requires the calculation of the cyclic steady state (CSS) in each iteration, which is computationally expensive and numerically challenging. In this work, the calculation of the CSS was the most time consuming step, which caused numerical errors in the function evaluation. Further research is recommended to improve the calculation of the CSS.

In summary, one can state that the tools and methods as applied in this thesis are suitable for more detailed optimization of dynamic processes via the proposed superstructure branch-and-bound (SBnB) method. A challenge remains to make the SBnB method itself more practically applicable before it can be used for a plant level optimization.

A

APPENDIX: CO_2 METHANATION PROCESS SYNTHESIS BY SUPERSTRUCTURE OPTIMIZATION

Here, GDS relates to the gas distribution system.

Table 20: Optimal result of individual units for $w_\eta = 1$, $w_C = 10^{-8}$, AE, 2% H_2

Layer	Unit		Compressor		Heat Exchanger	
		CAPEX [$]	W_u [kW]	CAPEX [$]	$\lvert Q_u \rvert$ [kW]	CAPEX [$]
	AE	1,025,000	0	0	0	0
2	Mixer	37,000	27.1	292,120	67.3	280,374
3	Reactor	10,180	0	0	44.8	74,279
4	Flash	1,361	0	0	57.6	180,952
6	Reactor	10,180	0	0	94.6	236,298
7	TSA	720,156	0	0	38.3	201,805
8	GDS	-	6.1	94,609	6.1	33,389
	Utilities				151.9	76,045
$\sum$		1,803,877	33.2	386,729	460.6	1,083,142

Table 21: Optimal result of individual units for $w_\eta = 1$, $w_C = 10^{-5}$, AE, 2% H_2

Layer	Unit		Compressor		Heat Exchanger	
		CAPEX [$]	W_u [kW]	CAPEX [$]	$\lvert Q_u \rvert$ [kW]	CAPEX [$]
	AE	1,025,000	0	0	0	0
2	Mixer	37,000	26.2	210,049	64.7	204,579
3	Reactor	10,180	0	0	91.1	13,064
4	Flash	1,361	0	0	75.5	162,363
6	Reactor	10,180	0	0	37.3	84,345
7	TSA	518,838	0	0	28.2	127,617
8	GDS		5.6	54,658	5.6	15,157
	Utilities				151.2	63,429
$\sum$		1,602,559	31.8	264,707	460.6	670,554

Table 22: Optimal result of individual units for TAC, AE, 2% H_2

Layer	Unit		Compressor		Heat Exchanger	
		CAPEX [$]	W_u [kW]	CAPEX [$]	$\|Q_u\|$ [kW]	CAPEX [$]
	AE	1,025,000	0	0	0	0
2	Mixer	37,000	26.2	210,144	58.0	195,574
3	Reactor	10,180	0	0	101.9	64,954
4	Flash	1,361	0	0	55.2	110,351
6	Reactor	10,180	0	0	27.2	56,133
7	TSA	518,947	0	0	19.3	102,732
8	GDS	-	5.6	54,667	5.6	15,159
	Utilities				267.1	62,208
$\sum$		1,602,668	31.8	264,811	534.3	607,111

Table 23: Optimal result of individual units for $w_\eta = 1$, $w_C = 10^{-8}$, AE, 10% H_2

Layer	Unit		Compressor		Heat Exchanger	
		CAPEX [$]	W_u [kW]	CAPEX [$]	$\|Q_u\|$ [kW]	CAPEX [$]
	AE	1,025,000	0	0	0	0
2	Mixer	37,000	27.6	219,238	68.6	241,151
3	Reactor	10,180	0	0	107.4	74,495
4	TSA	885,728	0	0	46.5	179,570
	GDS		6.4	60,530	6.4	16,520
	Utilities				124.1	45,150
$\sum$		1,957,908	34.0	279,768	343.0	573,406

Table 24: Optimal result of individual units for $w_\eta = 1$, $w_C = 10^{-5}$, AE, 10% H_2

Layer	Unit		Compressor		Heat Exchanger	
		CAPEX [$]	W_u [kW]	CAPEX [$]	$\lvert Q_u \rvert$ [kW]	CAPEX [$]
	AE	1,025,000	0	0	0	0
2	Mixer	37,000	26.2	210,049	64.7	204,579
3	Reactor	10,180	0	0	91.1	13,064
4	Flash	1,361	0	0	75.5	162,363
6	Reactor	10,180	0	0	37.3	84,345
7	TSA	518,838	0	0	28.2	127,617
8	GDS		5.6	54,658	5.6	15,157
	Utilities				302.4	63,429
$\sum$		1,602,559	31.8	264,707	460.6	670,554

Table 25: Optimal result of individual units for TAC, AE, 10% H_2

Layer	Unit		Compressor		Heat Exchanger	
		CAPEX [$]	W_u [kW]	CAPEX [$]	$\lvert Q_u \rvert$ [kW]	CAPEX [$]
	AE	1,025,000	0	0	0	0
2	Mixer	37,000	26.2	210182	58.0	202057
3	Reactor	10,180	0	0	101.9	66628
4	Flash	1,362	0	0	55.2	110381
6	Reactor	10,180	0	0	27.2	57852
7	TSA	519138	0	0	17.4	96774
8	GDS	-	5.6	54684	5.6	15163
	Utilities				265.2	62,025
$\sum$		1,602,860	31.8	264,866	530.5	610,880

Table 26: Optimal result of individual units for $w_\eta = 1$, $w_C = 10^{-8}$, SOEC, 2% H_2

Layer	Unit		Compressor		Heat Exchanger	
		CAPEX [$]	W_u [kW]	CAPEX [$]	$\lvert Q_u \rvert$ [kW]	CAPEX [$]
	SOEC	2,540,000	0	0	359.7	349,945
2	Mixer	37,000	28.6	214,783	120.5	584,456
3	Reactor	10,180	31.0	242,194	152.3	293,438
4	Flash	1,439	0	0	59.1	113,670
6	Reactor	10,180	0	0	62.3	93,302
7	TSA	855,665	0	0	24.9	129,071
8	GDS		8.2	73,567	8.2	19,477
	Utilities				355.7	76,787
$\sum$		3,454,464	67.8	530,544	1142.7	1,660,146

Table 27: Optimal result of individual units for $w_\eta = 1$, $w_C = 10^{-5}$, SOEC, 2% H_2

Layer	Unit		Compressor		Heat Exchanger	
		CAPEX [$]	W_u [kW]	CAPEX [$]	$\lvert Q_u \rvert$ [kW]	CAPEX [$]
	SOEC	2,540,000	0	0	359.7	363,523
2	Mixer	37,000	0	0	92.0	152,401
3	Reactor	10,180	38.8	280,861	179.7	441,194
4	Flash	1,608	0	0	68.8	121,486
6	Reactor	10,180	0	0	43.1	104,622
7	TSA	848,218	0	0	24.9	124,911
8	GDS		8.9	78,282	8.9	20,525
	Utilities				294.1	68,606
$\sum$		3,447,186	47.7	359,143	1071.2	1,397,268

Table 28: Optimal result of individual units for TAC, SOEC, 2% H_2

Layer	Unit		Compressor		Heat Exchanger	
		CAPEX [$]	W_u [kW]	CAPEX [$]	$\|Q_u\|$ [kW]	CAPEX [$]
	SOEC	2,540,000	0	0	359.7	720,291
2	Mixer	37,000	38.6	279,931	118.1	812,503
3	Reactor	10,180	0	0	209.9	392,543
4	Flash	1,777	0	0	76.9	128,351
6	Reactor	10,180	0	0	32.2	301,631
7	TSA	782,156	0	0	23.9	179,413
8	GDS	-	8.7	77,300	8.7	20,333
	Utilities				331.3	72,305
$\sum$		3,381,293	47.3	357,231	1160.7	2,627,370

Table 29: Optimal result of individual units for $w_\eta = 1$, $w_C = 10^{-8}$, SOEC, 10% H_2

Layer	Unit		Compressor		Heat Exchanger	
		CAPEX [$]	W_u [kW]	CAPEX [$]	$\|Q_u\|$ [kW]	CAPEX [$]
	SOEC	2,540,000	0	0	359.7	382,366
2	Mixer	37,000	38.5	279,365	92.0	188,734
3	Reactor	10,180	0	0	210.6	294,776
4	TSA	1,234,257	0	0	30.6	142,690
8	GDS		8.8	77,858	8.8	20,431
	Utilities				231.1	68,400
$\sum$		3,821,437	47.3	357,223	932.8	1,097,397

Table 30: Optimal result of individual units for $w_\eta = 1$, $w_C = 10^{-5}$, SOEC, 10% H_2

Layer	Unit		Compressor		Heat Exchanger	
		CAPEX [$]	W_u [kW]	CAPEX [$]	$\|Q_u\|$ [kW]	CAPEX [$]
	SOEC	2,540,000	0	0	359.7	349,945
2	Mixer	37,000	0	0	92.9	146,897
3	Reactor	10,180	38.4	278,817	195.1	287,675
4	Flash	1,536	0	0	64.7	118,252
6	Reactor	10,180	0	0	27.2	61,240
7	TSA	857,523	0	0	25.0	125,210
8	GDS		8.7	76,792	8.7	20,195
	Utilities				294.7	68,601
$\sum$		3,456,419	47.1	355,609	1068.0	1,178,015

Table 31: Optimal result of individual units for TAC, SOEC, 10% H_2

Layer	Unit		Compressor		Heat Exchanger	
		CAPEX [$]	W_u [kW]	CAPEX [$]	$\|Q_u\|$ [kW]	CAPEX [$]
	SOEC	2,540,000	0	0	359.7	354,176
2	Mixer	37,000	0	0	92.0	101,808
3	Reactor	10,180	38.7	280,352	210.8	440,609
4	TSA	1,243,326	0	0	30.7	143,155
8	GDS	-	8.9	78,592	8.9	20,594
	Utilities				329.8	81,335
$\sum$		3,830,606	47.6	358,944	1031.9	1,284,832

Table 32: Optimal result of individual units for $w_\eta = 1$, $w_C = 10^{-8}$, AE, 10% H_2, 96% Bioreactor

Layer	Unit		Compressor		Heat Exchanger	
		CAPEX [$]	W_u [kW]	CAPEX [$]	$\lvert Q_u \rvert$ [kW]	CAPEX [$]
	AE	1,025,000	0	0	0	0
1	Membrane	503,725	10.8	90,723	14.3	79,456
2	Mixer	37,000	4.2	46,494	4.2	13,940
3	Bioreactor	723,800	0	0	4.9	47,142
4	TSA	595,437	15.9	122,562	27.6	112,177
8	GDS	-	5.7	65,759	2.2	8,395
	Utilities				53.3	45,930
$\sum$		2,884,962	41.7	325,538	118.8	307,040

Table 33: Optimal result of individual units for $w_\eta = 1$, $w_C = 10^{-8}$, AE, 10% H_2, 65% Bioreactor

Layer	Unit		Compressor		Heat Exchanger	
		CAPEX [$]	W_u [kW]	CAPEX [$]	$\lvert Q_u \rvert$ [kW]	CAPEX [$]
	AE	1,025,000	0	0	0	0
1	Membrane	484,236	11.9	98,334	15.3	35,898
2	Mixer	74,000	5.3	61,076	5.3	27,267
3	Bioreactor	723,800	0.4	44,297	5.3	51,081
4	TSA	632,128	16.9	128,337	29.2	114,681
5	Membrane	202,343	0	0	0	0
8	GDS	-	7.2	78,587	3.8	11,922
	Utilities				59.9	46,160
$\sum$		3,141,507	41.7	410,631	118.8	287,009

Table 34: Optimal result of individual units for $w_\eta = 1$, $w_C = 10^{-8}$, SOEC, 10% H_2, 96% Bioreactor

Layer	Unit		Compressor		Heat Exchanger	
		CAPEX [$]	W_u [kW]	CAPEX [$]	$\lvert Q_u \rvert$ [kW]	CAPEX [$]
	SOEC	2,540,000	0	0	359.7	199,552
1	Membrane	676,861	14.4	113,896	19.2	41,863
2	Mixer	37,000	5.7	55,511	97.7	245,016
3	Bioreactor	493,500	0.3	43,476	5.3	37,625
4	TSA	800,095	21.3	153,869	36.2	94,664
8	GDS	-	7.8	82,556	3.0	10,171
	Utilities				241.5	83,769
$\sum$		4,547,456	49.5	449,308	762.6	712,660

Table 35: Optimal result of individual units for $w_\eta = 1$, $w_C = 10^{-8}$, SOEC, 10% H_2, 65% Bioreactor

Layer	Unit		Compressor		Heat Exchanger	
		CAPEX [$]	W_u [kW]	CAPEX [$]	$\lvert Q_u \rvert$ [kW]	CAPEX [$]
	SOEC	2,540,000	0	0	359.7	246,341
1	Membrane	679,738	14.5	114,270	19.3	41,979
2	Mixer	37,000	8.7	89,828	96.3	178,746
3	Bioreactor	493,500	0.6	46,318	3.0	26,970
4	TSA	887,339	23.7	166,633	39.9	97,837
5	Membrane	284,036	0	0	0	0
8	GDS	-	11.3	109,930	3.0	10,121
	Utilities				235.9	83,854
$\sum$		4,921,613	58.8	526,979	757.1	685,848

B

APPENDIX: CONSTRAINT QUALIFICATIONS OF PROCESS SYNTHESIS MINLP

In this appendix we describe an alternative formulation of the superstructure optimization problem of Chapter 5, which fulfills the LICQ. Let us write the superstructure optimization problem from Chapter 5 as follows: We describe the variables of the optimization problem as before: We have $\mathcal{V}$ as the set of all unit models in the superstructure, including the check of the product quality constraints. The indicator variables are still denoted by $x_T \in \{0,1\}^{n_\mathcal{V}}$. We lump the variables corresponding a unit model together as $x_\mathcal{V} = [x_U]_{U\in\mathcal{V}}$. The material streams entering and leaving the unit models are summarized by $x_{MS} = [x_U^{in}, x_U^{out}]_{U\in\mathcal{V}}$. The information of energy streams leaving or entering a unit model $U \in \mathcal{V}$, as given by the functions $W_U^{out}(x_U)$, $Q_U^{out}(x_U)$ is stored in variables we denote by $x_{e,U} = \left(w_U, Q_U^I, Q_U^{II}, T_{U,in}^I, T_{U,out}^I, T_U^{II}\right)^\top$. The variables $Q_{U,i}^I$, $Q_{U,i}^{II}$, $\underline{c}_{U,i}$, $\bar{c}_{U,i}$, and $Q_{ext,i}$ for utilities $i \in \{1,\dots,n_E\}$, which model the heat integration are included in x_E. We summarize all variables associated with the energy flows as $x_e = \left([x_{e,U}]_{U\in\mathcal{V}}^\top, x_E\right)^\top$. We add a notation to our constraints, similar as in Chapter 7. The constraints of our superstructure problem include the connections of material streams between the units, i.e., constraints of the form (38), which determine the material stream entering a unit model $U \in \mathcal{V}$. We cluster these material stream constraints as h_{MS}. The constraints, which determine the heat integration are denoted by g_e. The equality $h_\mathcal{V}$ describes the topology, as given by

$$h_{\mathcal{V}_j} := \sum_{U\in\mathcal{V}_j} x_{T,U} - 1 \tag{91}$$

for a layer $\mathcal{V}_j$ in the superstructure. This replaces the SOS type constraints (36), (37). We model the linear and nonlinear unit level models via big M formulation, because the vanishing constraints violate LICQ, see Section 5.1.2. Finally, the energy and material streams of the unit level models are fixed. Thus, we can write the superstructure optimization problem as

$$
\begin{aligned}
\min_{x=(x_T,x_\mathcal{V},x_{MS},x_e)^\top\in\mathbb{R}^n} \quad & f(x_{MS},\, x_e) \\
\text{s.t.} \quad & h_{MS}(x_{MS}) = 0 \\
& g_e(x_e) \leqslant 0 \\
& h_\mathcal{V}(x_T) = 0 \\
& g_u(x_u,\, x_u^{in}) - (1 - x_{T,u})M \leqslant 0, \qquad u \in \mathcal{V} \\
& x_u^{out} - X_u^{out}(x_u) = 0 \qquad u \in \mathcal{V} \\
& x_{e,u} - \left(W_u^{out}(x_u), Q_u^{out}(x_u)\right)^\top = 0 \quad u \in \mathcal{V}.
\end{aligned}
$$

To analyze the degeneracy of the problem, we assume that we have a feasible solution candidate with fixed binary variables. We call V_j the active unit model in the layer V_j, i.e., the node $V_j \in \mathcal{V}_j$ with $x_{T,V_j} = 1$.

Table 36 shows the structure of the derivatives of the constraints with respect to the variables. For the LICQ to hold, the rows of the equality constraints and the active inequalities must be linear independent. Here, I denotes the identity matrix and X denotes matrices with non-zero entries and suitable dimensions. We examine the blocks marked in red closer to show under which conditions LICQ hold.

Table 36: Pattern of the derivative of the optimization constraints

The pattern of the derivative of the optimization constraints with respect to the variables. Here, I denotes identity matrices and X denotes matrices with non-zero entries of suitable dimensions. The problem fulfills LICQ in a feasible point, if the rows of all equality constraints and all active inequality constraints are linear independent.

	x_T	$x_\mathcal{V}$	x^{in}	x^{out}	$[x_{e,u}]_{u\in\mathcal{V}}$	x_E
$h_{MS}(x_{MS})$	X	0	I	X	0	0
$g_e(x_e)$	0	0	0	0	X	X
$h_\mathcal{V}(x_T)$	X	0	0	0	0	0
$g_u(x_u,\, x_u^{in}) - (1 - x_{T,u})M$	$M \cdot I$	X	X	0	0	0
$x_u^{out} - X_u^{out}(x_u)$	0	X	0	I	0	0
$x_{e,u} - \left(W_u^{out}(x_u), Q_u^{out}(x_u)\right)^\top$	0	X	0	0	I	0

The derivatives of $g_e(x_e)$, which corresponds to Eqs. (39)-(46) as defined in Chapter 5, with respect to x_E violate the LICQ for some points. The heat integration must be regularized as stated below to avoid degeneracy:

Eqs. (40), (41), and (46) are not problematic, as the derivatives with respect to $\underline{c}_{U,I}$, $\bar{c}_{U,I}$, and $Q_{ext,i}$ give linear independent rows in form of an identity matrix.

Assuming that Eq. (39) is active for all units and utilities, the derivative of Eq. (39) with respect to the heat flows $Q^{II}_{U,i}$ gives a diagonal matrix of size $(n_E \cdot n_U) \times (n_E \cdot n_U)$, which is of full rank. This special case occurs if all heat of a unit is supplied to a single utility. In this case, Eqs. (44) becomes active as well, whose gradient with respect to $Q^{II}_{U,i}$ must be linear dependent to the gradient of Eq. (39) as by the number alone. The same problem occurs for heat flows of type II if $Q^{II}_U = 0$. We therefore regularize the problem, by adding a slack to the equality constraints (44) and (45)

$$\sum_i Q^I_{U,i} \leqslant Q^I_U + \epsilon, \qquad \sum_i Q^I_{U,i} \geqslant Q^I_U - \epsilon.$$
$$\sum_i Q^{II}_{U,i} \leqslant Q^{II}_U + \epsilon, \qquad \sum_i Q^{II}_{U,i} \geqslant Q^{II}_U - \epsilon.$$

Thus, from Eqs. (39) and (44) a maximum of $(n_E \cdot n_U)$ inequalities become active in any feasible point.

Another problem occurs with the temperature levels of the utilities in Eqs. (42) and (43). The derivative of these functions with respect to $Q^{II}_{U,i}$ becomes zero, if $\hat{T}_i + \Delta T - T^{II}_U = 0$ or $\hat{T}_i - \Delta T - T^{II}_U = 0$ holds. If $Q^{II}_{U,i}$ is also zero in a solution candidate, the matrix in Table 36 has an empty row, which implies degeneracy. We solve this problem, by fixing the temperatures of the utilities to temperatures with sufficient distance to the temperature level of all isothermal unit models, i.e., we make sure that

$$|\hat{T}_i + \Delta T - T^{II}_U| \geqslant \epsilon_T$$
$$|\hat{T}_i - \Delta T - T^{II}_U| \geqslant \epsilon_T$$

holds for a $\epsilon_T > 0$. This implies that for the outer temperature levels

$$\hat{T}_0 = T_{min} - \Delta T - \epsilon_T$$
$$\hat{T}_{n_E} = T_{max} + \Delta T + \epsilon_T$$

holds, where T_{min} and T_{max} denote the minimal and maximal temperatures occurring in the process. The temperature of intermediate units must be kept between temperatures at ambient temperatures and the methanation reactor, with sufficient distance to both directions. Thus $\hat{T}_i + \Delta T - T^{II}_U = 0$ or $\hat{T}_i - \Delta T - T^{II}_U = 0$ never hold. With this changes, the derivative of $g_e(x_e)$ with respect to x_E is linearly independent.

The topology constraints (91) have entries for each node in the corresponding layer, i.e.

$$\frac{\partial h_{\mathcal{V}_j}}{\partial x_{T,U}} = 1 \qquad U \in \mathcal{V}_j.$$

Thus, the matrix $\frac{\partial h_v}{\partial x_T}$ has at least one entry per row and exactly one entry per column, which makes the rows linear independent. In the special case that each layer has a single node, this results in an identity matrix.

Finally, if the derivatives of the unit model constraints

$$\frac{\partial g_u(x_u,\ x_u^{in}) - (1 - x_{T,u})M}{\partial (x_u,\ x_u^{in})} = \nabla g_u(x_u,\ x_u^{in})$$

are linear independent, the LICQ hold for the superstructure optimization problem. However, optimization of the superstructure in the case AE (G1) (O2) was not successful with the given memory limitations. The result had a gap between upper and lower bound of around 27 %. This is most likely caused by the ill-conditioned big M formulation for the unit model constraints.

Notation

C	mol/cm^3	concentration
C_p	J/K	heat capacity
c_p	$J/molK$	specific heat capacity
e	kJ/mol	exergy
$e_{chemical}$	kJ/mol	specific chemical exergy
e_{heat}	kJ/mol	specific thermal exergy of a heat flow
$e_{physical}$	kJ/mol	specific physical exergy
F	kW	exergy
$\mathcal{F}_{k,l}$		filter set
f		objective function
g		inequality constraints
h		equality constraints
m_{GC}	-	number of FVM grid cells
m_g	-	number of inequality constraints
m_h	-	number of equality constraints
N	mol/s	molar gas flow rate
n	-	number of variables
K_{eq}		equilibrium constant
LB		lower bound of branch-and-bound
lb		lower bound on variables
p	Pa	pressure
p_{amb}	Pa	ambient pressure
p_i	Pa	component i partial pressure
p_{vp}	Pa	pure component vapor pressure
Q, q	kW	heat flow
R	$cm^3Pa/molK$	gas constant
s		slack variables
T	K	temperature
T_{amb}	K	ambient temperature
t	s	time
t_f	s	final time
UB		upper bound of branch-and-bound

Notation

ub		upper bound on variables	
W, w	kW	work	
y_i	-	component i gas phase mole fraction	
γ	-	opt. algorithm meta parameter	
ΔT	K	temperature difference	
η		efficiency	
Ω		feasible set	
ρ	g/cm^3	density	
τ	-	barrier parameter	
θ	-	infeasibility measure	

Subscripts

ref	reference value
amb	at ambient conditions

Catalytic Methanation Reactor

$E_A, \Delta H_i^r$	kJ/mol	LHHW rate parameter	[39]
$K_{0,i}$	$1/bar$	LHHW rate parameter	[39]
k_0	$mol/bar\ s\ g$	LHHW rate parameter	[39]
r	$mol/s\ g$	reaction rate	

Pressure Swing Adsorption (PSA)

A, E_a	-	QHR isotherm parameter	[106]
a_{i1}, a_{i2}	-	Langmuir isotherm parameter	[53]
a	cm^2	cross sectional area	
b_{i0}, b_{i1}	-	Langmuir isotherm parameter	[53]
c_j	-	QHR isotherm parameter	[106]
c	$cal/mol\ K$	heat capacity	[53, 139]
h, U	$cal/cm^2\ s\ K$	heat transfer coefficients	[53, 139]
k_i	$1/s$	component i mass transfer coefficient	[53, 139]
n_t	mol/g	total amount adsorbed	
q_i	mol/g	component i amount adsorbed	
q_i^*	mol/g	component i adsorption capacity	
R_i, R_o	cm	inner and outer bed diameter	[53]
V_0	cm^3/g	QHR isotherm parameter	[106]
v	cm/s	interstitial velocity	
Z	cm	length of the adsorption bed	
z	cm	axial coordinate in the adsorption bed	
α	$1/s$	rate of pressure drop or rise	
ΔH_i	cal/mol	component i heat of adsorption	[53, 139]

Pressure Swing Adsorption (PSA)			
ϵ	-	bed void fraction	[53, 139]
Π_i	Pa	component i spreading pressure	

Pressure Swing Adsorption (PSA) Subscripts	
c	cooling medium
F	feed
g	gas phase
s	adsorbent
w	wall

Superstructure			
C	\$	cost	
CE		CE index, Guthrie parameter	
D	m	diameter	
d		number of material streams	
$\mathcal{E}$		edges of the superstructure graph	
L	m	length	
M		big M parameter	
MF		material factor, Guthrie parameter	
m_{MS}		dimension of material streams	
n_E		# utilities	
n_U		# variables in unit model U	
$n_{\mathcal{V}}$		# unit models in the superstructure	
r		recycle rate	
S	kW	Guthrie parameter	
s		separation fraction	
$\hat{T}$	K	utility temperature	
V	m^3	volume	
$\mathcal{V}$		nodes of the superstructure graph	
x_T		indicator variable	
α, β		Guthrie parameters	
ζ		extent of reaction	

Superstructure Subscripts	
ext	external heat demand/surplus
MS	material stream

Superstructure Superscripts	
in	ingoing stream
l	liquid phase
out	outgoing stream

Acronyms

AC	Activated carbon
AD	Anaerobic digestion
AE	Alkaline electrolyzer
ASC	Amine scrubbing
CCPP	Combined-cycle power plant
CQ	Constraint qualification
DAE	Differential algebraic equation
EU	European Union
FVM	Finite Volume method
GDS	Gas Distribution System
IVP	Initial value problem
KKT	Karush-Kuhn Tucker
LHV	Lower heating value
LICQ	Linear independence constraint qualification
MEM	Membrane separation
MFCQ	Mangasarian-Fromovitz constraint qualification
MILP	Mixed integer linear program
MINLP	Mixed integer nonlinear program
MS	Material stream
NLP	Nonlinear programm
ODE	Ordinary differential equation
PDE	Partial differential equation
PSA	Pressure swing adsorption
PtM	Power-to-methane
RES	Renewable energy sources
SOEC	Solid oxide electrolyzer cell
SQP	Sequential quadratic programming
TRF	Trust-region filter
TSA	Temperature swing adsorption
WSC	Water scrubbing
Z5A	Zeolite 5A

BIBLIOGRAPHY

[1] J. Uebbing, L. Rihko-Struckmann, and K. Sundmacher, "Exergetic assessment of CO2 methanation processes for the chemical storage of renewable energies," *Appl. Energy*, vol. 233-234, pp. 271–282, 2019.

[2] J. Uebbing, L. Rihko-Struckmann, S. Sager, and K. Sundmacher, "CO2 methanation process synthesis by superstructure optimization," *Journal of CO2 Utilization*, vol. 40, p. 101228, 2020.

[3] S. Koohi-Fayegh and M. Rosen, "A review of energy storage types, applications and recent developments," *Journal of Energy Storage*, vol. 27, p. 101047, 2020.

[4] C. Andrey, P. Barberi, L. Lacombe, L. van Nuffel, F. Gérard, J. G. Dedecca, K. Rademaekers, Y. E. Idrissi, and M. Crenes, "Study on energy storage – Contribution to the security of the electricity supply in Europe," Tech. Rep. March, European Commission, Brussels, 2020.

[5] T. M. Gür, "Energy & Environmental Science materials and systems: challenges and prospects for large-scale grid storage," *Energy and Environmental Science*, vol. 11, pp. 2696–2767, 2018.

[6] M. Mahmoud, M. Ramadan, A.-G. Olabi, K. Pullen, and S. Naher, "A review of mechanical energy storage systems combined with wind and solar applications," *Energy Conversion and Management*, vol. 210, p. 112670, 2020.

[7] M. S. Javed, "Solar and wind power generation systems with pumped hydro storage: Review and future perspectives," *Renewable energy*, vol. 148, pp. 176–192, 2020.

[8] E. Guelpa, "Towards future infrastructures for sustainable multi-energy systems: A review," *Energy (Oxford)*, vol. 184, pp. 2–21, 2019.

[9] W. Ji, H. Zhang, F. Ding, J. Wang, R. Zhang, and S. Guo, "A review of energy storage and its utilization in Integrated Energy Systems," *IOP Conference Series: Earth and Environmental Science*, vol. 512, p. 012016, 2020.

[10] S. Coss, "Waste-heat integration in smart thermal networks - a dynamic thermoeconomic approach," *Energy Procedia*, vol. 158, pp. 6419–6424, 2019.

[11] P. Huang, "A review of data centers as prosumers in district energy systems: Renewable energy integration and waste heat reuse for district heating," *Applied energy*, vol. 258, 2020.

[12] A. Bloess, W.-p. Schill, and A. Zerrahn, "Power-to-heat for renewable energy integration: A review of technologies, modeling approaches, and flexibility potentials," *Applied Energy*, vol. 212, pp. 1611–1626, 2018.

[13] A. Gautam, "A review on sensible heat based packed bed solar thermal energy storage system for low temperature applications," *Solar energy*, vol. 207, pp. 937–956, 2020.

[14] C. A. Schoeneberger, "Solar for industrial process heat: A review of technologies, analysis approaches, and potential applications in the united states," *Energy (Oxford)*, vol. 206, 2020.

[15] D. Tschopp, "Large-scale solar thermal systems in leading countries: A review and comparative study of denmark, china, germany and austria," *Applied energy*, vol. 270, 2020.

[16] Y. Lin, "Review on thermal performances and applications of thermal energy storage systems with inorganic phase change materials," *Energy (Oxford)*, vol. 165, pp. 685–708, 2018.

[17] D. V. Voronin, E. Ivanov, P. Gushchin, R. Fakhrullin, and V. Vinokurov, "Clay composites for thermal energy storage: A review," *Molecules*, vol. 25, p. 1504, 2020.

[18] D. Kumar, R. K. Nema, and S. Gupta, "A comparative review on power conversion topologies and energy storage system for electric vehicles," *International Journal of Energy Research*, vol. 44, pp. 7863–7885, 2020.

[19] J. Bierman and B. Bekker, "Review of control strategies for lithium-ion battery energy storage systems in distribution networks," in *2020 International SAUPEC/RobMech/PRASA Conference*, pp. 1–6, 2020.

[20] M. Sterner, "Notwendigkeit und Chancen für Power-to-X-Technologien - Energiewirtschaftliches Kurzgutachten," tech. rep., Ostbayerische Technischen Hochschule Regensburg, Regensburg, 2017.

[21] J. Gorre, F. Ortloff, and C. Van Leeuwen, "Production costs for synthetic methane in 2030 and 2050 of an optimized Power-to-Gas plant with intermediate hydrogen storage," *Applied Energy*, vol. 253, no. June, p. 113594, 2019.

[22] T. Kroher, "Elektroautos brauchen die Energiewende: Die Klimabilanz." https://www.adac.de/verkehr/tanken-kraftstoff-antrieb/alternative-antriebe/klimabilanz/. Accessed: 30. November 2020.

[23] A. Ajanovic and R. Haas, "Technological, ecological and economic perspectives for alternative automotive technologies up to 2050," *IEEE ICSET*, pp. 129–134, 2012.

[24] S. Schiebahn, T. Grube, M. Robinius, V. Tietze, B. Kumar, and D. Stolten, "Power to gas: Technological overview, systems analysis and economic assessment for a case study in Germany," *International Journal of Hydrogen Energy*, vol. 40, no. 12, pp. 4285–4294, 2015.

[25] M. Lehner, *Power-to-Gas: Technology and Business Models*. Cham: Springer International Publishing, 2014.

[26] H. Blanco and A. Faaij, "A review at the role of storage in energy systems with a focus on Power to Gas and long-term storage," *Renew. Sustain. Energy Rev.*, vol. 81, no. May 2017, pp. 1049–1086, 2018.

[27] M. Sterner, "Chemische Energiespeicher," in *Energiespeicher - Bedarf, Technologien, Integration*, ch. 8, pp. 295–453, Berlin, Heidelberg: Springer Berlin Heidelberg, 2014.

[28] M. Child, C. Kemfert, D. Bogdanov, and C. Breyer, "Flexible electricity generation, grid exchange and storage for the transition to a 100% renewable energy system in Europe," *Renewable Energy*, vol. 139, pp. 80–101, 2019.

[29] G. Leonzio, "Design and feasibility analysis of a Power-to-Gas plant in Germany," *Journal of Cleaner Production*, vol. 162, pp. 609–623, 2017.

[30] C. Wulf, J. Linßen, and P. Zapp, "Review of Power-to-Gas Projects in Europe," *Energy Procedia*, vol. 155, pp. 367–378, 2018.

[31] M. Götz, J. Lefebvre, F. Mörs, A. McDaniel Koch, F. Graf, S. Bajohr, R. Reimert, and T. Kolb, "Renewable Power-to-Gas: A technological and economic review," *Renew. Energy*, vol. 85, pp. 1371–1390, 2016.

[32] M. Bailera, P. Lisbona, L. M. Romeo, and S. Espatolero, "Power to Gas projects review: Lab, pilot and demo plants for storing renewable energy and CO2," 2017.

[33] S. Rönsch, J. Schneider, S. Matthischke, M. Schlüter, M. Götz, J. Lefebvre, P. Prabhakaran, and S. Bajohr, "Review on methanation - From fundamentals to current projects," *Fuel*, vol. 166, pp. 276–296, 2016.

[34] G. Gahleitner, "Hydrogen from renewable electricity: An international review of power-to-gas pilot plants for stationary applications," *International Journal of Hydrogen Energy*, vol. 38, no. 5, pp. 2039–2061, 2013.

[35] A. Maroufmashat and M. Fowler, "Transition of future energy system infrastructure; through Power-to-Gas pathways," *Energies*, vol. 10, no. 1089, 2017.

[36] J. de Bucy, "The potential of Power-to-Gas - Technology review and economic potential assessment," tech. rep., enea Consulting Paris, Paris, 2016.

[37] J. Bremer, P. Goyal, L. Feng, P. Benner, and K. Sundmacher, "POD-DEIM for efficient reduction of a dynamic 2D catalytic reactor model," *Comput. Chem. Eng.*, vol. 106, pp. 777–784, 2017.

[38] R. T. Zimmermann, J. Bremer, and K. Sundmacher, "Optimal catalyst particle design for flexible fixed-bed CO2 methanation reactors," *Chemical Engineering Journal*, vol. 387, no. October 2019, p. 123704, 2020.

[39] F. Koschany, D. Schlereth, and O. Hinrichsen, "On the kinetics of the methanation of carbon dioxide on coprecipitated NiAl(O)x," *Applied Catalysis B: Environmental*, vol. 181, pp. 504–516, 2016.

[40] A. Bensmann, R. Hanke-Rauschenbach, R. Heyer, F. Kohrs, D. Benndorf, U. Reichl, and K. Sundmacher, "Biological methanation of hydrogen within biogas plants: A model-based feasibility study," *Appl. Energy*, vol. 134, pp. 413–425, 2014.

[41] F. Graf, A. Krajete, and U. Schmack, "Abschlussbericht Techno-ökonomische Studie zur biologischen Methanisierung bei Power-to-Gas-Konzepten," *Deutscher Verein des Gas- und Wasserfaches e.V*, 2014.

[42] A. H. Seifert, S. Rittmann, and C. Herwig, "Analysis of process related factors to increase volumetric productivity and quality of biomethane with Methanothermobacter marburgensis," *Appl. Energy*, vol. 132, pp. 155–162, 2014.

[43] M. A. Voelklein, D. Rusmanis, and J. D. Murphy, "Biological methanation: Strategies for in-situ and ex-situ upgrading in anaerobic digestion," *Appl. Energy*, vol. 235, no. August 2018, pp. 1061–1071, 2019.

[44] H. A. E. S. Jee, N. Nishio, and S. Nagai, "Continuous CH_4 production from H_2 and CO_2 by methanobacterium thermoautotrophicum in a fixed-bed reactor," *J. Ferment. Technol.*, vol. 66, no. 2, pp. 235–238, 1988.

[45] M. P. Hoffarth, T. Broeker, and J. Schneider, "Effect of N_2 on biological methanation in a continuous stirred-tank reactor with methanothermobacter marburgensis," *Fermentation*, vol. 5, no. 3, 2019.

[46] J.-P. Peillex, M.-L. Fardeau, and J.-P. Belaich, "Growth of methanobacterium thermoautotrophicum on H_2CO_2 High CH_4 productivities in continuous culture," *Biomass*, vol. 21, pp. 315–321, 1990.

[47] A. Sternberg and A. Bardow, "Power-to-What? – Environmental assessment of energy storage systems," *Energy and Environmental Science*, vol. 8, no. 389, pp. 389–400, 2015.

[48] B. Castellani, S. Rinaldi, E. Morini, B. Nastasi, and F. Rossi, "Flue gas treatment by power-to-gas integration for methane and ammonia synthesis – Energy and environmental analysis," *Energy Convers. Manag.*, vol. 171, no. June, pp. 626–634, 2018.

[49] K. Ghaib, "Power-to-Methane: A state-of-the-art review," vol. 81, pp. 433–446, 2018.

[50] J. Witte, A. Calbry-Muzyka, T. Wieseler, P. Hottinger, S. M. Biollaz, and T. J. Schildhauer, "Demonstrating direct methanation of real biogas in a fluidised bed reactor," *Appl. Energy*, vol. 240, no. September 2018, pp. 359–371, 2019.

[51] F. Mohseni, M. Magnusson, M. Görling, and P. Alvfors, "Biogas from renewable electricity - Increasing a climate neutral fuel supply," *Appl. Energy*, vol. 90, no. 1, pp. 11–16, 2012.

[52] I. Ullah Khan, M. Hafiz Dzarfan Othman, H. Hashim, T. Matsuura, A. F. Ismail, M. Rezaei-DashtArzhandi, and I. Wan Azelee, "Biogas as a renewable energy fuel – A review of biogas upgrading, utilisation and storage," *Energy Convers. Manag.*, vol. 150, pp. 277–294, 2017.

[53] J. H. Park, J. N. Kim, and S. H. Cho, "Performance analysis of four-bed H_2 PSA process using layered beds," *AIChE J.*, vol. 46, no. 4, pp. 790–802, 2000.

[54] M. Carmo, D. L. Fritz, J. Mergel, and D. Stolten, "A comprehensive review on PEM water electrolysis," *International Journal of Hydrogen Energy*, vol. 38, pp. 4901–4934, 2013.

[55] M. Schalenbach, G. Tjarks, M. Carmo, W. Lueke, M. Mueller, and D. Stolten, "Acidic or alkaline? Towards a new perspective on the efficiency of water electrolysis," *Journal of The Electrochemical Society*, vol. 163, no. 11, pp. F3197–F3208, 2016.

[56] F. Herrmann, M. Gruenewald, and J. Riese, "Flexibility of Power-to-Gas plants: A case study," *Chemie Ingenieur Technik*, vol. 92, no. 12, pp. 1–10, 2020.

[57] E. Giglio, F. A. Deorsola, M. Gruber, S. R. Harth, E. A. Morosanu, D. Trimis, S. Bensaid, and R. Pirone, "Power-to-Gas through High Temperature Electrolysis and Carbon Dioxide Methanation: Reactor Design and Process Modeling," *Industrial and Engineering Chemistry Research*, vol. 57, no. 11, pp. 4007–4018, 2018.

[58] M. Thema, F. Bauer, and M. Sterner, "Power-to-Gas: Electrolysis and methanation status review," *Renew. Sustain. Energy Rev.*, vol. 112, no. January, pp. 775–787, 2019.

[59] P. Adler, E. Billig, A. Brosowski, J. Daniel-Gromke, I. Falke, E. Fischer, J. Grope, U. Holzhammer, J. Postel, J. Schnutenhaus, K. Stecher, G. Szomszed, M. Trommler, and W. Urban, "Leitfaden Biogasaufbereitung und -einspeisung," 2014.

[60] S. de Oliveira, *Exergy production, cost and renewability*. Springer-Verlag London, 2012.

[61] T. Kotas, *The exergy method of thermal plant analysis*. Malabar, Florida 32950: Krieger Publishing Company, 1995.

[62] I. Dincer, A. Midilli, and H. Kucuk, eds., *Progress in exergy, energy, and the environment*. Cham: Springer International Publishing, 2014.

[63] M. Shukuya, *Theory and applications in the built environment*. Springer-Verlag London, 2012.

[64] Perry, D. W. Green, and R. H. Perry, *Perry's chemical engineers' handbook*. New York: McGraw-Hill, 2008.

[65] Y. Haseli, "Chapter eleven - exergy," in *Entropy analysis in thermal engineering systems* (Y. Haseli, ed.), pp. 169 – 183, Academic Press, 2020.

[66] J. Nocedal and S. J. Wright, *Springer series in operations research and financial engineering*. Springer Series in Operations Research and Financial Engineering, 2 ed., 2006.

[67] "The NAG Library." https://www.nag.co.uk/content/nag-library. Accessed: 02. July 2020.

[68] A. Wächter and L. Biegler, "On the implementation of an interior-point filter line-search algorithm for large-scale nonlinear programming," *Math. Program.*, vol. 106, pp. 25–57, 2006.

[69] B. Hartono, P. Heidebrecht, and K. Sundmacher, "Combined branch and bound method and exergy analysis for energy system design," *Industrial and Engineering Chemistry Research*, vol. 51, no. 44, pp. 14428–14437, 2012.

[70] I. E. Grossmann, *Global optimization in engineering design*, vol. 9 of *Nonconvex Optimization and Its Applications*. Boston, MA: Springer US, 1996.

[71] G. R. Kocis and I. E. Grossmann, "Computational experience with DICOPT solving problems in process systems engineering," *Computers and Chemical Engineering*, vol. 13, no. 3, pp. 307–315, 1989.

[72] M. A. Duran and I. E. Grossmann, "An outer-approximation algorithm for a class of mixed-integer nonlinear programs," *Mathematical Programming*, vol. 36, pp. 307–339, 1986.

[73] P. Bonami, L. T. Biegler, A. R. Conn, G. Cornuéjols, I. E. Grossmann, C. D. Laird, J. Lee, A. Lodi, F. Margot, N. Sawaya, and A. Wächter, "An algorithmic framework for convex mixed integer nonlinear programs," *Discrete Optimization*, vol. 5, no. 2, pp. 186–204, 2008.

[74] T. Westerlund and F. Pettersson, "An extended cutting plane method for solving convex minlp problems," *Computers & Chemical Engineering*, vol. 19, pp. 131 – 136, 1995. European Symposium on Computer Aided Process Engineering 3-5.

[75] N. V. Sahinidis and I. E. Grossmann, "Convergence properties of generalized benders decomposition," *Comput. Chem. Eng.*, vol. 15, no. 7, pp. 481–491, 1991.

[76] V. P. Eronen, M. M. Mäkelä, and T. Westerlund, "Extended cutting plane method for a class of nonsmooth nonconvex MINLP problems," *Optimization*, vol. 64, no. 3, pp. 641–661, 2015.

[77] R. Misener and C. A. Floudas, "ANTIGONE: Algorithms for coNTinuous / Integer Global Optimization of Nonlinear Equations," *J Glob Optim*, no. 59, pp. 503–526, 2014.

[78] C. S. Adjiman, I. P. Androulakis, and C. A. Floudas, "A global optimization method, alphaBB, for general twice-differentiable constrained NLPs — II. Implementation and computational results," *Comput. Chem. Eng.*, vol. 22, no. 9, 1998.

[79] P. Belotti., "COUENNE: a user's manual," 2010.

[80] A. Gleixner, M. Bastubbe, L. Eifler, T. Gally, G. Gamrath, R. L. Gottwald, G. Hendel, C. Hojny, T. Koch, M. E. Lübbecke, S. J. Maher, M. Miltenberger, B. Müller, M. E. Pfetsch, C. Puchert, D. Rehfeldt, F. Schlösser, C. Schubert, F. Serrano, Y. Shinano, J. M. Viernickel, M. Walter, F. Wegscheider, J. T. Witt, and J. Witzig, "The SCIP Optimization Suite 6.0," ZIB-Report 18-26, Zuse Institute Berlin, July 2018.

[81] T. Achterberg, "SCIP: Solving constraint integer programs," *Math. Progr. Comput.*, vol. 1, no. 1, pp. 1–41, 2009.

[82] A. G. Stefan Vigerske, "SCIP: Global optimization of mixed-integer nonlinear programs in a branch-and-cut framework," vol. 24, no. May, 2016.

[83] S. Maher, "PYSCIPOPT: Mathematical programming in python with the SCIP optimization suite," *ZIB-Report*, vol. 64, no. December, 2016.

[84] J. Kronqvist, D. E. Bernal, A. Lundell, and I. E. Grossmann, *A review and comparison of solvers for convex MINLP*, vol. 20. Springer US, 2019.

[85] "BARON: the branch-and-reduce optimization navigator." https://minlp.com/baron. Accessed: 21. Juli 2020.

[86] J. E. Falk and K. R. Hoffmann, "A successive underestimation method for concave minimization problems," *Mathematics of Operations Research*, vol. 1, no. 3, pp. 251–260, 1976.

[87] A. C. Hindmarsh, P. N. Brown, K. E. Grant, S. L. Lee, R. Serban, D. E. Shumaker, and C. S. Woodward, "SUNDIALS: Suite of nonlinear and differential/algebraic equation solvers," *ACM Transactions on Mathematical Software (TOMS)*, vol. 31, no. 3, pp. 363–396, 2005.

[88] H. Bock and K. Plitt, "A multiple shooting algorithm for direct solution of optimal control problems," in *Proceedings of the 9th IFAC World Congress*, (Budapest), pp. 242–247, Pergamon Press, 1984.

[89] J. D. Logan, *Applied partial differential euations*. Cham: Springer International Publishing, 3rd ed. 2015 ed., 2015, 2015.

[90] T. Carraro, *Multiple shooting and time domain decomposition methods MuS-TDD, Heidelberg, May 6-8, 2013*. Cham: Springer International Publishing, 1st ed. 2015 ed., 2015, 2015.

[91] B. Castellani, A. M. Gambelli, E. Morini, B. Nastasi, A. Presciutti, M. Filipponi, A. Nicolini, and F. Rossi, "Experimental investigation on CO2 methanation process for solar energy storage compared to CO2-based methanol synthesis," *Energies*, vol. 10, no. 7, pp. 1–13, 2017.

[92] L. K. Rihko-Struckmann, A. Peschel, R. Hanke-Rauschenbach, and K. Sundmacher, "Assessment of methanol synthesis utilizing exhaust CO2 for chemical storage of electrical energy," *Industrial and Engineering Chemistry Research*, vol. 49, no. 21, pp. 11073–11078, 2010.

[93] T. k. Ibrahim, M. K. Mohammed, O. I. Awad, M. Rahman, G. Najafi, F. Basrawi, A. N. Abd Alla, and R. Mamat, "The optimum performance of the combined cycle power plant: A comprehensive review," *Renew. Sustain. Energy Rev.*, vol. 79, no. March, pp. 459–474, 2017.

[94] O. Awe, Y. Zhao, A. Nzihou, D. Minh, and N. Lyczko, "A Review of Biogas Utilisation, Purification and Upgrading Technologies," *Waste and Biomass Valorization*, vol. 8, no. 2, pp. 267–283, 2017.

[95] P. Weiland, "Biogas production: Current state and perspectives," *Applied Microbiology and Biotechnology*, vol. 85, no. 4, pp. 849–860, 2010.

[96] A. El Sibai, L. K. Rihko Struckmann, and K. Sundmacher, "Model-based optimal sabatier reactor design for power-to-gas applications," *Energy Technology*, vol. 5, no. 6, pp. 911–921, 2017.

[97] D. Stolten and V. Scherer, *Transition to renewable energy systems*. Weinheim, Germany: Wiley-VCH Verlag GmbH & Co. KGaA, may 2013.

[98] K. Stangeland, D. Kalai, H. Li, and Z. Yu, "CO2 Methanation: The Effect of Catalysts and Reaction Conditions," *Energy Procedia*, vol. 105, pp. 2022–2027, 2017.

[99] D. Schlereth and O. Hinrichsen, "A fixed-bed reactor modeling study on the methanation of CO2," *Chemical Engineering Research and Design*, vol. 92, no. 4, pp. 702–712, 2014.

[100] S. Fendt, A. Buttler, M. Gaderer, and H. Spliethoff, "Comparison of synthetic natural gas production pathways for the storage of renewable energy," *Wiley Interdisciplinary Reviews: Energy and Environment*, vol. 5, no. 3, pp. 327–350, 2016.

[101] K. Zhou, S. Chaemchuen, and F. Verpoort, "Alternative materials in technologies for Biogas upgrading via CO2 capture," *Renew. Sustain. Energy Rev.*, vol. 79, no. June, pp. 1414–1441, 2017.

[102] J. G. Jee, M. B. Kim, and C. H. Lee, "Adsorption characteristics of hydrogen mixtures in a layered bed: Binary, ternary, and five-component mixtures," *Industrial and Engineering Chemistry Research*, vol. 40, no. 3, pp. 868–878, 2001.

[103] J. Yang, C. H. Lee, and J. W. Chang, "Separation of hydrogen mixtures by a two-bed pressure swing adsorption process using zeolite 5A," *Industrial and Engineering Chemistry Research*, vol. 36, no. 7, pp. 2789–2798, 1997.

[104] F. Lopes, C. Grande, A. Ribeiro, J. Loureiro, O. Evaggelos, V. Nikolakis, and A. Rodrigues, "Adsorption of H_2, CO_2, CH_4, CO, N_2 and H_2O in activated carbon and zeolite for hydrogen production," *Separation Science and Technology*, vol. 44, no. 5, pp. 1045–1073, 2009.

[105] E. N. Rudisill, J. J. Hacskaylo, M. D. LeVan, and J. J. Hacskaylo, "Coadsorption of hydrocarbons and water on BPL activated carbon," *Industrial and Engineering Chemistry Research*, vol. 31, no. 4, pp. 1122–1130, 1992.

[106] Shaoying Qi, K. James Hay, Mark J. Rood, and Mark P. Cal, "Equilibrium and heat of adsorption for water vapor and activated carbon," *Journal of Environmental Engineering*, vol. 126, pp. 267–271, 2000.

[107] Y. Wang and M. D. LeVan, "Adsorption equilibrium of binary mixtures of carbon dioxide and water vapor on zeolites 5A and 13X," *Journal of Chemical & Engineering Data*, vol. 55, no. 9, pp. 3189–3195, 2010.

[108] D. M. Ruthven, *Principles of adsorption and adsorption processes*. New York [u.a.]: Wiley, 1984.

[109] R. Augelletti, M. Conti, and M. C. Annesini, "Pressure swing adsorption for biogas upgrading. A new process configuration for the separation of biomethane and carbon dioxide," *Journal of Cleaner Production*, vol. 140, pp. 1390–1398, 2017.

[110] L. Ohlin, P. Bazin, F. Thibault-Starzyk, J. Hedlund, and M. Grahn, "Adsorption of CO2, CH4, and H2O in zeolite ZSM-5 studied using in situ ATR-FTIR spectroscopy," *Journal of Physical Chemistry C*, vol. 117, no. 33, pp. 16972–16982, 2013.

[111] L. Ohlin, A. Farzaneh, A. Holmgren, J. Hedlund, and M. Grahn, "Ternary adsorption of methane, water, and carbon dioxide in zeolite Na-ZSM-5 studied using in situ ATR-FTIR spectroscopy," *Journal of Physical Chemistry C*, vol. 121, no. 27, pp. 14703–14711, 2017.

[112] J. Andersson, J. Gillis, and M. Diehl, "User documentation for CasADi v1.9.0+292.1492000," 2014.

[113] "CAPE-OPEN." Available at `https://www.amsterchem.com/capeopen.html`, Accessed: 2017-07-31.

[114] D. Peshev and A. G. Livingston, "OSN Designer, a tool for predicting organic solvent nanofiltration technology performance using Aspen One, MATLAB and CAPE OPEN," *Chemical Engineering Science*, vol. 104, pp. 975–987, 2013.

[115] P. Collet, E. Flottes, A. Favre, L. Raynal, H. Pierre, S. Capela, and C. Peregrina, "Techno-economic and life cycle assessment of methane production via biogas upgrading and power to gas technology," *Appl. Energy*, vol. 192, pp. 282–295, 2017.

[116] X. Hong, Z. Liao, B. Jiang, J. Wang, and Y. Yang, "Simultaneous optimization of heat-integrated water allocation networks," *Appl. Energy*, vol. 169, pp. 395–407, 2016.

[117] E. Ahmetović and Z. Kravanja, "Simultaneous synthesis of process water and heat exchanger networks," *Energy*, vol. 57, pp. 236–250, 2013.

[118] I. E. Grossmann, P. A. Aguirre, and M. Barttfeld, "Optimal synthesis of complex distillation columns using rigorous models," *Comput. Aided Chem. Eng.*, vol. 18, no. C, pp. 53–74, 2004.

[119] J. Gong and F. You, "Global optimization for sustainable design and synthesis of algae processing network for CO2 mitigation and biofuel production using life cycle optimization," *AIChE J.*, vol. 60, pp. 3195–3210, sep 2014.

[120] P. Linke and A. Kokossis, "Attainable reaction and separation processes from a superstructure-based method," *AIChE J.*, vol. 49, no. 6, pp. 1451–1470, 2003.

[121] Q. Chen and I. Grossmann, *Recent developments and challenges in optimization-based process synthesis*, vol. 8. Annual Reviews., 2017.

[122] F. Trespalacios and I. E. Grossmann, "Chapter 24: Review of mixed-integer nonlinear optimization and generalized disjunctive programming applications in process systems engineering," *Advances and Trends in Optimization with Engineering Applications*, pp. 315–329, 2017.

[123] M. Gruber, P. Weinbrecht, L. Biffar, S. Harth, D. Trimis, J. Brabandt, O. Posdziech, and R. Blumentritt, "Power-to-Gas through thermal integration of high-temperature steam electrolysis and carbon dioxide methanation - Experimental results," *Fuel Processing Technology*, vol. 181, no. September, pp. 61–74, 2018.

[124] L. T. Biegler, I. E. Grossmann, and W. Westerberg, *Systematic methods of chemical process design*. Prentice Hall, 1997.

[125] Zauba, "Export data and price of catalyst meth 134." https://www.zauba.com/export-CATALYST+METH+134/hs-code-38151100/p-1-hs-code.html. Accessed: 12. September 2019.

[126] Alibaba, "Methanation catalyst suppliers and manufacturers at alibaba.com." https://www.alibaba.com/showroom/methanation-catalyst.html. Accessed: 12. September 2019.

[127] J. M. Douglas, *Conceptual design of chemical processes*. Singapore: McGraw-Hill, 1988.

[128] F. Bauer, C. Hulteberg, T. Persson, and D. Tamm, "Biogas upgrading – Review of commercial technologies, SGC 2013:270," *Swedish Gas Technology Centre, SGC*, no. June, p. 82, 2013.

[129] F. Ferella, A. Puca, G. Taglieri, L. Rossi, and K. Gallucci, "Separation of carbon dioxide for biogas upgrading to biomethane," *Journal of Cleaner Production*, vol. 164, pp. 1205–1218, 2017.

[130] V. Kumar Gupta and M. G. Tuohy, *Biofuel and biorefinery technologies 6 biogas: Fundamentals, process, and operation*. Springer, 2018.

[131] M. Jung, C. Kirches, and S. Sager, "On perspective functions and vanishing constraints in mixed-integer nonlinear optimal control," in *Facets of Combinatorial Optimization – Festschrift for Martin Grötschel* (M. Jünger and G. Reinelt, eds.), pp. 387–417, Springer Berlin Heidelberg, 2013.

[132] M. N. Jung, C. Kirches, S. Sager, and S. Sass, "Computational approaches for mixed integer optimal control problems with indicator constraints," *Vietnam Journal of Mathematics*, vol. 46, pp. 1023–1051, 2018.

[133] M. Ulbrich, *Nichtlineare Optimierung*. Springer Basel, 1st ed. ed., 2012.

[134] D. Schack, G. Liesche, and K. Sundmacher, "The fluxmax approach: Simultaneous flux optimization and heat integration by discretization of thermodynamic state space illustrated on methanol synthesis process," *Chemical Engineering Science*, vol. 215, p. 115382, 2020.

[135] G. Liesche, D. Schack, and K. Sundmacher, "The fluxmax approach for simultaneous process synthesis and heat integration: Production of hydrogen cyanide," *AIChE Journal*, vol. 65, no. 7, p. e16554, 2019.

[136] "EWK Kühlturm GmbH." https://ewk-kuehlturm.de/.

[137] L. Jiang, L. T. Biegler, and V. G. Fox, "Simulation and optimization of pressure-swing adsorption systems for air separation," *AIChE J.*, vol. 49, no. 5, pp. 1140–1157, 2003.

[138] M. Xu, S. Chen, D.-k. Seo, and S. Deng, "Evaluation and optimization of VPSA processes with nanostructured zeolite NaX for post-combustion CO2 capture," *Chemical Engineering Journal*, vol. 371, no. March, pp. 693–705, 2019.

[139] R. L. S. Canevesi, K. A. Andreassen, E. A. Silva, C. E. Borba, and C. A. Grande, "Pressure swing adsorption for biogas upgrading with carbon molecular sieve," *Industrial & Engineering Chemistry Research*, vol. 57, pp. 8057–8067, 2018.

[140] I. Angelidaki, L. Treu, P. Tsapekos, G. Luo, S. Campanaro, H. Wenzel, and P. G. Kougias, "Biogas upgrading and utilization: Current status and perspectives," *Biotechnology Advances*, vol. 36, no. 2, pp. 452–466, 2018.

[141] H. Hahn, W. Ganagin, K. Hartmann, and M. Wachendorf, "Cost analysis of concepts for a demand oriented biogas supply for flexible power generation," *Bioresource Technology*, vol. 170, pp. 211–220, 2014.

[142] J. Walsh, C. Ross, M. Smith, and S. Harper, "Utilization of biogas," *Biomass*, vol. 20, no. 3, pp. 277 – 290, 1989.

[143] I. U. Khan, M. H. D. Othman, H. Hashim, T. Matsuura, A. F. Ismail, M. Rezaei-DashtArzhandi, and I. W. Azelee, "Biogas as a renewable energy fuel – A review of biogas upgrading, utilisation and storage," *Energy Conversion and Management*, vol. 150, pp. 277–294, 2017.

[144] A. W. Dowling, S. R. R. Vetukuri, and L. T. Biegler, "Large-scale optimization strategies for pressure swing adsorption cycle synthesis," *AIChE J.*, vol. 58, no. 12, 2012.

[145] Z. Ding, Z. Han, Q. Fu, Y. Shen, C. Tian, and D. Zhang, "Optimization and analysis of the VPSA process for industrial-scale oxygen production," *Adsorption*, vol. 24, no. 5, pp. 499–516, 2018.

[146] Y. Wang, A. W. Dowling, C. Krieft, A. Walther, and L. T. Biegler, "Pressure swing adsorption optimization strategies for CO2 capture," *Comput. Aided Chem. Eng.*, vol. 36, 2015.

[147] L. T. Biegler, L. Jiang, and V. G. Fox, "Recent advances in simulation and optimal design of pressure swing adsorption systems," *Separation & Purification Reviews*, vol. 33, no. 1, pp. 1–39, 2004.

[148] L. Jiang, V. G. Fox, and L. T. Biegler, "Simulation and optimal design of multiple-bed pressure swing adsorption systems," *AIChE J.*, vol. 50, no. 11, 2004.

[149] C. Tsay, R. C. Pattison, and M. Baldea, "A pseudo-transient optimization framework for periodic processes: Pressure swing adsorption and simulated moving bed chromatography," *AIChE J.*, vol. 64, no. 8, pp. 2982–2996, 2018.

[150] Q. Fu, H. Yan, Y. Shen, Y. Qin, D. Zhang, and Y. Zhou, "Optimal design and control of pressure swing adsorption process for N2/CH4 separation," *Journal of Cleaner Production*, vol. 170, pp. 704–714, 2018.

[151] O. J. Smith IV and A. W. Westerberg, "The optimal design of pressure adsorption systems," *Chemical Engineering Science*, vol. 46, no. 12, pp. 2967–2976, 1991.

[152] W. Tao, S. Ma, J. Xiao, P. Bénard, and R. Chahine, "Simulation and optimization for hydrogen purification performance of vacuum pressure swing adsorption," *Energy Procedia*, vol. 158, pp. 1917–1923, 2019.

[153] S. R. R. Vetukuri, L. T. Biegler, and A. Walther, "An inexact trust-region algorithm for the optimization of periodic adsorption processes," *Industrial & Engineering Chemistry Research*, vol. 49, no. 1, pp. 12004–12013, 2010.

[154] A. W. Dowling, S. R. R. Vetukuri, and L. T. Biegler, "Large-scale optimization strategies for pressure swing adsorption cycle synthesis," *AIChE J.*, vol. 58, no. 12, 2012.

[155] A. Agarwal, L. T. Biegler, and S. E. Zitney, "Simulation and optimization of pressure swing adsorption systems using reduced-order modeling," *Industrial & Engineering Chemistry Research*, vol. 48, pp. 2327–2343, mar 2009.

[156] A. Agarwal and L. T. Biegler, "A trust-region framework for constrained optimization using reduced order modeling," *Optimization and Engineering*, vol. 14, no. 1, pp. 3–35, 2013.

[157] K. S. Knaebel and F. B. Hill, "Pressure swing adsorption: Development of an equilibrium theory for gas separations," *Chemical Engineering Science*, vol. 40, no. 12, pp. 2351–2360, 1985.

[158] J. P. Eason, *A trust region filter algorithm for surrogate-based optimization*. PhD thesis, Carnegie Mellon University, 2018.

[159] J. P. Eason and L. T. Biegler, "Model reduction in chemical process optimization," *De Gruyter*, 2019.

[160] N. Yoshio and L. T. Biegler, "Demand-based optimization of a chlorobenzene process with high-fidelity and surrogate reactor models under trust region strategies," *AIChE Journal*, vol. 67, no. 1, p. e17054, 2021.

[161] A. Potschka, M. S. Mommer, J. P. Schlöder, and H. G. Bock, "Newton–picard-based preconditioning for linear-quadratic optimization problems with time-periodic parabolic pde constraints," *SIAM Journal on Scientific Computing*, vol. 34, no. 2, pp. A1214–A1239, 2012.

[162] F. M. Hante, M. S. Mommer, and A. Potschka, "Newton–picard preconditioners for time-periodic parabolic optimal control problems," *SIAM Journal on Numerical Analysis*, vol. 53, no. 5, pp. 2206–2225, 2015.

[163] R. C. Baliban, J. A. Elia, and C. A. Floudas, "Optimization framework for the simultaneous process synthesis, heat and power integration of a thermochemical hybrid biomass, coal, and natural gas facility," *Computers and Chemical Engineering*, vol. 35, no. 9, pp. 1647–1690, 2011.

[164] "COMSOL." https://www.comsol.com/chemical-reaction-engineering-module. Accessed: 10. February 2020.

[165] L. Ting, P. M. Castro, and L. Zhimin, "Models and relaxations for the wastewater treatment design problem," *Chemical Engineering Research and Design*, vol. 106, pp. 191–204, 2016.

[166] G. Jeanmonod, L. Wang, S. Diethelm, F. Maréchal, and J. Van herle, "Trade-off designs of power-to-methane systems via solid-oxide electrolyzer and the application to biogas upgrading," *Appl. Energy*, vol. 247, no. April, pp. 572–581, 2019.

[167] J. Bremer, K. H. G. Rätze, and K. Sundmacher, "CO2 methanation: Optimal start-up control of a fixed-bed reactor for power-to-gas applications," *AIChE J.*, vol. 63, pp. 23–31, jan 2017.